

Strongly Correlated Ultracold Bosons in an Optical Lattice

Dissertation
zur Erlangung des Doktorgrades
der Naturwissenschaften

vorgelegt beim Fachbereich Physik
der Goethe-Universität Frankfurt
in Frankfurt am Main

von
Yongqiang Li
aus Henan (China)

Frankfurt am Main 2012

vom Fachbereich Physik der Goethe-Universität Frankfurt als Dissertation
angenommen.

Dekan: Prof. Dr. Michael Huth
Gutachter: Prof. Dr. Walter Hofstetter
Prof. Dr. Peter Kopietz

Datum der Disputation

Contents

1	Introduction	1
1.1	Strongly correlated ultracold bosons	1
1.2	Why strongly correlated ultracold bosons?	2
1.3	Overview of ultracold gases	3
1.4	Outline of the thesis	5
2	Optical Lattice	7
2.1	The ac Stark effect	7
2.2	Optical lattice potential	8
2.3	Spin-dependent optical lattice	10
2.4	Interactions between atoms in optical lattices	11
2.4.1	Contact interactions	11
2.4.2	Inelastic collisions in loss processes	13
2.5	Heating processes in optical lattices	14
3	Bose-Hubbard Model	17
3.1	Many-body system	17
3.2	Standard Bose-Hubbard model	18
3.2.1	Single-component Bose-Hubbard model	19
3.2.2	Multi-component Bose-Hubbard model	21
3.3	Bose-Hubbard model for ultracold gases in an optical cavity	23
3.3.1	Many-body Hamiltonian	24
3.3.2	Extended Bose-Hubbard model	25
3.4	Bose-Hubbard model for dipolar bosonic gases	27
3.4.1	Dipole-dipole interaction	27
3.4.2	Dipolar bosonic gases in an optical lattice	28
4	Theoretical Approaches	31
4.1	Ground state of a quantum many-body system	32
4.1.1	Quantum phase transition	32
4.1.2	Symmetry breaking vs. phase transition	33
4.2	Mean-field approach	34
4.2.1	Superfluid phase	36
4.2.2	Mott-insulating phase	37
4.3	Bosonic dynamical mean field theory	38
4.3.1	BDMFT equations	39

4.3.2	Anderson impurity model	42
4.4	Real-space bosonic dynamical mean field theory	45
5	Quantum Magnetism and Pair Superfluidity	49
5.1	Quantum magnetism	50
5.1.1	Introduction	50
5.1.2	Magnetic phases of a homogeneous Bose-Hubbard model	51
5.1.3	Spin-ordering for an inhomogeneous Bose-Hubbard model	55
5.1.4	Summary	62
5.2	Pomeranchuk effect and spin-gradient cooling	63
5.2.1	Introduction	63
5.2.2	Model and method	65
5.2.3	Pomeranchuk effect and phase diagram at finite T	66
5.2.4	Entropy distribution in the trapped system with $B = 0$.	67
5.2.5	Adiabatic cooling via entropy redistribution for $B \neq 0$. .	70
5.2.6	Summary	75
5.3	Pair-superfluidity	75
5.3.1	Introduction	75
5.3.2	Homogeneous Bose gases with attractive interactions . .	76
5.3.3	Trapped Bose gases in 2D and 3D cases	81
5.3.4	Summary	85
6	Ultracold Bosonic Gases with Long-Range Interactions	87
6.1	BEC-cavity system	87
6.1.1	Introduction	87
6.1.2	Setup of the BEC-cavity system	88
6.1.3	Quantum phases of a homogeneous Bose gas	88
6.1.4	Quantum phases for an inhomogeneous system	94
6.1.5	Summary	96
6.2	Strongly correlated dipolar bosonic gases	96
6.2.1	Introduction	96
6.2.2	Model and method	97
6.2.3	Results	97
6.2.4	Summary	101
7	Spectroscopy of Strongly Correlated Ultracold Bosons	103
7.1	Introduction	103
7.2	Model and method	103
7.2.1	Model	103
7.2.2	Method	106
7.3	Results	107
7.3.1	Bragg spectroscopy beyond perturbation theory	107
7.3.2	Comparison with experimental observation	110
7.4	Summary	112

8	Conclusions and Outlook	113
9	Zusammenfassung und Ausblick	117
A	The Jaynes-Cummings Model	123
B	Gutzwiller vs. Mean-Field Approximations	125
C	Effective Action in BDMFT	127
D	Superfluid Order Parameter	131
	D.1 The first method: perturbation theory	131
	D.2 The second method	132
E	Self-Energy	135
F	Lattice Green's Function	139
	Bibliography	141
	Acknowledgements	161
	Curriculum Vitae	163

Chapter 1

Introduction

1.1 Strongly correlated ultracold bosons

The experimental discovery of Bose-Einstein condensation (BEC) has opened up the exploration of quantum phenomena in a qualitatively new regime [1]. Due to its universality, BEC has been regarded as a *quantum simulator* of many-body quantum physics in the field of condensed matter physics, high energy astrophysics, and quantum optics. Recent experimental progress in controlling quantum optical and atomic systems [2, 3] has given rise to tunable interactions, which allows to access the strongly interacting regime. Strongly correlated quantum gases thus provide an excellent playground for studying fundamental problems in many-body physics and, in particular, for entering regimes and new quantum phases that have never been accessible in condensed matter or nuclear physics, with an unprecedented level of precision and control [4]. This thesis focuses on strongly correlated ultracold bosonic gases trapped in optical lattices. Our motivation is to understand strongly correlated quantum phases and quantum magnetism of multi-component bosonic gases in optical lattices. Indeed, mixtures of bosonic flavors, either from different atomic species or different hyperfine states of a single species, give rise to a very rich phase diagram. To describe this physics, the Bose-Hubbard model [5], which incorporates strong correlations of the many-body system and successfully captures the Mott transition, is utilized as a generic model for the many-body system in an optical lattice. The Bose-Hubbard model is exactly solvable in one dimension system using the Bethe ansatz for the wave function [6]. For higher dimensions, however, numerical approaches need to be applied to tackle the many-body system. One of them is (real-space) bosonic dynamical mean field theory (R)BDMFT [7–13], which has been established as a nonperturbative approach and provides a comprehensive, thermodynamically consistent framework for the theoretical investigation of correlated lattice systems. The main task in this thesis is to study the strongly interacting many-body system captured by the Bose-Hubbard model, by means of BDMFT/RBDMFT.

1.2 Why strongly correlated ultracold bosons?

Interactions lie at the heart of strongly correlated solid-state systems, such as heavy fermions [14], high T_c superconductivity and Mott-insulator [15]. In these systems, interactions drive an instability towards ordered ground states which exhibit magnetism and superconductivity (especially those systems with partially occupied d - or f -electrons) [16]. Due to the high level of complexity in solid-state materials, however, a quantitative comparison between theory and experiment seems a very challenging task, if it is even possible at all. Therefore it is highly desirable to work with experimental systems which are able to simulate the original solid-state many-body systems, but in a much more controllable way. Over the past decade, considerable experimental and theoretical efforts have been made in ultracold gases, which provide a clean, controllable and tunable laboratory, to access the puzzling quantum phenomena of solid-state systems. However, the interactions in dilute, ultracold gases are naturally very weak, since particle distances are typically of order 10^2 nm [1] which is usually larger than the length scales of atom-atom interactions, and in this case the system can be well described by the Gross-Pitaevskii equation [17, 18]. Therefore, we can ask how we can make the systems strongly correlated, and whether we can provide new tools for the simulation of strongly correlated solid-state systems? Fortunately, interactions between atoms can easily be tuned experimentally to access the strongly interacting regime via Feshbach resonances [2, 19, 20] or optical lattices [3]. Typically, correlations of atoms in dilute ultracold gases are dominated by two-body interactions due to large particle separations, and can be treated as a two-particle quantum scattering problem governed by relevant interatomic potentials. To gain insight into properties of dilute quantum gases, therefore, it is important to understand the scattering of atoms under the influence of an interatomic potential [21]. Due to basic features of ultracold many-body systems, i.e. atoms with small kinetic energy and short-ranged interactions, the scattering process between two atoms can be considered in this low energy limit and, correspondingly, the interactions between bosons are governed entirely by the s-wave scattering length, which can be easily tuned in a wide range via Feshbach resonances due to the spin-dependence of the interatomic interactions. The tunability of the s-wave scattering length in ultracold gases provides the possibility to simulate strongly correlated many-body systems in ultracold experiments with a high degree of controllability and precision.

Long-range interactions are a further key ingredient for strongly correlated systems and tend to stabilize further novel phases [22, 23]. Long-range interactions often occur in materials science and compete with short-range interactions, which leads to spatially modulated phases [24]. Usually, there are two ways to create ultracold many-body quantum systems with dominant long-range interactions: one approach exploits dipolar forces in ultracold atoms and molecules [23]; another one is based on atoms inside a high-finesse optical

cavity, where the cavity field mediates infinitely long-range forces between all atoms [25]. Recently, experimental realizations of a dipolar Bose-Einstein condensate [26], polar molecules [27], and a Bose-Einstein condensate coupled to an optical cavity [25] have opened the path towards studies of quantum gases with long-range interactions and given access to novel quantum phases with intriguing properties.

1.3 Overview of ultracold gases

Let us consider two possible ways to observe coherence on the macroscopic scale: lasing of light and Bose-Einstein condensation. Even though the first successful optical laser was invented by T. H. Maiman in 1960 [28], Bose-Einstein condensation was not observed until 1995 due to large decoherence effects and the requirement of very low temperature. Thanks to intense efforts over many years on cooling and manipulating atoms (see Fig. 1.1), as summarized in the Nobel lectures given by W. D. Phillips, S. Chu and C. N. Cohen-Tannoudji [29–31], a Bose-Einstein condensate with macroscopic ground-state occupation of particles with integer spin at low temperature and high density, which was suggested by Einstein in 1925, was first observed experimentally in a dilute weakly-interacting ^{87}Rb gas in 1995, as described in the Nobel lectures of E. A. Cornell, C. E. Wieman and W. Ketterle [32, 33]. Since then, BEC has been observed in several physical systems, including cold atomic gases [34, 35], solid-state quasi-particles [36, 37], and photons [38], and the study of ultracold Bose gases has become one of the most active areas in contemporary physics [1, 4]. Ultracold fermions [39], which consist of another main branch in ultracold gases, were investigated as well after the first realization of quantum degeneracy in Fermi gases [40].

In the development of ultracold physics in recent years, a high degree of attention has been paid to strongly correlated systems which comprise a large variety of quantum many-body systems. Even though the interactions in dilute, ultracold gases are very weak, new experimental techniques have made it possible to access the strongly interacting regime in which interactions between particles are much larger than their kinetic energies. One method of reaching the strongly interacting regime in dilute, ultracold gases is via Feshbach resonances, which allow the scattering length to be increased to values beyond the average inter-particle spacing. Exploiting Feshbach resonances to tune the interactions has made it possible to study new properties of bosonic gases beyond the mean-field level [41], such as the crossover from a molecular Bose-Einstein condensate to BCS pairing [42], and ultracold polar molecules [27], as summarized in the review papers [43–45]. Another method that can access the strongly correlated regime is to reduce the kinetic energy of atoms via ramping up optical lattices, which has opened up new possibility for manipulation and control, in many cases creating structures far beyond those currently achievable in typical condensed-matter physics systems [46]. By loading

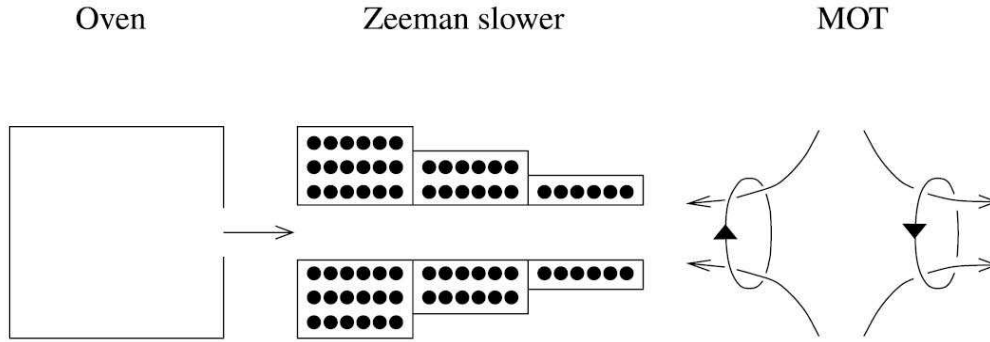


Figure 1.1: A typical experiment to cool and trap alkali atoms (From Ref. [1]): Sodium atoms, emerging from an oven at a temperature of ≈ 600 K (a speed of ≈ 800 ms^{-1}), pass through Zeeman slower with a reduced temperature of ≈ 1 K (a speed of ≈ 30 ms^{-1}), and then captured by magneto-optical trap (MOT) with a further cooled temperature of ≈ 100 μK .

ultracold gases into optical lattices, experimentalists have realized the superfluid to Mott-insulator transition of single-component bosonic gases [3], and formation of the Mott insulator of two-component fermionic gases in a three-dimensional optical lattice [47, 48]. One of the ultimate goals of cold-atomic gases in optical lattices is to include the spin degree of freedom and simulate solid-state phenomena, such as high T_c superconductivity whose mechanism has so far remained elusive [49]. However, the typical lowest temperatures in current experiments are of the order of $0.1T/T_F$ and $0.3T/T_c$ for fermions and bosons, respectively [50]. These experimental temperatures are too high to realize quantum magnetic phases due to superexchange processes governed by second-order tunneling [51, 52]. In other words, the temperature scale for magnetic ordering, such as the anti-ferromagnetic phase, is still out of reach, and the long-standing puzzle related to high T_c superconductivity, so far, remains unanswered experimentally. Recently, several cooling schemes have been proposed to lower the temperature of the atomic system, and by exploiting spin-gradient adiabatic demagnetization one has achieved a temperature of 350 picokelvin [53], which is the lowest value realized experimentally. After achieving sufficiently low temperatures, these novel magnetic phases are expected to be detected in the future by single-site addressing microscopy [54–56], developed recently for quantum gases in optical lattices.

The realization of novel quantum phases of many-body systems is also of large interest in the presence of long-range interactions. One method for introducing long-range interactions is to induce a strong dipole-dipole coupling between particles, which is long-range and anisotropic as opposed to the much more highly localized contact interaction of ultracold atoms. The dipole-dipole interactions as a result of, permanent or induced, magnetic or electric dipole moment of the electron can be easily tuned from attractive to repulsive by

an applied external electronic field. Within this framework, it offers a new means for controlling and manipulating ultracold gases and gives access to novel quantum states. Ultracold gases with strong dipolar interactions have been experimentally realized in systems of chromium or dysprosium Bose-Einstein condensates [57, 58], ultra-cold heteronuclear molecules [27] and BECs with Rydberg excitations [59]. An alternative way to introduce long-range interactions [25] is to couple the ultracold gas to a high-finesse optical cavity where photons can make many round-trips between the mirrors before decaying into the environment. High-finesse cavities have been widely used to study single atom detection [60], few atom cooling [61–63] and trapping [64, 65], due to the strong-coupling induced light force felt by atoms in the cavity. Currently, high-finesse cavities coupled to atomic many-body systems are attracting a large amount of attention [66]. In particular, a self-organized phase of atoms due to coherent scattering between the pump laser and the cavity mode has been predicted theoretically [67] and then further confirmed experimentally by laser-cooled atoms in a transversally pumped cavity [68]. However, combining a high-finesse cavity with ultracold gases in the strong-coupling regime has only recently been achieved, and properties of the Bose-Einstein condensate loaded into a cavity experimentally investigated [69–72]. The first realization of the self-organized phase of an ultracold gas coupled to an optical cavity has been achieved in T. Esslinger’s group [25], where a transition from a normal to a self-organized phase has been observed, with a measured lifetime up to 10ms for the self-organized phase indicating a steady state. This novel many-body state arises due to the small size of the cavity which makes the coupling between atoms and photons very strong. In this case, the mechanical action of the electromagnetic radiation field on the atoms should be considered, and, in turn, the back action of the atom on the cavity mode can not be neglected, as opposed to conventional laser fields where coupling between atoms and laser fields is treated as an external potential acting on atoms. Hence, the dynamics of atoms in the optical cavity can not be separated from that of the cavity mode, i.e. all the atoms are coupled together by the cavity mode which gives rise to cavity-mediated infinitely long-range interactions between atoms. If the long-range interaction between the condensed atoms is sufficiently strong, it will dominate the physical behavior of the system and provide access to novel quantum phases.

1.4 Outline of the thesis

The goal of this thesis is to provide a further step towards a theoretical understanding of the properties of strongly correlated ultracold bosonic gases in optical lattices, including quantum magnetism, pair-superfluidity, many-body cooling, new physics with long-range interactions, and excitational properties of the systems. The theoretical challenge we face lies in the strong interactions between atoms which invalidates perturbation theory that is well suited for

weakly interacting many-body systems. The central issue of this thesis is how interactions determine physical behaviors of many-body quantum systems.

In this chapter, we have introduced the motivation of this thesis and the related scientific background. The following Chapters are arranged as follows:

First, we will investigate a two-component Bose gas in two-dimensional (2D) and three-dimensional (3D) optical lattices. We investigate the homogeneous (untrapped) system for the special case of filling $n = 1$ and $n = 2$ per site by means of BDMFT [7–10] and the harmonically trapped case by its real-space generalization (RBDMFT) [12]. Special emphasis will be put on the magnetic phases for positive inter-species interactions, and the pair-superfluid phase for negative inter-species interactions. We map out phase diagrams for these two cases, which contain diverse quantum phases, such as superfluid and pair-superfluid phases, an unordered Mott state, and anti-ferromagnetic and XY-ferromagnetic ordering. In addition, we also study the effect of inhomogeneity which is connecting the work to the experimental situation. Then, we will focus on thermodynamical properties of two component bosons in a 3D optical lattices in the presence of an external trap, and investigate the validity of spin-gradient demagnetization and Pomeranchuk cooling. We will also investigate the finite temperature phase diagram in a 3D cubic lattice, and the entropy distribution in the trapped system. Our aim is to study the possibility of achieving critical temperatures of quantum magnetic phases.

Second, we will study the effect of long-range interactions on properties of the quantum many-body system. For a BEC coupled to an optical cavity, we mainly investigate the influence of on-site particle-particle interactions on the buildup of self-organized phases and identify the transition from a homogeneous superfluid to a self-organized phase. We also study the trapped BEC-cavity system and determine the effect of inhomogeneity on the buildup of self-organized phases. For dipolar systems, we mainly investigate the influence of dipole-dipole interactions on magnetic phases of Bose-Bose mixtures, and map out the phase diagram of dipolar bosons in an optical lattice.

In the following chapter, we focus on the spectroscopy of strongly correlated bosonic gases in an optical lattice. Our aim is to detect the Higgs-type amplitude mode using Bragg spectroscopy in a strongly interacting condensate of ultracold atoms in an optical lattice. This method allows for a clear identification of the amplitude mode, with full momentum resolution by going beyond the linear response regime. We will also make a quantitative comparison between theoretical simulation and experimental observation.

Finally, we will present a summary of the thesis and give an outlook on perspectives for future research arising from this work.

Chapter 2

Optical Lattice

In this chapter, we will explain how to create an optical lattice and how to trap neutral particles by laser light. Optical lattices, artificial crystals of light consisting of hundreds of thousands of optical microtraps, are routinely created by interfering optical laser beams [73]. They act as external potentials for trapping ultracold quantum gases of bosons, fermions or their mixtures. Here, the interfering laser beams form a crystal structure, and ultracold atoms in the lattice play the part of electrons in an artificial solid. This realizes powerful models of quantum many-body systems in periodic potentials for probing nonlinear wave dynamics and strongly correlated quantum phases, and fundamental properties of solid matter. The advantage of optical lattices is the possibility of the full control of lattice geometry, lattice depth and interactions. Ultracold gases in optical lattices represent a fast-paced modern and interdisciplinary field of research.

2.1 The ac Stark effect

Even though neutral atoms do not have an electric dipole moment, an applied electric field can induce a dipole moment which is known as the ac Stark shift. Considering a two-level (non-degenerate) atom and far-detuned laser light, the ac Stark effect on the atomic levels can be treated as a perturbation up to second order of the electric field, i.e. linear in terms of the applied electric field and the field intensity, which induces a shift of the atom's energy in the electric field. The energy shift of the atom can be given by time-independent perturbation theory:

$$E_{\text{shift}} = \langle i | \hat{H}_{\text{int}} | i \rangle + \sum_{j \neq i} \frac{|\langle j | \hat{H}_{\text{int}} | i \rangle|^2}{E_i - E_j}, \quad (2.1)$$

where $\hat{H}_{\text{int}} = -\hat{\mu}E$ denotes the interactions between a single atom and laser light with $\hat{\mu} = -er$ representing the electric dipole operator, and $E_{i,j}$ are energy levels of the free atom. Note that the linear Stark effect depends on the degeneracy of the energy levels and thus alkali metal atoms do not exhibit the linear Stark effect. Here we consider the ground state of the atoms which

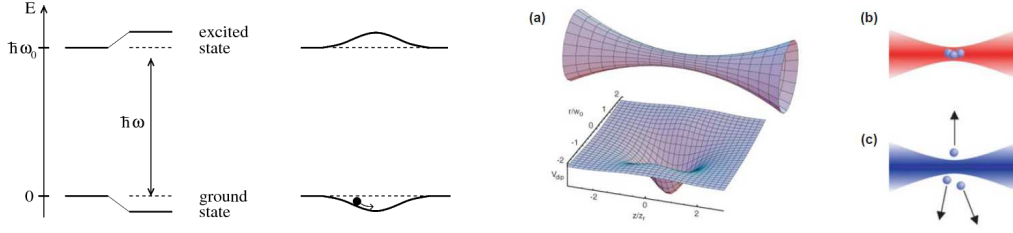


Figure 2.1: **Left:** Light shifts for a two-level atom (From Ref. [74]). **Right:** (a) Gaussian laser beam together with corresponding trapping potential for a red detuned laser beam. (b) A red detuned laser beams leads to an attractive dipole potential, whereas a blue detuned laser beam leads to a repulsive potential (c) (From Ref. [75]).

yields a total energy $E_i = n\hbar\omega$ for the the whole system, where ω denotes the light frequency. When the atom is excited by absorbing a photon, the total energy of the whole system becomes $E_j = \hbar\omega_0 + (n - 1)\hbar\omega = -\hbar\Delta_{ij} + n\hbar\omega$ with $E_i - E_j = -\hbar\Delta_{ij}$. For a two-level atom, the energy shift is:

$$E_{\text{shift}} = \pm \frac{|\langle e|\hat{\mu}|g\rangle|^2}{\Delta} |E|^2 \quad (2.2)$$

for the ground state and excited states, respectively. The optically induced energy shift of the ground state exactly corresponds to a conservative dipole potential for the two-level atoms. The energy shift indicates a very interesting fact: it is directly proportional to the time-averaged light intensity $I(r) \propto \langle E^2(r, t)_t \rangle$. Therefore, we can use a spatially inhomogeneous light field to generate different potential wells to trap atoms in the ground state at very low temperatures, as shown in Fig 2.1.

In the more general case, perturbation theory can be easily extended to a multi-level system to clarify the role of hyperfine structure, magnetic sub-structure and polarization of light. Based on this, one can derive a more general formula for the energy shift which depends on the total angular momentum F , magnetic quantum number m_F and polarization of the light. A more detailed discussion can be found in [74].

2.2 Optical lattice potential

Optical lattices, i.e. artificial crystals of light, give rise to a spatially periodic potential acting on atoms due to the ac Stark effect. Such a system is an analog to condensed matter systems and can be used to trap millions of atoms for simulating electrons in solids. It is possible to generate potentials which are periodic in one, two or three dimensions, by creating a standing-wave field formed by overlapping two counterpropagating laser beams in the corresponding direction.

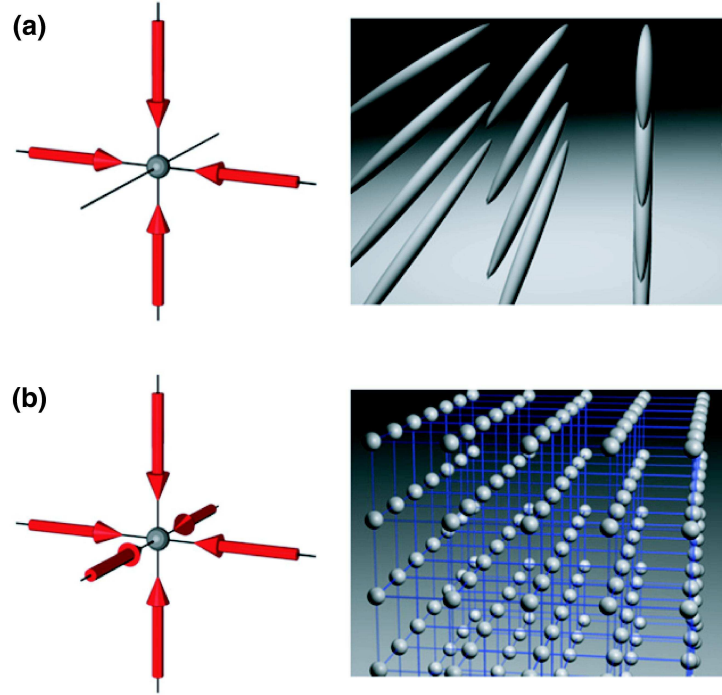


Figure 2.2: Optical lattices. (a) Two- and (b) three-dimensional optical lattice potentials formed by superimposing two or three orthogonal standing waves (From Ref. [4]).

First, let's consider the interference between two counterpropagating laser beams with frequency $\omega_{1,2}$ and wavelength $\lambda_{1,2}$. For simplicity, we assume that both beams are linearly polarized and the phase angles of the two beams are zero. In this case, the electrical field along the z -direction is:

$$E_z = \mathbf{E}_1 \cos(q_1 z - \omega_1 t) + \mathbf{E}_2 \cos(q_2 z + \omega_2 t) \quad (2.3)$$

and the average of its square is thus:

$$\langle E_z^2 \rangle_t = \frac{1}{2} E_1^2 + \frac{1}{2} E_2^2 + \mathbf{E}_1 \cdot \mathbf{E}_2 \cos \left[(q_1 - q_2) z - (\omega_1 - \omega_2) t \right]. \quad (2.4)$$

Here we assume that the dynamical time scale is much larger than the inverse laser frequency, and that the frequency difference of the two beams is small compared with the average. As a result, the atoms effectively feel the time-averaged potential $V(z) \propto \langle E_z^2 \rangle_t$. From Eq. (2.4) one can see that the last term corresponds to interference between the two beams, and it vanishes if the polarizations of the two beams are orthogonal. In the most frequently used case both beams are linearly polarized with the electric-field vector along the same axis, and the same frequency ω and wavelength λ . In this case, the time-averaged potential is

$$V(z) \propto \langle E_z^2 \rangle_t = E_0^2 (\cos 2qz + 1). \quad (2.5)$$

A periodic potential in higher dimensions can be formed in the same way, created by additional perpendicular laser beams with wavelength λ . For reasons of brevity, we only discuss a two-dimensional lattice in the following. The potential created by this set-up is:

$$V(y, z) \propto 2E_0^2 \left[\cos^2(ky) + \cos^2(kz) + 2\mathbf{e}_1 \cdot \mathbf{e}_2 \cos \phi \cos(ky) \cos(kz) \right], \quad (2.6)$$

where ϕ is the temporal phase between them, and \mathbf{e}_1 and \mathbf{e}_2 are the polarizations for the two laser beams directed in y and z directions. The interference term in (2.6) only arises if the two lasers are coherently coupled, which can be avoided by choosing orthogonal polarization vectors and by using slightly different wavelengths for the standing wave. The orthogonal polarization is most commonly used and leads to a spatial separation of standing waves, which turn out to be a square lattice (see Fig. 2.2). For three dimensions all polarizations can be chosen orthogonal to one another, yielding a direct three-dimensional realization of the cubic lattice (see Fig. 2.2). A further advantage of optical lattice compared to conventional solid-state systems is the independent tunability of the different components of the lattice with a high level of precision, allowing the realization of effective lower-dimensional systems. If the lattice in the z -direction is set sufficiently high, for example, tunneling in this direction is suppressed and one creates an array of two-dimensional lattice plates. When performing any measurement on the system, one measures the (classical) statistical average of the different two-dimensional subsystems of the respective quantity. Note that the Gaussian beam profile of the laser beams has been neglected when we derived the trapping potential, since the distance from the trap center is normally smaller than the beam waist in the experiment.

2.3 Spin-dependent optical lattice

In the previous section 2.1, we have derived the optical potential for ultra-cold atoms in the electromagnetic field based on a two-level approximation. In real atoms, however, the two-level approximation is not accurate due to the fine and hyperfine splitting, and a number of excited states of atoms. Actually, the spin-dependent potentials can be created via the more complex system by using interactions between atoms and electromagnetic fields, including effects from hyperfine splitting, Zeeman and ac Stark shifts. For large detunings of the laser light compared to the fine-structure splitting Δ'_{FS} of a typical alkali-metal atom, i.e. the fine-structure is not resolved, the resulting optical lattice potentials are almost the same for all magnetic sublevels in the ground-state manifold of the atom, and a two-level approximation is valid, as given by Eq. (2.2). However, for more near-resonant light fields, more complex potentials can be created, where different magnetic sublevels can be exposed to vastly different optical potentials. Such spin-dependent lattice potentials

can, for example, be created in a standing wave configuration formed by two counterpropagating laser beams with linear polarization vectors enclosing an angle. For a monochromatic laser field and an alkali atom with optical detuning large compared to the excited-state hyperfine splitting Δ'_{HFS} , a more general form for the ground state potential arising from the ac Stark effect is [74, 76]:

$$V(\mathbf{r}) = \frac{\pi c^2 \Gamma}{2\omega_0^3} \left(\left(\frac{2}{\Delta_{3/2}} + \frac{1}{\Delta_{1/2}} \right) I(\mathbf{r}) + g_F m_F \sum_{q=-1,0,1} q \left(\frac{1}{\Delta_{3/2}} - \frac{1}{\Delta_{1/2}} \right) I_q(\mathbf{r}) \right), \quad (2.7)$$

where c is the speed of light, Γ is the decay rate of the electric excited state, ω_0 is the angular frequency of the atomic transition, I_q is the laser intensity with polarization q ($I = \sum_{q=-1,0,1} I_q$), and $\Delta_{3/2}$ ($\Delta_{1/2}$) is the detuning of the laser frequency relative to the $S \rightarrow P_{3/2}$ ($S \rightarrow P_{1/2}$) transition (ω_L is the angular frequency of the laser). A more detailed discussion can be found in Ref. [74, 76].

Spin-dependent lattices have been used to coherently move atoms across lattices and realize quantum gates [77]. They furthermore offer a convenient way to tune interactions between two atoms in different spin states. By shifting the spin-dependent lattices relative to each other, the overlap of the on-site spatial wave function for two different spin states can be tuned, thus controlling the interspecies interaction strength within a restricted range [78].

2.4 Interactions between atoms in optical lattices

The knowledge of interaction potentials between two atoms in an optical lattice is crucial in order to determine properties of the strongly-correlated many-body system. However, the situation is complicated, as a atom might have a spin degree of freedom and atoms with different spins can interact with each other. On the one hand, this property can be used to tune the interactions between two atoms. On the other hand, it can lead to an unwanted loss of trapped atoms. In this section we will discuss this issue in detail.

2.4.1 Contact interactions

Interactions play an important role in many-body systems. Unlike real materials, the ultracold system in optical lattices can be tuned in a wide range of parameters, including the interactions between two particles. The physical origin of two-particle interactions is the short-ranged Van der Waals force, which gives rise to a short-ranged potential and is often well described by Lennard Jones potential [79] which falls off as $U(r - r') \propto \frac{1}{|r - r'|^6}$ on long-range scales. For ultracold atoms, a scattering model is widely used to describe the interactions. At sufficiently low temperatures, as in the case of ultracold atoms, scattering in states with $l \neq 0$ (l denotes angular momentum in relative motion) is frozen out due to the centrifugal barrier, and only s-wave channels

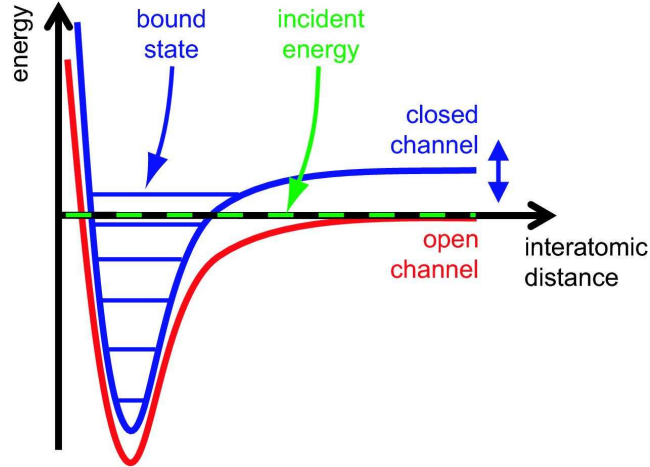


Figure 2.3: The two-channel model for a Feshbach resonance. Atoms prepared in the open channel, corresponding to the interaction potential $V_{\text{op}}(r)$ (in red), undergo a collision at low incident energy. In the course of the collision the open channel is coupled to the closed channel $V_{\text{cl}}(r)$ (in blue). When a bound state of the closed channel has an energy close to zero, a scattering resonance occurs. The position of the closed channel can be tuned with respect to the open one e.g. by varying the magnetic field B (From Ref. [4]).

need to be considered for the scattering problem. In the s-wave and low-energy limit, the exact shape of the short-ranged potential becomes irrelevant and the interactions are completely described by the scattering length a_s as the single parameter. One may use a short-ranged pseudopotential for the description of two-body interactions:

$$U(r - r') \approx \frac{4\pi\hbar^2 a_s}{2M_r} \delta(r - r'), \quad (2.8)$$

where M_r is reduced mass of the two particles. This pseudopotential approximation is valid in a wide range of situations, provided no longer-range contributions come into play as, e.g., in the case of dipolar gases.

The s-wave scattering length plays a central role for the description of two-particle interactions, since it is the only parameter to describe their strength. In addition, the s-wave scattering can be tuned via Feshbach resonances. A Feshbach resonance occurs in the elastic scattering process if the incoming atoms in an open channel (scattering state) are close to the energy of a bound state in a closed channel (see Fig. 2.3). It is usually accessible in experiments, since the true interaction potential has many bound states that can be shifted near resonance by the use of a magnetic field. Phenomenologically, the scattering length as a function of the magnetic field can be expressed as

$$a_s(B) = a_{\text{bg}} \left(1 - \frac{\Delta\Gamma}{B - B_0} \right), \quad (2.9)$$

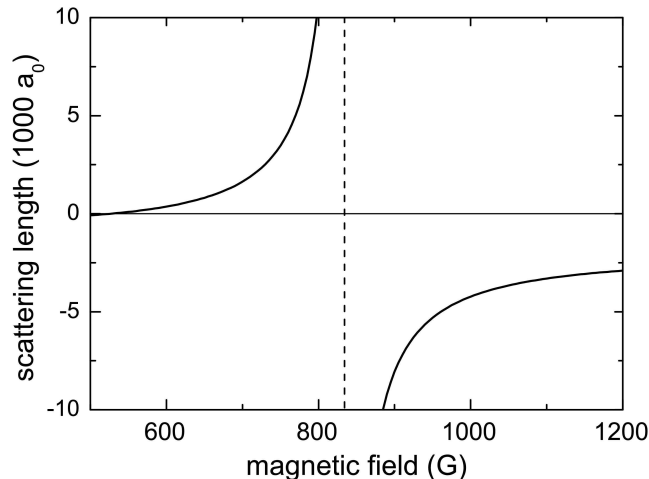


Figure 2.4: Magnetic field dependence of the scattering length between the two lowest magnetic sub-states of ${}^6\text{Li}$ with a Feshbach resonance at $B_0 = 834$ G and a zero crossing at $B_0 + \Delta B = 534$ G. The background scattering length $a_{\text{bg}} = -1405 a_B$ is exceptionally large in this case (a_B being the Bohr radius) (From Ref. [4]).

where a_{bg} is the off-resonance background scattering length, B_0 is the magnetic field at resonance and $\Delta\Gamma$ is the width of the resonance. In the Fig. 2.4 we plot the scattering length as a function of the magnetic field. A detailed derivation can be found in Ref. [1].

2.4.2 Inelastic collisions in loss processes

The interactions discussed above correspond to elastic scattering processes, where the atoms leave the collision region in the same state as they entered. This type of interactions is the dominating one for fermions due to the Pauli exclusion principle, as couplings between channels occur mostly at relatively short-ranges. For bosons, however, inelastic collisions between atoms should be carefully considered, especially in the larger scattering length regime. Hence, the effective interaction between two particles should be more closely examined. Here, the potential takes the form [44, 80]:

$$V = E_{f_1 m_1} + E_{f_2 m_2} + V_{\text{el}} + V_{\text{ss}}, \quad (2.10)$$

where $f_{1,2}$ and $m_{1,2}$ are total angular momentum and magnetic quantum numbers, respectively. Here $E_{f_i m_i} = \frac{\alpha}{4} \sigma_i^e \cdot \sigma_i^p + \mu_e \mathbf{B} \cdot \sigma_i^e - \mu_p \mathbf{B} \cdot \sigma_i^p$ are the hyperfine and Zeeman interactions for each of the atoms ($i = 1, 2$), where α is the hyperfine constant, μ_e and μ_p are the electron and proton magnetic moments, respectively, σ_i is the Pauli spin matrices, and \mathbf{B} is the external magnetic field. These terms are diagonal in the separate atom basis.

V_{el} describes the electric interactions which are responsible for the elastic

scattering and inelastic spin-exchange collisions. On the one hand, the spin-exchange interaction couples the scattering states to other closed channels, which gives rise to a broad scattering resonance. On the other hand, it can transfer atoms to other hyperfine states, which leads to loss of atoms from the trap if the final scattering states are not trapped. V_{ss} represents magnetic dipole-dipole interactions between two electron spins. On the one hand, the dipole-dipole interaction gives rise to narrow scattering resonances. On the other hand, it can change the initial spin states and release the Zeeman or hyperfine energy to the kinetic energy of the trapped atoms. The loss processes discussed above are the major contribution to the two-body decay which can be measured experimentally. For example, in a mixture of $f = 1$ and $f = 2$ hyperfine states of ^{87}Rb , the two body decay rate of the $f = 2$ state has been measured to be $8.8(15) \times 10^{-14} \text{cm}^3/\text{s}$ [81].

Another loss channel for trapped atoms is the three-body recombination process. This process depends on the atomic density, since the probability for three particles to collide is proportional to the cube of the atomic density. The decay rate for the hyperfine state $f = 1$ of ^{87}Rb has been measured to be $5.8(1.9) \times 10^{-30} \text{cm}^6/\text{s}$ [82].

2.5 Heating processes in optical lattices

Of greatest interest to manipulate ultracold gases as *quantum simulators* is to engineer and understand complex many-body systems, such as Mott insulator and high-temperature superconductivity [49]. The requirements to observe these novel quantum phases in ultracold gases are to achieve extremely low temperature (entropy). For example, the anti-ferromagnetic phase has been predicted to occur only for critical temperatures of $T_c \approx 100$ pK (entropy per particle of $s \approx 0.35k_B$ [50]). Due to heating processes in the present cooling schemes, however, there is a predicted temperature limit in optical lattices, which indicates that the temperature scale for magnetic ordering is still out of reach. Experimentally, the lowest reported temperature for strongly-interacting Bose gases in an optical lattice is around 350 pK, which is still higher than the critical temperature of magnetic ordering. The competition between cooling and heating makes it a big obstacle to simulate phases in condensed matter physics via ultracold gases. For this purpose, the interplay of heating and cooling power should be better understood. In this section, we will discuss it in further detail.

In this context, it is very important to be able to characterize and control heating processes arising in experiments. The intrinsic heating in all optical lattice experiments is mainly due to three contributions: incoherent scattering arising from spontaneous emission of photons or from zero-point fluctuations of the atomic electric dipole interacting with gradients in the standing-wave electric field [50, 83–85], fluctuations of laser beams which gives rise to the minimum heating rates [86], and collision losses of atoms [87]. In recent performed

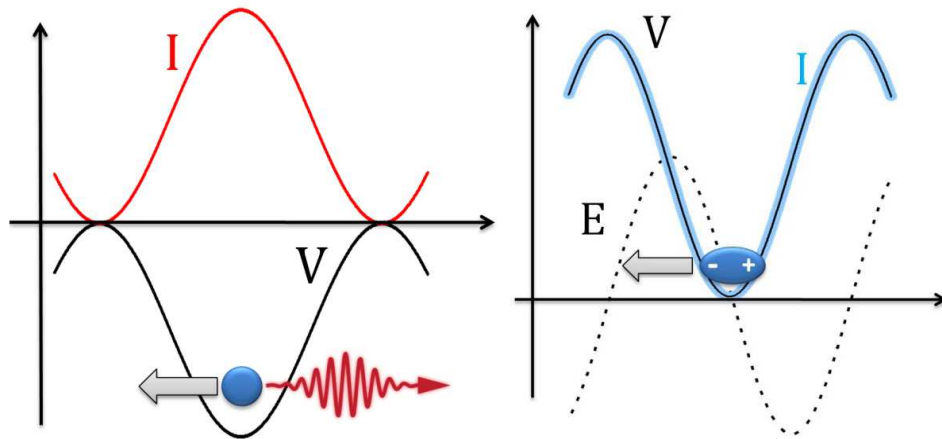


Figure 2.5: Heating arising in an optical lattice from photon recoil (**left**) and fluctuations in the atomic dipole (**right**). The minimum in the potential V (black) occurs at a maximum in the laser intensity I (red) for a red-detuned lattice (**left**). Heating arises from the random recoil (gray arrow) following photon scattering events. In a blue-detuned lattice, the potential V follows the optical intensity I (**right**). The gradient of the electric field E has a maximum at the minimum in the potential. The electromagnetic vacuum induces a fluctuating atomic dipole, which then experiences a force (gray arrow), leading to heating (From Ref. [50]).

experiments, incoherent scattering of light is expected to be dominant heating mechanism [88] (see Fig. 2.5). From a quantum point of view, the heating from incoherent scattering of light is relevant to the transition to higher momentum states in the lowest band or to higher bands. Up to now, most theoretical studies only include inter-band transitions but atoms excited to higher bands are artificially removed from the system. But it is still unclear whether it is valid to neglect higher-band excitations, since decay rates from higher bands are rapid in cubic lattices [50]. Further investigations based on a many-body quantum description are required to study the interplay between the atomic physics of heating processes and the many-body physics of quantum states.

Chapter 3

Bose-Hubbard Model

Realizing and studying tunable models of many-body physics is one of the major challenges with ultracold atoms since the advent of optical lattices [4]. One widely used model for minimal descriptions of the physics of interacting bosons on a lattice is the Bose-Hubbard model. It is a bosonic version of the Hubbard model which originated in solid-state physics as an approximate description of the motion of electrons in a crystalline solid. The Hubbard model was independently proposed by J. Hubbard, M. C. Gutzwiller, and J. Kanamori almost at the same time in the early sixties [89–91], and the corresponding review can be found in [92–94]. The Hubbard model describes the interplay between kinetic energy and strong correlations between electrons, and is suitable for materials with narrow energy bands. Historically, it is widely used in the theory of high-temperature superconductivity, band magnetism and metal-insulator transitions. The Hubbard model for bosonic systems was introduced by M. P. A. Fisher *et. al.* in 1989 [5] to describe the destruction of superfluidity due to strong interactions and disorder, and then suggested by D. Jaksch *et. al.* [95] to simulate this model using ultracold atoms in optical lattices, whose corresponding Mott transition was realized experimentally in three dimensions by M. Greiner *et. al.* [3] and then subsequently in one dimension and two dimensions [96–98]. In this chapter, we will derive and describe the Bose-Hubbard Hamiltonian for different bosonic many-body systems loaded into optical lattices, such as multi-component bosonic systems, BEC-cavity system and ultracold dipolar bosonic gases.

3.1 Many-body system

“Many-body system” is a common expression describing a vast category of physical systems, which are composed of a large number of interacting particles of the order of 10^{23} , such as solid and liquid systems. For these systems, the physical principles that govern their collective motion can be very different from the physical principles corresponding to a system of few particles. The difference is a result of repeated, extremely unordered collisions between numerous particles, which create correlations or entanglement. Correspondingly, the wave function of the many-body system is usually a complicated object and

consists of a large amount of information, leading to exact or analytical calculations impractical. Thus, many-body theoretical physics most often relies on a set of approximations, and it has often been proven difficult to obtain the underlying theory that yields an accurate description of the collective quantum phenomena on the microscopic level [99]. At the heart of quantum many-body system lies the concept of quantum field theory, which is intimately related to the method of second quantization. The reason for introducing the language of second quantization is that it turns out to be extremely convenient in the formulation of a quantum theory for many interacting particles.

To tackle the many-body system, we should first construct a complete set of basis states for the Fock space, and then introduce the creation and annihilation operators [99]. After expressing the quantum mechanical operators, such as kinetic energy, the external potential and the two-body interactions, in the language of second quantization, the many-body Hamiltonian becomes:

$$\begin{aligned} \hat{H} &= \int d\mathbf{x} \hat{\Phi}^\dagger(\mathbf{x}) \left(-\frac{\hbar\Delta^2}{2m} + V_{\text{ext}}(\mathbf{x}) \right) \hat{\Phi}(\mathbf{x}) \\ &+ \frac{1}{2} \int d\mathbf{x} \int d\mathbf{x}' \hat{\Phi}^\dagger(\mathbf{x}) \hat{\Phi}^\dagger(\mathbf{x}') U(\mathbf{x} - \mathbf{x}') \hat{\Phi}(\mathbf{x}') \hat{\Phi}(\mathbf{x}), \end{aligned} \quad (3.1)$$

where $\hat{\Phi}^\dagger(\mathbf{x})$ ($\hat{\Phi}(\mathbf{x})$) denotes the creation (annihilation) field operator at the position \mathbf{x} , $V_{\text{ext}}(\mathbf{x})$ the external potential, and $U(\mathbf{x} - \mathbf{x}')$ two-body interactions. This many-body Hamiltonian can be easily generalized to multi-spin systems.

3.2 Standard Bose-Hubbard model

In a many-body system in periodic potential, the atoms can be delocalized over the whole lattice or localized around a specific site, depending on the interplay between kinetic energy and interactions between atoms. For the former case, the Bloch functions, which are modulated plane waves and can be delocalized over the whole system, are a good approximation for the single-particle wave functions. Thus the field operator $\hat{\Phi}(\mathbf{r})$ can be expressed in the following form:

$$\hat{\Phi}(\mathbf{r}) = \sum_{n,q} \phi_{n,q}(\mathbf{r}) \hat{c}_{n,q}, \quad (3.2)$$

where $\phi_{n,q}(\mathbf{r})$ is the Bloch function for band n and quasimomentum q , and $\hat{c}_{n,q}$ is the annihilation operator for a single-particle Bloch state. If the particles are localized around one site, an alternative single-particle basis of the so-called Wannier states $w_{n,\mathbf{R}}(\mathbf{r})$, is more suitable for describing the behavior of particles. They are connected with the Bloch functions by a Fourier transform

$$\phi_{n,q}(\mathbf{r}) = \sum_R w_{n,\mathbf{R}}(\mathbf{r}) e^{i\mathbf{q}\cdot\mathbf{R}}. \quad (3.3)$$

The Wannier functions for all bands n and sites \mathbf{R} form a complete basis, and the field operator $\hat{\Phi}(\mathbf{r})$, which annihilates a particle at the position \mathbf{r} , can be expanded in the form:

$$\hat{\Phi}(\mathbf{r}) = \sum_{n,\mathbf{R}} w_{n,\mathbf{R}}(\mathbf{r}) \hat{b}_{\mathbf{R},n}, \quad (3.4)$$

where $\hat{b}_{\mathbf{R},n}$ denotes the annihilation operator of an atom in the Wannier state $w_{n,\mathbf{R}}(\mathbf{r})$ at site \mathbf{R} .

3.2.1 Single-component Bose-Hubbard model

If the temperature and mean-interaction energies at a single site are much smaller than the separation between the lowest and the first excited band, the atoms only occupy the lowest $n = 0$ band of the lattice. As a result, the Hamiltonian (3.1) becomes:

$$\begin{aligned} \hat{H} &= \sum_{\mathbf{R}_i, \mathbf{R}_j} \hat{b}_{\mathbf{R}_i}^\dagger \hat{b}_{\mathbf{R}_j} \int d\mathbf{r} w_{0,\mathbf{R}_i}(\mathbf{r}) \left(-\frac{\hbar\Delta^2}{2m} + V_{\text{ext}}(\mathbf{r}) \right) w_{0,\mathbf{R}_j}(\mathbf{r}) \\ &+ \frac{1}{2} \sum_{\mathbf{R}_i, \mathbf{R}_{i'}, \mathbf{R}_j, \mathbf{R}_{j'}} \hat{b}_{\mathbf{R}_i}^\dagger \hat{b}_{\mathbf{R}_{i'}}^\dagger \hat{b}_{\mathbf{R}_j} \hat{b}_{\mathbf{R}_{j'}} \\ &\int d\mathbf{r} \int d\mathbf{r}' w_{0,\mathbf{R}_i}^*(\mathbf{r}) w_{0,\mathbf{R}_{i'}}^*(\mathbf{r}') U(\mathbf{r} - \mathbf{r}') w_{0,\mathbf{R}_j}(\mathbf{r}') w_{0,\mathbf{R}_j}(\mathbf{r}). \end{aligned} \quad (3.5)$$

Here, we define the on-site energy

$$\epsilon_{\mathbf{R}_i} = \int d\mathbf{r} w_{0,\mathbf{R}_i}(\mathbf{r}) \left(-\frac{\hbar\Delta^2}{2m} + V_{\text{ext}}(\mathbf{r}) \right) w_{0,\mathbf{R}_i}(\mathbf{r}), \quad (3.6)$$

the tunneling amplitudes between sites i and j

$$t_{\mathbf{R}_i, \mathbf{R}_j} = - \int d\mathbf{r} w_{0,\mathbf{R}_i}(\mathbf{r}) \left(-\frac{\hbar\Delta^2}{2m} + V_{\text{ext}}(\mathbf{r}) \right) w_{0,\mathbf{R}_j}(\mathbf{r}), \quad (3.7)$$

and the interactions between the atoms

$$U_{\mathbf{R}_i, \mathbf{R}_{i'}, \mathbf{R}_j, \mathbf{R}_{j'}} = \int d\mathbf{r} \int d\mathbf{r}' w_{0,\mathbf{R}_i}^*(\mathbf{r}) w_{0,\mathbf{R}_{i'}}^*(\mathbf{r}') U(\mathbf{r} - \mathbf{r}') w_{0,\mathbf{R}_j}(\mathbf{r}') w_{0,\mathbf{R}_{j'}}(\mathbf{r}). \quad (3.8)$$

Next, we make a further assumption, namely tight-binding approximation, to obtain the tunneling between different sites. For a deep lattice, the hopping energy $t_{i,j}$ is exponentially suppressed for all sites $|i - j| \geq 2$, and it is a good approximation to take only nearest-neighbor tunneling processes into account, but neglecting all higher order matrix elements. Within the tight-binding approximation, the summation can be restricted to nearest neighbors only, where the corresponding summation is denoted by $\sum_{\langle i,j \rangle}$, and the nearest-neighbor hopping amplitude is denoted by $J = - \int d\mathbf{r} w_{0,\mathbf{R}_i}(\mathbf{r}) \left\{ -\frac{\hbar\Delta^2}{2m} + V_{\text{ext}}(\mathbf{r}) \right\} w_{0,\mathbf{R}_j}(\mathbf{r})$.

Finally, we simplify interactions involving both on-site and off-site terms to obtain space-averaged interaction parameters for practical purpose. For a moderately strong lattice, the Wannier functions are well localized and a noticeable contribution only occurs if the four different lattice site labels coincide. The on-site Hubbard interaction $U = \frac{4\pi\hbar^2 a_s}{2M_r} \int d\mathbf{r} w_{0,\mathbf{R}_i}^*(\mathbf{r}) w_{0,\mathbf{R}_i}^*(\mathbf{r}) w_{0,\mathbf{R}_i}(\mathbf{r}) w_{0,\mathbf{R}_i}(\mathbf{r})$ in the pseudopotential approximation (2.8). Here we take only the dominant interaction matrix elements into account, but it is sufficient to describe most physical phenomena originating from this type of interactions.

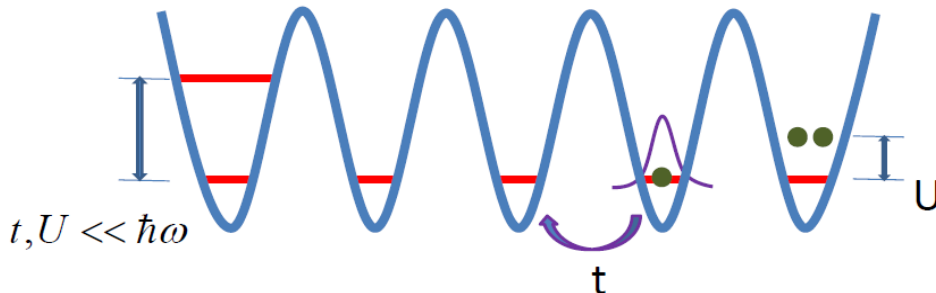


Figure 3.1: Sketch of the Bose-Hubbard model, where t denotes the hopping amplitude, U the interaction strength, and $\hbar\omega$ the vibrational level spacing.

Taking all the assumptions into account, the Bose-Hubbard model is obtained by writing the Hamiltonian in second quantization:

$$\hat{H} = -J \sum_{\langle i,j \rangle} (\hat{b}_i^\dagger \hat{b}_j + \text{h.c.}) + \frac{U}{2} \sum_i \hat{n}_i (\hat{n}_i - 1) + \sum_i \epsilon_i \hat{n}_i. \quad (3.9)$$

In addition to the optical-lattice potential, an external trap is always exist in the experiments, which leads to a spatial inhomogeneity. The confining potential is most often quadratic, and correspondingly, the Bose-Hubbard model is expressed as

$$\hat{H} = -J \sum_{\langle i,j \rangle} (\hat{b}_i^\dagger \hat{b}_j + \text{h.c.}) + \frac{U}{2} \sum_i \hat{n}_i (\hat{n}_i - 1) + \sum_i (V_i - \mu) \hat{n}_i. \quad (3.10)$$

Here $V_i = V_0 r_i^2$, where V_0 is the strength of the external harmonic trap, and μ is the global chemical potential which controls the total number of bosons.

The Bose-Hubbard model (see Fig. 3.1) describes the competition between the kinetic energy J , which is gained by delocalizing particles over the whole lattice, and the repulsive on-site interaction U , which favors localization, but disfavors having more than one particle at any given site. It is believed that the Bose-Hubbard model is the simplest many-body model one can write down, which can not be reduced to a single-particle theory. In addition, in an optical lattice loaded with ultracold atoms, the ratio U/J between these two energies can be tuned by varying the dimensionless depth V_s of the optical lattice, which indicates the Bose-Hubbard model can be simulated experimentally in a wide range of parameters via ultracold gases.

3.2.2 Multi-component Bose-Hubbard model

In this section, we extend the description of the Bose-Hubbard model to systems in which two or more quantum states (hyperfine states of atoms) are macroscopically occupied. In ultracold gases, different hyperfine states are related to different spins which can be described by spin operators that satisfy an angular momentum algebra. And, correspondingly, these multi-component systems are known as spinor condensates or mixtures of spins in the literature. Experimental realizations of mixtures [100] and spinor condensates [101, 102] have inspired the investigation of the corresponding many-body systems in many different directions, some of which have been reviewed in Refs. [103–105].

Bose-Bose mixtures — For a mixture of two-component bosonic gases in an optical lattice, which experimentally could consist of two different species, *e.g.* ^{87}Rb and ^{41}K as in Ref. [106] or two different hyperfine states of a single species, *e.g.* ^{87}Rb as in Refs. [51, 107], the Hamiltonian takes the form:

$$\begin{aligned}
\hat{H} = & \int d\mathbf{x} \left[\hat{\Phi}_1^\dagger(\mathbf{x}) \left(-\frac{\hbar\Delta^2}{2m_1} + V_1(\mathbf{x}) \right) \hat{\Phi}_1(\mathbf{x}) \right. \\
& \left. + \hat{\Phi}_2^\dagger(\mathbf{x}) \left(-\frac{\hbar\Delta^2}{2m_2} + V_2(\mathbf{x}) \right) \hat{\Phi}_2(\mathbf{x}) \right] \\
& + \frac{1}{2} \left(\frac{4\pi\hbar^2 a_{11}}{m_1} \right) \int d\mathbf{x} \int d\mathbf{x}' \hat{\Phi}_1^\dagger(\mathbf{x}) \hat{\Phi}_1^\dagger(\mathbf{x}') \hat{\Phi}_1(\mathbf{x}') \hat{\Phi}_1(\mathbf{x}) \\
& + \frac{1}{2} \left(\frac{4\pi\hbar^2 a_{22}}{m_2} \right) \int d\mathbf{x} \int d\mathbf{x}' \hat{\Phi}_2^\dagger(\mathbf{x}) \hat{\Phi}_2^\dagger(\mathbf{x}') \hat{\Phi}_2(\mathbf{x}') \hat{\Phi}_2(\mathbf{x}) \\
& + \left(\frac{4\pi\hbar^2 a_{12}}{2m_{12}} \right) \int d\mathbf{x} \int d\mathbf{x}' \hat{\Phi}_1^\dagger(\mathbf{x}) \hat{\Phi}_2^\dagger(\mathbf{x}') \hat{\Phi}_2(\mathbf{x}') \hat{\Phi}_1(\mathbf{x}), \quad (3.11)
\end{aligned}$$

where a_{11} , a_{22} and a_{12} denote the interactions between species 1, species 2, and inter-species interactions, respectively. m_1 and m_2 denote the masses of species 1 and 2, respectively, and m_{12} denotes the reduced mass of the particle 1 and 2. $V_1(\mathbf{x})$ and $V_2(\mathbf{x})$ denote the external trap potentials for species 1 and 2, respectively. $\hat{\Phi}_i(\mathbf{x})$ ($\hat{\Phi}_i^\dagger(\mathbf{x})$) denotes the creation (annihilation) field operator for species i at position \mathbf{x} . The field operator $\hat{\Phi}_i(\mathbf{x})$ can be expanded in terms of the Wannier functions, which form a complete basis set. In the tight-binding approximation, the lowest-band Bose-Hubbard Hamiltonian for Bose-Bose mixtures takes this form:

$$\begin{aligned}
\hat{H} = & - \sum_{\substack{\langle i,j \rangle \\ \nu=b,d}} t_\nu (\hat{b}_{i\nu}^\dagger \hat{b}_{j\nu} + \text{h.c.}) + \frac{1}{2} \sum_{i,\lambda\nu} U_{\lambda\nu} \hat{n}_{i\lambda} (\hat{n}_{i\nu} - \delta_{\lambda\nu}) \\
& - \sum_{i,\nu=b,d} \mu_{i\nu} \hat{n}_{i\nu}. \quad (3.12)
\end{aligned}$$

In this Hamiltonian, $\langle i, j \rangle$ represent the nearest neighbor sites i, j , and we denote the two bosonic species as b, d , which are labeled by the index $\lambda(\nu) = b, d$. The bosonic creation (annihilation) operator for species ν at site i is $\hat{b}_{i\nu}^\dagger$ ($\hat{b}_{i\nu}$) and the local density is $\hat{n}_{i\nu} = \hat{b}_{i\nu}^\dagger \hat{b}_{i\nu}$. Due to possibly different masses or a spin-dependent optical lattice, these two species in general hop with non-equal amplitudes t_b and t_d . $U_{\lambda\nu}$ denotes the inter- and intra-species interactions, which can be tuned via a Feshbach resonance or by spin-dependent lattices. $\mu_{i\nu}$ denotes the local chemical potential for species ν . In the presence of an external harmonic trap, $\mu_{i\nu} = \mu_\nu - V_0 r_i^2$, where V_0 is the strength of the external harmonic trap, and μ_ν is the global chemical potential for species ν .

Spinor bosonic gases — A spinor bosonic gas in an optical lattice is a mixture of hyperfine states of the same isotope. They system can undergo transitions between macroscopically occupied hyperfine states due to spin-exchange collisions, but it as a whole is in the ground state. For a system of bosonic gases with hyperfine spin f , for example, the spin-dependent interactions can be written in the second-quantized form [108, 109]:

$$V(\mathbf{x}_1 - \mathbf{x}_2) = \frac{4\pi\hbar^2}{m} \sum_{F=0}^{2f} a_F \sum_m |F, m_F\rangle \langle F, m_F| \delta(\mathbf{x}_1 - \mathbf{x}_2), \quad (3.13)$$

where $|F, m_F\rangle$ is the total hyperfine spin state formed by two atoms each with spin f , and a_F is the s-wave scattering length in the channel of total spin F . The spin-dependent interactions can also be written in the form of spin operators. For example, for a system of $f = 1$ bosons, it can be expressed as:

$$V(\mathbf{x}_1 - \mathbf{x}_2) = (c_0 + c_2 \hat{\mathbf{F}}_1 \cdot \hat{\mathbf{F}}_2) \delta(\mathbf{x}_1 - \mathbf{x}_2), \quad (3.14)$$

where $c_0 = \frac{4\pi\hbar^2}{m} \frac{a_0 + a_2}{3}$, $c_2 = \frac{4\pi\hbar^2}{m} \frac{a_2 - a_0}{3}$ and $\hat{\mathbf{F}}_i$ is spin operator for species i .

The derivation of the Bose-Hubbard Hamiltonian for ultracold spinor gases is performed in the same way as in the scalar case. For example, the many-body Hamiltonian for a system of $f = 1$ bosons takes the following form:

$$\begin{aligned} \hat{H} &= \int d\mathbf{x} \hat{\Phi}_\alpha^\dagger(\mathbf{x}) \left(-\frac{\hbar\Delta^2}{2m_\alpha} + V_\alpha(\mathbf{x}) \right) \hat{\Phi}_\alpha(\mathbf{x}) \\ &+ \frac{c_0}{2} \int d\mathbf{x} \int d\mathbf{x}' \hat{\Phi}_\alpha^\dagger(\mathbf{x}) \hat{\Phi}_{\alpha'}^\dagger(\mathbf{x}') \hat{\Phi}_{\alpha'}(\mathbf{x}') \hat{\Phi}_\alpha(\mathbf{x}) \\ &+ \frac{c}{2} \int d\mathbf{x} \int d\mathbf{x}' \hat{\Phi}_\alpha^\dagger(\mathbf{x}) \hat{\Phi}_{\alpha'}^\dagger(\mathbf{x}') \mathbf{F}_{\alpha\beta} \cdot \mathbf{F}_{\alpha'\beta'} \hat{\Phi}_{\beta'}(\mathbf{x}') \hat{\Phi}_\beta(\mathbf{x}), \end{aligned} \quad (3.15)$$

where $\hat{\Phi}_\alpha(\mathbf{x})$ is the field annihilation operator for an atom in the hyperfine state $|1, \alpha\rangle$ at point \mathbf{x} . And the corresponding Bose-Hubbard model can be written as:

$$\hat{H} = - \sum_{\langle i, j \rangle, \sigma} t_\nu (\hat{b}_{i\nu}^\dagger \hat{b}_{j\nu} + \text{h.c.}) + \frac{1}{2} c_0 \sum_i \hat{n}_i (\hat{n}_i - 1) + \frac{1}{2} c_2 \sum_i (\hat{\mathbf{F}}_i^2 - 2\hat{n}_i), \quad (3.16)$$

where $\hat{b}_{\sigma i}$ annihilates a boson in the hyperfine state $m_F = \sigma$ at site i , \hat{n}_i denotes the total number of particles at site i , and $\hat{\mathbf{F}}_i = \sum_{\sigma\sigma'} \hat{b}_{\sigma i}^\dagger \mathbf{T}_{\sigma\sigma'} \hat{b}_{\sigma' i}$ is the spin operator at site i ($\mathbf{T}_{\sigma\sigma'}$ being the usual spin matrices for a spin-1 particle).

3.3 Bose-Hubbard model for ultracold gases in an optical cavity

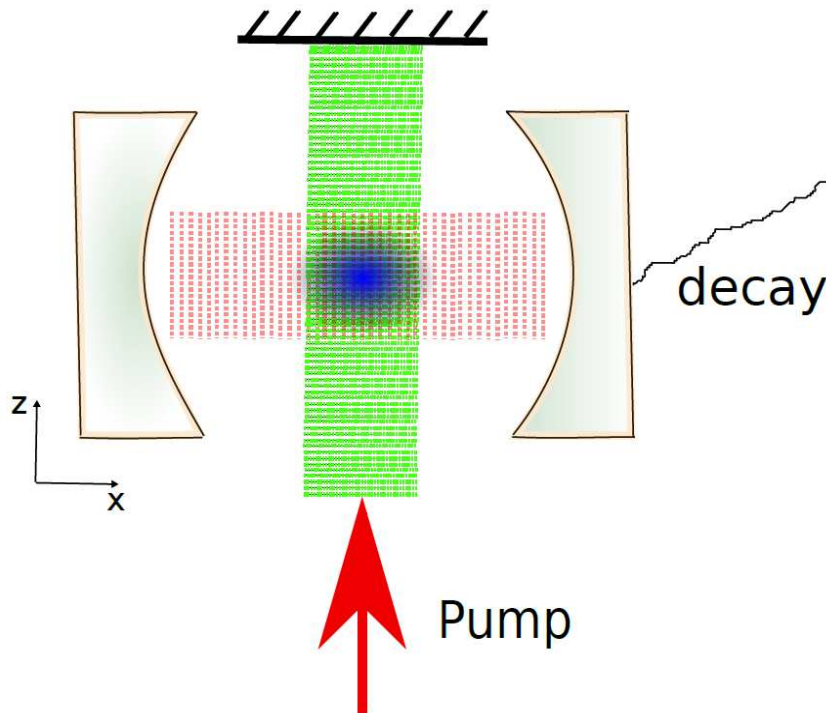


Figure 3.2: Sketch of the setup of the BEC-cavity system.

Experimental realization of a high-finesse cavity coupled to atomic many-body systems is of large interest in the past few years [66]. It bridges the gap between quantum optics and many-body physics, and paves the way to a fascinating area where both light and matter act as dynamical physical quantities. Particularly, combining ultracold gases with a high-finesse cavity in the strong coupling regime has been achieved recently [69–72]. Properties of the strongly coupled BEC-cavity system depend on its setup, where the pump laser can be directly coupled to the cavity mode via a pump in the cavity direction, or indirectly coupled through the atoms trapped in the cavity via a pump in the transverse direction. Here we only consider the latter case, and the sketch of the setup is given in Fig. 3.2, where all atoms in the high-finesse cavity are strongly coupled to the cavity mode [110, 111]. In this case, the light force strongly influences the motional degree of freedom of the atoms, and determines their distribution in the cavity. In turn, the atoms induce a phase shift to the cavity mode, and give rise to a dynamical cavity field which depends on

the spatial distribution of atoms. This implies that the cavity mode can not be described by a classical, externally imposed field, but should be treated as a quantized field and determined by the atom distribution. Usually, the description of this system is based on the Jaynes-Cummings model which captures the strong coupling between the cavity mode and a single atom. The detailed derivation of the Jaynes-Cummings model can be found in Appendix A.

3.3.1 Many-body Hamiltonian

We consider N two-level atoms with the mass m and the transition frequency ω_a interacting with a single cavity mode of the frequency ω_c in the x direction, and also a standing driving field (pump laser) with the frequency ω_p in the z direction (the motion of atoms in the third direction is considered to be frozen). The system can be described by an effective Hamiltonian, which is derived from the Jaynes-Cummings Hamiltonian in a rotating frame and dipole approximation [66, 112, 113]:

$$\begin{aligned} \hat{H} = & \int d\mathbf{x} \hat{\Psi}^\dagger(\mathbf{x}) \left\{ -\frac{\hbar^2}{2m} \nabla^2 + V_p \cos^2(kz) \right. \\ & \left. - \hbar \hat{a}^\dagger \hat{a} [\Delta_c - U_0 \cos^2(kx)] + \hbar \eta_{\text{eff}} \cos(kx) \cos(kz) (\hat{a} + \hat{a}^\dagger) \right\} \Psi(\mathbf{x}) \\ & + \frac{U}{2} \int d\mathbf{x} \hat{\Psi}^\dagger(\mathbf{x}) \hat{\Psi}^\dagger(\mathbf{x}) \hat{\Psi}(\mathbf{x}) \hat{\Psi}(\mathbf{x}), \end{aligned} \quad (3.17)$$

where $\Delta_a \equiv \omega_p - \omega_a$ and $\Delta_c \equiv \omega_p - \omega_c$ denote the atom-pump and cavity-pump detunings, respectively. \hat{a} (\hat{a}^\dagger) describes the annihilation (creation) operator of a cavity photon with frequency ω_c . $\hat{\Psi}$ ($\hat{\Psi}^\dagger$) denotes the atomic field operator, and $U = 4\pi a_s \hbar^2 / m$ is the contact interaction strength with a_s denoting the s-wave scattering length. $V_p = \hbar \Omega_p^2 / \Delta_a$ is the depth of the standing-wave potential created by the pump laser in the z direction, where Ω_p denotes the pump Rabi frequency. $U_0 = g_0^2 / \Delta_a$ is the light shift of a single maximally coupled atom, and also the depth of the single-photon dipole potential of the cavity mode, where g_0 is the atom-cavity coupling strength. $\eta_{\text{eff}} = g_0 \Omega_0 / \Delta_a$ describes the scattering between the pump field and the cavity mode. The first term on the right-hand side of Eq. 3.17 is the kinetic energy of the atoms in the cavity, the second term is the potential of the standing wave formed by the pump laser in the z direction, the third term is the cavity field with the shifted cavity resonance due to the back action of the atoms in the cavity mode, the fourth term describes the coherent scattering between the pump laser and the cavity field, and the last term is the contact interactions between atoms. Here the excited state is adiabatically eliminated, which is valid for large detuning Δ_a and low temperature T ensuring negligible spontaneous emission.

3.3.2 Extended Bose-Hubbard model

Following the standard procedures, the Hamiltonian (3.17) can be rewritten in the single-atom Wannier basis to obtain an extended Bose-Hubbard model as developed in Refs. [114, 115]. Expanding the atomic field operator in the Wannier basis set $\hat{\Psi}_g(\mathbf{x}) = \sum_n \sum_i \hat{b}_{n,i} w_n(\mathbf{x} - \mathbf{x}_i)$, where $\hat{b}_{n,i}$ ($\hat{b}_{n,i}^\dagger$) is the annihilation (creation) operator and $w_n(\mathbf{x} - \mathbf{x}_i)$ is the n -th band Wannier function centered at $\mathbf{x} = \mathbf{x}_i$, the Bose-Hubbard Hamiltonian with on-site interaction has the following form (here only including the lowest band $w_0(\mathbf{x} - \mathbf{x}_i)$):

$$\begin{aligned} \hat{H} &= \sum_{i,j} E_{i,j} \hat{b}_i^\dagger \hat{b}_j + V_p \sum_{i,j} J_{ij}^p \hat{b}_i^\dagger \hat{b}_j \\ &- \hbar \hat{a}^\dagger \hat{a} \left(\Delta_c - U_0 \sum_{i,j} J_{ij}^c \hat{b}_i^\dagger \hat{b}_j \right) + \hbar \eta_{\text{eff}} (\hat{a} + \hat{a}^\dagger) \sum_{i,j} J'_{ij} \hat{b}_i^\dagger \hat{b}_j \\ &+ \frac{1}{2} \sum_{i,j,k,l} U_{ijkl} \hat{b}_i^\dagger \hat{b}_j^\dagger \hat{b}_k \hat{b}_l, \end{aligned} \quad (3.18)$$

where the coupling matrix elements are

$$E_{i,j} = \int d\mathbf{x} w_0(\mathbf{x} - \mathbf{x}_i) \left(-\frac{\hbar \nabla^2}{2m} \right) w_0(\mathbf{x} - \mathbf{x}_j), \quad (3.19)$$

$$J_{i,j}^p = \int d\mathbf{x} w_0(\mathbf{x} - \mathbf{x}_i) \cos^2(kz) w_0(\mathbf{x} - \mathbf{x}_j), \quad (3.20)$$

$$J_{i,j}^c = \int d\mathbf{x} w_0(\mathbf{x} - \mathbf{x}_i) \cos^2(kx) w_0(\mathbf{x} - \mathbf{x}_j), \quad (3.21)$$

$$J'_{i,j} = \int d\mathbf{x} w_0(\mathbf{x} - \mathbf{x}_i) \cos(kx) \cos(kz) w_0(\mathbf{x} - \mathbf{x}_j). \quad (3.22)$$

We note that the introduced extended Bose-Hubbard Hamiltonian has two major differences compared to the standard one: first, the hopping amplitudes $J_{i,j}^p$ in the direction of the pump laser are different from the hopping amplitudes $J_{i,j}^c$ in the cavity direction; second, the hopping amplitudes $J_{i,j}^c$ in the cavity direction depend on the photon number in the cavity mode. Hence, the on-site and higher-order terms arising from the kinetic energy can not be simply merged with the potential terms generated by the cavity mode, as opposed to the standard Bose-Hubbard model (3.9).

In our calculations, we only keep hopping terms up to the nearest-neighbor order, which is justified as long as the depth of the pump field and cavity

mode are deep enough (tight binding approximation). Then, the effective Hamiltonian can be written in a simplified form:

$$\begin{aligned}
\hat{H} &= (E_0 + V_p J_0^p) \sum_i \hat{b}_i^\dagger \hat{b}_i + \sum_{\langle i,j \rangle} J_{x(z)} \hat{b}_i^\dagger \hat{b}_j \\
&\quad - \hbar \hat{a}^\dagger \hat{a} (\Delta_c - U_0 J_0^c \sum_i \hat{b}_i^\dagger \hat{b}_i) + \hbar \eta_{\text{eff}} J_0' (\hat{a} + \hat{a}^\dagger) \sum_i (-1)^{i+1} \hat{b}_i^\dagger \hat{b}_i \\
&\quad + \frac{1}{2} U \sum_i \hat{b}_i^\dagger \hat{b}_i^\dagger \hat{b}_i \hat{b}_i - \mu \sum_i \hat{b}_i^\dagger \hat{b}_i.
\end{aligned} \tag{3.23}$$

Here E_0 , J_0^p , J_0^c and J_0' are zeroth-order hopping amplitudes (the terms involving E_0 and J_0^p can be absorbed in the chemical potential), and the first-order hopping amplitude is $J_x = E_1(x) + \hbar U_0 J_1^c \hat{a}^\dagger \hat{a}$ ($J_z = E_1(z) + V_p J_1^p$) in the $x(z)$ -direction, where E_1 , J_1^p and J_1^c are the first-order hopping amplitudes for nearest-neighbor sites $\langle i, j \rangle$ (the first-order hopping amplitudes can be different in x and z directions). μ is the global chemical potential. Note that an external optical lattice can be added to the cavity direction to guarantee a minimum potential in the case of zero cavity photons [113].

The system described by the effective Hamiltonian (3.23) is still complicated for theoretical description due to the cavity mode-dependence of the parameters of the Bose-Hubbard model, therefore we make a further simplification by assuming that the cavity field is in a coherent state, which gives an excellent agreement with experimental measurements [25]. Under the coherent-state approximation, the cavity mode can be described by a complex amplitude α , and the parameters of the extended Bose-Hubbard model only depend on the average photon numbers. We thus finally obtain the effective Hamiltonian used in our calculations:

$$\begin{aligned}
\hat{H} &= - \sum_{\langle i,j \rangle} \tilde{J}_{x(z)} \hat{b}_i^\dagger \hat{b}_j + \frac{1}{2} U \sum_i \hat{b}_i^\dagger \hat{b}_i^\dagger \hat{b}_i \hat{b}_i \\
&\quad + 2\text{Re}[\alpha] \hbar \eta_{\text{eff}} J_0' \sum_i (-1)^{i+1} \hat{b}_i^\dagger \hat{b}_i - \tilde{\mu} \sum_i \hat{b}_i^\dagger \hat{b}_i,
\end{aligned} \tag{3.24}$$

where $\tilde{J}_x = -E_1(x) - \hbar U_0 J_1^c |\alpha|^2$, $\tilde{J}_z = -E_1(z) - V_p J_1^p$ and $\tilde{\mu} = \mu - (E_0 + V_p J_0^p + \hbar U_0 J_0^c |\alpha|^2)$ with $\alpha = \eta_{\text{eff}} J_0' \sum_i (-1)^{i+1} \langle \hat{b}_i^\dagger \hat{b}_i \rangle / (\Delta_c' + i\kappa)$ [116], where $\Delta_c' = \Delta_c - U_0 (J_0^c \sum_i \langle \hat{b}_i^\dagger \hat{b}_i \rangle + J_1^c \sum_{\langle i,j \rangle} \langle \hat{b}_i^\dagger \hat{b}_j \rangle)$, and κ is the decay rate of the cavity mode. To simplify Eq. (3.23), all zeroth-order tunneling terms are absorbed in the global chemical potential $\tilde{\mu}$ (except the effective staggered potential due to induced long-rang interactions). $\hbar |\alpha|^2 \Delta_c$ is also neglected in the Hamiltonian (3.24), since it only shifts the chemical potential of the system globally.

In the presence of an external harmonic trap, the Bose-Hubbard model is

described by

$$\begin{aligned} \hat{H} = & - \sum_{\langle i,j \rangle} \tilde{J}_{x(z)} \hat{b}_i^\dagger \hat{b}_j + \frac{1}{2} U \sum_i \hat{b}_i^\dagger \hat{b}_i^\dagger \hat{b}_i \hat{b}_i \\ & + 2\text{Re}[\alpha] \hbar \eta_{\text{eff}} J'_0 \sum_i (-1)^{i+1} \hat{b}_i^\dagger \hat{b}_i + \sum_i (V_i - \tilde{\mu}) \hat{b}_i^\dagger \hat{b}_i. \end{aligned} \quad (3.25)$$

Here $V_i = V_0 r_i^2$, where V_0 is the strength of the external harmonic trap.

3.4 Bose-Hubbard model for dipolar bosonic gases

The design and realization of novel many-body quantum phases is of large interest in recent years. The possibility for the realization of novel quantum phases has been recently extended by a new ingredient: the system with dipolar interactions, which provides the possibility of access to strongly correlated quantum phases involving quantum magnetism, spontaneous spatial symmetry breaking, and exotic superfluidity. In contrast to the contact interaction, it has two new properties, namely the anisotropy and the long-range character. In this section, we will derive the extended Bose-Hubbard model with long-range dipole-dipole interactions by following Ref. [23].

3.4.1 Dipole-dipole interaction

The long-range interaction potential between particle 1 and 2 is a result of the dipole-dipole interaction, and, at a relative distance \mathbf{r} and with dipole moments along the unit vector \mathbf{e}_1 and \mathbf{e}_2 , is given by

$$U_{\text{dd}}(\mathbf{r}) = \frac{C_{\text{dd}}}{4\pi} \frac{(\mathbf{e}_1 \cdot \mathbf{e}_2)r^2 - 3(\mathbf{e}_1 \cdot \mathbf{r})(\mathbf{e}_2 \cdot \mathbf{r})}{r^5}, \quad (3.26)$$

where $r = |\mathbf{r}|$, and the dipolar coupling constant C_{dd} is given by $C_{\text{dd}} = \mu_0 \mu^2$ for particles with a permanent magnetic dipole moment μ , or $C_{\text{dd}} = d^2/\epsilon_0$ for particles with a permanent electric dipole moment d (the lattice constant is set to unity). Here μ_0 is the vacuum permeability, and ϵ_0 is the vacuum permittivity.

Contrary to the typical van der Waals potential, we can see that the dipole-dipole interaction has two typical characters, *i.e.* long-range since it decays as $U_{\text{dd}} \propto 1/r^3$, and anisotropic since it depends on the relative angles between the dipoles. For polarized particles, *i.e.* all dipoles pointing in the same direction in the presence of electric or magnetic field, the interaction (see Fig. 3.3) reduces to

$$U_{\text{dd}}(\mathbf{r}) = \frac{C_{\text{dd}}}{4\pi} \frac{1 - 3 \cos^2 \theta}{r^3}, \quad (3.27)$$

where θ is the angle between the dipoles. For parallel dipoles with $\theta = \pi/2$ the interaction is repulsive, while the interaction is attractive for $\theta = 0$.

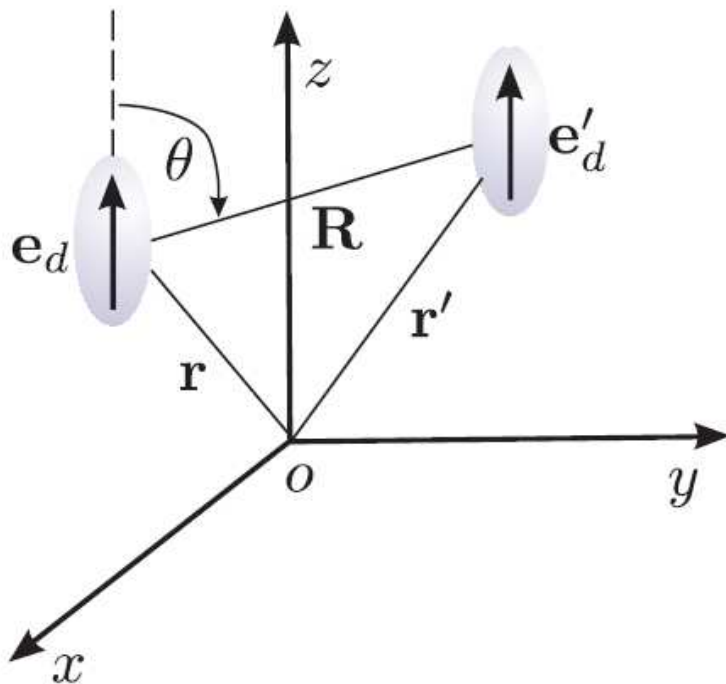


Figure 3.3: Sketch of dipole-dipole interaction between two polarized dipoles (From Ref. [117]).

3.4.2 Dipolar bosonic gases in an optical lattice

In this part, we turn to discuss the physics of dipolar bosonic gases trapped in an optical lattice with dipoles polarized along a certain direction. Qualitatively, there are two extreme scenarios depending on the shape of the confining potential: (1) in a cigar-shaped trap, elongated along the z -axis and with a strong confinement in radial direction, the dipole-dipole interaction is attractive, which can lead to an instability of the gas; (2) in a pancake-shaped trap, with a strong confinement along the z -axis, the dipolar interaction is repulsive, which leads to a stability of the gas. One can quantitatively include the contribution from the dipole-dipole interactions in the Hamiltonian (3.1), which leads to the final Hamiltonian

$$\begin{aligned}
 \hat{H} &= \int d\mathbf{r} \hat{\Phi}^\dagger(\mathbf{r}) \left(-\frac{\hbar\Delta^2}{2m} + V_{\text{ext}}(\mathbf{r}) \right) \hat{\Phi}(\mathbf{r}) \\
 &+ \frac{1}{2} \int d\mathbf{r}_1 \int d\mathbf{r}_2 \hat{\Phi}^\dagger(\mathbf{r}_1) \hat{\Phi}^\dagger(\mathbf{r}_2) U(\mathbf{r}_1 - \mathbf{r}_2) \hat{\Phi}(\mathbf{r}_2) \hat{\Phi}(\mathbf{r}_1) \\
 &+ \frac{1}{2} \int d\mathbf{r}_1 \int d\mathbf{r}_2 \hat{\Phi}^\dagger(\mathbf{r}_1) \hat{\Phi}^\dagger(\mathbf{r}_2) U_{\text{dd}}(\mathbf{r}_1 - \mathbf{r}_2) \hat{\Phi}(\mathbf{r}_1) \hat{\Phi}(\mathbf{r}_2). \quad (3.28)
 \end{aligned}$$

Following the standard process, we can expand field operators in terms of Wannier functions, and keep terms only in the lowest Bloch band (single-band picture). Within this approximation, one obtains the Bose-Hubbard

Hamiltonian for dipolar bosonic gases. In addition to the normal hopping and short-ranged interaction terms, the dipolar term leads to a further contribution to the Hamiltonian

$$\hat{H}_{\text{dd}} = \sum_{i,j,k,l} \frac{V_{ijkl}^{\text{dd}}}{2} \hat{b}_i^\dagger \hat{b}_j^\dagger \hat{b}_k \hat{b}_l, \quad (3.29)$$

where the matrix elements V_{ijkl}^{dd} is written as

$$V_{ijkl}^{\text{dd}} = \int d\mathbf{r}_1 \int d\mathbf{r}_2 w^*(\mathbf{r}_1 - \mathbf{R}_i) w^*(\mathbf{r}_2 - \mathbf{R}_j) U_{\text{dd}}(\mathbf{r}_1 - \mathbf{r}_2) w(\mathbf{r}_1 - \mathbf{R}_k) w(\mathbf{r}_2 - \mathbf{R}_l). \quad (3.30)$$

Usually, the Wannier functions are localized around the minima of the optical lattice wells with a spatial broadening Γ . For sufficiently deep optical lattices, we can assume Γ to be much smaller than the optical lattice spacing a , i.e. $\Gamma \ll a$. In this limit, each function $w(\mathbf{r} - \mathbf{R}_i)$ is significantly centered around \mathbf{R}_i , and, correspondingly, the integral (3.30) is significantly non-zero for the indices $i = k$ and $j = l$. Therefore, there are two main contributions to the integral (3.30): the *off-site* matrix element V_{ijij}^{dd} corresponding to $k = i \neq j = l$, and the *on-site* V_{iiii}^{dd} with $k = i = j = l$. In the following, we explain the physical meaning of these terms.

Off-site — For two particles localized at the different lattice sites i and j , the dipolar potential $U_{\text{dd}}(\mathbf{r}_1 - \mathbf{r}_2)$ varies slowly on the scale of Γ , therefore one may approximate its contribution by a constant $U_{\text{dd}}(\mathbf{R}_i - \mathbf{R}_j)$ and then take it out of the integration for off-site terms. Then one obtains a reduced integral

$$V_{ijij}^{\text{dd}} \simeq U_{\text{dd}}(\mathbf{R}_i - \mathbf{R}_j) \int d\mathbf{r}_1 |w(\mathbf{r}_1 - \mathbf{R}_i)|^2 \int d\mathbf{r}_2 |w(\mathbf{r}_2 - \mathbf{R}_j)|^2, \quad (3.31)$$

which yields the off-site Hamiltonian

$$\hat{H}_{\text{dd}}^{\text{off-site}} = \sum_{i \neq j} \frac{V_{ij}^{\text{dd}}}{2} \hat{n}_i \hat{n}_j, \quad (3.32)$$

where $V_{ij}^{\text{dd}} = U_{\text{dd}}(\mathbf{R}_i - \mathbf{R}_j)$, and $\hat{n}_i = \hat{b}_i^\dagger \hat{b}_i$ denotes the bosonic number operator at site i .

On-site — For two particles localized at the same lattice site i , the dipolar potential varies very rapidly for $|\mathbf{r}_1 - \mathbf{r}_2| \sim \Gamma$, and diverges for $|\mathbf{r}_1 - \mathbf{r}_2| \rightarrow 0$. The approximation used for off-site terms is thus not valid here, and the on-site integral

$$V_{iiii}^{\text{dd}} = \int d\mathbf{r}_1 \int d\mathbf{r}_2 \rho(\mathbf{r}_1) U_{\text{dd}}(\mathbf{r}_1 - \mathbf{r}_2) \rho(\mathbf{r}_2), \quad (3.33)$$

has to be calculated by taking into account the atomic spatial distribution at site i , where $\rho(\mathbf{r}) = |w(\mathbf{r})|^2$ is the single particle density, and the corresponding solution can be obtained by Fourier transforming,

$$V_{iiii}^{\text{dd}} = \frac{1}{(2\pi)^3} \int d\mathbf{k} \widetilde{U_{\text{dd}}}(\mathbf{k}) \tilde{\rho}^2(\mathbf{k}). \quad (3.34)$$

This term leads to the on-site dipolar contribution to the Hamiltonian

$$\hat{H}_{\text{dd}}^{\text{on-site}} = \sum_i \frac{V_{iii}^{\text{dd}}}{2} \hat{n}_i (\hat{n}_i - 1). \quad (3.35)$$

Extended Bose-Hubbard model — Taking into account all the terms contributed from dipolar interactions, the extended Bose-Hubbard Hamiltonian is given by

$$\hat{H}_{\text{eBH}} = -J \sum_{\langle ij \rangle} \hat{b}_i^\dagger \hat{b}_j + \frac{U}{2} \sum_i \hat{n}_i (\hat{n}_i - 1) - \sum_i \mu_i \hat{n}_i + \sum_{i \neq j} \frac{V_{ij}^{\text{dd}}}{2} \hat{n}_i \hat{n}_j. \quad (3.36)$$

Here the contact interaction U is modified, by taking into account the on-site dipolar terms as an effective on-site interaction, and written as

$$U = g \int d\mathbf{r} |w(\mathbf{r})|^4 + \frac{1}{(2\pi)^3} \int d\mathbf{k} \widetilde{U}_{\text{dd}}(\mathbf{k}) \tilde{\rho}^2(\mathbf{k}), \quad (3.37)$$

where $g = \frac{4\pi\hbar^2 a_s}{2M_r}$ is given by Eq. (2.8). We notice that the resulting on-site interaction can be increased or decreased by changing the lattice confinement depth.

In conclusion of this section, it should be mentioned that the phase diagram of dipolar ultracold gases is very rich. Theoretical studies have shown that there are self-organized vortex phases, charge-density waves and supersolid phases in dipolar quantum gases. Experimentally, there are two possible ways to achieve strong dipole-dipole interactions: one can use atoms with large magnetic dipole moments [57, 58], or use molecules with large electric dipole moments [27].

Chapter 4

Theoretical Approaches

As discussed in the previous chapter, the Hubbard model for both bosonic and fermionic systems is one of the most successful models of strongly correlated many-body systems, which effectively describes the interplay between the kinetic energy J and interactions U . Due to its structural simplicity and its wide range of applications, it represents the standard model for tackling strong correlations. Despite its simplicity, the Hubbard model is not exactly solvable for finite value of U/J except in one spatial dimension. Historically, analytical and numerical methods, such as the decoupling method [89, 118, 119], Bethe ansatz approximation [120–122] and perturbation theory [123, 124], have been used to obtain rather unique insights into the physics of many-body systems. However, the reliability of the methods discussed above is limited to special coupling regimes or simplified versions of the Hubbard model. Therefore the need for an alternative method, which can reliably describes a general many-body system from weak to strong coupling, is inevitable.

One possible efficient way to study such a system is using quantum Monte Carlo (QMC) simulations [125, 126]. But the disadvantage of this method is that one can study only small systems and then extrapolate to the thermodynamical limit, which limits the effort to understand a wide range of quantum systems. Another powerful technique is the dynamical mean field theory (DMFT) [127–129] which was proposed in the 1980s by M. Metzner, D. Vollhardt, A. Georges, and G. Kotliar for investigations of strongly correlated electron systems, and gives the exact solution in the limit of dimension $d = \infty$ [127]. Recently, inspired by the case of fermions, dynamical mean field theory for bosonic systems has been developed [7] and implemented [8–11] to give a non-perturbative description of zero- and finite-temperature properties of the homogeneous Bose-Hubbard model. In this chapter, we first introduce the basic descriptions of the macroscopical ground states of the many-body system. Then, we introduce the Gutzwiller method and BDMFT as its higher-order extension. Finally, we extend BDMFT to a real-space BDMFT (RBDMFT) formalism [12] to account for the trapped system which is crucial in the experiments.

4.1 Ground state of a quantum many-body system

Determining properties of the ground state of a quantum many-body system is one of the most important problems in theoretical solid-state physics. The basic feature of the ground state is that it can macroscopically exist with all physical properties are essentially uniform, which is normally known as phase. A system can be in different phases, which depend on the parameters of the system. And the system can go through a macroscopic transition from one phase to another driven by microscopic fluctuations, such as thermal or quantum fluctuations, accompanied by a qualitative change of ground-state correlations. In ultracold gases, quantum fluctuations usually dominate due to the strong suppression of thermal fluctuations. In this section, we focus on the phase transition driven by quantum fluctuations.

4.1.1 Quantum phase transition

Phase transition describes an abrupt change of the ground state due to thermal or quantum fluctuations. Thermal phase transitions, which are caused by a competition between the energy of system and the entropy of its thermal fluctuations, are common in our daily life. The underlying physics is that the system seeks to minimize the free energy $F = E - TS$ in thermal equilibrium, where E is energy, T temperature and S entropy. At $T = 0$, classical systems usually freeze into a fluctuationless ground state, since the corresponding phase transition is solely driven by thermal fluctuations, which die out. In contrast, quantum systems have fluctuations due to the Heisenberg uncertainty principle even at $T = 0$, since it is impossible to simultaneously specify both momentum and position of the atoms. The interplay between kinetic energy and interactions indicates that it is possible to have more than one ground states, while thermodynamics tells us that the system should be in one of its possible ground states. This is the physical mechanism of quantum phase transition, driven by quantum fluctuations. In a more formal language, we consider a Hamiltonian $\hat{H}(g)$ which varies as a function of parameter g . If one or more of *discrete* characteristics is distinct between large and small g , distinct quantum phases are realized in these limiting cases. This indicates that there is at least one special value $g = g_c$, where the system can not be smoothly connected as g is varied, and we treat the non-analytical point g_c as a quantum phase transition [130]. A detailed discussion of quantum phase transition can be found in Ref. [131]. At finite temperature, if quantum fluctuations with an energy scale of $\hbar\omega$ are larger than thermal fluctuations with an energy scale of $k_B T$, quantum fluctuations dominate the properties of the many-body system. Due to the impossibility of achieving absolute zero temperature, finite-temperature systems with dominant quantum fluctuations have drawn much attention and become a widespread topic in recent years. Now it is possible to cool a many-body system down to low temperatures of the order of 10^{-9} K in the laboratory, which provides an ideal model system for understanding quantum phenomena

resulting from many-body correlations. Due to the high degree of tunability of ultracold gases, quantum phase transitions for bosonic [3] and fermionic [47, 48] lattice systems, which were predicted long ago by the Bose- and Fermi-Hubbard model, have been observed experimentally. Specifically, the recently developed quantum-gas microscopy [54–56] provides a new tool to study the dynamics of individual atoms and the transitions between different quantum phases in real-times [132].

4.1.2 Symmetry breaking vs. phase transition

At zero temperature, as pointed out in the previous section, two or more ground states of the Hamiltonian can appear in a many-body system. Due to quantum fluctuations, the macroscopic system can evolve into one particular ground state which does not possess the same symmetry as the Hamiltonian (such as gauge symmetry, translational symmetry, rotational symmetry in real space or in spin space). Tuning the parameters of the system, such as interaction, the system could undergo a phase transition from one ground state to another, and this corresponding process usually relates to a concept, namely symmetry breaking, which was introduced by Landau in the 1930’s as a mean to describe the dramatic changes in properties of different phases. Landau’s theory of phase transitions relates to the spontaneous development of an order parameter which breaks the symmetry of the system. In a formal language, the symmetry of the system can be described by the symmetry operator \hat{O} . If

$$[\hat{O}, \hat{H}] = 0, \quad (4.1)$$

we say the Hamiltonian \hat{H} has the \hat{O} symmetry. For example, the conservation of particle number guarantees the continuous $U(1)$ symmetry (gauge symmetry) of the Bose-Hubbard model in Eq. (3.9), i.e. the Hamiltonian is invariant under a gauge transformations

$$\hat{b} \rightarrow e^{i\phi} \hat{b}, \quad (4.2)$$

where ϕ denotes the angle of phase shift. When the superfluid phase appears, with the development of a finite value of superfluid order parameter $\langle \hat{b} \rangle$, it breaks the gauge symmetry of the Bose-Hubbard model.

For two-component bosonic systems in an optical lattice, the superfluid phase spontaneously breaks the gauge symmetry; the anti-ferromagnetic phase develops a checkerboard density wave pattern, and thereby breaks the translational symmetry of the system; the XY-ferromagnetic phase develops a finite value of particle-hole correlation, characterized by a two-body correlator $\langle \hat{b} \hat{d}^\dagger \rangle$ (b and d denotes the two species) and corresponding to a spin polarized in the xy plane, and thus breaks the $SU(2)$ symmetry (rotational symmetry for spin 1/2 Hamiltonian); the supersolid phase breaks both translational and gauge symmetry. In the following chapters, we will employ different order parameters for characterizing different phases.

4.2 Mean-field approach

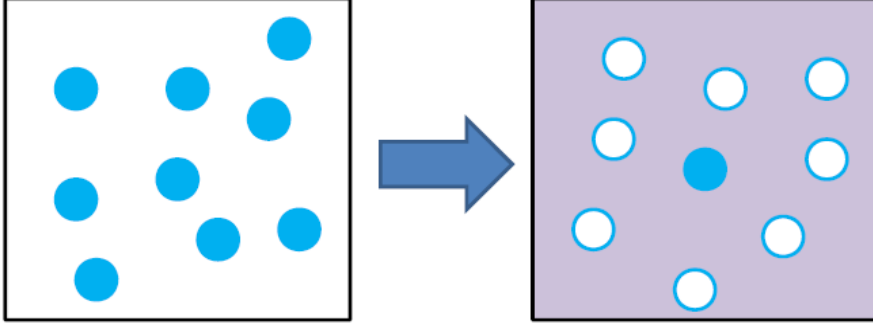


Figure 4.1: Sketch of mean-field theory. The left box shows the real physical system where the two-particle interaction leads to correlations between particles. The right box shows that the interactions felt by a particle (full circle) are replaced by an average interaction due to the average density of the other particles (indicated by open circles).

As pointed out in the previous chapter, the many-body problem is very complicated since all the atoms are correlated due to the interactions between atoms. To solve this problem, we need to make some approximations which can partially take into account correlations and give a reliable physical picture [133]. Mean-field theory is one of them, which is based on the replacement of the interactions by an effective mean field and reduces the many-body problem to a single-particle problem (see Fig. 4.1). In quantum field theory, it is equivalent to replacing the Hamiltonian by expanding in terms of fluctuations around the average of the field. And correspondingly, mean-field theory can be viewed as zero-order expansion of the total Hamiltonian. Mean-field theory can be applied to a number of physical systems, and in this section we will apply it to the Bose-Hubbard model in Eq. (3.9). Within the framework of mean-field theory, the creation operator can be separated into an average value ϕ and a fluctuation term \tilde{b} :

$$\hat{b}_i = \phi_i + \tilde{b}_i \quad (4.3)$$

and if neglecting the second-order fluctuation terms, it yields

$$\begin{aligned} \hat{b}_i^\dagger \hat{b}_j &= (\phi_i^* + \tilde{b}_i^\dagger)(\phi_j + \tilde{b}_j) \\ &\approx \phi_i^* \phi_j + (\tilde{b}_i^\dagger - \phi_i^*) \phi_j + \phi_i^* (\tilde{b}_j - \phi_j) \\ &= \phi_i^* \tilde{b}_j + \tilde{b}_i^\dagger \phi_j - \phi_i^* \phi_j. \end{aligned} \quad (4.4)$$

Substituting Eq. (4.4) into Eq. (3.9) gives rise to

$$\hat{H} = -J \sum'_{\langle i,j \rangle} \left(\hat{b}_i^\dagger \phi_j + \text{h.c.} - \frac{\phi_i^* \phi_j + \phi_i \phi_j^*}{2} \right) + \frac{U}{2} \sum_i \hat{n}_i (\hat{n}_i - 1) + \sum_i \epsilon_i \hat{n}_i, \quad (4.5)$$

where the sum is over all sites i , and \sum' denotes that the summation over j is all the nearest neighbors for each site i .

We notice that the mean-field theory decouples the tunneling between nearest-neighbor sites and reduces the original problem to a single-site problem. The method discussed above is known as site-decoupling mean-field theory [5, 134], which is actually equivalent to the Gutzwiller method (see Appendix B). The Gutzwiller ansatz was originally used as an approximation method for fermionic models [90, 135–137], and afterwards extended by Rokhsar and Kotliar in 1991 to bosons on a lattice [138]. The Gutzwiller method generally is based on the variational state:

$$\Phi = \prod_{i=1}^L \sum_{n=0}^{\infty} f_n^{(i)} |n_i\rangle, \quad (4.6)$$

where $|n_i\rangle$ denotes the normalized state with n_i bosons in the single-particle ground state at site i . We notice that this ansatz discards almost all spatial correlations, but becomes exact in the limit of infinite dimensions and yields reasonably good phase diagrams in two and three dimensions [139]. In the next section, we will show that it is actually a coherent state description, which is well suited for real experiments. The physical reason why the Gutzwiller method works so well for the Bose-Hubbard model is that it is a successful method to treat Hilbert space constraints due to strong particle correlations, and that it includes the spontaneous symmetry breaking, namely a finite order parameter $\langle b \rangle$, in contrast to fermions. Therefore, it can recover the limiting cases: the limit $U = 0$ with the corresponding ground state of a pure BEC (superfluid state), and the opposite limit $U \gg J$ with the corresponding ground state of a Mott insulator at integer filling (see Fig. 4.2).

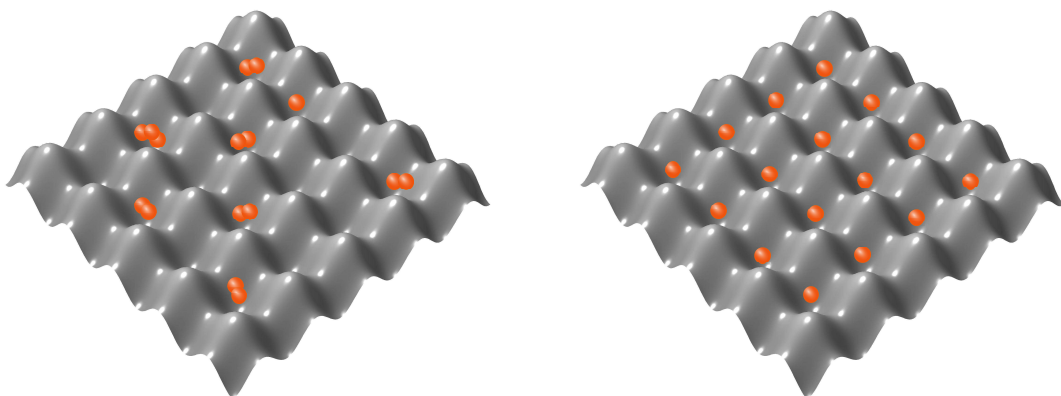


Figure 4.2: Sketch of superfluid state where atoms are delocalized (**left**), and Mott-insulating state where atoms are localized (**right**).

4.2.1 Superfluid phase

Superfluidity, which occurs in a variety of systems with frictionless flow, was first observed in ^4He in 1938 by two groups, Kapitza in Moscow [140] and Allen and Misener in Cambridge [141], and then explained in a quantitative description by Landau in 1941 [142]. Since then, numerous work has been devoted to this area and the corresponding physical concepts developed for liquid He are widely used later in ultracold gases. In some sense, superfluidity is a dynamical quantum phenomenon of the many-body system and usually involves more than just the ground state. However, it usually occurs with the condensation phenomena and properties of superfluidity can be understood in terms of Bose-Einstein condensation [143], even though a Bose-Einstein condensate does not necessarily exhibit superfluidity, such as ideal bosonic gases. For lattice bosonic systems, if the interactions U between particles are much smaller than the kinetic energy J , the system will minimize its energy by delocalizing particles. At sufficiently low temperature, the thermal de Broglie wavelength is so long that all the particles are correlated. As a result, a large fraction of atoms share the same single-particle ground state, i.e. collectively condense into the lowest accessible quantum state, resulting in a new state of matter, namely Bose-Einstein condensate. The Bose-Einstein condensate is responsible for the phenomenon of superfluidity, and, by conversion, is usually referred to as a superfluid. In the trivial $U = 0$ limit, the system of N particles is a pure BEC with all particles in the $q = 0$ Bloch state of the lowest band (single-particle ground state in the homogeneous system). The corresponding canonical condensate state of N particles on N_L lattice sites is

$$\begin{aligned}\Phi_N &= \frac{1}{\sqrt{N!}} (\hat{c}_k^\dagger)^N |0\rangle \\ &= \frac{1}{\sqrt{N!}} \left(\frac{1}{\sqrt{N_L}} \sum_l \hat{b}_l^\dagger \right)^N |0\rangle,\end{aligned}\quad (4.7)$$

which is equivalent to the coherent state

$$\begin{aligned}\Phi_N &= e^{\sqrt{N}\hat{c}_k^\dagger - \sqrt{N}\hat{c}_k} |0\rangle \\ &= e^{-\frac{N}{2}} e^{\sqrt{N}\hat{c}_k^\dagger} |0\rangle \\ &= e^{-\frac{N}{2}} e^{\sqrt{N} \frac{1}{\sqrt{N_L}} \sum_l \hat{b}_l^\dagger} |0\rangle \\ &= \prod_{l=1}^L e^{-\frac{N}{2}} e^{\sqrt{\frac{N}{N_L}} \hat{b}_l^\dagger} |0\rangle\end{aligned}\quad (4.8)$$

in the thermodynamical limit, where \hat{c}_k^\dagger denotes the creation operator for the single-particle state with quasimomentum k , and \hat{b}_l^\dagger the one for a single-particle state at site l . Both states give identical expectation values for number-conserving operators [144]. Thus, the coherent state can be used to describe

the physical state of real experiments (the physical state in the trap is typically a canonical state of fixed particle number), since the total particle number is usually conserved on the experimental time-scale and the particle number fluctuations for the coherent state are negligible in comparison to the mean particle number in the thermodynamic limit. The coherent state description is very convenient, due to its separation into an unentangled direct product of *local* coherent states in real space. This many-body state can be directly used in the mean-field description as a variational function, as discussed in the previous section. It is worth noticing that multi-species BECs could macroscopically coexist with new physics appearing [78], if the spin degree of freedom is included, and the coherent state described above can be easily extended to the multi-species system.

4.2.2 Mott-insulating phase

Although the band-structure theory is successful in describing *electronic phases* of crystalline materials such as metals, insulators and semiconductors, there are numerous transition-metal oxides which are poor conductors and indeed often insulators, which was first reported by de Boer and Verwey in 1937 [145]. This type of insulators are known as Mott insulator, named after the physicist Nevill Francis Mott [146–148], who took the first important step towards the understanding of the Mott-insulating state through including strong correlations between electrons. Since then, a large amount of work has been done on this topic, where the details can be found in Ref. [149, 150]. Physically, the abnormality of this kind of insulators arises due to electron-electron interactions, whereas the band insulator results from electron-ion interactions.

In ultracold gases, Mott phases have been observed experimentally in recent years, both for bosons [3, 96–98] and fermions [47, 48]. To understand the properties of these phases, we can first consider the case $U \gg J$. In this case, the tunneling between nearest neighbors can be neglected and the ground state can be written as a product over different sites:

$$\Phi_N = \prod_{l=1}^L (\hat{b}_l^\dagger)|0\rangle, \quad (4.9)$$

where we assume one particle per lattice site. When finite hopping appears, atoms can tunnel from one site to another. The system remains in the Mott state as long as the gain in kinetic energy due to hopping is smaller than U , and the system exists with an absence of off-diagonal long-range order. The corresponding physical picture is that the system exhibits particle-hole fluctuations around the pure ground state with $J = 0$. When the hopping becomes of the order of U , however, the system will undergo a phase transition from a Mott insulator to a superfluid phase, where the atoms are delocalized over the whole lattice. The Mott-insulating phase can thus be regarded as a state with a strong suppression of density fluctuations. When the spin degree

of freedom is included, the Mott insulator would possess spin fluctuations governed by another low-energy scale via second-order tunneling (compared to particle-hole excitations), and the system could develop competing spin ordering at sufficiently low temperature [151, 152].

We notice that the Gutzwiller ansatz can recover the two limiting cases of the Bose-Hubbard model both $J \gg U$ and $U \gg J$, at least for the integer filling. That is the reason why the Gutzwiller method is well suited for predicting the superfluid to Mott insulator phase transition. Within the Gutzwiller approximation, the critical value for the transition from a superfluid to a Mott insulator phase is given by $U/J = 5.8z$ for filling $n = 1$ and $J/J = 4nz$ for filling $n \gg 1$ [5, 134, 153], where z is the lattice coordination number.

4.3 Bosonic dynamical mean field theory

Whereas it is most often possible to write down effective Hamiltonians for strongly correlated systems, it is more difficult to solve such model systems, analytically or numerically, due to the existence of strong correlations which invalidate perturbation theory. Strong correlation is a challenging fundamental obstacle for the fully understanding of the physics of solid-state phenomena. Even though static mean-field theory can be applied to qualitatively capture the properties of spinless bosonic system, it can not resolve spin order as a result of dynamical correlations for a multi-species system. Formerly, a theory beyond static mean-field for the fermionic Hubbard model, namely dynamical mean field theory [127–129] proposed in the late 1980s as a generalization of Weiss mean-field theory and a development of previous works for lattice models in high dimensions [154–156], has been applied as a non-perturbative formalism to study strongly-correlated electronic systems. The key point of dynamical mean field theory is to map the many-body lattice system to a single-site problem, which is then solved self-consistently. The advantage of dynamical mean field theory beyond static mean-field theory is that it includes the local quantum fluctuations of the strongly correlated system. It has thus led to considerable progress in our understanding in solid-state physics. Recently, a bosonic version of dynamical mean field theory has been proposed to tackle the strongly correlated bosonic system [7], which includes condensed and normal bosons consistently. It is also a non-perturbative formalism and hence can be applied within the full range from small to large couplings, which becomes exact in infinite dimensions. Whereas the original version of BMDFT [7] requires a different scaling of superfluid and normal parts of the action and is constructed as a well-defined theory in strictly infinite dimensions, our derivation here is based on a uniform scaling of the bosonic hopping amplitude, i.e. we treat condensed and normal bosons on equal footing as in Refs. [8, 11, 12]. Specifically, we present the BDMFT equations as a systematic expansion up to subleading order in the small parameter $1/z$, where the control parameter z is the lattice coordination number. To leading order, this yields Gutzwiller

mean-field theory, while from the subleading terms of order $1/z$ we obtain BDMFT equations. We thus regard BDMFT as an higher order expansion around Gutzwiller theory. Note that the final equations in all proposals (for finite dimensions) coincide.

4.3.1 BDMFT equations

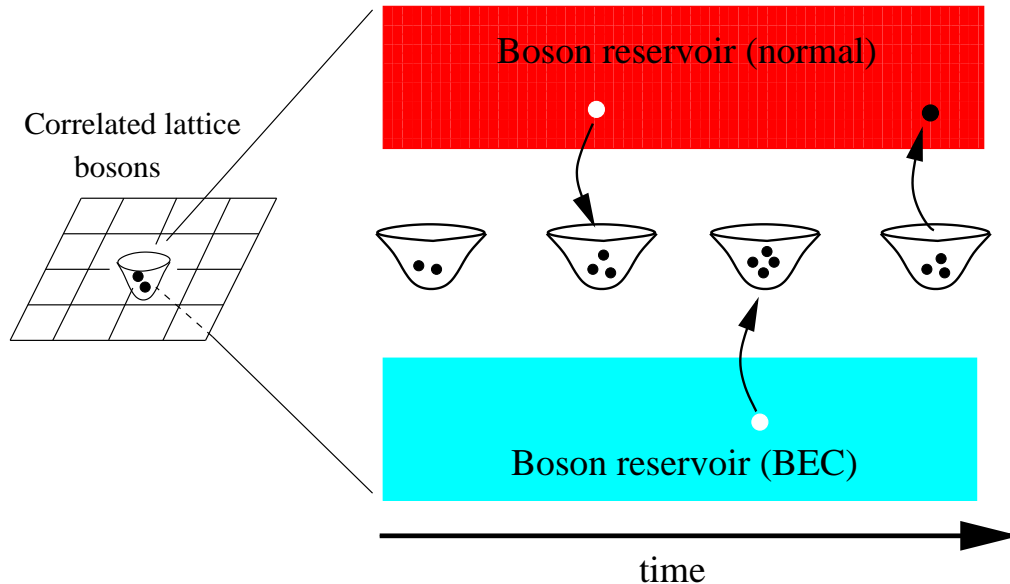


Figure 4.3: Bosonic dynamical mean-field theory (B-DMFT): Within BDMFT the full many-body lattice problem is reduced to a single-site problem which is coupled to two reservoirs corresponding to bosons in the Bose-Einstein condensate and in the normal state. This schematic picture visualizes the idea of DMFT for lattice bosons in analogy to the fermionic counterpart (From Ref. [7]).

As in fermionic dynamical mean field theory, the main idea of the BDMFT approach is to map the quantum lattice problem with many degrees of freedom onto a single site - “impurity site” - coupled self-consistently to a noninteracting bath (see Fig. 4.3). To derive self-consistency equations within BDMFT, we use the “cavity method” [7, 129]: one considers a single site of the lattice and integrates out the remaining degrees of freedom on all other sites (see Fig. 4.4). The underlying physics is that, if the number of neighboring sites goes to infinity, the central limit theorem holds so that the fluctuations from site-to-site can be neglected. This indicates that this method is exact for infinite dimensions, and is a reasonable approximation for high but finite dimensions, with the influence from other sites being integrated out and replaced by an effective bath. The dynamics at the impurity site can thus be thought of as the interaction (hybridization) of this site with the bath. Therefore, properties of the many-body system can be captured by a single impurity model, and

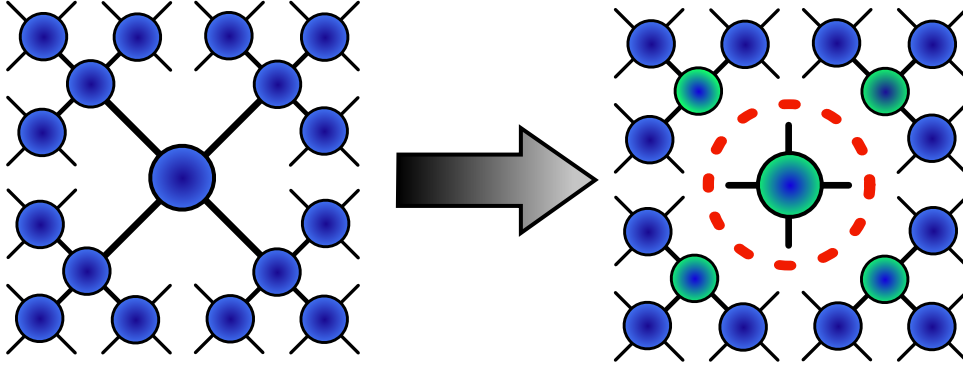


Figure 4.4: Illustration of the cavity method. Sites which are connected to the impurity (coloured greenish) have one neighbor less once the impurity is removed (From Ref. [8]).

that is the reason why we can return to the Anderson impurity Hamiltonian representation, as will be discussed in the following.

Within the tight-binding approximation, bosonic gases in a strong optical lattice can be described by the multi-species single-band Bose-Hubbard model in Eq. (3.12). To derive the self-consistency relations within BDMFT, we use the path integral formalism in the coherent state representation. Inspired by the cavity derivation of fermionic DMFT equations [129], we consider the impurity site of the bosonic system and formally integrate out all the other degrees of freedom. In this way we obtain the effective action of the impurity site

$$Z_{\text{imp}} \equiv \frac{Z}{Z^{(0)}} = \int \prod_{\nu} \mathcal{D}b_{0,\nu}^* \mathcal{D}b_{0,\nu} e^{-S_{\text{imp}}}, \quad (4.10)$$

where Z is the full partition function and $Z^{(0)}$ is the partition function of the cavity system without the impurity. The detailed derivation of the effective action can be found in Appendix C. For brevity, we derive the self-consistency loop within the framework of BDMFT for the case of a cubic lattice in this section.

In deriving the effective impurity action, we consider the limit of a high but finite dimensional optical lattice, and formally rescale all hopping parameters as $t_{\nu} = t_{\nu}^*/z$ with the coordination number z being treated as a small parameter. Based on the linked cluster theorem, the action of the impurity site up to subleading order in $1/z$ is then expressed in the standard way [129] as:

$$S_{\text{imp}} = - \int_0^{\beta} d\tau d\tau' \sum_{\lambda\nu} \begin{pmatrix} b_{0\lambda}^*(\tau) \\ b_{0\lambda}(\tau) \end{pmatrix}^T \mathbf{g}_{0,\lambda\nu}^{-1}(\tau - \tau') \begin{pmatrix} b_{0\nu}(\tau') \\ b_{0\nu}^*(\tau') \end{pmatrix} + \int_0^{\beta} d\tau \quad (4.11)$$

$$\left\{ \frac{1}{2} \sum_{\lambda\nu} U_{\nu\lambda} n_{0\nu}(\tau) (n_{0\lambda}(\tau) - \delta_{\nu\lambda}) - \sum_{\langle 0i \rangle, \nu} t_{\nu} (b_{0\nu}^*(\tau) \phi_{i,\nu}(\tau) + b_{0\nu}(\tau) \phi_{i,\nu}^*(\tau)) \right\}.$$

Here we have defined the Weiss Green's function,

$$\mathcal{G}_{0,\lambda\nu}^{-1}(\tau - \tau') = - \quad (4.12)$$

$$\begin{pmatrix} (\partial_{\tau'} - \mu_\lambda)\delta_{\lambda\nu} + t_\lambda t_\nu \sum_{\langle 0i \rangle, \langle 0j \rangle} G_{\lambda\nu,ij}^1(\tau, \tau') & t_\lambda t_\nu \sum_{\langle 0i \rangle, \langle 0j \rangle} G_{\lambda\nu,ij}^2(\tau, \tau') \\ t_\lambda t_\nu \sum_{\langle 0i \rangle, \langle 0j \rangle} G_{\lambda\nu,ij}^{2*}(\tau', \tau) & (-\partial_{\tau'} - \mu_\lambda)\delta_{\lambda\nu} + t_\lambda t_\nu \sum_{\langle 0i \rangle, \langle 0j \rangle} G_{\lambda\nu,ij}^1(\tau', \tau) \end{pmatrix},$$

and introduced

$$\phi_{i,\nu}(\tau) = \langle b_{i,\nu}(\tau) \rangle_0 \quad (4.13)$$

as the superfluid order parameters, and

$$G_{\lambda\nu,ij}^1(\tau, \tau') = -\langle b_{i,\lambda}(\tau) b_{j,\nu}^*(\tau') \rangle_0 + \phi_{i,\nu}(\tau) \phi_{j,\lambda}^*(\tau'), \quad (4.14)$$

$$G_{\lambda\nu,ij}^2(\tau, \tau') = -\langle b_{i,\lambda}(\tau) b_{j,\nu}(\tau') \rangle_0 + \phi_{i,\nu}(\tau) \phi_{j,\lambda}(\tau') \quad (4.15)$$

as the diagonal and off-diagonal parts of the connected Green's functions, respectively, where $\langle \dots \rangle_0$ denotes the expectation value in the cavity system (without the impurity site). We now check the order for different terms which survive up to subleading order in the action (4.11). The terms for the Weiss Green's functions are of order $O(1/z)$, since they come with two factors of $t_\nu \sim 1/z$ and one factor of z arising from one summation over neighboring sites. All the other terms are of order $O(1)$. The last term, for example, involves one factor of $t_\nu \sim 1/z$ and one factor of z arising from the summation over neighboring sites. The action (4.11) to leading order $O(1)$ yields Gutzwiller mean-field theory [138], while by including the subleading terms of order $O(1/z)$ we obtain the BDMFT equations. Hence we regard BDMFT as an expansion in $1/z$ around Gutzwiller method. Another issue needed to be addressed is that expectation values in the cavity system should be identical to those on the impurity site, since in the original system they are independent of the lattice position. Considering sites at the edge of the cavity with one neighbor less compared to the impurity site (see Fig. 4.4), simply identifying the expectation values yields an error of order $1/z$. For the Green's functions, this process has no problem, because they already appear at subleading order in the action, but it yields a relevant correction to the superfluid order parameter and turns out to be essential for quantitatively accurate predictions of the phase boundary. Details regarding the implementation for the superfluid order parameter are given in Appendix D. Note that the effective action (4.11) for finite z coincides with the previous proposal [7]. However, our derivation is different from the original derivation, since we focus on finite dimensions and our goal is to make direct predictions for the three-dimensional experimental situation.

In the Matsubara frequency representation, the Weiss Green's function has the following form:

$$\mathcal{G}_{0,\lambda\nu}^{-1}(i\omega_n) = (i\omega_n \sigma_z + \mu_\lambda)\delta_{\lambda\nu} - t_\lambda t_\nu \sum'_{i,j} \mathbf{G}_{ij,\lambda\nu}(i\omega_n), \quad (4.16)$$

where \sum' means summation only over the nearest neighbors of the “impurity” site, $n = 2n\pi/\beta$ are Matsubara frequencies, and

$$\begin{aligned}\mathbf{G}(i\omega_n) &= \int_0^\beta d\tau e^{i\omega_n\tau} \mathbf{G}(\tau) \\ \mathcal{G}(i\omega_n) &= \int_0^\beta d\tau e^{i\omega_n\tau} \mathcal{G}(\tau).\end{aligned}\quad (4.17)$$

To close the self-consistency loop, the next step is to express the Weiss Green’s function by means of the Green’s function of the original lattice which is given by

$$\mathbf{G}_{\text{lat}}(i\omega_n) = \int d\epsilon \frac{1}{i\omega_n + \mu - \epsilon - \Sigma_{\text{imp}}(i\omega_n)}, \quad (4.18)$$

where we make the approximation that the impurity self-energy $\Sigma_{\text{imp}}(i\omega_n)$ coincides with the lattice self-energy $\Sigma_{\text{lat}}(i\omega_n)$, and that it is a local (i.e. momentum-independent) quantity which is exact in infinite dimensions. After a few derivation steps [129], it yields the local Dyson equation

$$\mathcal{G}_0^{-1} = \Sigma_{\text{imp}}(i\omega_n) + \mathbf{G}_{\text{lat}}^{-1}(i\omega_n). \quad (4.19)$$

The self-consistency BDMFT loop is closed and has the following structure: We start from an initial guess of the Weiss Green’s function. The effective action of the model is then given by Eq. (4.11), which allows us to calculate all expectation values, including local Green’s functions and self-energies. And then the new Weiss Green’s function can be obtained by using Eq. (4.19) for a general lattice. This procedure is repeated until convergence is reached.

4.3.2 Anderson impurity model

The most difficult step in the procedure discussed above is to find a solver for the effective action. However, one cannot do this analytically. To obtain BDMFT equations, it is better to return back to the Hamiltonian representation. Thus one has to find a Hamiltonian which has the same effective action as given by Eq. (4.11). It is easy to notice that the corresponding Hamiltonian can not contain only on-site degrees of freedom, since then we would lose retardation effects. The best way to express the effective action of Eq. (4.11) is using the single impurity Anderson model.

The effective action (4.11) can be represented by an Anderson impurity Hamiltonian

$$\begin{aligned}\hat{H}_A = & - \sum_{\nu} z t_{\nu} (\phi_{\nu}^* \hat{b}_{\nu} + \text{h.c.}) + \frac{1}{2} \sum_{\lambda\nu} U_{\lambda\nu} \hat{n}_{\nu} (\hat{n}_{\lambda} - \delta_{\lambda\nu}) - \sum_{\nu} \mu_{\nu} \hat{n}_{\nu} \\ & + \sum_l \epsilon_l \hat{a}_l^{\dagger} \hat{a}_l + \sum_{l,\nu} \left(V_{\nu,l} \hat{a}_l^{\dagger} \hat{b}_{\nu} + W_{\nu,l} \hat{a}_l \hat{b}_{\nu} + \text{h.c.} \right),\end{aligned}\quad (4.20)$$

where the chemical potential and interaction term are directly inherited from the Hubbard Hamiltonian. The bath of condensed bosons is represented by the Gutzwiller term with superfluid order parameters ϕ_ν for each component. The bath of normal bosons is described by a finite number of orbitals with creation operators \hat{a}_l^\dagger and energies ϵ_l , where these orbitals are coupled to the impurity via normal-hopping amplitudes $V_{\nu,l}$ and anomalous-hopping amplitudes $W_{\nu,l}$. The anomalous hopping terms are needed to generate the off-diagonal elements of the hybridization function.

We now turn to the solution of the impurity model. The Anderson Hamiltonian can straightforwardly be implemented in the Fock basis, and the corresponding solution can be achieved by exact diagonalization (ED) of fermionic DMFT [129, 157]. After diagonalization, the local Green's function, which includes all the information about the bath, can be obtained from the eigenstates and eigenenergies in the Lehmann-representation

$$\begin{aligned} G_{\text{imp},\lambda\nu}^1(i\omega_n) &= \frac{1}{Z} \sum_{mn} \langle m | \hat{b}_\lambda | n \rangle \langle n | \hat{b}_\nu^\dagger | m \rangle \frac{e^{-\beta E_n} - e^{-\beta E_m}}{E_n - E_m + i\hbar\omega_n} \\ &+ \beta\phi_\lambda\phi_\nu \end{aligned} \quad (4.21)$$

$$\begin{aligned} G_{\text{imp},\lambda\nu}^2(i\omega_n) &= \frac{1}{Z} \sum_{mn} \langle m | \hat{b}_\lambda | n \rangle \langle n | \hat{b}_\nu | m \rangle \frac{e^{-\beta E_n} - e^{-\beta E_m}}{E_n - E_m + i\hbar\omega_n} \\ &+ \beta\phi_\lambda\phi_\nu. \end{aligned} \quad (4.22)$$

Integrating out the orbitals leads to the same effective action as in Eq. (4.11), if the following identification is made

$$\Delta_{\lambda\nu}(i\omega_n) \hat{=} t_\lambda t_\nu \sum'_{i,j} \mathbf{G}_{ij,\lambda\nu}^0(i\omega_n), \quad (4.23)$$

where we have defined the hybridization functions:

$$\begin{aligned} \Delta_{\lambda\nu}^1(i\omega_n) &\equiv - \sum_l \left(\frac{V_{\lambda,l} V_{\nu,l}}{\epsilon_l - i\omega_n} + \frac{W_{\lambda,l} W_{\nu,l}}{\epsilon_l + i\omega_n} \right) \\ \Delta_{\lambda\nu}^2(i\omega_n) &\equiv - \sum_l \left(\frac{V_{\lambda,l} W_{\nu,l}}{\epsilon_l - i\omega_n} + \frac{W_{\lambda,l} V_{\nu,l}}{\epsilon_l + i\omega_n} \right). \end{aligned} \quad (4.24)$$

Hence, the Weiss Green's function can be expressed by the hybridization functions, and it reads

$$\begin{aligned} \mathcal{G}_{\lambda\nu}^{-1}(i\omega_n) &= (i\omega_n \sigma_z + \mu_\lambda) \delta_{\lambda\nu} - \Delta_{\lambda\nu}(i\omega_n) \\ &= \Sigma_{\text{imp},\lambda\nu}(i\omega_n) + \mathbf{G}_{\text{imp},\lambda\nu}^{-1}(i\omega_n). \end{aligned} \quad (4.25)$$

The detailed derivation for the self-energy can be found in Appendix E.

We make the approximation that the lattice self-energy $\Sigma_{\text{lat},\lambda\nu}$ coincides with the impurity self-energy $\Sigma_{\text{imp},\lambda\nu}$, that is, we neglect all non-local components $\Sigma_{i \neq j} \approx 0$ and approximate the on-site ones $\Sigma_{ii} \approx \Sigma_{\text{imp}}$. It immediately

yields $\mathbf{G}_{\text{lat},\lambda\nu} = \mathbf{G}_{\text{imp},\lambda\nu}$, and the self-consistency loop is then completed by the conditions for lattice Green's function

$$\mathbf{G}_{\text{lat}}(\mathbf{k}, i\omega_n) = \frac{1}{i\omega_n \sigma_z + \mu_\lambda - \Sigma_{\text{imp}}(i\omega_n) - \epsilon_{\mathbf{k}}} \quad (4.26)$$

and for the superfluid order parameter

$$\phi_\nu = \langle \hat{b}_\nu \rangle_0, \quad (4.27)$$

where the notation $\langle \dots \rangle_0$ means that the expectation value is calculated in the cavity system. Equations (4.25), (4.26) and (4.27) thus constitute the set of BDMFT self-consistency conditions. The self-consistency loop is solved as follows: starting from an initial choice for the Anderson parameters and the superfluid order parameter, the Anderson Hamiltonian is constructed in the Fock basis and diagonalized to obtain the eigenstates and eigenenergies. The eigenstates and energies allow us to calculate the superfluid order parameter $\phi_\nu = \langle \hat{b}_\nu \rangle_0^{z-1}$, the impurity Green's functions and self-energies, and then obtain the lattice Green's functions via Eq. (4.26). Subsequently, new Anderson parameters are obtained, by fitting the Anderson hybridization functions from Eq. (4.24) to new hybridization functions obtained from the lattice Dyson equation, which is done by a conjugate gradient method. With this new Anderson parameters, the procedure is iterated until convergence is reached.

It is worth noticing that the derivation described above is independent of temperature. This indicates that we cannot only determine ground state properties, but also obtain information about the thermodynamics of lattice bosons, as we will show in the next chapter. Similar to fermionic DMFT, another question is how well BDMFT deals with situations with broken symmetries, in which case Goldstone modes are present in the spectrum but absent from the DMFT spectrum [129]. However, since in three dimensions the spectral weight of the Goldstone mode is finite and generally small, this approximation can be justified and does not prohibit excellent qualitative and often even quantitative agreement between (B)DMFT results and more exact methods (if available), even in symmetry-broken states [8]. We also note that, in dynamical mean field theory, all the spatial fluctuations of the self-energy have been neglected, while the local quantum fluctuations are fully taken into account. This is the reason why the theory is called "dynamical". Here the impurity model describes the local dynamics of the quantum many-body system. Therefore, this quantum impurity model remains an interacting many-body problem which requires reliable methods for calculating the local self-energy of the impurity model. Moreover, recently improved versions of dynamical mean field theory have been proposed to include the nonlocal correlations for clusters in momentum space [158] or in real space [159, 160].

4.4 Real-space bosonic dynamical mean field theory

BDMFT, described in the previous section, is for homogeneous systems. However, experimentally the spatial inhomogeneity due to the external trap is always present, leading to a spatially varying density. For these trapped systems, the concept of the long range order has to be modified and the development of ordered phases on finite length scales should be also examined. Therefore, it is inevitable to make a real-space extension of BDMFT for tackling the inhomogeneity of trapped systems. Formerly, for the fermionic Hubbard model, a real-space generalization of DMFT has been developed and implemented successfully to address inhomogeneous fermionic systems [161, 162]. In the spirit of the case of fermions, here we extend BDMFT to a real-space BDMFT formalism [12] for inhomogeneous systems, as is relevant for most experiments. Within the RBDMFT, the self-energy is taken to be local, but depends on the lattice site in an inhomogeneous system, i.e. $\Sigma_{ij,\lambda\nu} = \Sigma_{\lambda\nu}^i \delta_{ij}$, where δ_{ij} is a Kronecker delta. RBDMFT is capable of providing an accurate and non-perturbative description of the low-energy state of the inhomogeneous Bose-Hubbard model.

In this section, we take the system, consisting of a two-component bosonic gas in an optical lattice with either 2D square or 3D cubic geometry, as an example to derive the real-space BDMFT formalism. Experimentally the Bose-Bose mixture could consist of two different species, or two different hyperfine states of a single species. In addition we include an external harmonic trapping potential which gives rise to inhomogeneity. This system can be described by a two-component inhomogeneous Bose-Hubbard model (3.12).

In a more formal language within RBDMFT, we first map the Hamiltonian (3.12) onto a set of individual single-site problems, each of which is described by a *local* effective action

$$\begin{aligned}
S_{\text{eff}}^{(i)} &= \int_0^\beta d\tau d\tau' \sum_{\lambda,\nu=\{b,d\}} \mathbf{b}_\lambda^{(i)}(\tau)^\dagger \mathcal{G}_{0,\lambda\nu}^{(i)}(\tau - \tau')^{-1} \mathbf{b}_\nu^{(i)}(\tau') \\
&+ \int_0^\beta d\tau \left\{ \sum_{\lambda,\nu} \frac{1}{2} U_{\lambda,\nu} n_\lambda^{(i)}(\tau) (n_\nu^{(i)}(\tau) - \delta_{\lambda\nu}) \right. \\
&\left. - \sum_{\langle ij \rangle, \nu} t_\nu (b_\nu^{(i)}(\tau)^* \phi_{j,\nu}^{(i)}(\tau) + b_\nu^{(i)}(\tau) \phi_{j,\nu}^{(i)}(\tau)^*) \right\}, \quad (4.28)
\end{aligned}$$

where i is the index of the lattice site. In this equation τ is imaginary time and the function $\mathcal{G}_{0,\lambda\nu}^{(i)}(\tau - \tau')$ is a local non-interacting propagator interpreted as a *local* dynamical Weiss mean-field which is determined in a self-consistent manner. Here we use the Nambu notation $\mathbf{b}_\nu^{(i)}(\tau) \equiv (b_\nu^{(i)}(\tau), b_\nu^{(i)}(\tau)^*)$. Moreover the static bosonic mean-fields are defined in terms of the bosonic operator $b_{j,\nu}$ as

$$\phi_{j,\nu}^{(i)}(\tau) = \langle b_{j,\nu} \rangle_0. \quad (4.29)$$

The index 0 indicates that all averages are taken for the cavity system, i.e. excluding the impurity site. Now each of the local actions can be treated as an impurity in the presence of a bath (representing the influence of the rest of the lattice) and therefore captured via an Anderson impurity Hamiltonian. There are several techniques to solve the impurity model. Here we apply exact diagonalization (ED) [8, 129, 157].

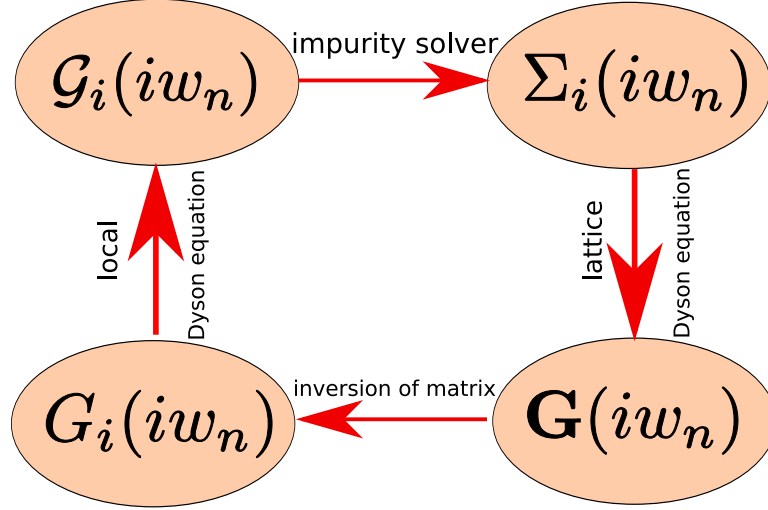


Figure 4.5: Schematic picture of the real-space bosonic dynamical mean field theory loop.

In practice, we start with an initial set of local Weiss Green's functions and local bosonic superfluid order parameters $\phi_{j,\nu}^{(i)}(\tau)$. After solving the action (4.28), we obtain a set of local self-energies $\Sigma_{\lambda\nu}^{(i)}(i\omega_n)$ with ω_n being the Matsubara frequency. Then we employ the Dyson equation in real-space representation in order to compute the interacting lattice Green's function

$$\mathbf{G}(i\omega_n)^{-1} = \mathbf{G}_0(i\omega_n)^{-1} - \Sigma(i\omega_n). \quad (4.30)$$

The site-dependence of the Green's functions is shown by boldface quantities that denote a matrix form with site-indexed elements. Here $\mathbf{G}_0(i\omega_n)^{-1}$ stands for the inverse non-interacting Green's function

$$\mathbf{G}_0(i\omega_n)^{-1} = (\mu + i\omega_n)\mathbf{1} - \mathbf{t} - \mathbf{V}. \quad (4.31)$$

In this expression, $\mathbf{1}$ is the unit matrix, the matrix elements t_{ij} are hopping amplitudes for a given lattice structure. The detailed derivation of the non-interacting Green's function can be found in Appendix F. The external harmonic trapping potential is included via $V_{ij} = \delta_{ij}V_i$ with $V_i \equiv V_0 r_i^2$ and r_i being the distance from the trap center. Eventually the self-consistency loop is closed by specifying the Weiss Green's function via the local Dyson equation

$$\left(\mathcal{G}_{0,\lambda\nu}^{(i)}(i\omega_n)\right)^{-1} = \left(\mathbf{G}_{\lambda\nu}^{(i)}(i\omega_n)\right)^{-1} + \Sigma_{\lambda\nu}^{(i)}(i\omega_n), \quad (4.32)$$

where the diagonal elements of the lattice Green's function yield the interacting local Green's function $\mathbf{G}_{\lambda\nu}^{(i)}(i\omega_n) = (\mathbf{G}_{\lambda,\nu}(i\omega_n))_{ii}$. This self-consistency loop is repeated until the desired accuracy for superfluid order parameters and Weiss Green functions is obtained. In Fig. 4.5 we schematically depict the R-DMFT loop.

Complementary to RBDMFT, in this thesis we employ single-site BDMFT combined with a local density approximation (LDA) to explore the physics of the model (3.12), where we adjust the chemical potential on each lattice site according to LDA as $\mu_\nu(r) = \mu_\nu^0 - V(r)$ and treat the problem as locally homogeneous. The advantage of this approach is that larger system sizes can be treated. We validate it by comparison with the more rigorous RBDMFT approach.

Chapter 5

Quantum Magnetism and Pair Superfluidity

In ultracold gases, properties of strongly correlated many-body systems are mostly governed by contact interactions. They play an important role in determining physical phenomena, especially in lattice systems, since the optical lattice reduces the kinetic energy and makes interaction and kinetic energy comparable. Due to interplay between the kinetic energy and contact interactions, the system can be in different phases and go through phase transition from one phase to another. As an important example, the phase transition from the superfluid to the Mott-insulating phase has been realized experimentally for single-component bosonic gases [3], based on loading them into an optical lattice. We can now ask what will happen if the spin degree of freedom is included in the many-body system, which can be easily achieved through loading different hyperfine states of the same species or different species in ultracold experiments. Theoretical studies indicate that multi-species bosonic gases in an optical lattice have rich phase diagram, and the system can be in different types of magnetic insulating states, depending on the interplay between kinetic energy, contact interactions and spin fluctuations. Our goal is to study strongly correlated multi-species bosonic gases, and to reveal the underlying physics of magnetically ordered states and even d -wave superfluid states (analog of superconducting states where the corresponding microscopic picture is still unclear).

In this chapter, we focus on two-component bosonic gases in an optical lattice, and answer two questions: which phases arise in this system and how to cool the system to observe the corresponding phases. Firstly, we address magnetic ordering at zero and finite temperature both in homogeneous and trapped Bose-Bose mixtures with repulsive interspecies interactions in optical lattices. By using bosonic dynamical mean field theory, we obtain phase diagrams of the homogeneous two-component Bose-Hubbard model in a three-dimensional cubic lattice, which features competing magnetic order of XY-ferromagnetic and anti-ferromagnetic type in addition to the Mott-insulating and superfluid state. We show that these magnetic phases are stable even in the presence of a harmonic trap. Then, we investigate finite-temperature thermodynamics

and demagnetization cooling of Bose-Bose mixtures in a cubic optical lattice. We calculate the finite-temperature phase diagram, and remarkably find that the system can be *heated* from the superfluid into the Mott insulator at low temperature, analogous to the Pomeranchuk effect in ^3He . This provides a promising many-body cooling technique. We examine the entropy distribution in the trapped system and discuss its dependence on temperature and an applied magnetic field gradient. Our numerical simulations quantitatively validate the spin-gradient demagnetization cooling scheme proposed in recent experiments. Finally, we simulate the pair-superfluid phase of both homogeneous and trapped ultracold gases with attractive inter-species interaction in an optical lattice. We obtain the phase diagram of a Bose-Bose mixture with filling number $n = 1$ at zero and finite temperature in a three dimensional cubic optical lattice, and confirm the stability of pair superfluidity for asymmetric hopping of the two species. We calculate the critical temperature of the pair-superfluid phase. In the presence of an external trap, we discuss the effects of inhomogeneity. We also investigate the influence of population imbalance of the two species on the pair-superfluid phase, and observe that it is destroyed already by small population imbalance of the two species.

5.1 Quantum magnetism

5.1.1 Introduction

In this section, we will investigate quantum magnetism, which is one of the most intriguing areas in condensed-matter physics. Even though many theoretical and experimental efforts have been devoted to revealing the mechanisms behind magnetic ordering of solid-state systems [130], a quantitative comparison between theory and experiment seems a very challenging task due to the high level of complexity. Therefore, it is highly desirable to find controllable quantum systems which are able to work as *quantum simulator* for the original solid-state many-body systems, such as ultracold quantum gases in optical lattices which provide an excellent laboratory for investigating many-body quantum systems with an unprecedented level of precision and control. In recent years, fundamental many-body phenomena of interacting bosons, such as the superfluid to Mott-insulator transition [3], correlated atom tunneling [51], and superexchange due to second-order atom tunneling [52], have been observed. These studies involve the basic mechanisms leading to quantum magnetism and pave the way to realize and detect magnetic long-range ordering of spinful fermions or bosons, which may eventually give insight into the mechanism of high- T_c superconductivity as well [49].

Here, we theoretically investigate a two-component bosonic gas in 2D and 3D optical lattices, which is modeled by the single-band Bose-Hubbard model. We investigate the homogeneous (untrapped) system by means of bosonic dynamical mean field theory [7–11] and the harmonically trapped case by its

real-space generalization, which extends the original BDMFT formalism to the study of inhomogeneous systems. We map out the phase diagram for the low-filling case with $n = 1$ and $n = 2$ per site and obtain diverse phases such as superfluid, unordered Mott state and XY-ferromagnetic order. In addition we turn to the inhomogeneous (trapped) Bose-Hubbard model which is more closely related to the experimental situation. We include the effect of the external confining potential by RBDMFT, which assumes site-dependent self-energies. To our best knowledge, this is the first systematic and non-perturbative study of the magnetic properties of a two-component inhomogeneous Bose-Hubbard model. It will bring more insight into ongoing experiments on Bose-Bose mixtures in optical lattices.

5.1.2 Magnetic phases of a homogeneous Bose-Hubbard model

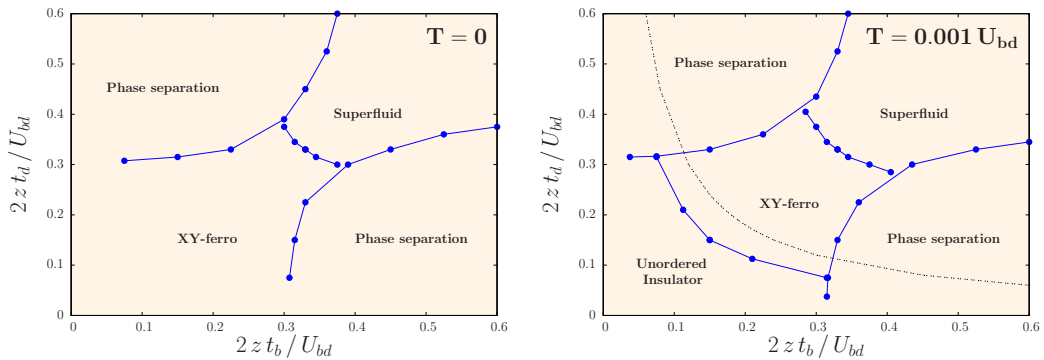


Figure 5.1: Left panel: zero-temperature phase diagram for the two-component Bose-Hubbard model in a 3D cubic lattice, as a function of hopping parameters. The interaction values are $U_b = U_d = 1.01 U_{bd}$ and the total filling is $n = 1$ with $n_b = n_d = 0.5$ (except in the phase separation regime). Right panel: finite temperature phase diagram ($T = 0.001 U_{bd}$). The energy scale of the magnetic coupling $4t_b t_d / U_{bd}$ is shown by the black dashed line.

We start by exploring the two-component Bose-Hubbard model in the homogeneous case. We consider a 3D cubic lattice and focus on the situation of total filling $n = n_b + n_d$, *i.e.* $n = 1$ and $n = 2$ with balanced densities $n_b = n_d = 0.5$ and $n_b = n_d = 1$ respectively. For each filling, we calculate both zero and finite temperature phase diagrams. We focus on the interaction regime where the inter-species interactions, $U_{bb} \equiv U_b, U_{dd} \equiv U_d$, and intra-species interaction, U_{bd} , are just slightly different, *i.e.* $U_b = U_d = 1.01 U_{bd}$. This particular regime of interactions is accessible by Feshbach resonances, and indeed our choice is motivated by a recent experiment at MIT [107], where a sample of ^{87}Rb atoms in hyperfine states $|1, -1\rangle$ and $|2, -2\rangle$ with nearly equal inter- and intra-species interactions has been prepared. The selection of interactions (U_{bd} slightly smaller than $U_{b,d}$) is due to a larger variety of novel

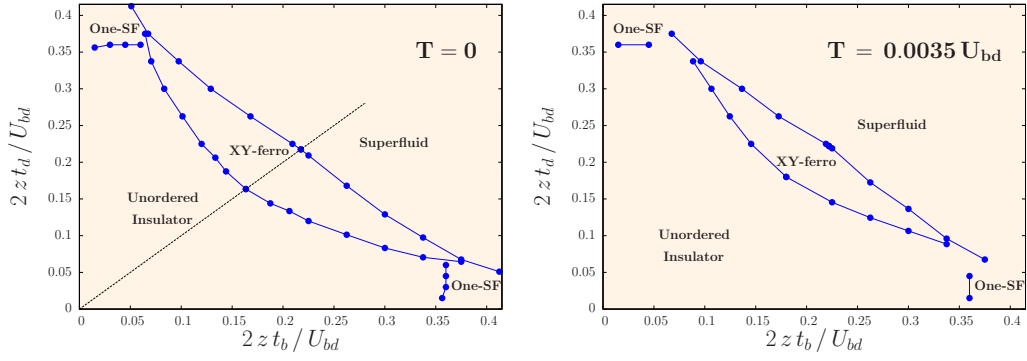


Figure 5.2: Left panel: zero-temperature phase diagram for the two-component Bose-Hubbard model in a 3D cubic lattice, as a function of hopping parameters. The diagonal dotted line indicates $t_b = t_d$. The interaction values are $U_b = U_d = 1.01 U_{bd}$ and the total filling is $n = 2$ with $n_b = n_d = 1$. Right panel: finite temperature phase diagram ($T = 0.0035 U_{bd}$).

magnetic phases appearing in this regime [152]. In all our calculations we set $U_{bd} = 1$ as the unit of energy, and z is the coordination number.

Fig. 5.1 displays the zero and finite temperature phase diagrams of the system with a total filling of one particle per site, $n = 1$. At $T = 0$ (left panel) we find three distinct phases which are characterized according to the value of the superfluid order parameters ϕ_b, ϕ_d and the two-body correlator $\phi_{bd} = \langle b d^\dagger \rangle - \langle b \rangle \langle d^\dagger \rangle > 0$ which indicates the XY-ferromagnetic spin-ordering. When both species have comparably large hopping, we find a superfluid phase characterized by $\phi_{b,d} \neq 0$. Instead when the hopping amplitudes are very anisotropic, the species with larger hopping is more easily delocalized and therefore superfluid, while the other component favors a Mott insulating phase. In this parameter regime, we do not find a homogeneous converged BDMFT solution where each component has the same filling, which indicates phase separation between the superfluid and the Mott insulator. We notice that the phase diagram is symmetric upon species interchange and this symmetry is also manifested in the Hamiltonian (3.12). The third phase emerges when the hopping amplitudes are small. This non-superfluid (*i.e.* Mott insulating) phase possesses an XY-ferromagnetic spin order and is characterized by $\phi_{b,d} = 0$ and $\phi_{bd} > 0$.

We investigate also the effect of finite temperature on the phase diagram as shown in the right panel of Fig. 5.1. We observe that the superfluid remains robust against small finite T . On the other hand, the XY-ferromagnetic spin-ordered phase is sensitive to finite temperature since it is formed in the low-hopping regime and therefore easily destroyed by thermal fluctuations. At finite T , the parameter regimes of ordered phase is reduced in favor of developing a non-magnetically ordered Mott state which is characterized by $\phi_{bd} = 0$

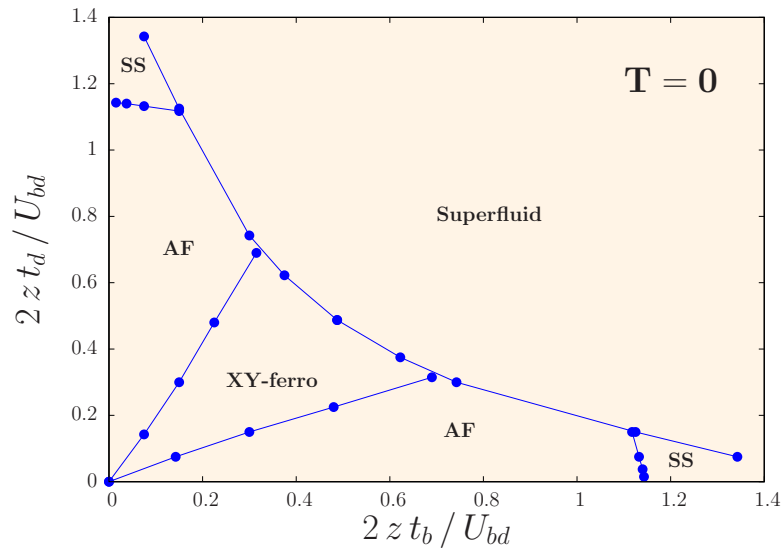


Figure 5.3: Zero-temperature phase diagram for a two-component Bose-Hubbard model in a 3D cubic lattice, as a function of hopping parameters. The interaction values are $U_b = U_d = 12 U_{bd}$ and the total filling is $n = 1$ with $n_b = n_d = 0.5$.

and $\phi_{b,d} = 0$, and which we denote as “unordered insulator” in the following. The black dashed line shows the energy scale of the magnetic coupling $4t_b t_d / U_{bd}$ [152].

Now we turn to the case when the total filling at each site is $n = 2$. Fig. 5.2 (left panel) shows the zero-temperature phase diagram for this case. The main difference compared to $n = 1$ is the presence of a large unordered (Mott) insulator regime at low hopping values. As for $n = 1$, here we also find a sizable superfluid regime when both species have large hopping amplitudes. On the other hand, when the hopping amplitude for one component is very small and the other one very large, the system will be in a new phase with one component being superfluid and the other one Mott insulating. This *one-component superfluid* phase, *e.g.* for the d component, is defined by $\phi_b = 0$ and $\phi_d > 0$. There are also two Mott states: the XY-ferromagnet at intermediate hopping and the unordered (Mott) insulator in the lower hopping regime. At finite temperature (right panel) both superfluid phases remain robust and almost unchanged. The main effect of finite T is to reduce the XY-ferromagnetic phase in favor of the unordered Mott insulator.

A further important spin-ordered state is the anti-ferromagnetic (AF) phase. Its existence in the Mott domain has been shown in previous investigations [151, 152]. In order to address this phase within our formalism, we adopt a set of parameters in which the inter-species interactions $U_{b,d}$ are much larger than the intra-species one: $U_b = U_d = 12 U_{bd}$. This specific choice is inspired by a

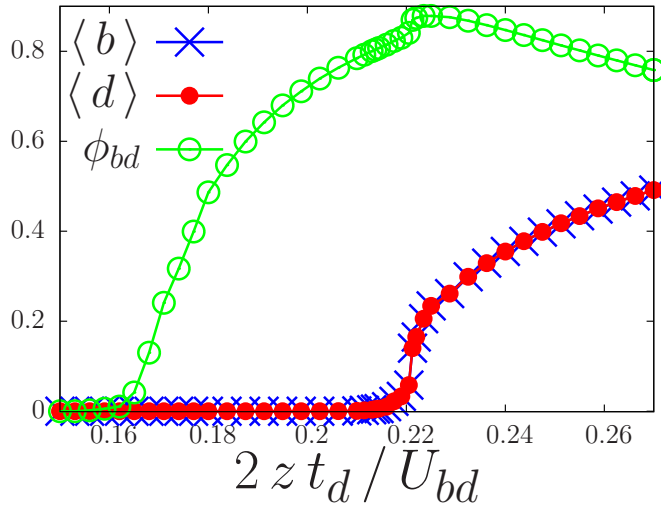


Figure 5.4: t_d dependence of order parameters $\langle b \rangle$, $\langle d \rangle$, and ϕ_{bd} along the diagonal black dotted line in the left panel of Fig. 5.2. The interaction regime is set to $U_b = U_d = 1.01 U_{bd}$ and the hopping amplitudes $t_b = t_d$ with filling factors $n_b = n_d = 1$.

previous BDMFT study [8] in which the corresponding phase diagram was obtained on the Bethe lattice. Here, we map out the phase diagram on a 3D cubic lattice which is directly relevant for experimental studies. Fig. 5.3 sketches the phase diagram for this case with the total particle filling $n = 1$. In addition to the two previously discussed phases, superfluid and XY-ferromagnet (see Fig. 5.1, 5.2), we find two other ordered states here: AF phase and super-solid. For unequal hopping in the Mott domain, we identify a magnetically ordered phase of AF type. This non-superfluid phase (*i.e.* $\phi_{b,d} = 0$) is characterized by a finite value of the AF order parameter $\Delta_{\text{AF}}^\nu = |n_{\nu,\alpha} - n_{\nu,\bar{\alpha}}| > 0$, where ν denotes the component and α is the sublattice index ($\bar{\alpha} = -\alpha$), together with vanishing XY-ferromagnetic order $\phi_{bd} = 0$. Finally for a very large difference in the hopping of the two species we observe a small window of a super-solid phase with $\phi_b > 0, \phi_d = 0$ and $\Delta_{\text{AF}} > 0$ if $t_b \gg t_d$, and vice versa.

To investigate in detail the quantum phase transition into the ordered state, for $n = 2$ and at $T = 0$, in Fig. 5.4 we plot the dependence of the individual superfluid order parameters and also the correlator ϕ_{bd} along the line $t_b = t_d$ (the diagonal black dotted line shown in the left panel of Fig. 5.2) on the hopping. This indicates a second-order quantum phase transition from the Mott state to the XY-ferromagnet and also a second-order phase transition from the XY-ferromagnet to the superfluid.

One crucial question regarding the observation of AF and XY-ferromagnetic order is how fragile they are against thermal fluctuations. To address this important issue, we compute the respective critical temperatures. Fig. 5.5 shows T_c as a function of the hopping amplitude of species b while we keep the hop-

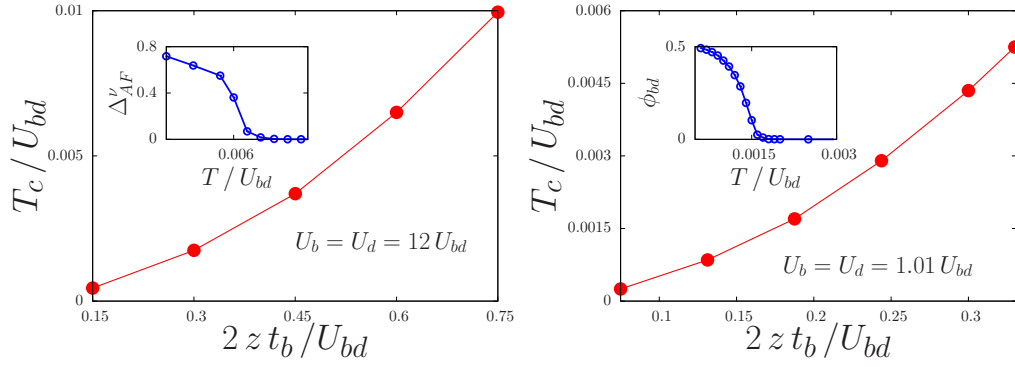


Figure 5.5: Critical temperature of AF and XY-ferromagnetic order as a function of the hopping amplitude t_b in a 3D homogeneous cubic lattice with total filling $n = 1$. **Left panel:** AF phase with hopping amplitude ratio $t_b = 4t_d$. Inset: melting of the AF phase vs temperature with hopping amplitudes $2zt_b = 0.6U_{bd}$ and $2zt_d = 0.15U_{bd}$. **Right panel:** XY-ferromagnetic phase for equal hopping amplitudes $t_b = t_d$. Inset: melting of the XY-ferromagnetic phase vs temperature with hopping amplitudes $2zt_b = 2zt_d = 0.1875U_{bd}$.

ping ratio fixed as $t_d = 4t_b$ for the AF phase (left panel) and as $t_b = t_d$ for the XY-ferromagnetic phase (right panel). We notice that T_c rises as the hopping amplitudes increase, due to the growing effective exchange couplings which stabilize magnetic order. We also note that the zero-temperature phase diagram on a 3D cubic lattice for filling $n = 1$, containing the AF phase (Fig. 5.3), has the same structure as the corresponding one on the Bethe lattice [8]. Therefore we anticipate that the finite- T counterpart of this phase diagram should also be similar on both lattices, and therefore expect that there is a region of unordered Mott insulator at low hopping. The inset of Fig. 5.5 (left panel) shows the temperature dependence of Δ_{AF}^v . It indicates a second-order phase transition from the AF phase to the unordered Mott insulator. We have also computed the order parameter ϕ_{bd} for the XY-ferromagnetic phase as shown in the right inset of Fig. 5.5 which indicates a second order transition from the XY-ferromagnetic phase to an unordered Mott insulator as well. The critical temperatures of the magnetic phases shown here are notably smaller than the lowest temperatures which have been measured in most experiments until now, except in W. Ketterle's group where temperatures as low as 350 pK ($\approx 0.01U_{bd}$) have been achieved which are estimated to be reasonably close to magnetic ordering [53].

5.1.3 Spin-ordering for an inhomogeneous Bose-Hubbard model

In the previous section, we focused on homogeneous systems. However all experiments with cold gases are carried out in the presence of an external confining potential. Therefore we extend the BDMFT scheme to real-space BDMFT to address the inhomogeneous system. In this section, using RB-

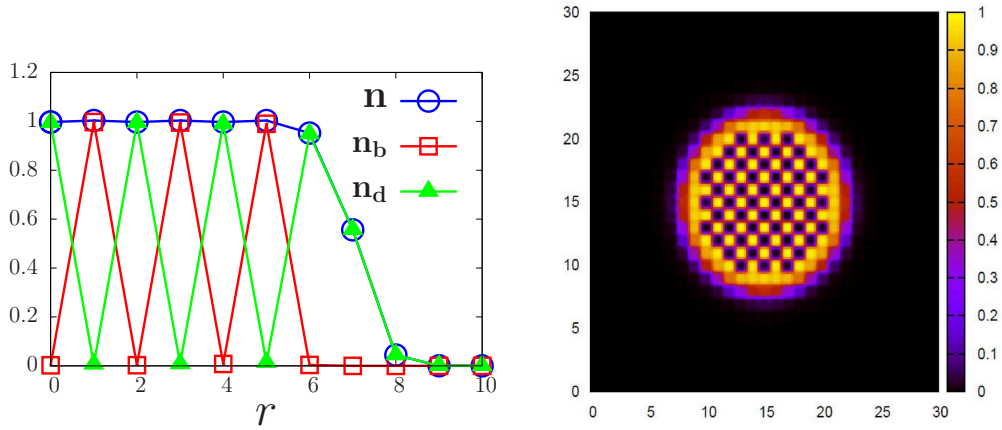


Figure 5.6: Néel-type AF order in 2D at central filling $n = 1$ and $T = 0$. **Left:** particle densities of the two species as a function of radial distance r . The interactions are set to $U_b = U_d = 12U_{bd}$, the hopping amplitudes $2zt_b = 0.1U_{bd}$ and $2zt_d = 0.25U_{bd}$ and the harmonic trap $V_0 = 0.01U_{bd}$. The chemical potentials are $\mu_b = \mu_d = 0.5U_{bd}$. **Right:** density distribution of the d component in the lattice.

DMFT and LDA+BDMFT, we will explore an inhomogeneous two-component Bose-Hubbard model both in 2D and 3D.

2D trapped Bose gas — In this section we discuss the AF phase, the XY-ferromagnet and the unordered Mott state in a 2D square lattice in the presence of a harmonic trap. We first investigate AF ordering on a 31×31 lattice and then the XY-ferromagnetic phase and the unordered Mott state on a 32×32 lattice. The choice of different lattice sizes is solely due to computational convenience.

One of the most desirable goals in current experiments on cold atomic-gases is to reach the regime of (Néel-type) AF ordering which is (for fermionic systems) expected to be a key step towards realizing a d -wave superfluid phase [49]. Here we investigate this phase for trapped two component bosons in an optical lattice. At the beginning we focus on AF order at $T = 0$. We choose the interaction parameters as $U_b = U_d = 12U_{bd}$ with unequal hopping for the two species fixed as $2zt_b = 0.1U_{bd}$ and $2zt_d = 0.25U_{bd}$. We choose a maximum local filling of $n = 1$ at the center of the trap. The left panel of Fig. 5.6 shows the RBDMFT results for the particle densities as a function of radial distance r from the trap center. The AF phase forms in the central area of the lattice as a checker-board pattern and vanishes smoothly with increasing distance r from the lattice center. This indicates that AF order is stable at the center of an external trap. However, due to the unequal hopping, the lighter species (*i.e.* the one with the larger hopping) explores the lattice more freely and forms a superfluid ring around the central checker-board pattern. This behavior is visible in the right panel of Fig. 5.6. To see how robust AF order is against

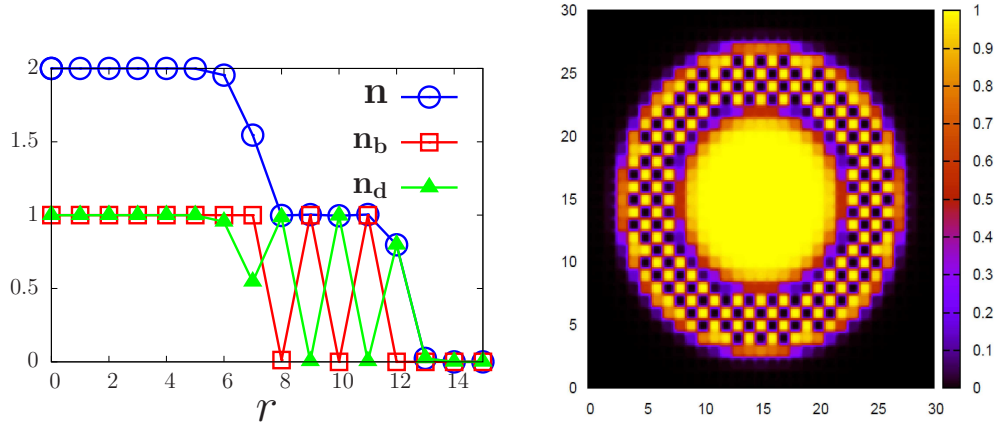


Figure 5.7: Néel-type AF order in 2D at central filling $n = 2$ and $T = 0$. **Left:** particle densities of the two species versus radius, obtained by RBDMFT. Interactions are set to $U_b = U_d = 48 U_{bd}$, the hopping amplitudes to $2zt_b = 0.1 U_{bd}$ and $2zt_d = 0.25 U_{bd}$, with a harmonic trap strength $V_0 = 0.01 U_{bd}$. The chemical potentials are $\mu_b = \mu_d = 1.5 U_{bd}$. **Right:** density distribution of the d component in the lattice.

changes of the total atom filling number, we increase the filling at the center of the trap to $n = 2$, and observe that AF order now forms as a ring around the center as shown in Fig. 5.7. We conclude that also in 2D and in the presence of a trapping potential, AF order exists in regions of total filling $n = 1$ at $T = 0$.

As is evident in the phase diagrams of the homogeneous system (Figs. 5.1, 5.2), a common magnetic phase which appears for both fillings $n = 1$ and $n = 2$ is the XY-ferromagnet. Here we investigate the stability of the XY-ferromagnetic phase in a trapped 2-component system on a 2D lattice of size 32×32 at $T = 0$. We first focus on the case of equal hopping $2zt_b = 2zt_d = 0.175 U_{bd}$ for both species and choose the interactions as $U_b = U_d = 1.01 U_{bd}$. In Fig. 5.8 the atom densities, their corresponding superfluid order parameters and the correlator ϕ_{bd} are shown, as determined by RBDMFT (left panel) and LDA+BDMFT (right panel). At the center of the lattice, we have a total filling of $n = 2$. We observe a finite value of the correlator ϕ_{bd} which implies a stable XY-ferromagnetic phase in this inhomogeneous system. With increasing distance from the trap center, we find non-zero values for the superfluid order parameters with a maximum inside the atomic cloud, indicating superfluidity for both species. We can also see that the correlator ϕ_{bd} remains finite in the superfluid regime. Moving further towards the edge of the trap, the XY-ferromagnetic phase with $n = 1$ appears and eventually a further superfluid domain. For comparison, we have computed the same quantities within LDA+BDMFT, which are shown in the right panel of Fig. 5.8. We find excellent agreement between RBDMFT and LDA+BDMFT deep inside each phase,

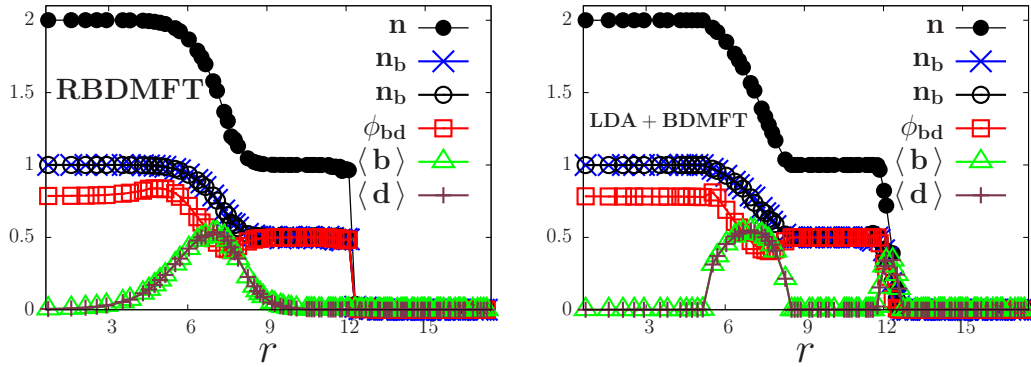


Figure 5.8: Left: RBDMFT results on a 2D square lattice for atom densities, superfluid order parameters and the XY-ferromagnetic correlator ϕ_{bd} as a function of radial distance r at $T = 0$. Interactions are set to $U_b = U_d = 1.01 U_{bd}$, with hopping amplitudes $2zt_b = 2zt_d = 0.175 U_{bd}$ and harmonic trap $V_0 = 0.01 U_{bd}$. The chemical potentials are $\mu_b = \mu_d = 1.5 U_{bd}$. Right: LDA+BDMFT results for the same parameters as the right panel.

but RBDMFT provides the more accurate description of the smooth transition between the different phases. Note that the second superfluid ring is very narrow within RBDMFT which is most likely a finite-size effect.

We now consider the case of low hopping amplitudes. This situation corresponds to the regime of a large area of the unordered Mott state (without symmetry breaking) in the homogeneous phase diagram (see Figs. 5.1, 5.2 for the 3D case). In Fig. 5.9 we show results for the atomic densities, superfluid order parameters, and the correlator ϕ_{bd} for the case $2zt_b = 2zt_d = 0.1 U_{bd}$ at $T = 0$. In the center of the lattice where we have filling $n = 2$, the low-energy Hilbert space of each lattice site includes the three possible local spin states $|\uparrow\uparrow\rangle$, $|\downarrow\downarrow\rangle$ and $|\uparrow\downarrow\rangle$, where \uparrow and \downarrow denote the two bosonic species. With the choice of the interactions as $U_{b,d} > U_{bd}$, the third state has the lowest energy and therefore we obtain a Mott state with $\phi_{bd} = 0$ and no symmetry breaking. For intermediate radii, where $1 < n < 2$ and both species are superfluid, ϕ_{bd} rises to a finite value and remains constant in the $n = 1$ region where the XY-ferromagnet is stable.

3D trapped case — In this final part, we consider the experimentally most interesting case of a 3D cubic optical lattice in the presence of an external harmonic trap. Due to the computational limitations for RBDMFT, here we only apply LDA+BDMFT which we previously benchmarked versus RBDMFT. Throughout this section, we consider a lattice with $41 \times 41 \times 41$ sites.

We begin the 3D trapped lattice analysis by investigating the stability of the XY-ferromagnetic phase. We first choose intermediate hopping as $2zt_b = 2zt_d = 0.195 U_{bd}$ and interactions $U_b = U_d = 1.01 U_{bd}$. This choice corresponds to the XY-ferromagnet in the homogeneous phase diagrams (Fig. 5.1, 5.2).

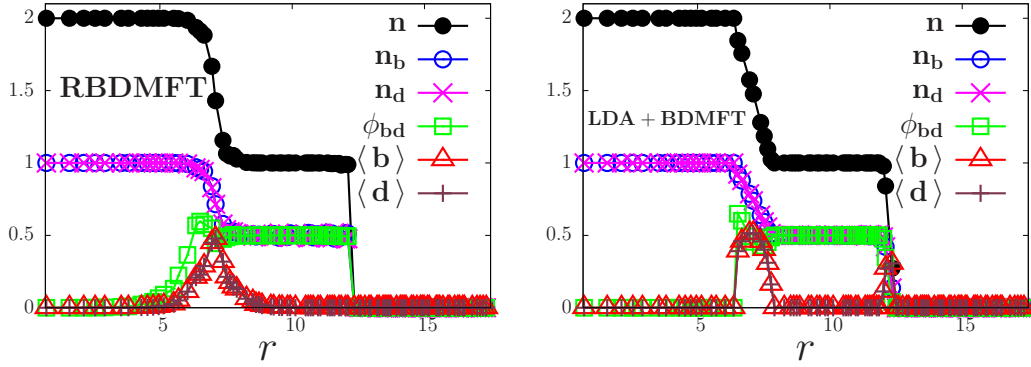


Figure 5.9: Unordered Mott state in 2D at $n = 2$ for weak hopping amplitudes at $T = 0$, calculated by RBDMFT (left panel) and LDA+BDMFT (right panel). The interactions and hopping amplitudes are $U_b = U_d = 1.01 U_{bd}$ and $2zt_b = 2zt_d = 0.1 U_{bd}$, with the harmonic trap strength $V_0 = 0.01 U_{bd}$. The chemical potentials are $\mu_b = \mu_d = 1.5 U_{bd}$.

We enforce filling $n = 2$ at the center of the lattice by adopting the proper chemical potentials. In Fig. 5.10 (left panel) we show the particle densities, superfluid order parameters and the correlator ϕ_{bd} at $T = 0$ (left panel) and at finite T (right panel). For $T = 0$ we observe a wedding-cake structure of the atomic densities, *i.e.* two plateaus with $n = 1$ and $n = 2$ and intermediate areas with non-integer filling. However we are more interested in the magnetic properties which are revealed by the correlator ϕ_{bd} . We observe that in the $n = 2$ domain, there is a XY-ferromagnetic phase, manifested by a finite value of ϕ_{bd} and vanishing superfluid order parameters. In the intermediate area $1 < n < 2$, we obtain a superfluid phase with both $\langle b \rangle$ and $\langle d \rangle$ being finite. Note that the onset of superfluidity leads to non-zero XY-ferromagnetic correlations as well. By approaching the second Mott plateau with $n = 1$, the superfluid order parameters vanish again and we obtain a non-zero value for ϕ_{bd} , indicating once again an insulating XY-ferromagnet. Finally for $n < 1$ we find a further superfluid domain.

As in the previous section, we are interested in the effect of temperature on magnetic order. Fig. 5.10 (right panel) represents the correlator ϕ_{bd} for different temperatures. First we notice that for all the temperatures considered here, the correlator possesses a larger value at $n = 2$ compared to $n = 1$. In other words, XY-ferromagnetic order is more pronounced for $n = 2$ compared to $n = 1$ as long as all other parameters of the Bose-Hubbard model are identical. To make this point clearer, we calculate the critical temperature for ferromagnetic order for both $n = 1$ and $n = 2$, and find respectively $T_c = 0.0018 U_{bd}$ (≈ 70 pK) and $T_c = 0.0051 U_{bd}$ (≈ 190 nK). We also calculate the maximum value $T_{c,max}$ of the critical temperature for XY-ferromagnetic order at filling $n = 1$ and $n = 2$, and find that $T_{c,max}$ is around 200 pK and 230 pK, respectively, when the 3D cubic lattice is formed by laser beams

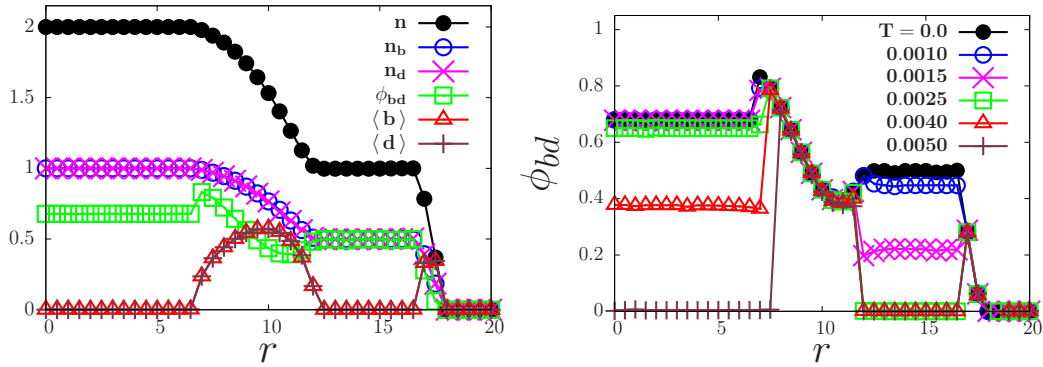


Figure 5.10: Left: particle densities, superfluid order parameters and XY-ferromagnetic correlator as a function of radius r on a 3D cubic lattice at $T = 0$, calculated within LDA+BDMFT. Interactions are set to $U_b = U_d = 1.01 U_{bd}$, hopping amplitudes are $2zt_b = 2zt_d = 0.195 U_{bd}$ with a harmonic trap $V_0 = 0.005 U_{bd}$ and $N_{\text{tot}} = 2.6 \times 10^4$. Right: Temperature dependence of the XY-ferromagnetic correlator for the same parameters as the top panel.

of wave-length 1064 nm and the scattering length is around $100a_b$ (a_b is the Bohr radius). This fact could be significant for ongoing experiments, *e.g.* in Refs. [53, 107] where spin gradient thermometry has been used to measure temperatures as low as 350 pK in a 3D optical lattice. Our calculation here indicates that it is much easier to observe XY-ferromagnetism for higher filling due to the enhanced critical temperature.

We now consider asymmetric values for the hopping amplitudes $2zt_b = 0.15 U_{bd}$ and $2zt_d = 0.225 U_{bd}$. By adjusting the chemical potentials, we obtain a globally almost balanced mixture with $N_b \simeq N_d \simeq (48\% - 52\%) N_{\text{tot}}$ with $N_{\text{tot}} = 2.6 \times 10^4$. Fig. 5.11 shows the atomic densities and XY-ferromagnetic spin-order for different temperatures (four panels). The most remarkable new feature of the asymmetric hopping regime is the vanishing ferromagnetic order in the $n = 1$ domain where $\phi_{bd} = 0$ even at $T = 0$. We also find that the total density profile first becomes sharper and then smoother again with increase of temperature. This is due to the higher spin entropy of the unordered two-component Mott insulator. Details will be discussed in the section 5.2.

It is visible in Fig. 5.11 that the lighter species (*i.e.* the one with larger hopping) always dominates the density distribution in the superfluid area where $n \neq 1, 2$, since in this regime the particle mobility plays a more important role than in the Mott domains. For the Mott state ($n = 1, 2$) the situation differs. In the spin model language [151, 152], different hopping amplitudes lead to the existence of an effective magnetic field [152],

$$h = z(2S + 1) \frac{t_b^2 - t_d^2}{U_{bd}} + \mu_b - \mu_d.$$

where $S \equiv n/2$. This effective magnetic field gives rise to an imbalance be-

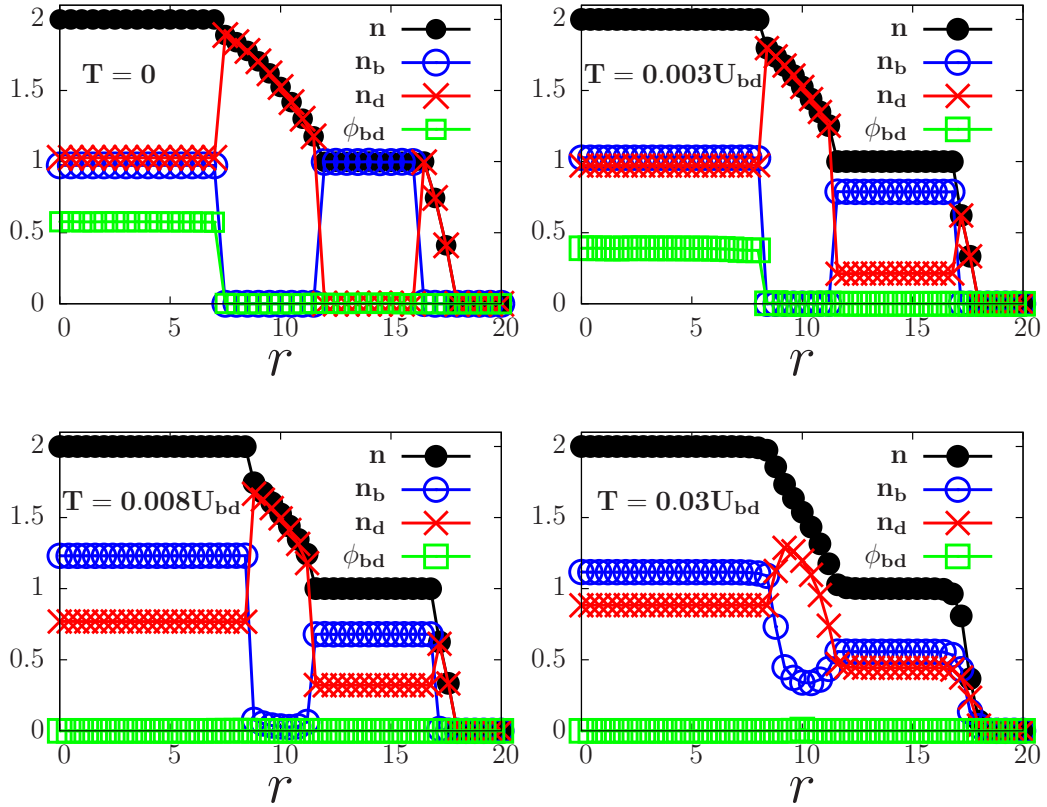


Figure 5.11: Particle densities and XY-ferromagnetic correlator vs. radial distance r for asymmetric hopping amplitudes $2zt_b = 0.15U_{bd}$ and $2zt_d = 0.225U_{bd}$ on a 3D cubic lattice. Interactions are $U_b = U_d = 1.01U_{bd}$, the trapping potential is $V_0 = 0.005U_{bd}$ and $N_{\text{tot}} = 2.6 \times 10^4$.

tween n_b and n_d which we quantify by the Z-magnetization $S_z = (n_b - n_d)/2$. At the Mott plateau with $n = 1$, the magnetization will shrink from $1/2$ (maximum of Z-magnetization due to a large effective magnetic field) to zero with increasing T due to thermal fluctuations. At the Mott plateau with $n = 2$, the magnetization depends non-monotonically on temperature. In Fig. 5.12, we show the temperature dependence of the magnetization at the filling $n = 2$ plateau by focusing on the trap center and performing a finite- T study with a single-site BDMFT for the *homogeneous* model. This behavior can be understood if we notice that in the filling $n = 2$ region the system favors a state with a small magnetization S_z at zero temperature due to a non-zero effective magnetic field. Once the temperature starts to increase from zero to a finite value, thermal fluctuations will come into play and compete with quantum fluctuations, which makes the imbalance reach a maximum at finite T , since both types of fluctuations can delocalize the atoms and smoothen the imbalance between the two species. When the temperature increases even further, the larger thermal fluctuations will simply smear out the imbalance.

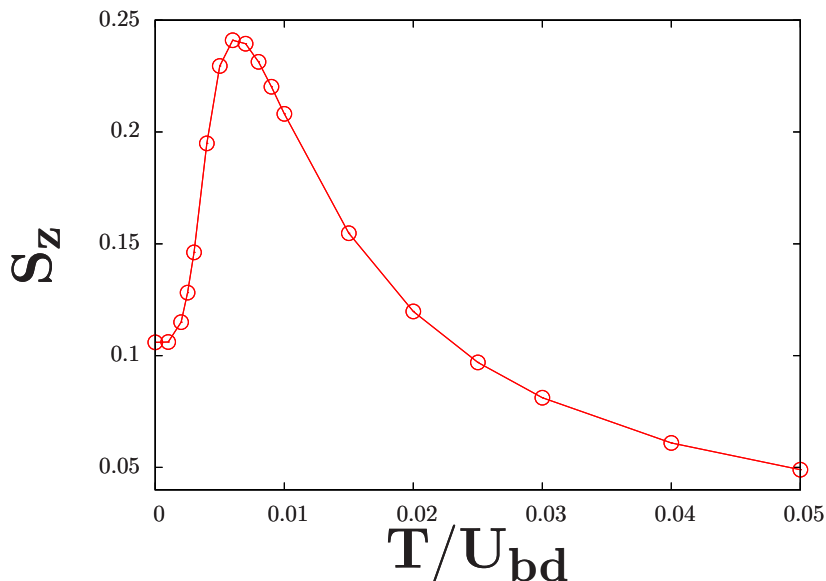


Figure 5.12: Z-magnetization (imbalance) S_z vs temperature for the *homogeneous* system. Interactions are set to $U_b = U_d = 1.01 U_{bd}$ with hopping amplitudes $2zt_b = 0.15 U_{bd}$ and $2zt_d = 0.225 U_{bd}$ and total filling $n = 2$.

Finally, we also investigate the non-magnetic Mott state without symmetry breaking which occurs at $n = 2$ for relatively low hopping amplitudes $2zt_b = 2zt_d = 0.15 U_{bd}$ (see also the homogeneous phase diagrams Fig. 5.2). Fig. 5.13 shows the results for atomic densities, their superfluid order parameters and the correlator ϕ_{bd} . At the center of the trap we indeed find a Mott state without symmetry breaking similar to the 2D case (Fig. 5.9).

5.1.4 Summary

In conclusion, we have studied magnetic ordering of a two-component Bose gas in 2D and 3D optical lattices. By using BDMFT we have calculated the phase diagrams of the homogeneous Bose-Hubbard model in a 3D cubic lattice with total particle filling $n = 1$ and $n = 2$, which feature superfluid and Mott-insulating phases and also notably reveal ordered phases with XY-ferromagnetism and Néel-antiferromagnetism in the Mott domain. We have investigated the critical temperatures of these long-range ordered states. Moreover we have confirmed the stability of these magnetic phases in a trapped 2D or 3D system. In the case of a 3D cubic lattice, we have in particular computed XY-ferromagnetic ordering at finite temperatures which is relevant for current experiments [53, 107]. Another important issue is the detection of novel magnetic phases with long-range spin order. For the anti-ferromagnetic phase, spin-sensitive detection can be used to detect the Néel-type order, i.e. one spin component can be detected after removing the other one using spin-selective

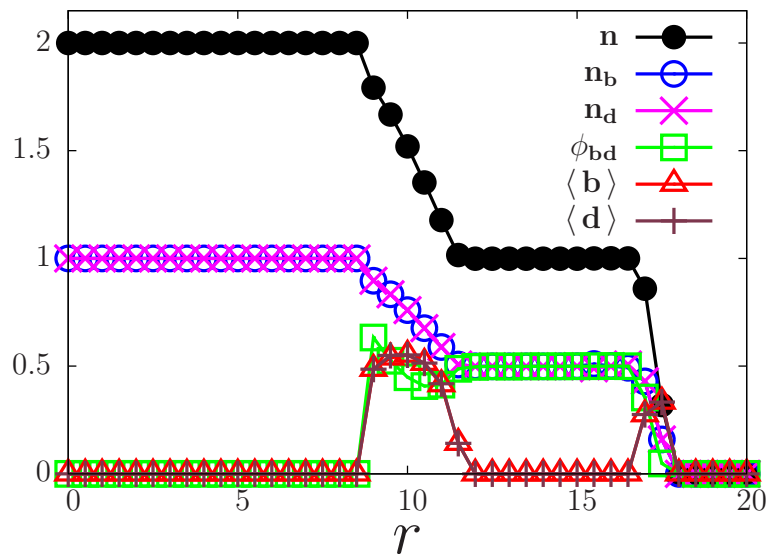


Figure 5.13: Unordered Mott state at $n = 2$ for weak hopping amplitudes at $T = 0$, calculated in 3D within LDA+BDMFT. Interactions are $U_b = U_d = 1.01 U_{bd}$, hopping amplitudes $2zt_b = 2zt_d = 0.15 U_{bd}$, with a harmonic trap $V_0 = 0.005 U_{bd}$ and $N_{\text{tot}} = 2.6 \times 10^4$.

single-site addressing, as pointed recently [163, 164]. For the XY-ferromagnetic phase, one could apply a $\pi/2$ pulse with a position-dependent phase (linear gradient), thus probing locally with different phases. For XY-ferromagnetic long-range order one would thus observe stripes with regular spacing when the phase matches and the $\pi/2$ pulse transfers all atoms into one of the two spin states [165].

Achieving the necessary ultra-low temperatures for detecting magnetic ordering of cold bosons in optical lattices has so far remained elusive. However, it is anticipated that by further experimental advances this obstacle will be overcome in the near future [50]. Our results provide theoretical benchmarks which in the future will also be extended to other geometries such as triangular or hexagonal lattices.

5.2 Pomeranchuk effect and spin-gradient cooling

5.2.1 Introduction

We have so far investigated novel quantum phases of two-component bosonic gases in an optical lattice, and focused on their emergence at very low temperatures of the order of 100 pK, which is governed by second-order tunneling processes. At present, it is still challenging to observe these quantum phases due to their low critical temperatures, and new cooling schemes are needed

to achieve them. In this section, we will investigate new cooling schemes for strongly correlated ultracold gases, and discuss the physical possibility to reach the critical temperature of magnetic ordering. This study is related to the thermodynamics of strongly correlated many-body systems. Exploring their thermodynamical properties has been arguably one of the most important experimental achievements of ultracold atomic gases, whether solely trapped by an external potential or loaded into an optical lattice. One of the goals of experiments related to thermodynamics for ultracold lattice gases is to cool the many-body systems for simulating solid-state phenomena, such as quantum magnetic phases [8, 78, 106, 107, 151, 152, 166] and high-temperature superconductivity whose underlying mechanism is still elusive [49, 167]. Different cooling schemes have been proposed for lowering temperature, such as cooling based on extracting entropy from the region or species of interests [50, 168–171]. Recently, a cooling approach using spin-gradient adiabatic demagnetization was proposed in Ketterle’s group [107], and based on it a temperature of 350 pK has been achieved for a two-component Mott insulator of ^{87}Rb in a 3D cubic lattice [53, 172]. However, this temperature is still higher than the critical temperature of the magnetic phase transition [12, 173]. Another possible cooling scheme is the Pomeranchuk effect, which is historically used to discover superfluid ^3He [174]. And we found that the multi-species bosonic gases can also be cooled by the Pomeranchuk effect, due to the spin physics [13]. In the ultracold gases, entropy is more suitable than temperature for characterizing thermodynamical properties, due to isolation of the system from the environment. Specifically, a crucial issue, related to cooling and needed to be addressed, is how entropy is distributed in the strongly interacting many-body systems in current experiments [53, 78, 107, 171].

In this section, we focus on thermodynamical properties of Bose-Bose mixtures in optical lattices in the presence of an external harmonic trap. While the thermodynamics of strongly interacting two-component Fermi gases has been investigated in detail [175–185] and the resulting critical entropy per particle $s \approx k_B \ln 2$ at the fermionic Mott-insulator transition has been achieved experimentally in a 3D cubic lattice [47, 185], less attention has been paid to the thermodynamics of two-component bosonic systems. In Ref. [173], the critical entropy for magnetic ordering of two-component *hard-core* bosons has been investigated in a 3D homogeneous system, where a critical entropy per particle of $0.35k_B$ for the XY-ferromagnetic phase and $0.5k_B$ for the Z-Néel anti-ferromagnetic phase have been found. Here, we investigate the thermodynamical properties of realistic two-component bosons in a 3D cubic optical lattice *in the presence of an external trap*, and demonstrate the validity of spin-gradient demagnetization cooling, which is in principle capable of cooling the system down to the critical temperature of magnetic order. This system can be approximately described by a single-band Bose-Hubbard model and is investigated by bosonic dynamical mean field theory, both in combination with a local density approximation and by its full real-space implementation.

5.2.2 Model and method

In this section we will consider a mixture of two species of bosonic atoms [106] or, alternatively, atoms in two different hyperfine states [78, 107], in an optical lattice in the presence of an external harmonic trap and a magnetic field gradient. Within the tight-binding picture, this system can be described by a single-band Bose-Hubbard model:

$$\begin{aligned} \hat{\mathcal{H}} = & - \sum_{\substack{\langle i,j \rangle \\ \nu=b,d}} t_\nu (\hat{b}_{i\nu}^\dagger \hat{b}_{j\nu} + \text{h.c.}) + \frac{1}{2} \sum_{i,\lambda\nu} U_{\lambda\nu} \hat{n}_{i\lambda} (\hat{n}_{i\nu} - \delta_{\lambda\nu}) \\ & + \sum_{i,\nu=b,d} (V_i - \mu_\nu) \hat{n}_{i\nu} - \sum_{i,\nu} \mu_{\text{mag}}^\nu B(x_i) \hat{n}_{i\nu}. \end{aligned} \quad (5.1)$$

Moreover, we consider a linear position-dependence of the magnetic field in x direction, that is, $B(x_i) = c x_i$ where c is the magnetic field gradient and x_i is the distance from the harmonic trap center, which describes the recent experiment [53]. This leads to

$$\begin{aligned} \hat{H}_{\text{mag}} = - \sum_{i,\nu} \mu_{\text{mag}}^\nu B(x_i) \hat{n}_{i\nu} &= - \sum_{i,\nu} \mu_{\text{mag}}^\nu c x_i \hat{n}_{i\nu} \\ &\equiv - \sum_{i,\nu} V_{\text{gra}}^\nu x_i \hat{n}_{i\nu}. \end{aligned} \quad (5.2)$$

In the Hamiltonian, $\langle i, j \rangle$ denotes the summation over nearest-neighbor sites and the two species are labeled by the index $\lambda(\nu) = b, d$. t_b and t_d denote hopping amplitudes for the two species. $\hat{b}_{i\nu}^\dagger$ ($\hat{b}_{i\nu}$) denotes the bosonic creation (annihilation) operator for species ν at site i , and $\hat{n}_{i,\nu} = \hat{b}_{i\nu}^\dagger \hat{b}_{i\nu}$ represents the local density operator. $U_{\lambda\nu}$ denotes the inter- and intra-species interactions, which can be tuned via a Feshbach resonance [186] or by a spin-dependent lattice [78], μ_ν is the global chemical potential for species ν , and $V_i \equiv V_0 r_i^2$ represents the harmonic trapping potential. μ_{mag}^ν denotes the magnetic moment of component ν , and $B(x_i)$ is the magnetic field along the x axis.

In general, it is difficult to calculate the entropy within BDMFT or RBDMFT directly. But assuming that the strongly interacting many-body system is in equilibrium, we can use the Maxwell relation $\frac{\partial s}{\partial \mu} = \frac{\partial n}{\partial T}$ to obtain the local entropy [47] at temperature T and chemical potential $\mu_s(r) = (\mu_b(r) + \mu_d(r))/2$:

$$s(\mu_s(r_0), T) = \int_{-\infty}^{\mu_s(r_0)} \frac{\partial n(r)}{\partial T} d\mu_s(r), \quad (5.3)$$

where $n(r) = n_b + n_d$ is the local density (i.e., number of particles per lattice site) at radius r . Note that formula (5.3) is only valid at fixed $\Delta\mu(r) = \mu_b(r) - \mu_d(r)$ for the two-component mixture. The density distribution obtained from BDMFT and RBDMFT is accurate enough to yield precise results for the

derivative $\frac{\partial n}{\partial T}$. This relation will be used in the following to obtain the entropy distribution.

In ongoing experiments, two hyperfine states of ^{87}Rb have been loaded into optical lattices [78, 107], with inter-species and intra-species interactions in the regime $U_b \approx U_d \approx U_{bd}$. Considering the tunability of interactions via Feshbach resonances [186] or state-dependent optical lattices [78], here we choose $U_b = U_d = 1.01U_{bd}$. In the following, we investigate the finite temperature quantum phases of this system in a cubic optical lattice, as well as the temperature dependence of the entropy distribution in the presence of a harmonic trap. Finally, these thermodynamical properties are used to quantitatively describe the adiabatic spin gradient cooling scheme of [53]. In all our calculations we choose $U_{bd} = 1$ as the unit of energy, and set $k_B = 1$. z denotes the number of nearest neighbors for each lattice site. The lattice constant is set to unity.

5.2.3 Pomeranchuk effect and phase diagram at finite T

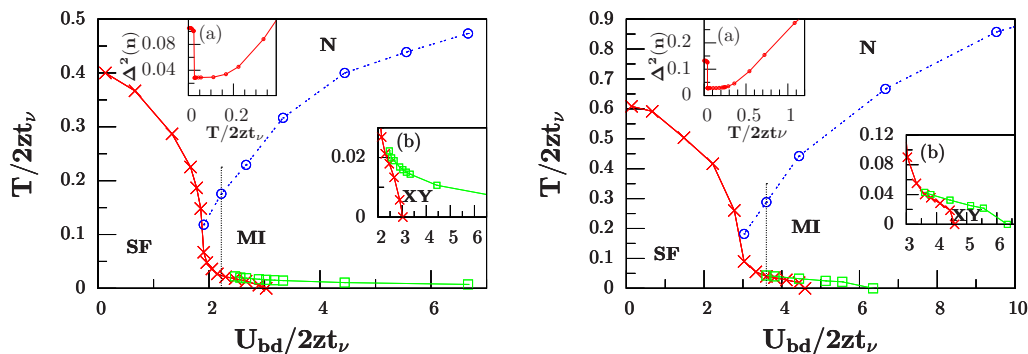


Figure 5.14: Finite temperature phase diagram of a two-component bosonic gas in a cubic optical lattice with filling $n_b = n_d = 0.5$ (**left**) and $n_b = n_d = 1.0$ (**right**). The interactions are set to $U_b = U_d = 1.01U_{bd}$, and the hopping amplitudes are $t_b = t_d$. Inset (a): fluctuations of the total filling $n = n_b + n_d$ as a function of temperature along the vertical dotted line of the main figure. Note the reduction of local number fluctuations by heating, analogous to the *Pomeranchuk effect*. Inset (b): zoom of the main figure around the critical point of magnetic order.

In this section, we explore the finite-temperature phase diagram of two-component bosons in a homogeneous and infinite optical lattice. For strongly interacting two-component Fermi gases, the critical parameters such as the critical temperature and entropy for the transition to a superfluid state have been determined experimentally [175] by considering entropy versus energy. For one-component bosonic gases in an optical lattice, the finite-temperature phase diagram has been studied experimentally in combination with Monte Carlo simulations [88]. However, for two-component bosonic gases, the critical behavior of the superfluid-normal phase transition has not been determined

yet. In the section 5.1, phase diagrams at filling $n = 1$ and $n = 2$ for zero and fixed finite temperature have been determined for the cubic lattice. But there we mainly focused on the emergence of long-range magnetic order, which is governed by second-order tunneling and only develops at very low temperatures of the order of 100 pK. On the contrary, here we will investigate quantum phase transition of the system at higher temperatures. We choose interactions $U_b = U_d = 1.01U_{bd}$ and hopping amplitudes $t_b = t_d$. Fig. 5.14 shows the phase diagram of a Bose-Bose mixture in a cubic optical lattice with filling $n_b = n_d = 0.5$ (left) and $n_b = n_d = 1$ (right). We observe four different phases. When the interaction is weak, the atoms are delocalized and at low temperature the system is in the superfluid phase (SF), characterized by a finite value of the superfluid order parameter $\phi_\nu \equiv \langle b_\nu \rangle$. When the temperature is increased, thermal fluctuations destroy the coherence between atoms and the system goes through a phase transition into the normal phase (N). For sufficiently strong interactions, the atoms are localized and hopping processes are strongly suppressed. The system is in the XY-ferromagnetic phase (characterized by $\langle bd^\dagger \rangle > 0$ and $\phi_\nu = \langle b_\nu \rangle = 0$) at low temperature, with magnetic long-range order governed by second-order tunneling processes. Since the corresponding energy scale is very small, even weak thermal fluctuations can destroy the long-range magnetic order, and the system will go through a phase transition into a Mott insulator (MI). Upon further increase of temperature, the Mott insulator melts into a normal phase which is characterized by large density fluctuations $\Delta^2(n) = \langle (n - \langle n \rangle)^2 \rangle$ where the n is the total filling per site. Compared to the single-component system in a cubic optical lattice, new features of two-component bosons appear at low temperature. Near the critical interaction strength of the zero-temperature MI-SF transition, with increasing temperature, the system will first go through a phase transition from superfluid to Mott-insulator, and then cross over to the normal phase. This is because upon heating at low temperature, the system favors localization - analogous to the Pomeranchuk effect in liquid ^3He [174, 183] - since the Mott insulating phase of spinful bosons carries more entropy in the spin degree of freedom than the superfluid. Interestingly, the first-order phase transition from superfluid to Mott-insulator occurs at a higher temperature for filling $n = 2$ (right plot in Fig. 5.14) compared to $n = 1$, indicating that it is easier to observe the Pomeranchuk effect discussed above for higher filling. Note that the XY-ferromagnetic phase at filling $n = 2$ only extends up to a finite maximum value of $U_{bd}/2zt_\nu$, which is consistent with our previous work [12].

5.2.4 Entropy distribution in the trapped system with $B = 0$

In the former section, we have studied the homogeneous system and mapped out the finite-temperature phase diagram. We will now study the thermodynamics of Bose-Bose mixtures in an optical lattice in the presence of a harmonic trap. More specifically, we investigate the temperature dependence of the entropy distribution, motivated by recent experiments [78, 106, 107]. Com-

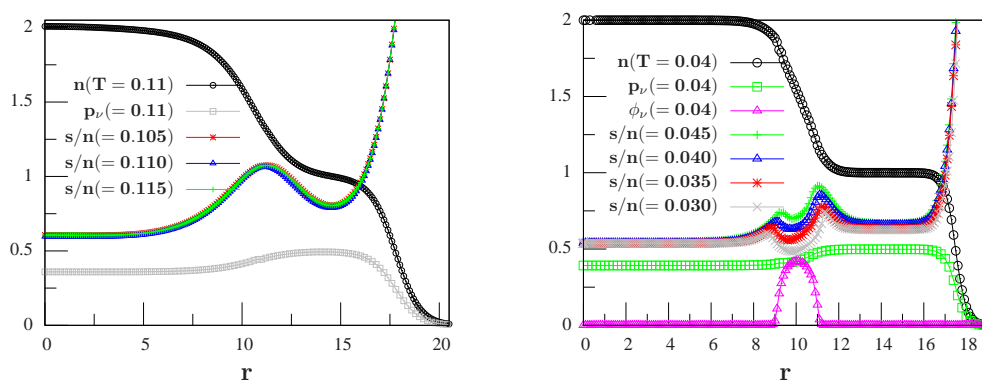


Figure 5.15: Radial profile for the total local density ($n \equiv n_b + n_d$), parity (p_ν), local entropy per particle (s/n), and superfluid order parameter (ϕ_ν) in a 3D cubic lattice obtained by BDMFT+LDA at different temperatures. The interactions are set to $U_b = U_d = 1.01U_{bd}$, with hopping amplitudes $2zt_b = 2zt_d = 0.195U_{bd}$ and harmonic trap strength $V_0 = 0.005U_{bd}$. The unit of temperature is U_{bd} .

parison between RBMDFT and BDMFT+LDA calculations has been made to check the validity of LDA for determining the entropy. Only the results of BDMFT+LDA are given here for the 3D case in a $51 \times 51 \times 51$ cubic lattice. Throughout this section, the interactions are set to $U_b = U_d = 1.01U_{bd}$ with a harmonic trap strength $V_0 = 0.005U_{bd}$ and a total filling $n = 2$ at the trap center.

In the left panel of Fig. 5.15 at high temperatures $T/U_{bd} = 0.105, 0.11$ and 0.115 (corresponding to the normal phase in Fig. 5.14), the Mott-insulator plateaux melt into a normal phase with entropy per site $s > \ln 3$ around the center of the harmonic trap and $s > \ln 2$ at the second Mott-insulating ring. Naturally, we can also identify the melting of the Mott insulator into the normal phase from the density profile, i.e., the corresponding Mott-plateaux at filling $n = 2$ and $n = 1$ have disappeared at this temperature. Due to the insensitivity of the density profile to a small variation of temperature, only a single density profile at temperature $T/U_{bd} = 0.11$ is shown here. There are also two peaks of the entropy density in the normal shells surrounding the Mott-insulating regions. Our simulations indicate that the transfer of entropy from superfluid to Mott insulator due to the Pomeranchuk effect does not occur in this high temperature region, since here the local entropy per particle in the superfluid is higher than in the Mott-insulator. We observe that the local entropy per particle is reduced when the temperature decreases, as shown in the right panel of Fig. 5.15 at low temperatures of $T/U_{bd} = 0.03, 0.035, 0.04$ and 0.045 (corresponding to the Mott insulator region in Fig. 5.14). Here the system has a Mott-insulator core with filling $n = 2$ in the trap center and also a Mott-insulating shell with filling $n = 1$. Correspondingly, the local entropy

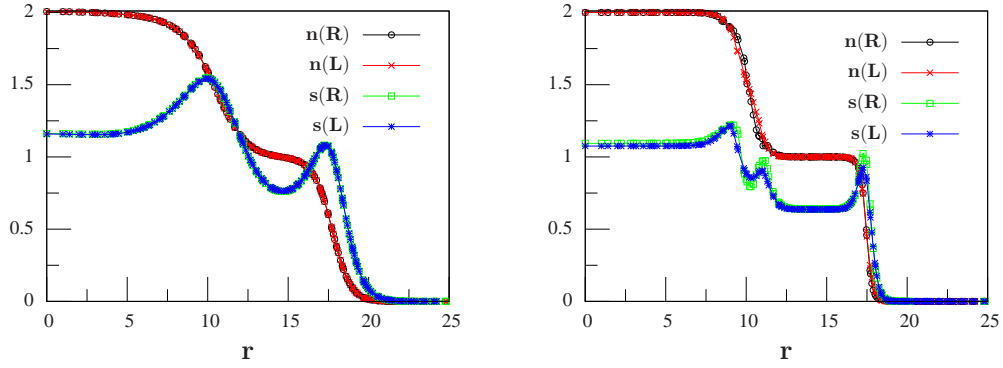


Figure 5.16: Validity of BDMFT+LDA benchmarked against RBDMFT. Density profile n_{tot} and entropy distribution s along the radial direction r at temperature $T = 0.1U_{bd}$ (**left**) and $T = 0.03U_{bd}$ (**right**) obtained by RBDMFT (R) and BDMFT+LDA (L) for 2D case. The interactions are set to $U_b = U_d = 1.01U_{bd}$ and the hopping amplitudes are $2zt_b = 2zt_d = 0.175U_{bd}$ with harmonic trap $V_0 = 0.005U_{bd}$.

per site of the Mott-insulator region is $s \approx \ln 3$ in the filling $n = 2$ region and $s \approx \ln 2$ in the $n = 1$ region, respectively, since there are three possible local spin states $|\uparrow\uparrow\rangle$, $|\downarrow\downarrow\rangle$ and $|\uparrow\downarrow\rangle$ for $n = 2$, and two possible spin states $|\uparrow\rangle$, $|\downarrow\rangle$ for $n = 1$, where \uparrow and \downarrow denote the two bosonic species. Between the two Mott-insulating regions, there is also a superfluid shell with non-zero value of the superfluid order parameter. Interestingly, we observe a sudden drop of the entropy density around the peak of the superfluid order parameter, which indicates a fine structure in the density distribution of the phases with non-integer filling (superfluid and normal phase). A similar structure is also found for a one-component Bose gas in an optical lattice plus external harmonic trap [187]. Physically, the sudden change of entropy in the superfluid region is caused by the reduced number of many-body states of the system due to the formation of a condensate. It is expected that, if the temperature is lowered further, another superfluid domain forms in the region with filling $n < 1$. We have also shown the parity profile $p_\nu = \langle (1 - e^{i\pi\hat{n}_\nu})/2 \rangle$ for the individual components in Fig. 5.15, which can be directly measured experimentally [55, 56]. Interestingly, the local parity for the individual components in the Mott-insulating region with total filling $n = 2$ is finite.

In addition, we now observe (right plot of Fig. 5.15) that the local entropy per particle in the first superfluid ring is smaller in some regions than that in the Mott insulator with $n = 2$, which indicates that a transfer of entropy from superfluid to Mott insulator can lower the temperature of the system in this regime, which is consistent with the phase diagram for the homogeneous system in Fig. 5.14. This interaction-induced cooling mechanism (Pomeranchuk effect) of two-component bosonic gases in an optical lattice is expected to be visible experimentally [78, 106, 107], after further lowering the

temperature. For example, in the experiment this effect could be observed via ramping up the optical lattice, where the temperature should be decreased beyond single-particle adiabatic cooling due to the Pomeranchuk effect, since the Mott-insulating region increases.

To check the validity of BDMFT+LDA around quantum degeneracy, we investigate the density and entropy distribution for the 2D case and test the accuracy of BDMFT+LDA against RBDMFT, as shown in Fig. 5.16. We find excellent agreement deep inside each phase, while RBDMFT provides the slightly more accurate description of the transition region. We therefore expect that BDMFT+LDA will also give quantitatively reliable results for the 3D case.

5.2.5 Adiabatic cooling via entropy redistribution for $B \neq 0$

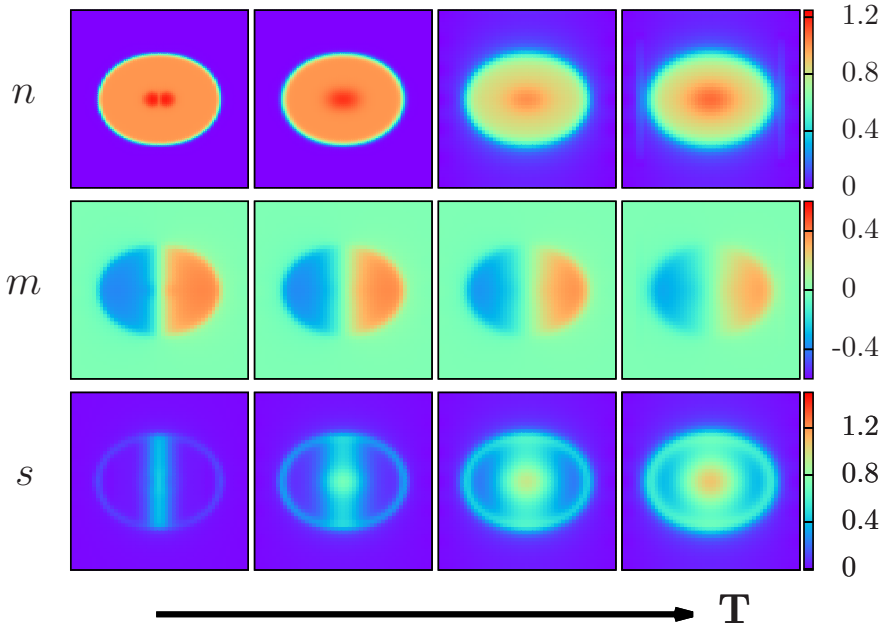


Figure 5.17: Real-space profile (here in the x - y plane of the lattice) for the local density n , magnetization m and entropy s along the $z = 0$ plane of a 3D cubic lattice using BDMFT+LDA. From left to right, the temperatures are $T/U_{bd} = 0.020, 0.040, 0.070$ and 0.095 , respectively. The interactions are set to $U_b = U_d = 1.01U_{bd}$ and the hopping amplitudes are $2zt_b = 2zt_d = 0.12U_{bd}$, with total particle number $N_{\text{tot}} \approx 17000$ in a harmonic trap $V_0 = 0.004U_{bd}$ and magnetic field gradient $V_{\text{gra}} = 0.01U_{bd}$.

We have so far investigated thermodynamical properties for equal filling of the two components. In this section, we will now study a scenario with the two species separated by a magnetic field with constant gradient which can be used experimentally to cool the system. Specifically, we simulate the adiabatic

process of the spin-gradient cooling scheme proposed by Weld *et al.* [107]. To this end, we calculate the entropy distribution of the inhomogeneous system in the presence of the field gradient, and the dependence of the entropy per particle on temperature. To simplify the calculation, we assume that the two components of the bosonic mixture have the same absolute value of the magnetic moment.

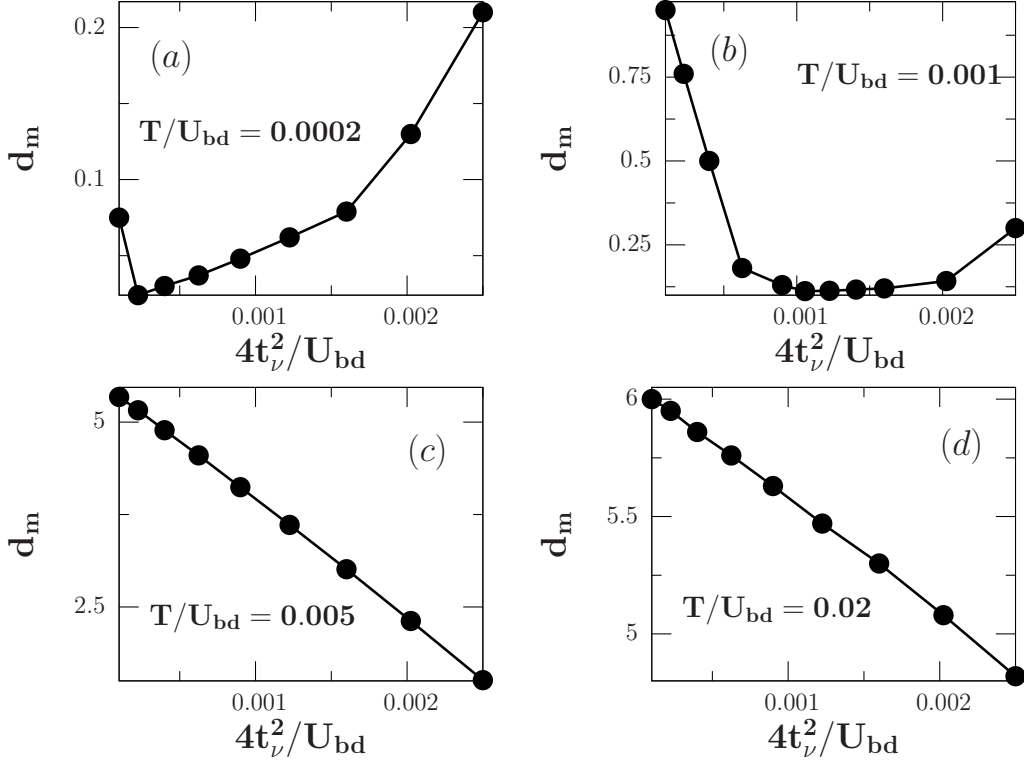


Figure 5.18: Domain-wall width d_m (in units of lattice constant) as a function of superexchange coupling at different temperatures. The width is defined as the distance from the trap center to the position where the magnetization is half of the maximum value. The interactions are set to $U_b = U_d = 1.01U_{bd}$ in a harmonic trap $V_0 = 0.004U_{bd}$ and a magnetic field gradient $V_{\text{gra}} = 0.0005U_{bd}$.

Entropy distribution in the presence of field gradient — The two-component bosonic mixture can be separated to opposite sides of the trap by the magnetic field. At zero temperature, the two components are completely separated and a sharp domain wall forms in the trap center. At finite temperature, spin excitations, such as a pair of opposite-spin atoms swapping positions via second-order tunneling, will broaden the width of the domain wall (the width is defined as the distance from the trap center to the position where the magnetization is half of the maximum value). As pointed out in [107, 188] the width of the domain wall depends in a simple way on the field gradient and can be used as a thermometer in the zero-tunneling limit. Fig. 5.17 shows the distribution of local density n , magnetization $m = (n_b - n_d)/2$, and entropy s in

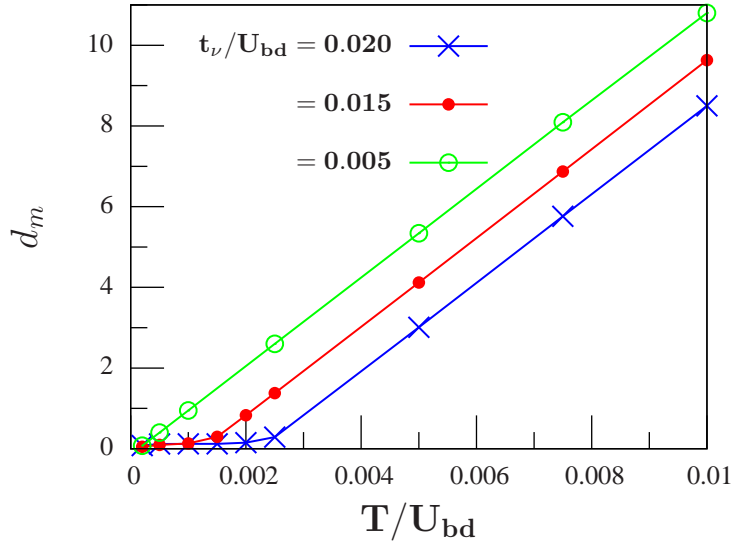


Figure 5.19: Domain-wall width d_m (in units of lattice constant) as a function of temperature at different hopping amplitudes. The width is defined as the distance from the trap center to the position where the magnetization is half of the maximum value. The interactions are set to $U_b = U_d = 1.01U_{bd}$ in a harmonic trap $V_0 = 0.004U_{bd}$ and a magnetic field gradient $V_{\text{gra}} = 0.0005U_{bd}$.

the $z = 0$ plane. Since the density and magnetization distributions depend on the temperature, they can be used for thermometry via *in situ* measurements with single-site resolution [55, 56]. In particular, the magnetization distribution can be used as a thermometer at low temperatures down to the critical temperature of magnetic phases. From the middle row of Fig. 5.17 we observe that the narrow mixed region of the two components broadens with increasing temperature, which is consistent with measurements where temperatures as low as 350 pK have been measured [53, 107]. The bottom row of Fig. 5.17 shows the entropy distribution. The entropy is mainly carried by the spin degree of freedom of particles around the trap center, and also by delocalized particles near the edge of trap. When the temperature is lowered, the delocalized particles form a condensate. As a result, the entropy drops quickly as a function of temperature in the superfluid ring. On the other hand, the spin degree of freedom in the mixed region can still carry a large amount of entropy, even at low temperature where the entropy of the single-component superfluid becomes very small. Therefore, if one prepares the system in a state where entropy is mainly carried by a single species (i.e., if one initially separates the two species by a field gradient) and then transfers the entropy from the single species to the spin degree of freedom, the temperature of the system can be lowered dramatically.

The domain-wall width can also be used as a tool to measure the strength of the resulting superexchange interactions between the atoms. As shown

in Fig. 5.18(a) and 5.18(b), when superexchange interactions dominate over thermal fluctuations ($4t_\nu^2/U_{bd} > T$), we observe a linear dependence of the domain-wall width on the strength of the superexchange in the Mott-insulating regime. We also observe that the domain-wall width increases faster at larger hopping parameters, since in that case the mixed region is in the superfluid regime and the first-order tunneling dominates. When thermal fluctuations dominate ($4t_\nu^2/U_{bd} < T$), as shown in Fig. 5.18(a)-5.18(d), the increase of the superexchange decreases the width of the domain wall due to minimizing the energy of the spin-spin coupling. If the temperature is increased, the minimum of the domain-wall width is shifted to higher hopping amplitudes, as shown in Fig. 5.18(a) and 5.18(b). We also observe that the linear dependence [107, 188] of the domain-wall width d_m only holds for temperature above the critical values T_c for magnetic ordering (see Fig. 5.19). The change of slope at T_c is a clear indication of the phase transition.

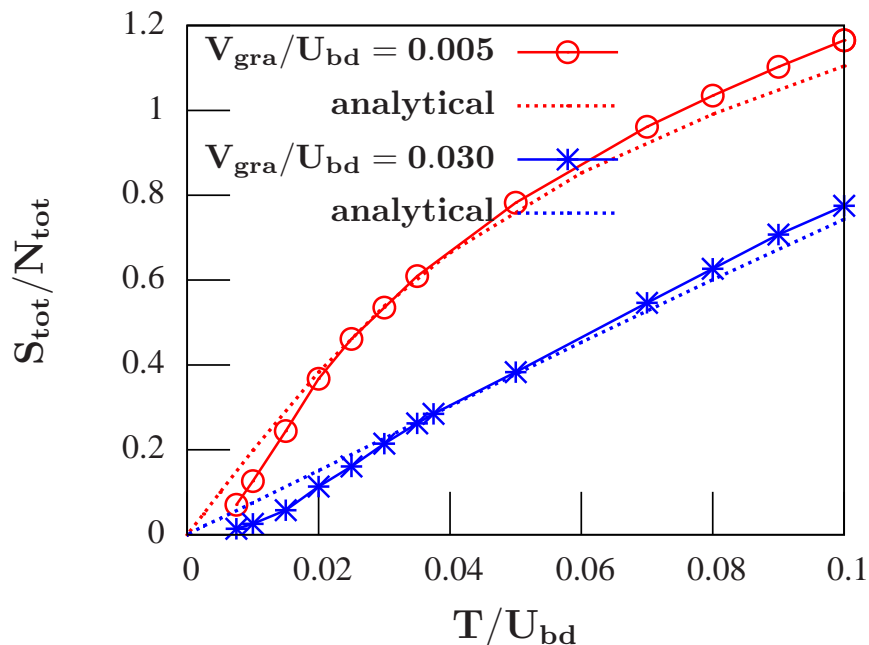


Figure 5.20: Entropy per particle versus temperature in a cubic optical lattice obtained by BDMFT+LDA, compared with the analytical zero-tunneling approximation [172]. The interactions are set to $U_b = U_d = 1.01U_{bd}$ and the hopping amplitudes to $2zt_b = 2zt_d = 0.12U_{bd}$, with total particle number $N_{\text{tot}} \approx 17000$ in a harmonic trap of strength $V_0 = 0.004U_{bd}$.

Entropy per particle versus temperature — We now focus on the relation of entropy versus temperature, which gives insight how adiabatic changes affect the temperature of the system. Fig. 5.20 shows the entropy-temperature curve for strongly interacting two-component bosons in an optical lattice in the presence of the magnetic field, where the dashed lines are obtained by the

zero-tunneling approximation [172]. Due to the deep optical lattice, our results obtained by BDMFT+LDA are in good agreement with the approximate analytical results except at low and high temperatures. At high temperature, thermal fluctuations will induce hopping of atoms. This effect is neglected in the zero-tunneling approximation, which therefore gives a lower prediction for the entropy. At low temperature, on the other hand, the entropy of the motional degree of freedom drops quickly due to condensate formation in the superfluid regime. This effect is neglected as well in the zero-tunneling approximation, which therefore gives a larger prediction for the entropy. We note that quantum Monte Carlo simulations [173] also reveal the inadequacy of the zero-tunneling approximation in the low temperature regime.

Adiabatic cooling via spin-gradient demagnetization — The spin-gradient cooling scheme relies on the inhomogeneous entropy distribution of the system. The main effect of the demagnetization process is to decrease the local entropy per particle in the spin-mixed regions, which is essential for long-range spin order. There are three different regions corresponding to different phases of the system, namely the superfluid, spin-mixed and one-component Mott-insulating region. Initially, the superfluid and spin-mixed region carry almost all the entropy of the system, while the entropy in the one-component Mott insulator is close to zero. When the magnetic field gradient is decreased, the spin-mixed region expands, while the one-component Mott-insulating region shrinks, and the average entropy per particle in the spin mixed region is decreased. At the same time, the temperature drops, since entropy carried by hot mobile particles is drained into the expanding mixed region with a drop of local entropy per particle. Here, we will quantitatively establish this scenario by considering the spatial entropy distribution and entropy-temperature relation. In the left panel of Fig. 5.21, the local entropy per particle s/n is shown at different field gradient strengths for fixed total particle number and entropy. We observe that s/n decreases in the central region as the field gradient is adiabatically decreased. Since the number of spin excitations (with respect to the ferromagnet at zero temperature and in the presence of the field gradient) due to exchange of $|\uparrow\rangle$ and $|\downarrow\rangle$ particles between neighboring sites is increased in the demagnetization process, the total energy of the system decreases as well and, as a result, the temperature drops from $T/U_{bd} = 0.065$ to 0.035 when the field gradient adiabatically decreases from $V_{\text{gra}}/U_{bd} = 0.03$ to 0.005. The resulting cooling efficiency is shown in the right panel of Fig. 5.21. The demagnetization cooling curve obtained via BDMFT simulations is in good agreement with results from the zero-tunneling limit [172], since here we choose the optical lattice relatively deep which makes t_ν/U_{bd} very small. In addition, the demagnetization cooling appears to be less efficient at larger magnetic field gradients. This is because the strong field gradient repels particles to the outer regions of the trap, which makes the trap center superfluid with enhanced entropy compared to the Mott insulator. This effect reduces

the entropy capacity of the spin degree of freedom at high field gradients.

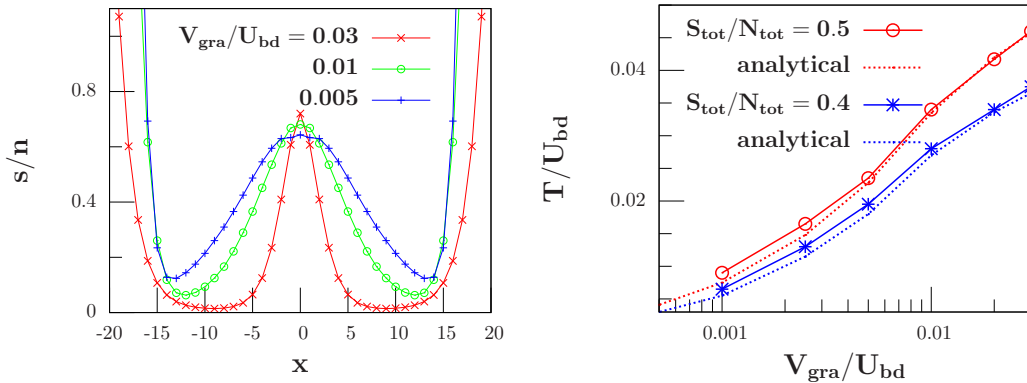


Figure 5.21: **Left:** Field-gradient dependence of local entropy per particle s/n along the x direction on the $y, z = 0$ axis, for an entropy per particle $S_{\text{tot}}/N_{\text{tot}} = 0.7$. The red, green and blue lines correspond to field gradients of $V_{\text{gra}}/U_{bd} = 0.03, 0.01$ and 0.005 , respectively. **Right:** Adiabatic cooling due to spin-gradient demagnetization in a cubic lattice. Data are obtained by BDMFT+LDA and compared to the analytical zero-tunneling approximation [172]. Interactions are set to $U_b = U_d = 1.01U_{bd}$, and the hopping amplitudes are $2zt_b = 2zt_d = 0.12U_{bd}$ for total particle number $N_{\text{tot}} \approx 17000$ in a harmonic trap $V_0 = 0.0025U_{bd}$.

5.2.6 Summary

In conclusion, we have investigated the thermodynamics of a two-component Bose gas loaded into an optical lattice in the presence of an external trap and a magnetic field gradient, using BDMFT+LDA and the newly developed real-space BDMFT. We obtain the finite-temperature phase diagram and find that at low temperature, remarkably, the system can be *heated* into a Mott insulator, analogous to the Pomeranchuk effect in ^3He . By investigating the entropy redistribution of the system during adiabatic spin-gradient demagnetization, we observe efficient cooling due to entropy transfer from the mixed region to the single-species Mott-insulating domains, and provide a quantitative theoretical validation of recent experiments [53, 107]. We expect our work to provide valuable insight for realizing quantum magnetic phases in upcoming experiments.

5.3 Pair-superfluidity

5.3.1 Introduction

In the previous sections, we have presented results for ultracold gases with repulsive inter-species interactions. In this section, we will study a Bose-Bose mixture for attractive inter-species interactions in an optical lattice, where a

pair-superfluid phase (PSF) could arise. This phase has been proposed and investigated theoretically in several previous works [189–198]. However, it is widely believed that the stability of the bosonic many-body system is questionable when the interactions between atoms are negative. Recently, it was found that a three-body hard-core constraint can stabilize the system of single-component bosons in an optical lattice with attractive two-body interactions [199], and afterwards numerical simulations have been performed to study pair superfluidity in the system [200–202]. For two-component bosons, stable heteronuclear ^{87}Rb - ^{41}K mixtures with negative inter-species interactions tuned via Feshbach resonances [203], have been realized recently. Now the question is how to theoretically understand the PSF of two-component bosonic gases. Qualitatively, the PSF can be viewed as a bosonic pair condensate, where the pair consists of different species or hyperfine states, and the pair condensate is a result of second-order hopping of the pair but with a strongly suppressed first-order tunneling of single atoms. It is apparent that the PSF can only exist at very low temperature of the order of the critical temperature of quantum magnetic phases which are also governed by second-order tunneling processes, which have been clearly observed for a double-well system [51, 52]. At the current stage, it is still challenging to achieve the critical temperatures of the PSF and magnetic phases. After achieving these low temperatures, it is expected that the corresponding phases can be detected by the momentum correlations via time-of-flight expansion [195, 204] or by single-site-resolution probing techniques [55, 56].

Up to now, most of the studies on the PSF in a two or three dimensional optical lattice consider the symmetric cases between the two species except in Ref. [190, 196, 197], but there is still a lack of detailed theoretical simulations of the PSF for the homogeneous system with asymmetric hopping amplitudes of the two species at zero and finite temperature, and for the experimentally relevant trapped system with balanced/imbalanced mixtures of the two species. Here, we bridge this gap and study properties of the PSF of two-component bosonic ultracold gases with attractive inter-species interaction both in a homogeneous and a trapped optical lattice. For the homogeneous model, we focus on the phase diagram with filling number $n = 1$. In particular, we present a phase diagram for the experimentally realized heteronuclear ^{87}Rb - ^{41}K mixture, where double-species Bose-Einstein condensates with attractive inter-species interactions have been observed [203]. For the trapped Bose-Bose mixtures, we study the stability and coexistence of Mott insulator, superfluid and PSF.

5.3.2 Homogeneous Bose gases with attractive interactions

In this part, we investigate Bose-Bose mixtures with negative inter-species interactions $U < 0$ in a 3D optical lattice. Generally, the system is unstable for $|U| > U_{b,d}$, since the strongly attractive inter-species interaction between the atoms can not be compensated by repulsive intra-species interactions. As a result, it leads to a collapse of the systems. Here we will demonstrate the sta-

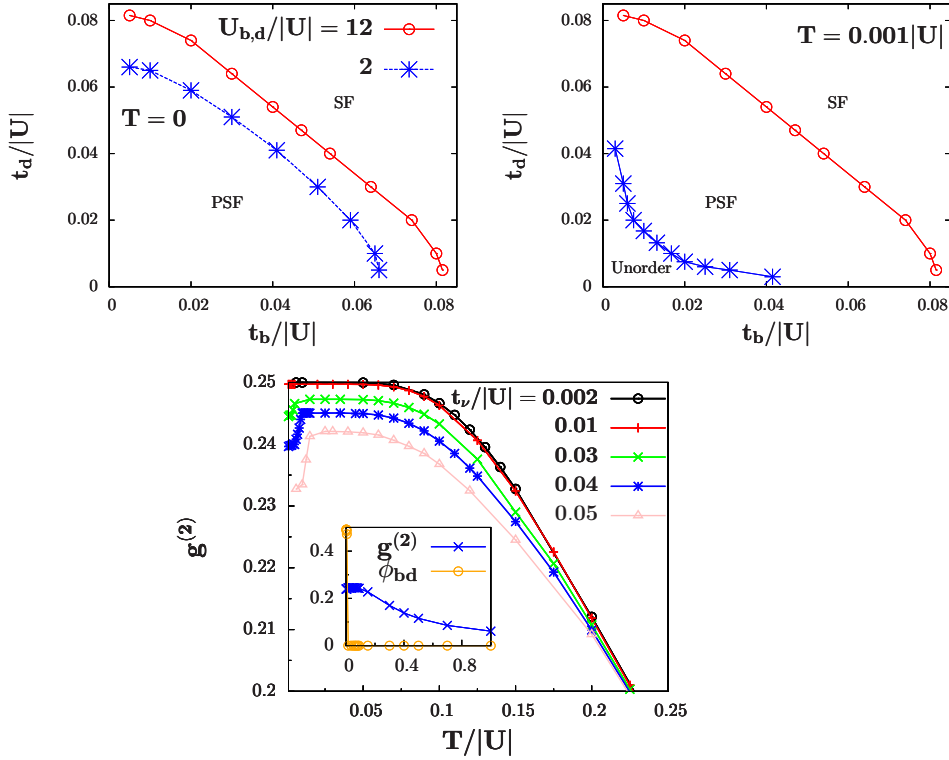


Figure 5.22: **Upper:** zero- (left) and finite- (right) temperature phase diagram for two-component bosons in a 3D cubic lattice vs. the hopping amplitudes. **Lower:** local density-density correlator $g^{(2)}$ as a function of temperature for different hopping amplitudes. Inset: zoom of main figure for $t_\nu = 0.04|U|$ ($\nu = b, d$). The interactions are set to $U_b = U_d = 12|U|$ and the total filling is $n = 1$ with $n_b = n_d = 0.5$.

bility of the PSF of two-component mixtures when the interactions are set to $|U| < U_{b,d}$. Specifically, we explore phase diagrams of two-component bosonic gases in a 3D cubic lattice with total filling $n = 1$ ($n_b = n_d = 0.5$) for different interactions, as shown in the upper left panel of Fig. 5.22 at temperature $T = 0$. We observe two different phases in the phase diagram: a PSF characterized by $\langle b \rangle = \langle d \rangle = 0$ and $\langle bd \rangle \neq 0$, and a superfluid phase (SF) with $\langle b \rangle, \langle d \rangle > 0$. We confirm the existence of the PSF of Bose-Bose mixtures with asymmetric hopping amplitudes. In the lower hopping regime for both species, the first order tunneling is suppressed by the strong interactions between atoms, but interestingly formation of bosonic pairs between different species can be energetically favored. At low temperatures the bosonic pairs can hop as a whole via second-order tunneling and develop a long-range order, which typically compete with single-species condensation. As a result, the PSF has a non-vanishing PSF order parameter $\langle bd \rangle$ but vanishing superfluid order parameters $\langle b \rangle$ and $\langle d \rangle$. On the contrary, when both species acquire large hopping, a superfluid phase will appear with $\langle b \rangle > 0$ and $\langle d \rangle > 0$. In addition, when the intra-species

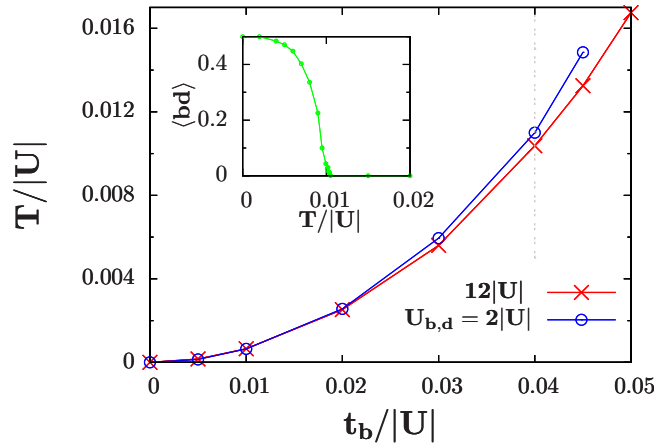


Figure 5.23: Critical temperature of the PSF as a function of hopping amplitudes $t_b = t_d$ on a 3D homogeneous cubic lattice with total filling $n = 1$. Inset: melting of the PSF vs. temperature along the vertical dashed line with hopping amplitudes $t_b = t_d = 0.04|U|$.

interaction $U_{b,d}$ decreases from $U_b = U_d = 12|U|$ to $2|U|$, the PSF shrinks due to the decrease of the effective pair-tunneling amplitudes. We also prove that the phase transition from a PSF to a superfluid phase with symmetric hopping amplitudes occurs at the same point as that from XY-ferromagnetic to superfluid phase for $U_{bd} > 0$ and half filling. We study also the effect of finite temperature on the phase diagram of two-component bosonic gases with interactions $U_b = U_d = 12|U|$ and $n_b = n_d = 0.5$, as shown in the upper right panel of Fig. 5.22. Generally, the PSF is sensitive to temperature, since the pairs are formed in the lower hopping regime and their coherence can be easily destroyed by thermal fluctuations, due to small effective tunneling of order $O(t^2/|U|)$. At finite temperature, the PSF regime shrinks in favor of developing a new unordered phase with vanishing expectation values for $\langle bd \rangle$, $\langle b \rangle$ and $\langle d \rangle$. To further understand this unordered phase which consists of either pairs or single particles, we calculate the dependence of the local density-density correlator $g^{(2)} \equiv \langle n_b n_d \rangle - \langle n_b \rangle \langle n_d \rangle$ on temperature, as shown in the lower panel of Fig. 5.22. We observe that $g^{(2)}$ starts to decrease noticeably only above temperatures of the order of $10^{-1}|U|$, which indicates the local pair of different species still exists below this temperature. We therefore conclude that the unordered phase, shown in the upper right panel of Fig. 5.22, consists of non-coherent pairs of different species. In sufficiently deep optical lattices, these particle-particle pairs are localized, while for larger hopping the pairs delocalize over the whole lattice. As a result, the local density-density correlator decreases as a function of t_ν ($\nu = b, d$), as shown in the lower panel of Fig. 5.22. Another interesting feature of the temperature dependence of $g^{(2)}$ is the increasing (non-monotonic) trend in low temperatures, since thermal fluctuations first localize and then break the pairs. We remark here that

the temperature regime of non-condensed pairs ($\approx 0.1|U|$) is experimentally accessible [50], and could be detected via radio frequency spectroscopy [205]. Note that the unordered phase considered here is qualitatively different from the one due to “melting” of the XY-ferromagnetic phase, and the unordered phase due to melting of the PSF can also exist for non-integer filling. We also observe that the superfluid phase is robust against small finite temperature and remains almost unchanged for temperatures up to $T = 0.001|U|$.

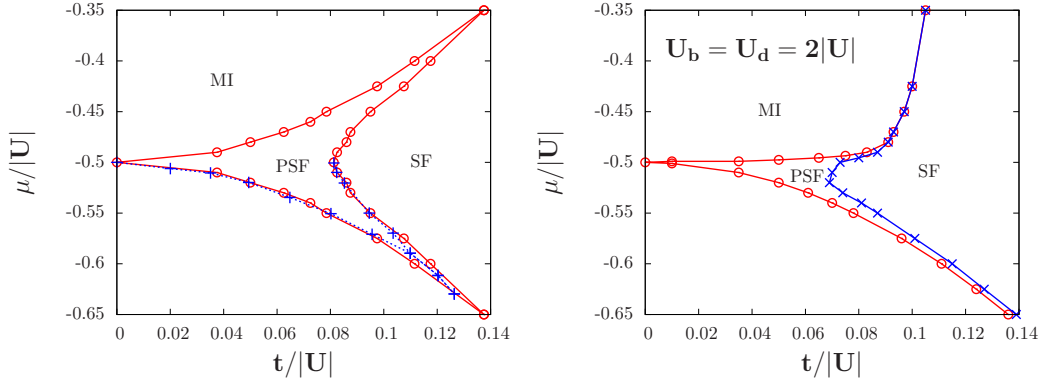


Figure 5.24: **Left:** Comparison of the zero-temperature phase diagram with two-component hard-core bosons analyzed with the tensor-product-state approximation [198] on a square lattice with completely symmetric parameters: $t = t_b = t_d$, $\mu = \mu_b = \mu_d$. The red solid lines are phase boundaries obtained by BDMFT for $U_b = U_d = 200|U|$, while the blue dashed lines are the results of the tensor-product-state approximation. **Right:** Zero-temperature phase diagram for two-component soft-core bosons with $U_b = U_d = 2|U|$ obtained via BDMFT.

One crucial question regarding the observation of PSF is how fragile it is against finite-temperature effects. To address this issue, Fig. 5.23 shows T_c as a function of the hopping amplitudes $t_b = t_d$ at different interactions. We notice that T_c rises as the hopping amplitudes increases, due to the growing second-order tunneling which stabilize long-range order. The inset of Fig. 5.23 shows the temperature dependence of $\langle bd \rangle$, which indicates a second-order phase transition from the PSF to the unordered phase. We also find that the critical temperatures for the long-range ordered phase shown here are of the same order as for the XY-ferromagnetic phase [12] and notably smaller than the coldest temperatures which have been measured in most experiments until now, apart from W. Ketterle’s group where temperatures as low as 350 pK ($\approx 0.01U_{bd}$ with $t_b/U_{bd} \approx 0.029$) have been achieved [53].

To verify the validity of the BDMFT results, comparison has been made with a hard-core boson model analyzed within a tensor-product-state approximation [198]. Fig. 5.24 shows the zero-temperature phase diagram of attractive hard-core two-component bosons in a square lattice with completely symmetric parameters: $t = t_b = t_d$, $\mu = \mu_b = \mu_d$. The solid lines are results of

BDMFT with $U_b = U_d = 200|U|$, while the dashed lines are obtained for hard-core bosons using a tensor-product-state approximation [198]. We find excellent agreements between the two methods. We also plot the phase diagram for soft-core bosons ($U_b = U_d = 2|U|$), and observe that in this case the phase boundary between the PSF and the superfluid phase is shifted to lower hopping values.

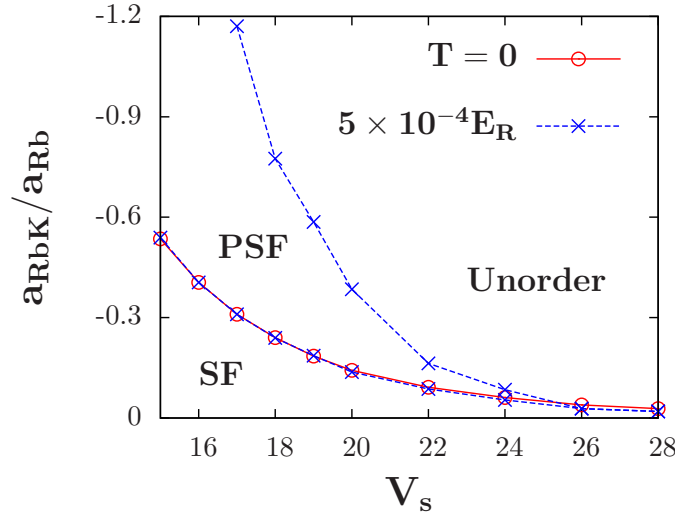


Figure 5.25: Phase diagram for a mixture of ^{87}Rb and ^{41}K in a 3D cubic lattice as a function of lattice depth V_s and Rb-K scattering length (in units of the background scattering length of ^{87}Rb). The total filling is $n = 1$ with $n_b = n_d = 0.5$.

Rubidium-potassium mixture — The phase diagrams obtained so far focus on symmetric interactions with $U_b = U_d$, which is a good approximation for mixtures of hyperfine states of rubidium [107]. However, this symmetry is not present for mixtures of rubidium and potassium in the experiment, in which a negative inter-species interaction has been achieved via a Feshbach resonance [203]. In this part, we focus on a mixture of ^{87}Rb and ^{41}K which was loaded into a 3D cubic lattice with wavelength of $\lambda = 757$ nm, which yields equal dimensionless lattice strength V_s for the two species. Due to different masses of the two species, the ratio of the intra-species interactions is then fixed to $U_{\text{Rb}}/U_{\text{K}} = m_{\text{K}}a_{\text{Rb}}/m_{\text{Rb}}a_{\text{K}} \approx 0.72$ and the ratio of the hopping amplitudes $t_{\text{Rb}}/t_{\text{K}} \approx 0.47$. Here E_{R} is the recoil energy of rubidium.

Now we explore the phase diagram of ^{87}Rb and ^{41}K mixtures in a 3D cubic lattice and make predictions for ongoing experiments. Since the depth V_s of the optical lattice and the inter-species scattering length a_{RbK} is tunable with high accuracy experimentally, we show the phase diagram in the $a_{\text{RbK}}-V_s$ plane for total filling $n = 1$ ($n_b = n_d$). Fig. 5.25 shows the phase diagram of a ^{87}Rb and ^{41}K mixture in a 3D lattice at zero and finite temperatures. At zero temperature, there are two phases appearing: superfluid and PSF. When the

scattering length a_{RBK} is small, the system features a superfluid phase for a shallow lattice. When the depth of the lattice is increased, the ratio of t_ν/U_ν becomes smaller with a strong suppression of first-order tunneling, and atoms of two different species form pairs and hop together with a development of the PSF at sufficiently low temperature. At finite temperature, the PSF can be easily destroyed by thermal fluctuations which induce a second-order phase transition into an unordered phase with $\langle bd \rangle = 0$. Since the PSF is formed via a second-order tunneling process and the corresponding energy scale is very small, for the parameters chosen here, this transition already occurs at a low temperature $T = 0.0005E_R$. On the other hand we observe that at the same temperature the superfluid phase is very stable against low temperature and the phase boundary between superfluid and PSF is almost unchanged.

5.3.3 Trapped Bose gases in 2D and 3D cases

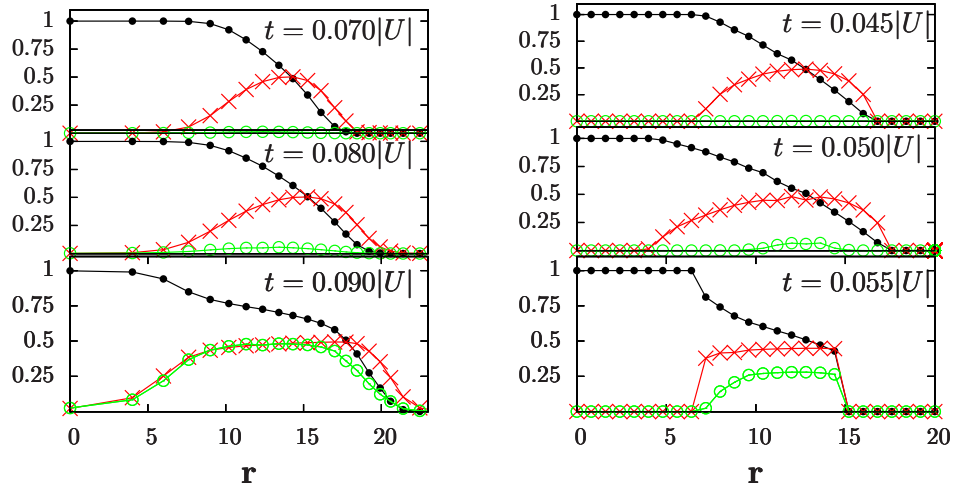


Figure 5.26: Density distributions n_b (black line), order parameter ϕ_b (green line) and PSF correlator $\langle bd \rangle$ (red line) vs. radial distance r for different hopping amplitudes at zero temperature. **Left:** Results are obtained within RBDMFT for a 2D square lattice. The interactions are $U_b = U_d = 2|U|$, hopping amplitudes $t = t_b = t_d$ and harmonic trap $V_0 = 0.0002|U|$. **Right:** Results are obtained within BDMFT+LDA for a 3D cubic lattice. The interactions are set to $U_b = U_d = 12|U|$, hopping amplitudes $t = t_b = t_d$ and harmonic trap $V_0 = 0.0002|U|$

In this section, we investigate the two-component bosonic system both in 2D and 3D optical lattices in the presence of a harmonic trap as relevant in most experiments, and focus on the stability of the PSF in the trapped system. Here we choose a 41×41 lattice for the 2D case and a $41 \times 41 \times 41$ lattice in 3D. For the 2D case, we will apply both RBDMFT and BDMFT+LDA, while we will only use BDMFT+LDA for the 3D case due to the large computational

cost.

Balanced mixture — Fig. 5.26 displays the density distribution n_b , order parameter ϕ_b and correlator $\langle bd \rangle$ for the PSF vs. radius r at different hopping amplitudes in a trapped 2D square (left) and 3D cubic (right) lattice. Since the PSF is stabilized only within a limited region for the symmetric parameters [198], the harmonic trap should be very shallow and the hopping amplitudes controlled in a narrow regime. Otherwise, the system will go through a phase transition directly from a Mott insulator to a superfluid phase. Here we choose completely symmetric parameters $t = t_b = t_d$ and $U_b = U_d$ with balanced filling for the two components. Hence, only one value for $n_{b,d}$ and $\phi_{b,d}$ respectively is shown in Fig. 5.26. We observe that a wedding-cake structure appears in the trapped system, and that the coexistence of different phases sensitively depends on the hopping amplitudes. In the left panel, for example, there are only two states appearing at a lower hopping amplitude of $t = 0.55|U|$, and the corresponding phase transition is from the Mott insulator with total filling $n = 2$ to the PSF with total filling $0 < n < 2$. If the hopping amplitudes are increased, the tunneling of single atoms from one site to another becomes easier, which implies that the system has large density fluctuations and undergoes a phase transition from a PSF to a superfluid phase. We can observe this point from the left middle panel of Fig. 5.26, where the superfluid phase starts to appear around the middle region of the PSF. It is expected that the PSF will disappear with a further increase of the tunneling amplitudes and the corresponding region will be occupied by the superfluid phase, since the first-order tunneling increases quickly as a function of the hopping amplitudes, as shown in the left lower panel of Fig. 5.26, where the PSF completely disappears at a hopping amplitude of $t = 0.7|U|$. Now we turn to investigate the stability of the PSF in a 3D cubic lattice, as shown in the right panel of Fig. 5.26. Here we also choose complete symmetric parameters: $t = t_b = t_d$ and $U_b = U_d = 12|U|$ with balanced filling for the two components. Compared with the trapped 2D case, we observe a similar trend of phase coexistence in two-component bosonic gases in a 3D cubic lattice.

Fig. 5.27 shows the comparison between the results of RBDMFT and those of BDMFT+LDA for a 2D square lattice, and good agreements are obtained between the two methods except in the phase-transition regime. In spite of the sharp phase-transition feature of LDA, the results of BDMFT+LDA are still reliable with a sufficient accuracy in the regime away from phase transition. Therefore, we will apply BDMFT+LDA to tackle the 3D case due to the high computational cost of RBDMFT in the 3D case.

We are also interested in the effect of temperature on the PSF. Fig. 5.28 shows the radial profile for correlator $\langle bd \rangle$ at different temperatures. We observe that the PSF is sensitive to finite T . At finite T , the PSF is reduced in favor of developing an unordered phase which is characterized by $\langle bd \rangle = 0$. We remark here that the density distributions at finite but low T are similar to

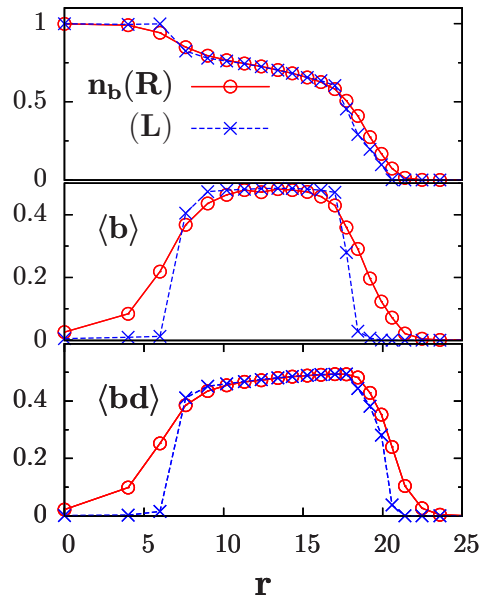


Figure 5.27: Comparison between results from RBDMFT (R) and those from BDMFT+LDA (L) for a 2D square lattice. Density distributions n_b , order parameter ϕ_b and PSF correlator $\langle bd \rangle$ vs. radial distance r at zero temperature in a 2D square lattice. The interactions are $U_b = U_d = 2|U|$ and the hopping amplitudes $t_b = t_d = 0.09|U|$ with a harmonic trap $V_0 = 0.0002|U|$.

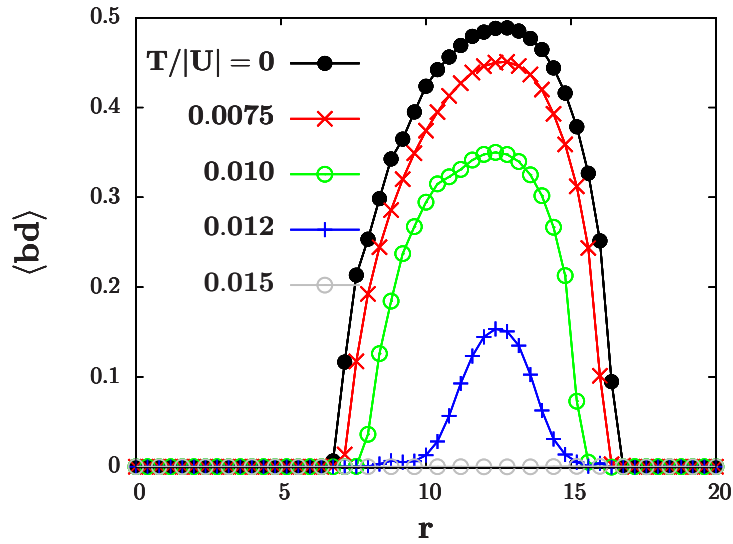


Figure 5.28: Temperature dependence of PSF correlator as a function of radius r for a 3D cubic lattice obtained within BDMFT+LDA. The interactions are set to $U_b = U_d = 12|U|$, the hopping amplitudes $t_b = t_d = 0.045|U|$ and the harmonic trap $V_0 = 0.0002|U|$.

zero temperature, as shown in the right panel of Fig. 5.26.

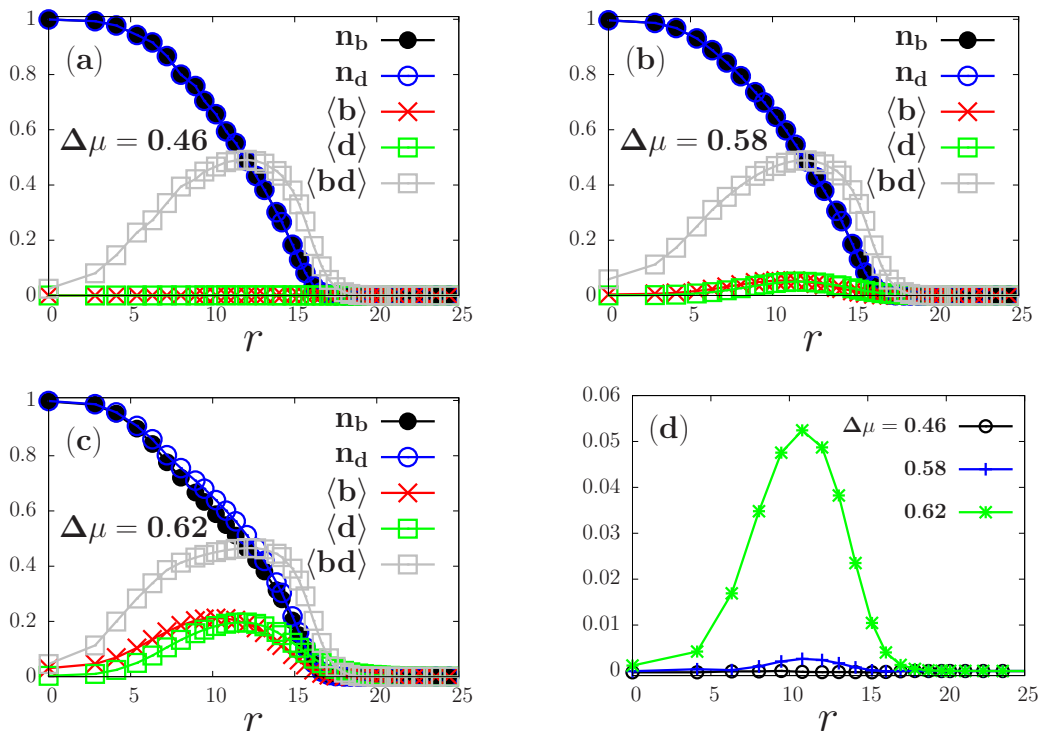


Figure 5.29: Density distributions $n_{b,d}$, order parameters $\langle b \rangle$, $\langle d \rangle$ and PSF correlator $\langle bd \rangle$ vs. radius r for different $\Delta\mu$ at zero temperature in a 2D cubic lattice within BDMFT+LDA. Panel (d) shows filling difference ($n_b - n_d$) vs. radius r . The interactions are set to $U_b = U_d = 12|U|$, hopping amplitudes $t_b = t_d = 0.05|U|$, $(\mu_b + \mu_d)/2 = 0.48$ and harmonic trap $V_0 = 0.00015|U|$.

Imbalanced mixture — As pointed out in the previous section 5.3.2, the PSF is stable for antitropic parameters for the two species. In this part, we study the effects of imbalance between the two species on the stability of PSF, where unequal filling between the species may hinder the formation of the pairs [195]. The imbalance, $N_b \neq N_d$, will be controlled by the nonzero chemical potential difference $\Delta\mu = \mu_b - \mu_d$ which can be viewed as an effective magnetic field. Fig. 5.29 shows density distributions, superfluid order parameters and PSF order parameter vs. radius r in a 2D square lattice, obtained using RBDMFT. Upon increasing the imbalance parameter $\Delta\mu$, the PSF ceases to exist and goes through a phase transition from a PSF to a superfluid phase, since $\Delta\mu$ can finally exceed the pairing gap for the PSF, allowing unpaired excess atoms to enter the PSF region. Surprisingly, the PSF is sensitive to population imbalance, and even small population imbalance can destroy the existence of the PSF in a trapped system, but with a formation of superfluid order resulting from unpaired particles. As shown in Fig. 5.29, the density distributions are almost unchanged even for large values of the imbalance pa-

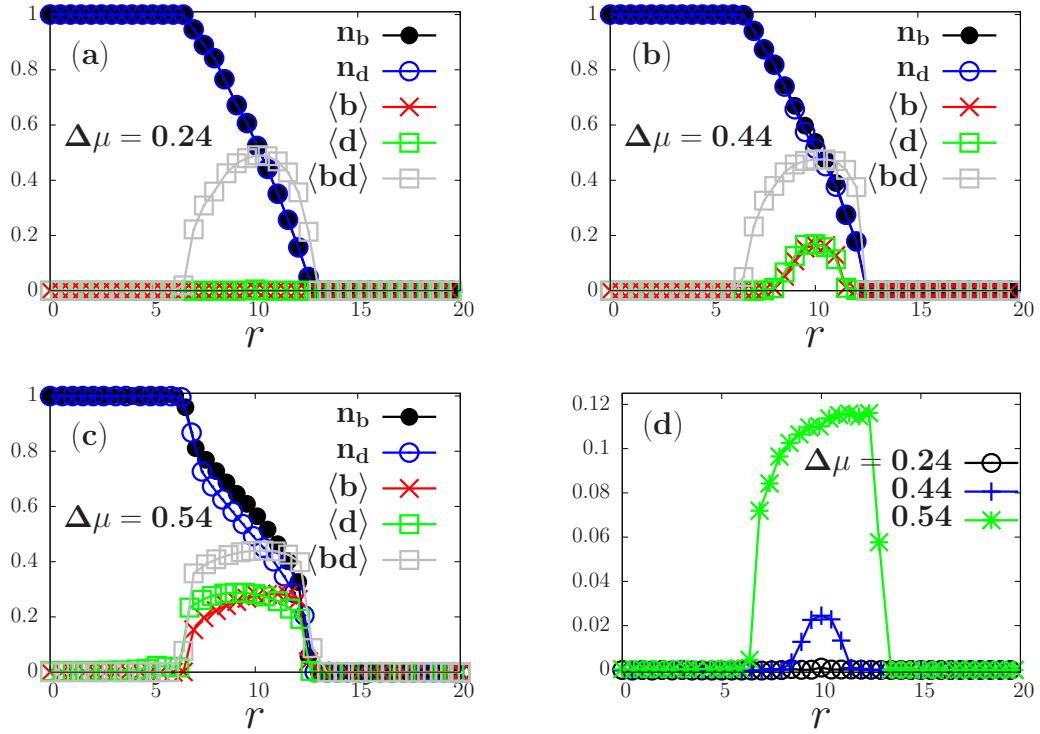


Figure 5.30: Density distributions $n_{b,d}$, order parameters $\langle b \rangle$, $\langle d \rangle$ and PSF correlator $\langle bd \rangle$ vs. radial distance r for different $\Delta\mu$ at zero temperature in a 3D cubic lattice obtained within BDMFT+LDA. Panel (d) shows the radial profile for the filling difference ($n_b - n_d$). The interactions are $U_b = U_d = 12|U|$, hopping amplitudes $t_b = t_d = 0.04|U|$, $(\mu_b + \mu_d)/2 = 0.47$ and harmonic trap $V_0 = 0.0003|U|$.

parameter $\Delta\mu$. If increasing $\Delta\mu$ further, the pairing gap breaks and superfluid order develops. We do not find any phase separation regime in our study.

Next, we discuss the influence of the population difference on the PSF in a trapped 3D cubic lattice using BDMFT+LDA. Fig. 5.30 shows density distributions, order parameter and PSF order parameter vs. radius r in a 3D cubic lattice, obtained via BDMFT+LDA. We observe that here the physics is qualitatively similar to the 2D case, as shown in Fig. 5.29.

5.3.4 Summary

In conclusion, we have investigated low-temperature properties of Bose-Bose mixtures with negative inter-species interactions both in 2D and 3D optical lattices by means of BDMFT/RBDMFT. We obtained phase diagrams of Bose-Bose mixtures with filling $n = 1$ at zero and finite temperature in a 3D cubic optical lattice, and found that the PSF is stable also for asymmetric hopping of the two species. We obtained critical temperatures of the PSF, which we found to be of the order of XY-ferromagnetic phase of a Bose-Bose mix-

ture with repulsive inter-species interaction. We have confirmed the stability of the PSF in a balanced Bose-Bose-mixture in the presence of the harmonic trap both in 2D and 3D. We have also investigated the influence of density imbalance between the two species on the PSF, and found that it is destroyed already by small population imbalance of the two species. This novel quantum phase can be observed via the signatures of the pair condensate in the future experiments, by detecting the momentum distribution of pairs [195, 206].

Chapter 6

Ultracold Bosonic Gases with Long-Range Interactions

In the previous chapter, we presented theoretical results for strongly correlated systems with only contact interactions. In this chapter, we will investigate novel quantum phases of strongly correlated bosonic gases in optical lattices in the presence of long-range interactions. Usually, there are two common ways to realize long-range interactions: either to use ultracold gases coupled to a high-finesse optical cavity [25], or dipolar gases with strong dipole-dipole coupling, which is long-range and anisotropic as a result of permanent or induced magnetic or electric dipole moment [27, 57–59]. If the long-range interactions between the condensed atoms are sufficiently strong, they will govern the physics of the many-body system and provide new access to novel quantum phases. Our goal of this chapter is to investigate the underlying physics of these novel quantum phases. Firstly, we simulate strongly correlated ultracold bosons in a high-finesse optical cavity, and establish the phase diagram which contains two novel self-organized quantum phases, namely supersolid and checkerboard solid, in addition to conventional phases such as superfluid and Mott insulator. In the presence of a harmonic trap, we discuss the effects of inhomogeneity on the buildup of self-organized phases, as relevant to experiments. Then, we study quantum phases of dipolar bosonic gases in an optical lattice, which features charge-density-wave, anti-ferromagnetic, supersolid and superfluid phases.

6.1 BEC-cavity system

6.1.1 Introduction

As opposed to ultracold gases loaded into conventional optical lattices, novel quantum phases of BEC-cavity system arise, due to the strong coupling between atomic gases and the cavity mode [67–72, 207, 208]. Up to now, however, there is still a lack of many-body simulations of strongly-correlated bosons coupled to an optical cavity, even though an extended Bose-Hubbard model has been derived [114, 115] for studying ultracold gases trapped in a

periodic optical potential, generated by a high-finesse cavity. In this section, we will study a one-component ultracold Bose gas coupled to a single-mode cavity field, pumped by a standing-wave laser beam in the transverse direction. Since the cavity field mediates infinitely long-range forces between all atoms [25, 110, 111], we investigate the system by means of real-space bosonic dynamical mean field theory, which captures both strong correlations and spatial inhomogeneity in a unified framework [12]. For the homogeneous case, we mainly investigate the influence of local two-particle interactions on the buildup of self-organized phases and identify the transition from a normal to a self-organized phase. We then focus on the trapped BEC-cavity system and study the effect of inhomogeneity.

6.1.2 Setup of the BEC-cavity system

Motivated by a recent experiment [25], we consider a system of ^{87}Rb atoms with scattering length $a_s = 5.77$ nm and atomic transition wave length $\lambda = 780.2$ nm. This system is driven by a linearly polarized standing-wave laser with a red-detuned wave length $\lambda_p = 784.5$ nm in the direction perpendicular to the cavity axis. We fix the cavity decay rate as $\kappa = 300\omega_R$ which is close to the experimental value of $\kappa = 2\pi \times 1.3$ MHz [25], where ω_R is the frequency corresponding to the recoil energy, i.e. $E_R = \hbar\omega_R = \hbar^2/(m\lambda_p^2) (\approx 2\pi \times 3.8$ kHz). We choose $U_0 = g_0^2/\Delta_a = 0.1$, which leads to an atom-cavity coupling strength g_0 two orders of magnitude larger than the cavity decay rate κ and is in the strong-coupling regime of cavity quantum electrodynamics [209]. The setup of our simulation consists of a cavity in the x -direction, driven by a pump laser in the z -direction, and a strong confinement freezing the motional degree of freedom of the atoms in the third direction [210], as shown in Fig. 3.2. To make the tight-binding approximation valid, we add an external optical lattice in the cavity direction with a depth of $V_{\text{ext}} = 5E_R$. The hopping amplitudes for nearest neighbors are given by $\tilde{J}_{x,z}/E_R = (4/\sqrt{\pi})(V_{x,z}/E_R)^{(3/4)} \exp(-2\sqrt{V_{x,z}/E_R})$ and the Hubbard interaction parameter is $U/E_R = 4\sqrt{2\pi}(a_s/\lambda_p)(V_x V_z V_y/E_R^3)^{(1/4)}$ [139], where V_x (V_y, V_z) is the standing-wave depth in the x (y, z) direction. For the on-site coupling matrix elements J_0^c and J_0' , we use a Gaussian approximation of the Wannier states. In all our calculations, we choose the recoil energy E_R (ω_R) as the unit of energy, where we set $\hbar = 1$ ($E_R = \omega_R$).

6.1.3 Quantum phases of a homogeneous Bose gas

In this part, we simulate a BEC-cavity system in a 2D homogeneous optical cavity using RBDMFT. The influence of on-site interactions and temperature on the buildup of self-organized states (supersolid and checkerboard solid) of bosonic gases in an optical cavity will be investigated. We predict a phase transition from a superfluid to a supersolid phase of strongly interacting bosonic gases due to cavity-mediated long-range interactions, and study the robustness of the supersolid phase in an optical cavity. Here we consider a $N_{\text{lat}} = 16 \times 16$ lattice.

Phase diagram of the BEC-cavity system — A supersolid is a quantum solid in which a fraction of the mass is superfluid [211], which can be realized with ultracold quantum gases in an optical lattice, such as Bose or Fermi mixtures with contact interactions [8, 212], or single-component Bose gases with long-range interactions [25, 213, 214]. Here, we investigate for experimentally relevant parameters the robustness of the supersolid phase of single-component bosonic gases with strong on-site and long-range interactions in an optical cavity, and the phase transition from the homogeneous superfluid phase to a supersolid phase. The supersolid phase can be characterized by the coexistence of the staggered order parameter $\Phi \equiv \frac{\langle \sum_i (-1)^{i+1} b_i^\dagger b_i \rangle}{\langle \sum_i b_i^\dagger b_i \rangle} > 0$ and superfluid order $\phi \equiv \langle b \rangle > 0$. There are two possible signs of Φ , i.e. the atoms occupy even sites for $\Phi > 0$ or odd sites for $\Phi < 0$ [215]. Naively, if we set the order parameter $\Phi > 0$, which implies a larger atom density at the even sites, and at the same time choose a negative shifted cavity detuning $\Delta'_c < 0$, this implies that the coherent scattering between the pump laser and cavity generates a potential with minima at the even sites, as indicated by the staggered term in Eq. (3.24). As a result, the corresponding potential will attract more atoms towards even sites and the system self-organizes into a steady state. In the following, we will confirm this general argument via numerical simulations based on RBDMFT.

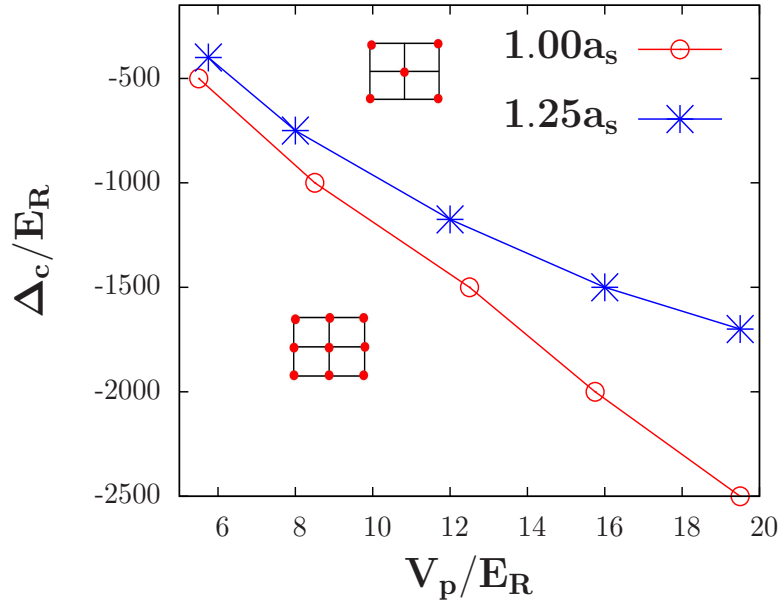


Figure 6.1: Phase diagram at zero temperature with total particle number $N_{\text{tot}} = 506$. The observed phases here are the superfluid and supersolid phases, respectively. The cavity decay rate is set to $\kappa = 300E_R$ and the light shift is $U_0 = -0.1E_R$.

Fig. 6.1 shows the phase diagram of the system with scattering length $1.0a_s$ and $1.25a_s$ at zero temperature. There are two distinct phases which

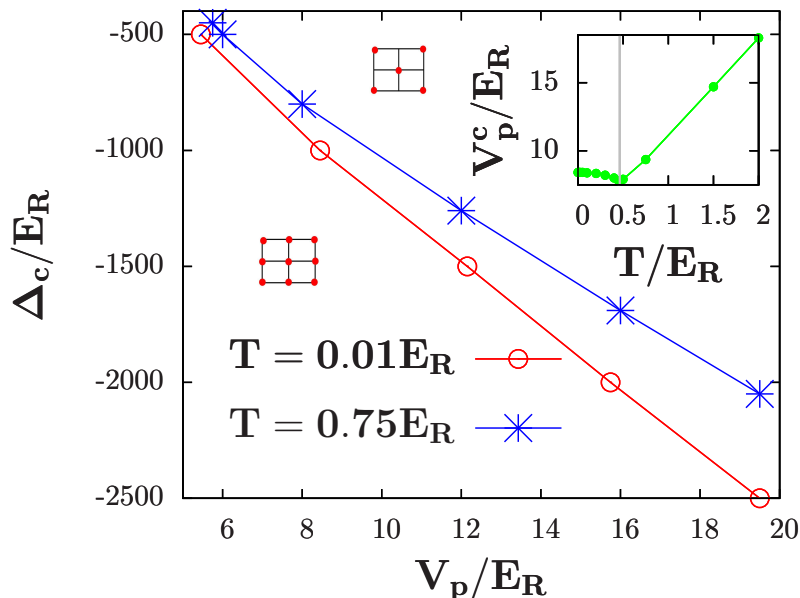


Figure 6.2: Phase diagram at finite temperature for total particle number $N_{\text{tot}} = 506$, decay rate $\kappa = 300E_R$, light shift $U_0 = -0.1E_R$ and scattering length $1.0a_s$. The phases shown here are conventional superfluid and supersolid at $T = 0.01E_R$, while, at $T = 0.075E_R$, the phase transition is between *normal* phases ($\phi = 0$). Inset: critical strength V_p^c of the standing-wave pump laser vs temperature for detuning $\Delta_c = -1000E_R$, where the grey curve shows the disappearance of the superfluid order parameter ϕ .

are characterized by Φ . When the pump laser is weak, the system is in the superfluid phase with homogeneous density distribution and $\Phi = 0$. In this case, the mean photon number in the cavity is zero. On the other hand, when the pump laser is strong enough, more photons will be scattered into the cavity mode and the atoms will organize themselves into a checkerboard pattern with $|\Phi| > 0$. Our simulations confirm the existence of a supersolid phase of single-component bosons with cavity-mediated long-range interactions plus strong on-site interactions. In Fig. 6.1 we observe that the trend of the phase transition from the superfluid phase to the supersolid phase as a function of V_p at fixed scattering length a_s is consistent with experimental observations [25]. We also investigate the effect of on-site interactions on the phase transition and notice that the phase boundary is considerably shifted upwards for larger scattering length, which indicates that more pump laser power is needed to drive the system into the self-organized phase. We also observe that on-site interactions have a more pronounced effect on the buildup of the supersolid phase for a stronger pump laser field. Generally, there is also an unstable state for positive shifted cavity detuning $\Delta'_c > 0$ [25, 216], which is beyond the scope of this work.

We now turn to investigate the effect of finite temperature on the critical pump strength. At a finite temperature, as shown in Fig. 6.2, the critical pump strength is shifted as a result of the competition between thermal and quantum fluctuations. From the inset of Fig. 6.2, We observe a minimum of V_p^c at low but finite temperature, since thermal fluctuations excite the atoms from ground state and thus reduce the energy gap between initial and self-organized states. As a result, less power of the pump laser is needed to stabilize the self-organized pattern. On the other hand, at high temperature, thermal fluctuations tend to smear out the self-organized density pattern, and as a result, more power is needed to stabilize it. To observe the supersolid phase, however, the temperature should be low enough to maintain the off-diagonal long-range order ϕ , as shown by the grey line in the inset of Fig. 6.2, which indicates a vanishing superfluid order parameter $\phi = 0$. The phase transition at a temperature of $T = 0.01E_R$ is between the superfluid and the supersolid phase with $\phi > 0$, while at $T = 0.75E_R$ it is between two normal phases with $\phi = 0$. Note that the superfluid long-range order at $T > 0$ with $\phi \neq 0$ in two dimensions is a mean-field artifact in the thermodynamical limit, while in reality, the system should exhibit a Kosterlitz-Thouless transition [217].

Mott physics in BEC-cavity system — In the previous section, we have found that on-site interactions strongly shift the phase boundary between the superfluid and the supersolid phase. We will now investigate this effect in detail at different fillings. We choose a cavity detuning $\Delta_c = -500\omega_R$, a scattering length of $2.5a_s$ and a lattice depth $V_p = 15E_R$ of the standing-wave pump laser. This choice of parameters is motivated by the recent experiment [25].

Fig. 6.3 shows the checkerboard order Φ (blue line) as a function of filling, where four possible phases of the BEC-cavity system are observed. Panels (a)-(d) in Fig. 6.3 show the density distribution in real space (left) and in quasi-momentum space (right), a) superfluid phase ($\phi \neq 0$ and $\Phi = 0$) with off-diagonal long-range order (phase coherence), b) supersolid ($\phi \neq 0$ and $\Phi \neq 0$) with diagonal long-range order (periodic density pattern) and off-diagonal long-range order, c) Mott insulator ($\phi = 0$ and $\Phi = 0$) and zero mean-photon number in the cavity mode, and d) checkerboard solid ($\phi = 0$ and $\Phi \neq 0$) with diagonal long-range order with finite mean-photon number in the cavity mode. Now the question is, how we understand the buildup of self-organized phases of single-component bosonic gases with photon excitation in the cavity mode. Generally, the excitation of the cavity mode is a collective effect which is induced by all the atoms in the cavity and depends on the total particle number, i.e. the more particles occupy the cavity, the more photons will be coherently scattered into the cavity mode, and the easier the checkerboard pattern of the density distribution can be formed. In the absence of long-range interactions, there are two possible phases for strongly interacting bosonic gases in an optical lattice, superfluid and Mott insulator. The lowest excitation of superfluid phase is the sound mode which can be easily excited

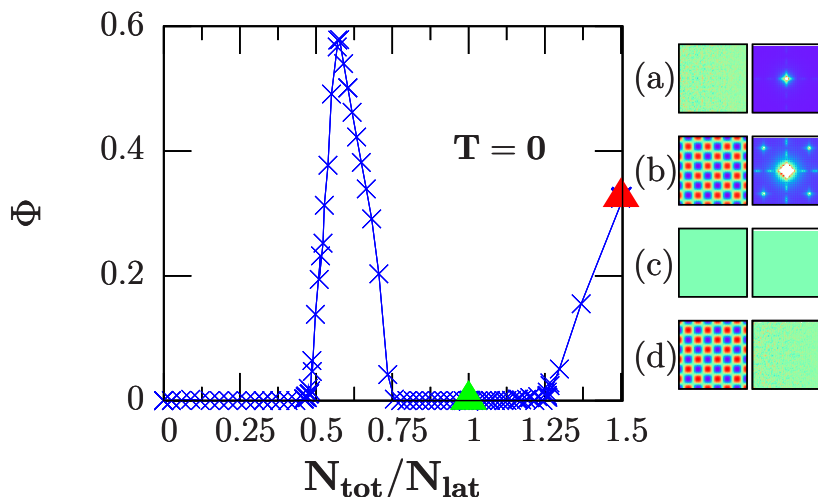


Figure 6.3: Left: Buildup of self-organized phases of strongly interacting bosons in an optical cavity at $T = 0$. The blue line represents the order parameter Φ , the green triangle the Mott insulator and the red triangle the checkerboard solid. (a)-(d): sketches of superfluid, supersolid, Mott insulator and checkerboard solid, respectively, with the density distribution in real space (left) and in quasi-momentum space (right). Parameters are $\Delta_c = -500E_R$, $\kappa = 300E_R$, $U_0 = -0.1E_R$ and $V_p = 15E_R$.

due to the lack of the energy gap [218], while the lowest lying excitations of the Mott-insulating phase are the creation of a particle-hole pairs, where an energy up to the energy gap U is required [3]. Different excitation properties of the system in these phases strongly influence the buildup of the self-organized phase. We can see this trend from the blue line in Fig. 6.3: the order parameter Φ becomes nonzero with the increase of the total particle number, and after a certain value Φ decreases to zero in the vicinity of the Mott insulator. With further increase of the filling, the checkerboard supersolid phase appears again in the BEC-cavity system. Interestingly, there is also a checkerboard *solid* phase appearing at a filling of $n = 1.5$. Since more photons are scattered into the cavity mode due to the large particle number, the standing wave in the cavity direction suppresses the tunneling of atoms and supports the formation of a superfluid. It is expected that the supersolid phase of the BEC-cavity system will appear again with a further increase of the total particle number.

To better understand the novel quantum phases discussed above, panels (a)-(d) in Fig. 6.3 show four sets of sketches for the real-space (left) and quasi-momentum space (right) density distributions, respectively. The self-organized phases are induced by a two-photon process between the cavity mode and the pump field which effectively gives rise to cavity-mediated long-range interaction. It can be described by the Dicke model, which is essentially an approximation of equation (3.24) [25, 219, 220]. For the supersolid phase, besides the

zero-momentum peak $|0, 0\rangle$ corresponding to the ground state of the ultracold gases, we observe four additional peaks $|\pm \hbar k, \pm \hbar k\rangle$ associated with the lowest excited states of the BEC. This indicates that this phase has diagonal long-range order (periodic density pattern) and off-diagonal long-range order (phase coherence), as pointed out in Ref. [25, 221]. Here $|0, 0\rangle$ and $|\pm \hbar k, \pm \hbar k\rangle$ are momentum eigenstates of atoms $|p_x, p_z\rangle$ where $p_x(p_z)$ is momentum along the $x(z)$ -direction. In the checkerboard solid, however, the system only has diagonal long-range order, associate with the periodic density modulation. All four phases can easily be detected experimentally by combining the time-of-flight method with detection of photons which leak from the cavity.

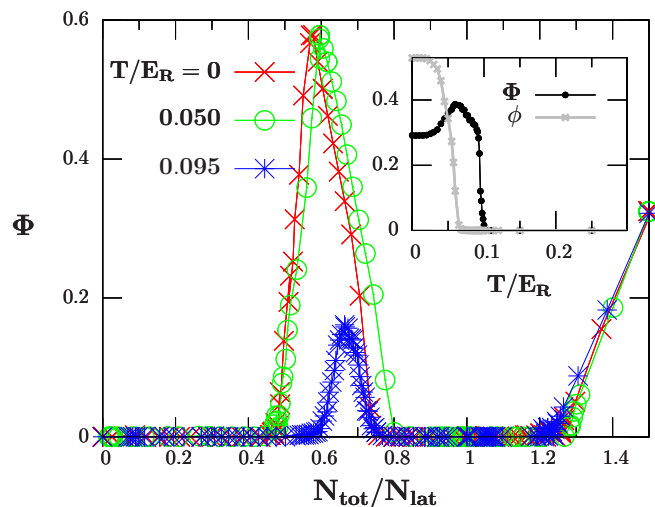


Figure 6.4: Effects of temperature on the checkerboard order parameter Φ . Parameters are $\Delta_c = -500E_R$, $\kappa = 300E_R$, $U_0 = -0.1E_R$ and $V_p = 15E_R$. Inset: Melting of the self-organized phase as a function of temperature at fixed filling $N_{\text{tot}}/N_{\text{lat}} = 0.68$, where the grey line indicates the disappearance of superfluid order.

At zero temperature, the phase transition from conventional phases (superfluid and Mott insulator) to self-organized phases (supersolid and checkerboard solid) is driven by quantum fluctuations. At finite temperature, thermal fluctuations also play an important role, which can be understood from a naive picture: thermal fluctuations excite particles from a site to its neighbor and as a result smoothen the checkerboard pattern. The inset of Fig. 6.4 shows the order parameter Φ as a function of temperature, which behaves non-monotonically. This trend can be understood from the competition between quantum and thermal fluctuations, as explained in the previous section. We can confirm this statement from the main panel of Fig. 6.4. We observe that the order parameter Φ at temperature $T = 0.05E_R$ increases compared to its zero-temperature value in some region, while Φ decreases again and the window of the self-organized phase shrinks at a temperature of $T = 0.095E_R$.

It is expected that the self-organized phase will disappear completely at even higher temperatures due to thermal fluctuations. The grey curve in the inset of Fig. 6.4 shows the disappearance of the superfluid order parameter ϕ which indicates that thermal fluctuations destroy off-diagonal long-range order. Correspondingly, in the main plot of Fig. 6.4 at temperature $T = 0.095E_R$, the supersolid phase only exists in the region $1.2 < n < 1.5$, while for $0.6 < n < 0.8$ the system shows a phase transition into a normal phase without off-diagonal long-range order.

6.1.4 Quantum phases for an inhomogeneous system

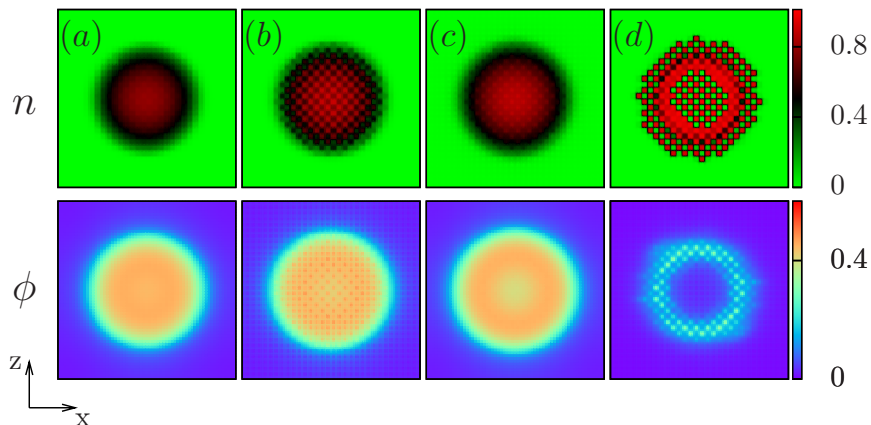


Figure 6.5: Density distribution n and superfluid order parameter ϕ versus position on the square (32×32) lattice for different number of atoms $N_{\text{tot}} = 139, 167, 184$ and 220 in panels (a), (b), (c) and (d) respectively. Parameters are $\Delta_c = -500E_R$, $\kappa = 300E_R$, $U_0 = -0.1E_R$, $V_p = 15E_R$, with a harmonic trap $V_0 = 0.003E_R$.

We have so far studied the homogeneous case, but in real experiments the external trap gives rise to inhomogeneity in the system which stabilizes the coexistence of superfluid phase, Mott insulator, supersolid and checkerboard solid. In contrast to the case of contact interactions only, we find that the properties of the system in the optical cavity are strongly influenced by inhomogeneity, due to cavity-mediated long-range interactions which are determined by the density distribution of the whole system. In this section, we will investigate the effect of the inhomogeneity on the buildup of self-organized phases of the BEC-cavity system in the presence of a harmonic trap using RBDMFT. Subsequently, we answer the question how the phases described in Fig. 6.3 will manifest themselves in the experiment. Observation of the different phases is possible by using single-site addressing techniques in an optical lattice based on optical or electron microscopy [54–56]. Here we choose a 32×32 lattice with a harmonic trap $V_0 = 0.003E_R$. All residual parameters are chosen as in Fig. 6.3.

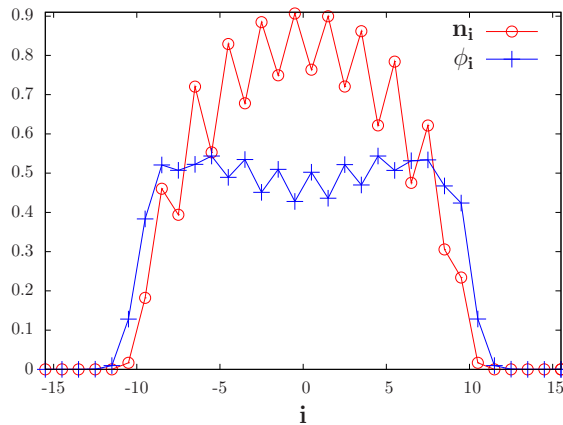


Figure 6.6: Density distribution n_i and superfluid order parameter ϕ_i along the y axis through the center of the trap, where i is the lattice site index. Data points are extracted from panel (b) of Fig. 6.5. n_i^0 is the density distribution without photons in the cavity mode but with the same total particle number.

Fig. 6.5 shows the density distributions (upper panels) and superfluid order parameters (lower panels) in real space for four different total particle numbers $N_{\text{tot}} = 139, 167, 184$ and 220 , respectively. Generally, the larger the total particle number, the more photons are scattered into the cavity mode, and thus the easier the system can form the self-organized phase. We observe that at $N_{\text{tot}} = 139$, there is almost no checkerboard region, as shown in panel (a). At $N_{\text{tot}} = 167$, the supersolid phase can be clearly observed in the center of the trap, since the superfluid core expands at the trap center and more photons are scattered into the cavity mode. From Fig. 6.3, we expect that the self-organized phase will disappear again when the number of particles increases to a value at which a Mott gap arises in the center of the trap. This is clearly shown in panel (c) at $N_{\text{tot}} = 184$ with an almost vanishing checkerboard order. After further increase of the particle number to $N_{\text{tot}} = 220$, the checkerboard order reappears again. Moreover, we observe a checkerboard solid core with average filling $n = 0.5$ building up, which only exists at filling $n = 1.5$ in the homogeneous case for the parameters of Fig. 6.3, i.e. we observe the checkerboard solid for parameters where it was not yet visible in the homogeneous system, since spatial inhomogeneity strongly enhances the scattering between pump laser and cavity mode by modifying the amplitude of the cavity mode through the density distribution in the presence of a harmonic trap.

To see the supersolid phase more clearly, in Fig. 6.6 we plot a cut of the density profile along the y -axis through the center of the harmonic trap. We observe that the smooth density profile in a conventional optical lattice (green line) has been strongly changed by the cavity-mediated long-range interaction due to scattering processes between pump laser and cavity mode in the optical cavity.

6.1.5 Summary

In conclusion, we have investigated the self-organized phases (supersolid and checkerboard solid) of both homogeneous and trapped ultracold Bose gases coupled to a high-finesse optical cavity by means of RBDMFT, and found the self-organized phases are robust against strong on-site interactions. At zero temperature the self-organized phase transition is solely driven by quantum fluctuations, while at finite temperature thermal fluctuations compete with quantum fluctuations which enhances the buildup of self-organized phases at finite but low temperature. In the presence of an external harmonic trap, the coexistence of superfluid, Mott-insulating, supersolid and checkerboard solid phases is observed. We found that the buildup of the self-organized phases is strongly influenced by inhomogeneities in the presence of an external trap, due to the density dependence of scattering between pump laser and cavity mode via atoms in the cavity. In principle, these quantum phases in the homogeneous system can be detected by combining the time-of-flight method and detecting photons leaking from the cavity mode [25], while the coexistence of different phases in the presence of an external trap can be directly observed by single-site addressing microscopy [54–56]. Our results provide new insight into the BEC-cavity system in the strong coupling regime, regarding emergent crystallinity and experimental feasibility of observing novel quantum phases using single-site-resolution probing techniques.

6.2 Strongly correlated dipolar bosonic gases

6.2.1 Introduction

In this section, we will investigate strongly correlated dipolar bosonic gases in an optical lattice. Usually, interactions in ultracold gases are isotropic and short ranged. However, dipolar gases have additional long-range anisotropic interactions, which can give rise to new physics. Actually, numerous interesting phenomena have already been studied by theoretical and experimental investigations of ultracold dipolar gases [26, 27, 58, 214, 222–233]. The door towards exploring the many-body physics originating from dipole-dipole interactions in ultracold gases has thus been opened. Up to now, however, there is still a lack of theoretical studies of the effect of strong dipole-dipole interactions on quantum magnetic phases of two-component dipolar bosonic gases in an optical lattice.

In this section, we investigate quantum phases of ultracold dipolar bosonic gases in a 2D square optical lattice, by means of real-space bosonic dynamical mean field theory. This section is organized as follows: firstly, we give a description of the model and our approach. We then study the finite-size effect on the phase diagram of a homogenous dipolar system, and discuss the influence of dipole-dipole interactions on magnetic phases.

6.2.2 Model and method

Expanding field operators in the basis of Wannier functions and keeping terms only in the lowest band, one can obtain the extended Bose-Hubbard Hamiltonian for dipolar bosonic gases, as shown in Eq. (3.36). For two-component dipolar bosonic gases loaded into an optical lattice, the physics of this system can be captured by an extended two-component Hubbard model

$$\begin{aligned} \hat{\mathcal{H}} = & -t_\sigma \sum_{\langle i,j \rangle \sigma} (\hat{b}_{i\sigma}^\dagger \hat{b}_{j\sigma} + \text{h.c.}) + \frac{1}{2} U \sum_{i\sigma\sigma'} \hat{n}_{i\sigma} (\hat{n}_{i\sigma'} - \delta_{\sigma\sigma'}) \\ & + \sum_{i \neq j, \sigma\sigma'} \frac{V_{i\sigma,j\sigma'}^{\text{dd}}}{2} \hat{n}_{i\sigma} \hat{n}_{j\sigma'} + \sum_{i\sigma} (V_i - \mu_\sigma) \hat{n}_{i\sigma}. \end{aligned} \quad (6.1)$$

In this Hamiltonian, $\langle i, j \rangle$ represent the nearest neighbor sites i, j . The bosonic creation (annihilation) operator for species σ at site i is $\hat{b}_{i\sigma}^\dagger$ ($\hat{b}_{i\sigma}$), and the local density is $\hat{n}_{i,\sigma} = \hat{b}_{i\sigma}^\dagger \hat{b}_{i\sigma}$. t_σ denotes the hopping amplitude for species σ , $U_{\sigma\sigma'}$ the inter- and intra-species interactions, μ_σ the global chemical potential for species σ , and V_i the harmonic trap. In the following we focus on a 2D square lattice, and assume that the external electric field, which polarizes the dipole moment in a certain direction, is oriented perpendicular to the optical lattice plane, with $V_{i\sigma,j\sigma'}^{\text{dd}} = C_{\text{dd}}/4\pi|\mathbf{R}_i - \mathbf{R}_j|^3$ where \mathbf{R}_i is the dimensionless position vector of lattice site i .

In this Hamiltonian, it is worth noticing that inter-site interactions only contribute on the Hartree level in the high-dimensional limit, this motivates us to keep only the Hartree contribution of the inter-site interaction in the Hamiltonian as an approximation to the original one [234, 235]

$$\frac{V_{\text{dip}}}{2} \sum_{i \neq j, \sigma\sigma'} \frac{\hat{n}_{i\sigma} \hat{n}_{j\sigma'}}{|\mathbf{R}_i - \mathbf{R}_j|^3} \simeq \sum_{i \neq j, \sigma\sigma'} \frac{V_{\text{dip}}}{|\mathbf{R}_i - \mathbf{R}_j|^3} \langle \hat{n}_{j\sigma} \rangle \left(\hat{n}_{i\sigma'} - \frac{1}{2} \langle \hat{n}_{i\sigma'} \rangle \right), \quad (6.2)$$

where the strength of dipole-dipole interaction is $V_{\text{dip}} = C_{\text{dd}}/4\pi$. After taking the Hartree approximation, we perform investigations of the strongly correlated dipolar system with long-range interactions by using RBDMFT, which is an extension of BDMFT and fully captures the spontaneous breaking of translational symmetry of the lattice system.

6.2.3 Results

In this section, we consider a homogenous system in a 2D square lattice and focus on the situation of total filling $n = n_b + n_d = 1$ with balanced densities $n_b = n_d = 0.5$. We calculate ground-state phase diagrams of the dipolar bosonic gases for different dipole strengths, and investigate the influence of dipole-dipole interactions on magnetic phases. To study the anti-ferromagnetic phase, we focus on a typical interaction regime with the interactions $U_b = U_d = 12U_{bd}$, which can be accessible by Feshbach resonances. In all our calculations we set

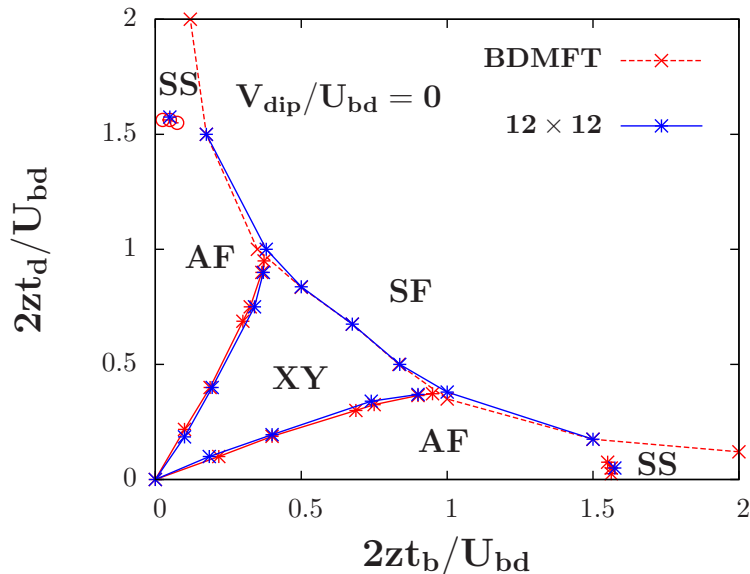


Figure 6.7: Zero-temperature phase diagram for a two-component dipolar gas in a 2D square lattice (12×12) as a function of hopping parameters. The interaction parameters are $U_b = U_d = 12 U_{bd}$, the total filling is $n = 1$ with $n_b = n_d = 0.5$, and the dipolar interaction strength $V_{\text{dip}}/U_{bd} = 0.0$.

$U_{bd} = 1$ as the unit of energy, and z is the number of nearest neighbors for each site.

First, we study the phase diagram of Bose-Bose mixtures with dipolar interaction strength $V_{\text{dip}} = 0$ and check the finite-size-effect on the phase diagram. In Fig. 6.7, we obtain the zero-temperature phase diagram for a 2D lattice system, which is qualitatively similar to the 3D system, as shown in Fig. 5.3. Here, we observe four distinct phases, i.e. superfluid (SF), XY-ferromagnetic phase (XY), anti-ferromagnetic phase (AF), and supersolid (SS). As discussed in subsection (5.1.2), superfluid phase is characterized by the superfluid order parameter $\phi_\nu > 0$, XY-ferromagnetic phase by the two-body correlator $\phi_{bd} = \langle bd^\dagger \rangle - \langle b \rangle \langle d \rangle > 0$ with $\phi_\nu = 0$, the anti-ferromagnetic phase by $\Delta_{AF}^\nu = |n_{\nu,\alpha} - n_{\nu,\bar{\alpha}}| > 0$, and the supersolid phase by both $\Delta_{AF}^\nu > 0$ and $\phi_b > 0, \phi_d = 0$ (if $t_b \gg t_d$), where ν denotes the component and α is the sublattice ($\alpha = -\alpha$). As shown in Fig. 6.7, we find that the results obtained from RBDMFT for a $N_{\text{lat}} = 12 \times 12$ square lattice, are in a good agreement with single-site BDMFT simulations. Therefore, we simulate a dipolar bosonic system in a $N_{\text{lat}} = 12 \times 12$ square lattice in the following of this section.

Next, we study the phase diagram of Bose-Bose mixtures, with a weak dipolar interaction strength $V_{\text{dip}}/U_{bd} = 0.1$ (Fig 6.8) and all the other parameters as in Fig 6.7. Again, we observe four phases in the system, i.e. the superfluid, supersolid, XY-ferromagnetic and anti-ferromagnetic phase. When both species acquire large hopping amplitudes, we observe a superfluid phase

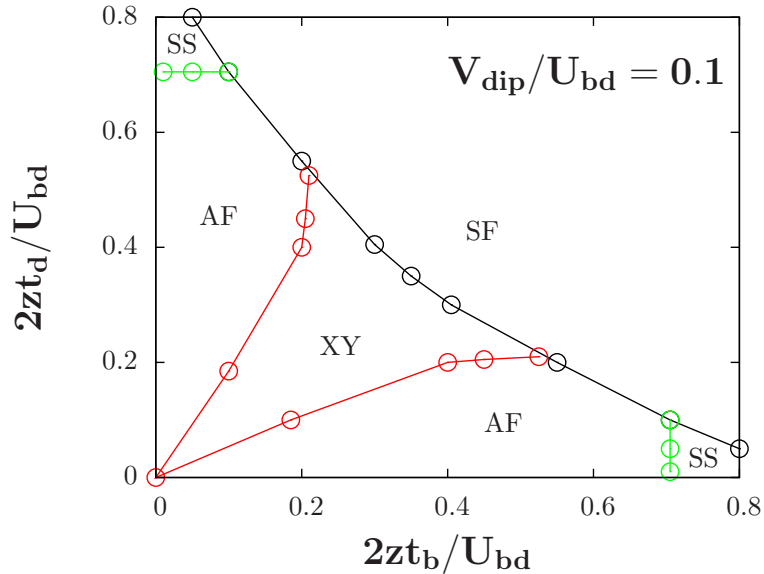


Figure 6.8: Zero-temperature phase diagram for a two-component dipolar gas in a 2D square lattice (12×12) as a function of hopping parameters. The interaction parameters are $U_b = U_d = 12 U_{bd}$, the total filling is $n = 1$ with $n_b = n_d = 0.5$, and the dipolar interaction strength $V_{\text{dip}}/U_{bd} = 0.1$.

with atoms delocalized over the whole lattice. In contrast, when the hopping amplitudes of both species are relatively small, the system manifests itself as a Mott insulator with magnetic ordering at sufficiently low temperature, i.e. XY-ferromagnetic or anti-ferromagnetic phase. Another phase appears when the hopping amplitudes are very anisotropic. The species with larger hopping is more easily delocalized and develops a superfluid order along with a spatial density wave pattern in real space, which corresponds to a supersolid phase. Since the dipole-dipole interaction is weak, the whole structure of the phase diagram is qualitatively similar to Fig. 6.7, but we observe that the Mott-insulating region of the dipolar gas shrinks, since the long-range dipole-dipole interactions effectively enhance the total interaction. This leads to the phase transition from the Mott insulator to the superfluid phase occurring earlier and correspondingly, the phase boundary shifts to lower hopping.

Finally, we investigate the phase diagram of Bose-Bose mixtures with a strong dipolar interaction strength $V_{\text{dip}}/U_{bd} = 0.3$. As before, we observe four phases in the system but with new phases appearing, and the structure of the phase diagram is strongly influenced by the long-range dipole-dipole interactions. When both species have comparably small hopping, a charge-density-wave (CDW) pattern emerges, characterized by a checkerboard density distribution, i.e. a total filling $n = 2$ on one site but with vanishing density on its neighbors, as shown in Fig. 6.10. Upon increasing the hopping of one species, the corresponding atoms tunnel to its neighbors to lower the energy of

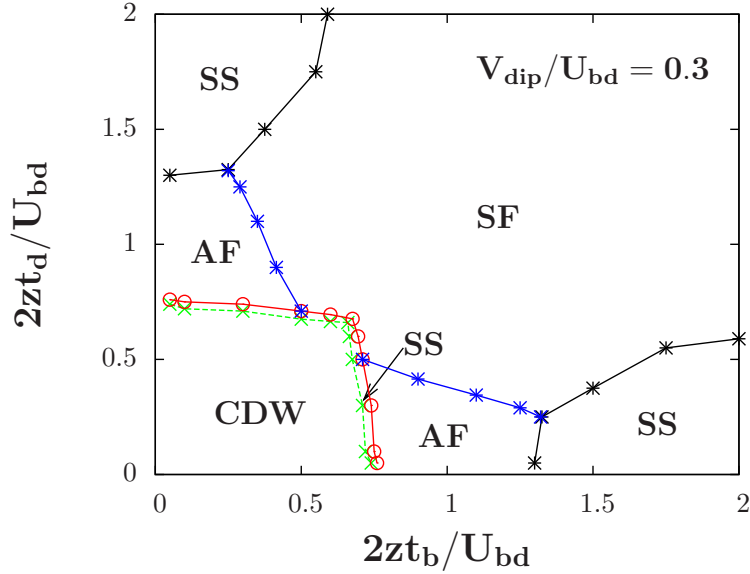


Figure 6.9: Zero-temperature phase diagram for a two-component dipolar gas in a 2D square lattice (12×12) as a function of hopping parameters. The interaction parameters are $U_b = U_d = 12U_{bd}$, the total filling is $n = 1$ with $n_b = n_d = 0.5$, and the dipolar interaction strength $V_{\text{dip}}/U_{bd} = 0.3$.

the system, which indicates that an anti-ferromagnetic phase can develop, as shown in Fig. 6.9. We find that the first-order transition region between CDW and anti-ferromagnetic phase is connected by a small window of supersolid phase rather than ordinary coexistence, due to the presence of the long-range interactions [236]. Increasing the hopping amplitude further on, the corresponding atoms delocalize over the whole lattice and the system manifests itself as a supersolid phase. We observe the small window of supersolid phase for only contact interactions (see Fig. 5.3, 6.7) becomes larger, which indicates the supersolid phase is more favorable in the system with long-range interactions. When both of the species have comparably large hopping amplitudes, the atoms are more easily delocalized and therefore superfluid.

To better understand the corresponding phases discussed in Fig. 6.9, we plot four sets of density distributions n_b (upper panels) and n_d (lower panels) in real space in Fig. 6.10. From the left to the right, the corresponding phases are CDW, supersolid, anti-ferromagnetic and superfluid phase, respectively. For the CDW phase, we observe a charge-density wave pattern with both species sitting in the same sites, while for the anti-ferromagnetic phase, the system develops anti-ferromagnetic order Δ_{AF}^ν . In the supersolid phase, a checkerboard pattern arises for the light atoms (larger hopping) with non-integer filling which indicates finite superfluid long-range order. Hence it has diagonal and off-diagonal long-range order. This density profile could be detected via *in situ* measurement with single-site addressability in optical lattices using electron or optical microscopy [54–56].

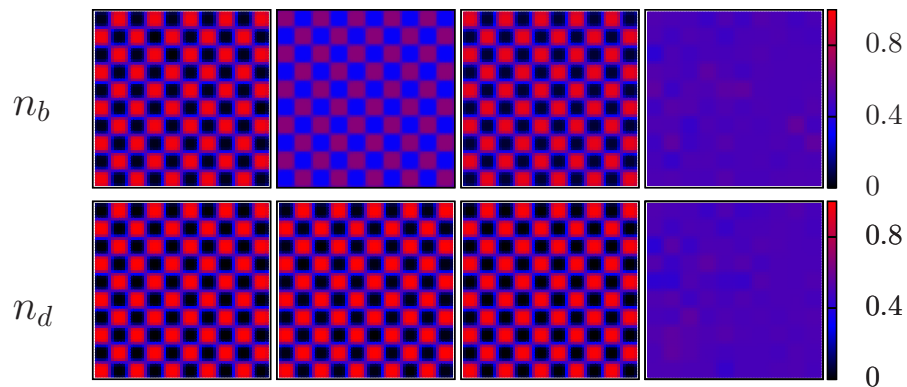


Figure 6.10: Zero-temperature density profile for a two-component dipolar gas in a 2D square lattice, with a dipolar interaction strength $V_{\text{dip}}/U_{bd} = 0.3$. From the left to the right: CDW, supersolid, anti-ferromagnetic, and superfluid phase, respectively.

6.2.4 Summary

In conclusion, in this section we have investigated the physics of strongly correlated dipolar bosonic gases in optical lattices, and studied the influence of long-range interactions on the magnetic phases. Due to the competition between the on-site and long-range interactions, novel quantum phases appear, which feature charge-density and also notably ordered phases with anti-ferromagnetism in the Mott domain. We have observed that the supersolid phase is more favorable due to the presence of the long-range interactions.

Chapter 7

Spectroscopy of Strongly Correlated Ultracold Bosons

7.1 Introduction

The results presented in the previous chapters, are for ground-state properties or thermodynamics of ultracold gases in optical lattices. In this chapter, we address the momentum-resolved excitational properties of strongly correlated bosonic gases in an optical lattice via Bragg spectroscopy [237], using the time-dependent Gutzwiller method. In recent years, spectroscopic techniques have been successfully applied to ultracold atoms, such as RF spectroscopy [238], lattice shaking [96, 239], and Bragg spectroscopy [41, 240–252], which opens up the possibility of studying excitations of strongly correlated model systems. Up to now, these Bragg spectroscopic experiments mostly focused on weakly interacting condensates [240–242] or the Mott insulating [241] regime. In this chapter, we investigate the excitational properties of a strongly interacting superfluid, and identify the recently described *amplitude mode* [237, 246, 253–255]. In the weakly interacting regime, the gapless sound mode, corresponding to the collective mode of Bogoliubov excitations in a lattice has been investigated experimentally [240–242]. There exists a new type of excitation in addition to the gapless sound mode for the strongly interacting superfluid, namely the gapped *amplitude mode*. However, this strongly interacting system cannot be described by linear response calculations in the perturbative limit with Bragg spectroscopy [237] and there has been no clear observation of the amplitude mode yet in previous experiments [241]. To bridge the gap between existing idealized theory predictions and our experimental observations, we present a number of important experimental effects of Bragg spectroscopy and investigate the underlying physics of the gapped mode in this chapter.

7.2 Model and method

7.2.1 Model

We consider bosonic atoms in an optical lattice in the presence of external Bragg lasers. At sufficiently high lattice depth and moderate filling, the system

is well described by the single-band Bose-Hubbard model

$$\hat{\mathcal{H}} = -J \sum_{i,j} (\hat{b}_i^\dagger \hat{b}_j + \text{h.c.}) + \sum_i \epsilon_i \hat{b}_i^\dagger \hat{b}_i + \frac{U}{2} \sum_i \hat{b}_i^\dagger \hat{b}_i^\dagger \hat{b}_i \hat{b}_i + V_{\text{bra}}, \quad (7.1)$$

where \hat{b}_i^\dagger denotes the creation operator for an atom at lattice site i , J the tunneling between nearest neighboring sites, U the on-site interaction parameter, and ϵ_i the local energy offset. V_{bra} denotes the effect of the Bragg beams on the many-body system, which are used for probing the energy and momentum resolved excitational structure of ultracold gases [41, 240–245].

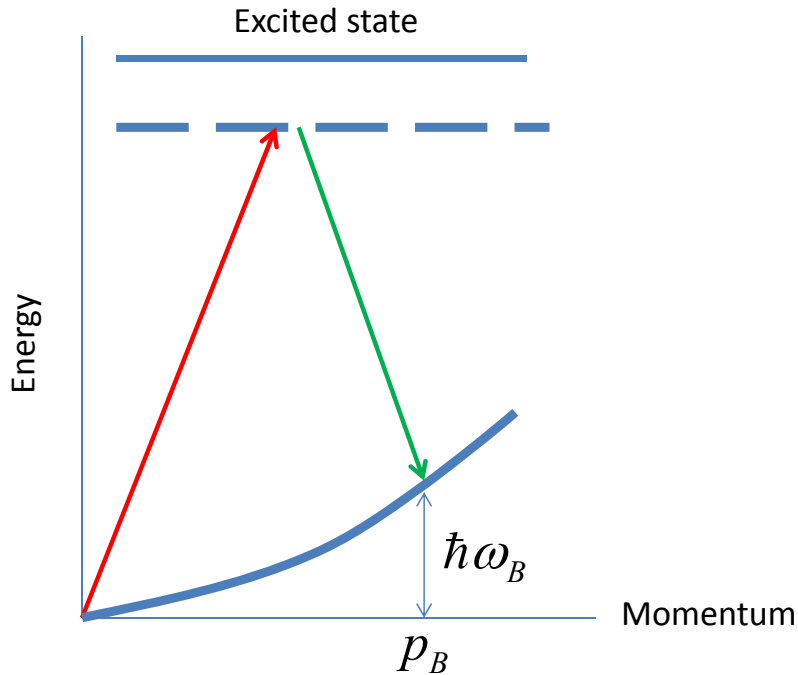


Figure 7.1: Sketch of Bragg scattering, where $\hbar\omega_B$ denotes the energy shift and p_B the momentum kick between the initial and final states.

Bragg Spectroscopy — We consider a single-component ultracold gas in an optical lattice, exposed to a pulse of two intersecting laser beams, which has a slight frequency detuning $\omega_1 - \omega_2 = E_B/\hbar = \omega_B$ and wavevector difference $p_B = k_1 - k_2$, where the two different lasers are at frequencies (wavevectors) ω_1 (k_1) and ω_2 (k_2). When the condition for Bragg scattering becomes a resonance condition (the incident frequency and momentum differences matched to a many-body excitation), atomic many-body states with the corresponding momentum and energy difference are coupled, the condensate will be illuminated and excited, and a fraction of the condensate atoms will be transferred from the ground state to an excited state with finite momentum due to the Bragg kick (see Fig. 7.1). Since all relevant atomic states correspond to the same internal hyperfine atomic state and the Doppler-shift can be neglected

in this regime, the effect of the Bragg lasers on a single atom can thus be expressed by the Hermitian operator [218, 256]

$$\hat{V}_{\text{bra}} = \frac{V_I}{2} \int dp' (e^{i\omega_B t} |p' + p_B\rangle \langle p'| + e^{-i\omega_B t} |p'\rangle \langle p' + p_B|), \quad (7.2)$$

where $V_I = 2\hbar\omega_R$ denotes the Bragg intensity (the Bragg lasers are described by a classical field, via replacing the photon creation and destruction operators with c -numbers, as long as the Bragg beams are sufficiently strong), where ω_R denotes the two-photon Rabi frequency. The physical picture of this process is: the two laser beams interfere to form a *moving* wave intensity modulation, and, due to the ac Stark effect, atoms exposed to this intensity modulation experience a conservative optical potential with a spatial modulation. At resonance, momentum and energy will be transferred from the two laser beams to the condensate. Based on this, the excitation properties of the condensate can be extracted via Bragg spectroscopy.

The question is how to express the Bragg operator (7.2) in the Wannier basis in the Hamiltonian (7.1). As we know, any operator can be expressed in a complete basis set, such as localized Wannier functions in multiple bands. Within a single band Gutzwiller calculation, the lowest-band approximation entails neglecting all terms that do not couple states within the lowest band. Within this approximation, any single particle operator can be written as

$$\hat{A} = \sum_{l,l'} A_{l,l'} \hat{b}_l^\dagger \hat{b}_{l'}. \quad (7.3)$$

The Bragg operator can also be described in the Wannier basis. For the sake of simplicity, here we assume the transfer of momentum (Bragg kick) along one lattice axis only, which we will call the x -direction. The extension to other directions is straightforward. The effect of the Bragg lasers on the atomic system can be described by

$$\hat{V}_{\text{bra}} = \sum_{l,l',l_y,l_z} (e^{i\omega_B t} A_{l,l'} + e^{-i\omega_B t} A_{l',l}^*) \hat{b}_{l,l_y,l_z}^\dagger \hat{b}_{l',l_y,l_z}. \quad (7.4)$$

We still need to derive an explicit formula for the Bragg operator for real calculations. To proceed, Eq. (7.2) is written in another form:

$$\hat{V}_{\text{bra}} = \frac{V_I}{2} \left(e^{-i\omega_B t} \hat{\rho}^\dagger(p_B) + e^{-i\omega_B t} \hat{\rho}(p_B) \right). \quad (7.5)$$

Here $\hat{\rho}^\dagger(p_B) = \sum_p \hat{a}_{p_B+p}^\dagger \hat{a}_p$, where $\hat{a}_p^\dagger (\hat{a}_p)$ is the creation (annihilation) operator for an atom with momentum p . In a two-dimensional setup, where the angle between momentum kick and the x -axis of the lattice is ϕ , $\hat{\rho}^\dagger(p_B, \phi) = \sum_p \hat{a}_{p_x+p_B \cos \phi, p_y+p_B \sin \phi}^\dagger \hat{a}_p$. Expressing this single particle operator in the basis

of two-dimensional single-band Wannier states yields the matrix elements of the Bragg operator in factorized form

$$\begin{aligned} \hat{\rho}_{(l_x, l_y), (l'_x, l'_y)}^\dagger(p_B, \phi) &= e^{iap_B(l_x \cos \phi + l_y \sin \phi)} \\ &\left[\frac{1}{L} \sum_{p_x} e^{iap_x(l_x - l'_x)} c_{N(p_x + p_B \cos \phi)}^{(\alpha_0, k=K(p_x + p_B \cos \phi))} c_{N(p_x)}^{(\alpha_0, k=K(p_x))} \right] \\ &\times \left[\frac{1}{L} \sum_{p_y} e^{iap_y(l_y - l'_y)} c_{N(p_y + p_B \cos \phi)}^{(\alpha_0, k=K(p_y + p_B \cos \phi))} c_{N(p_y)}^{(\alpha_0, k=K(p_y))} \right], \end{aligned} \quad (7.6)$$

where $c_{N(p)}^{(\alpha_0, k=K(p))}$ denotes an eigenvector of a single particle in an optical lattice with momentum $2N(p)q_l + k$ in the lowest band α_0 , where the indices are defined as $N(p) = \lfloor \frac{p}{2q_l} \rfloor$ and $K(p) = p - q_l \lfloor \frac{p}{2q_l} \rfloor$ with q_l being the wave vector of the lattice laser. In free space, $\hat{\rho}^\dagger(p_B)$ acts as a translation operator in momentum space and simply transfers atoms into higher momentum states p_B , if energetically allowed. However, in the presence of an optical lattice, multiple scattering processes are enhanced and may lead to the occupation of a broad distribution of momentum components.

7.2.2 Method

For weakly interacting bosonic system, the Bose-Einstein condensate can be described by the Gross-Pitaevskii equation. For strongly interacting bosons, the time-dependent Gutzwiller mean-field theory [257] can be applied, where the coupling between the lattice sites is treated in a mean-field approximation. Within this approximation, the total many-body wavefunction is given by $|\Psi\rangle = \prod_i \sum_{n=0}^{\infty} f_n^i \frac{(b_i^\dagger)^n}{\sqrt{n!}} |0\rangle$. In practice, the infinite sum over the particle numbers n is truncated by introducing a cut-off N_c , depending on the interaction strength and the local density. The dynamics is then governed by the finite set of coupled differential equations [257, 258]

$$\begin{aligned} i\dot{f}_n^i &= - \sum_{\langle ij \rangle} \left(\sqrt{n+1} \Phi_j^* f_{n+1}^i + \sqrt{n} \Phi_j f_{n-1}^i \right) \\ &+ \left(\frac{U}{2} n(n-1) + V_{\text{bra}}(t) + \epsilon_i \right) f_n^i, \end{aligned} \quad (7.7)$$

where $\Phi_i = \langle b_i \rangle = \sum_n \sqrt{n} (f_{n-1}^i)^* f_n^i$.

This time-dependent Gutzwiller method is a highly efficient method for studying dynamics in higher dimensional lattices and it conserves particle number and energy exactly. The validity of the Gutzwiller approximation is justified by the fact that for small interactions it incorporates Gross-Pitaevskii dynamics [257]. While for a strongly interacting condensate in the vicinity of the Mott transition, it includes the physics of the effective theories [218, 237, 246]. Therefore, it correctly recovers both the atomic limit $U/J \rightarrow \infty$ and time-dependent Gross-Pitaevskii theory within a coherent state description for weak

interactions. However, the Gutzwiller approximation, described here, is restricted to zero temperature, since it neglects phase fluctuations. Therefore, we only consider $T = 0$ here. In the following section of this chapter, the ground state is first determined and subsequently time evolved in the presence of the Bragg beams. The time evolution is determined by a set of effective local Eqs. (7.7), coupled non-linearly to the states at other sites.

7.3 Results

In this part, we will measure dispersion relations of a single-component ultracold bosonic lattice system via Bragg spectroscopy, using the time-dependent Gutzwiller method. Based on a classical treatment of the laser field, as long as the Bragg beams are sufficiently strong, the effect of the time-dependent Bragg field on the atomic system can be described by the single-particle operator in Eq. (7.5). In this section, the influence of on-site interactions on the dispersion relation of strongly correlated ultracold bosonic systems in an optical lattice will be investigated, and comparison between theoretical results and experimental observations made. In all our calculations, we focus on the physics within the lowest band, requiring all relevant energy scales to be lower than the band gap. We choose the recoil energy E_r as the unit of energy.

7.3.1 Bragg spectroscopy beyond perturbation theory

In this section, we investigate beyond perturbation theory the effect of finite Bragg laser intensity on the dispersion relations of the ultracold bosonic gas in an optical lattice. Qualitatively, ultracold atoms exposed to the Bragg lasers can be transferred between different quasi-momentum states such as $\mathbf{k}=0 \rightarrow \mathbf{p}_B$, while at the same time the ultracold gas will absorb energy from the Bragg lasers, due to two-photon Raman processes. If the Bragg lasers are in resonance, a large fraction of the ultracold gas is excited to a finite momentum state, as shown in Fig. 7.2. To obtain quantitative information about excited states, the effect of the Bragg pulse shape and intensity on the response of the ultracold gas should be investigated. In particular, a strong probing intensity V_I is experimentally required for strongly correlated bosonic gases, considering the exponentially growing time scale $1/J$ versus lattice depth V_s and the limited coherence time for the pulse. Correspondingly, the effect of the probing beams should be treated beyond the linear response framework. Analyzing the response of the ultracold gas, we can extract the dispersion relation of the strongly correlated many-body system. For brevity, all dispersion relations and results shown in the following are along the line, connecting the $\Gamma = (0, 0, 0)$ and $M = (1, 1, 0)$ points in the first Brillouin zone.

The first effect on the response of ultracold gases needed to be addressed in a realistic simulation of Bragg spectroscopy is the pulse shape of Bragg beams. As we know from time-dependent perturbation theory, it leads to the characteristic sinc^2 response in frequency space for a square pulse with

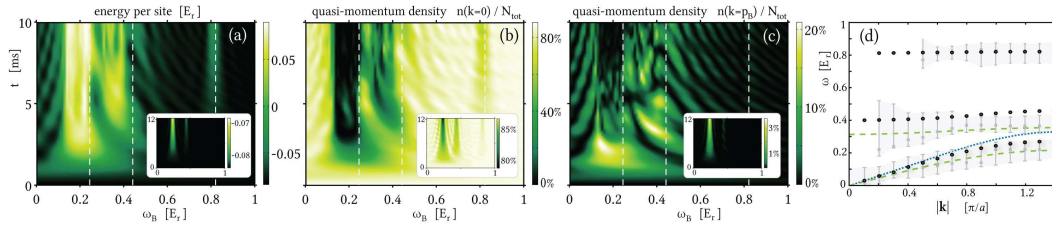


Figure 7.2: Dispersion relation of strongly correlated single-component ultracold gases in an optical lattice: Energy absorption (a) and quasi-momentum density (b),(c) spectra for a square pulse at high intensity $V_I = 0.1E_r$ (insets: weak intensity $V_I = 0.005E_r$) in the intermediate interaction $V_s = 9$ regime and for Bragg momentum $|\mathbf{p}_B| = \pi/a$ (From Ref. [218]). The resonance frequencies predicted from the maxima of the high intensity energy absorption spectra (plotted as gray squares in (d)) contain a systematic uncertainty quantified by the FWHM of the pulse after 10ms $\approx 3.26/J$ indicated by the error bars and shaded region in (d). The comparison with the true quasiparticle energies (dashed white lines in (a-c), black circles in (d)) reveals significant discrepancies. For comparison in (d): The blue dotted line is the Bogoliubov result, the green dashed lines are the results from Ref. [237] for the amplitude and sound modes ($\omega(\mathbf{k}) = \psi_0 \sqrt{2U n \epsilon_{\mathbf{k}}}$ with ψ_0 determined by Gutzwiller method).

the Bragg intensity V_I being constant over a fixed time interval t , as shown in Fig. 7.2. Another essential effect that has to be considered is the finite intensity of the probing beam. The analysis of this effect requires a treatment beyond the linear response of the system, as shown in the spectra of the full time-dependent Gutzwiller calculation in Fig. 7.2. While the response in the limit of small probing intensity V_I , shown in the insets of Fig. 7.2(a)-(c), is given by δ -shaped peaks as expected, there is a drastic non-trivial broadening of the different peaks for typical experimental probing intensities $V_I \approx 0.1E_r$, shown in the corresponding main figures, respectively. This indicates a breakdown of the non-interacting quasiparticle picture of the many-body excitations, due to the influence of the probing beams. Whereas the amplitude mode's signature is generally stronger in the energy- and $n(\mathbf{k} = 0)$ than in the $n(\mathbf{k} = \mathbf{p}_B)$ profile, it indicates that the scaling of its spectral weight is nonlinear in the probing intensity V_I , that is, it is beyond linear response in this large $V_I \cdot t$ regime, as shown in Figs. 7.2(a),(b).

In addition to the broadening of the spectra at high probing intensity V_I , the supposed resonance frequencies of all modes (gray squares in Fig. 7.2(d)) are systematically shifted to lower frequencies with respect to the true quasiparticle energies (indicated by dashed white lines in Fig. 7.2(a)-(c) and circles in d)), consistent with RPA [255]), i.e. the quasiparticle energies are influenced by probing Bragg beams. The error bars and shaded areas in Fig. 7.2(d) indicate the FWHM of the energy absorption profile after $t = 10$ ms, quan-

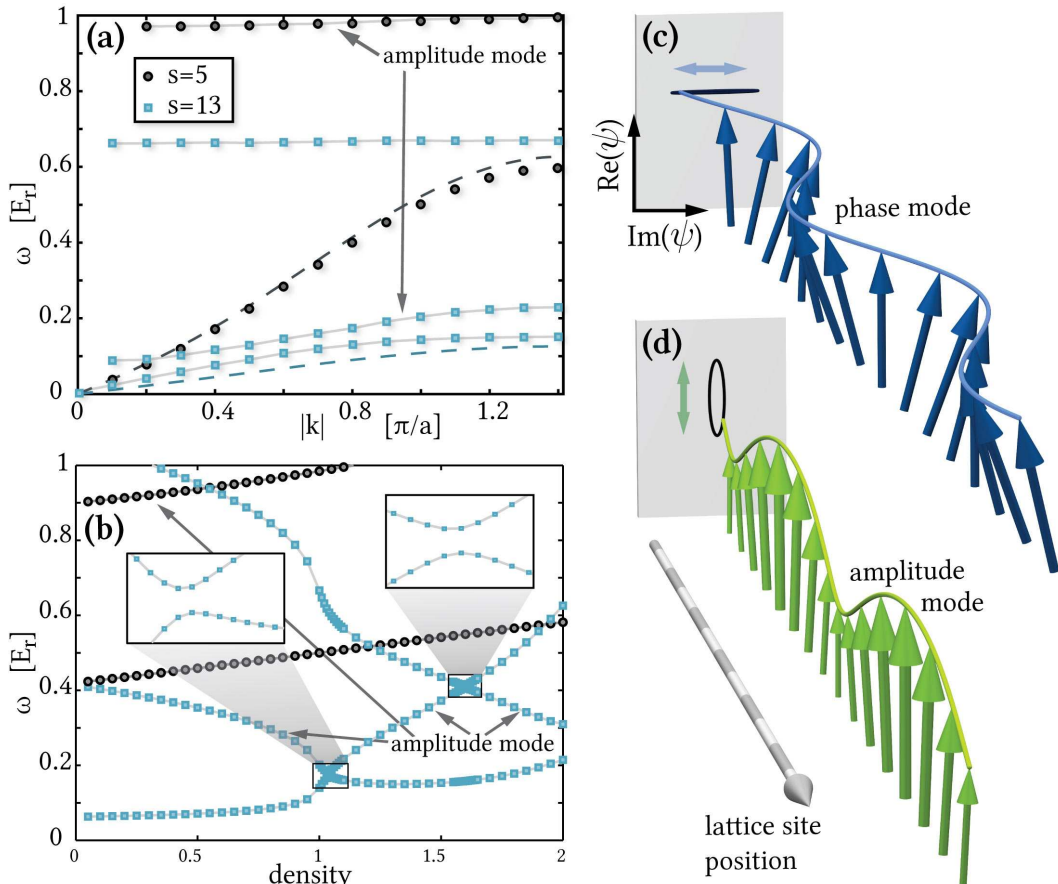


Figure 7.3: (a,b): Dispersion relations for the homogeneous system in the linear response limit at $n = 1$ (a) and density-dependence at $|\mathbf{k}| = \pi/a$ (b) in the superfluid for weak ($V_s = 5$, black circles) and strong ($V_s = 13$, blue squares) interactions (From Ref. [218]). Corresponding Bogoliubov results [259] are shown as black dashed lines in (a). (c,d): Illustration of the order parameter for a coherent excitation of the phase (sound) mode (c) and the amplitude mode (d) in a homogeneous condensate at $\mathbf{k} = (0.8/a, 0, 0)$ and $V_s = 13$. The projection of all ψ_i 's in the complex plane is shown by the black ellipses: for the sound mode (c), the oscillation is almost exclusively in the tangential, for the amplitude mode (d) mainly in the radial (i.e. in the amplitude) direction.

tifying the systematic uncertainty in the resonance energies. To the best of our knowledge, this has not been investigated in the analysis of experimental data thus far. In addition, two further broadening effects accounted for in our simulation are the frequency broadening due to the finite pulse time, as well as the inhomogeneous trapping potential. A shallow trap and low filling $n \lesssim 1.05$, due to the strong density dependence of the mode resonance frequencies, are crucial for an unambiguous identification of the amplitude mode.

After taking all these broadening effects into account, the good quantitative agreement between theory and experiment in the spectra is achieved, as will later be shown in Fig. 7.4(b). In addition, at intermediate interactions $V_s = 9$ ($U/J \approx 8.55$) and density $n = 1$ shown in Fig. 7.2(d), neither Bogoliubov theory (dotted blue line), nor the theory for strongly correlated systems [237] (dashed green lines) remains valid, while the dispersion relation obtained by the dynamic Gutzwiller method (black circles in Fig. 7.2(d)) is valid and continuously connects these two limiting theories.

We now turn to address the dependence of quasiparticle energies of the different modes on the density. To suppress the effect of Bragg lasers on the dispersion relation, we apply weak Bragg beams to the strongly correlated ultracold many-body system, i.e. linear response theory is valid. From Fig. 7.3(a), we observe that Bogoliubov theory is valid and gives reasonable results in the weakly interacting limit. It is worth noticing that the dependence is non-trivial for strongly interacting bosonic systems, even though for the weakly interacting case, it depends approximately linearly on the density (black dotted lines in Fig. 7.3(b)). The strong dependence can be understood from the excitational particle and hole branches, which may cross each other in the Mott insulator, i.e., crossing the phase transition into the superfluid, the emerging condensate couples the particle/hole branches in the equations of motion, hybridizing these and leading to avoided mode crossings at the previous intersection points, as is shown by the blue squares in Fig. 7.3(b). We notice that in the superfluid regime the sound (amplitude) mode remains the energetically lowest (second lowest) lying mode. Experimentally, a probing beam at resonance induces time- and position-dependent oscillations of the density and the spatial order parameters $\psi_{\mathbf{i}} = \langle b_{\mathbf{i}} \rangle$. In the theoretical description, these excitations correspond to coherent states of the respective quasiparticle, as illustrated in Fig. 7.3(c),(d): a gapless sound mode excitation leads to a dominant spatial and temporal oscillation of the phase and a density wave, whereas an excitation of the amplitude mode leads mainly to an oscillation of the amplitude of $\psi_{\mathbf{i}}$ and a strong suppression of the density modulation. The oscillation of $|\psi_{\mathbf{i}}|$ at constant density can thus be understood as a local periodic transfer of particles between the condensate and the non-condensate.

7.3.2 Comparison with experimental observation

In this part, we make comparisons between the numerical simulations and experimental observations. In the experiment, a Bose-Einstein condensate of ^{87}Rb atoms is loaded into the lowest band of a 3D cubic optical lattice with a spacing of $a = 515\text{nm}$ and intensity of V_s recoil energies E_r , as described in details in Ref. [240], where the system is well described by the Bose-Hubbard model. Subsequently, two Bragg laser beams with a slight frequency detuning ω_B , but essentially the same wavelength $\lambda = 781.37\text{nm}$ (i.e. $|\omega_B| \ll c/\lambda$), lying in the x - y -plane of the optical lattice at a coincident angle $\theta_B = 45^\circ$, are applied. This allows the ultracold atoms to undergo a two-photon Raman

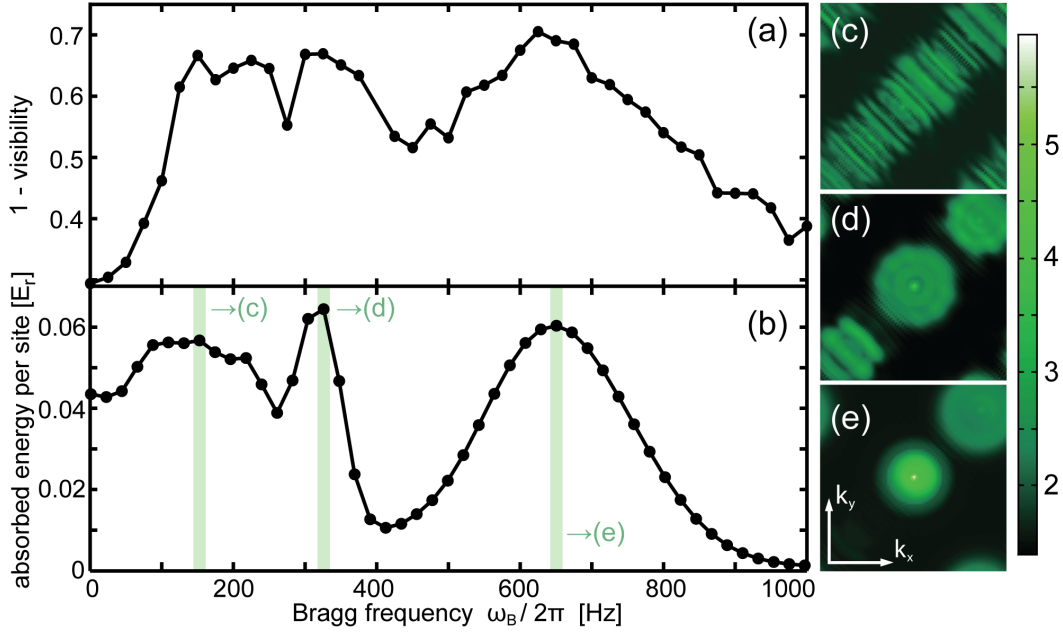


Figure 7.4: Comparison of the experimental visibility (a) and theoretically predicted energy absorption (b) at $|\mathbf{p}_B| = \pi/a$ using a Blackman-Harris pulse of 10ms in an optical lattice with $V_s = 13$ in a 3D trap (From Ref. [218]). A maximum intensity $V_I = 0.27E_r$ and the experimentally determined total particle number $N_{\text{tot}} = 5 \cdot 10^4 \pm 33\%$ and $\omega = 2\pi \cdot (26, 26, 21)$ Hz trapping frequency were used for (b), leading to a maximum central density $n = 1.05$. The lower peak is the sound mode, mainly broadened by the high intensity of the Bragg beam to lower frequencies. The upper peak at 650Hz is the gapped amplitude mode, broadened mainly by the trap. Figures (c,d,e) show the theoretically predicted trap broadened logarithmic quasi-momentum distributions in the first Brillouin zone at the frequencies marked by the green lines in (b).

process, in which the momentum kick an atom experiences is given by $|\mathbf{p}_B| = (4\pi/\lambda)\sin(2\theta_B)$. This specific experimental setup allows the system to be probed along the nodal direction. To minimize the oscillatory response due to the restricted Bragg pulse time and pulse shape, a Blackman-Harris pulse [260] is applied to obtain the main results shown in Fig. 7.4, both in experiment and theory.

The resonance frequency can be determined from the strongest loss in the momentum component $n(\mathbf{k} = 0)$, gain in $n(\mathbf{k} = \mathbf{p}_B)$, energy absorption or reduction in the condensate fraction, as shown in Fig. 7.4(a),(b), where the theoretical simulation is in good agreement with the experimental observation. The lower peak at ~ 200 Hz in the spectra is the trap- and intensity-broadened sound mode, whereas the higher peak at ~ 650 Hz is the amplitude mode, broadened mainly by the strong density dependence. Experimentally, an addi-

tional complication arises due to the large depletion of the condensate at large V_s . To avoid the noise, therefore, the lattice depth is ramped down linearly over 10ms to $V_s = 10$ after exposure to the Bragg beams. Subsequently, the visibility, shown in Fig. 7.4(a), is extracted from the time-of-flight image of the equilibrated atoms and is monotonically related to the absorbed energy. Determining these resonance positions for a range of different momenta \mathbf{p}_B leads to the dispersion relations for the Bogoliubov, amplitude and gapped modes. We also notice that for the lattice system, with increasing U/J , backscattering transitions are enhanced and at longer times higher order transitions become relevant. This can also be observed from the physical momentum distribution $n(\mathbf{p}) = \langle a_{\mathbf{p}}^\dagger a_{\mathbf{p}} \rangle$, which is directly related to the quasi-momentum distribution, as shown in Fig. 7.4(c)-(e).

7.4 Summary

In conclusion, we have theoretically and experimentally observed the gapped amplitude mode of a strongly correlated superfluid, by using Bragg spectroscopy. Good quantitative agreement between the experimental visibility and the theoretical prediction of a time-dependent bosonic Gutzwiller calculation is found, after taking the full spatial trap profile, finite pulse time and high intensity of the probing beam into account. This shows that Bragg spectroscopy is a suitable method for probing, not only the momentum-resolved quasiparticle structure of Bogoliubov mode, but also the more exotic collective amplitude mode excitation. For a clear signal of the latter in a strongly interacting superfluid, a shallow trap on the experimental side and a theoretical treatment beyond the perturbative linear response regime are essential. Whereas a finite Bragg beam intensity is vital for a clear spectroscopic response of the amplitude mode, it leads to a renormalization of the sound- and amplitude-mode resonance frequencies, which has to be accounted for in a quantitative comparison of experiment and theory.

Chapter 8

Conclusions and Outlook

In this thesis, we have investigated strongly correlated bosonic gases in an optical lattice, mostly based on a bosonic version of dynamical mean field theory and its real-space extension. Emphasis is put on possible novel quantum phenomena of these many-body systems and their corresponding underlying physics, including quantum magnetism, pair-superfluidity, thermodynamics, many-body cooling, new quantum phases in the presence of long-range interactions, and excitational properties. Our motivation is to simulate many-body phenomena relevant to strongly correlated materials with ultracold lattice gases, which provide an excellent playground for investigating quantum systems with an unprecedented level of precision and controllability. Due to their high controllability, ultracold gases can be regarded as a *quantum simulator* of many-body systems in solid-state physics, high energy astrophysics, and quantum optics. In this thesis, specifically, we have explored possible novel quantum phases, thermodynamic properties, many-body cooling schemes, and the spectroscopy of strongly correlated many-body quantum systems. The results presented in this thesis provide theoretical benchmarks for exploring quantum magnetism in upcoming experiments, and an important step towards studying quantum phenomena of ultracold gases in the presence of long-range interactions. To take into account the strong correlations in lattice systems, BDMFT/RBDMFT has been developed and implemented to provide a non-perturbative description of zero- and finite-temperature properties of the homogeneous/inhomogeneous Bose-Hubbard model including magnetic ordering, which cannot be resolved within static mean-field methods.

BDMFT treats condensed and normal bosons on equal footing and is a non-perturbative method, which describes bosonic gases in an optical lattice. It can be regarded as an expansion in $1/z$ around the Gutzwiller method, where z denotes lattice coordination number, and it captures the dynamical correlations, which are crucial in particular for multispecies systems in optical lattices. This method is well-controlled in the limit of high lattice coordination number z and becomes exact in infinite dimensions. We derive the self-consistency equations and present the BDMFT equations as a controlled $1/z$ expansion up to subleading order, based on a uniform scaling $\sim 1/z$ of the bosonic hopping amplitude. To leading order, this yields Gutzwiller Mean-Field theory,

while the natural extension to the subleading terms of order $O(1/z)$ yields the BDMFT equations. We then developed real-space bosonic dynamical mean-field theory for describing systems in an inhomogeneous environment, e.g. in an external harmonic trap. The crucial difference to the standard homogeneous BDMFT is that here we are going beyond a single-site approach and taking into account that different sites are not equivalent to each other, thus accounting for the inhomogeneity of the system.

With this newly developed BDMFT/RBDMFT, we have theoretically investigated Bose-Bose mixtures in 2D and 3D optical lattices. Due to the inter-species interactions, the phase diagram is very rich. This system can be effectively described by the Bose-Hubbard model. We have specifically considered the case of filling $n = 1$ and $n = 2$ per site. We have mapped out the phase diagram and obtained diverse phases such as the superfluid, unordered Mott state, XY-ferromagnet and anti-ferromagnet for positive inter-species interactions, and the pair-superfluid phase for negative inter-species interactions. In addition, we have investigated the inhomogeneous (trapped) bosonic gases, which are more closely related to the experimental situation. We have included the effect of the external confining potential via RBDMFT, which assumes site-dependent self-energies. In parallel, we performed also a complementary calculation based on a Local Density Approximation (LDA) combined with BDMFT which is computationally more affordable. Comparing results of both methods, we examined the magnetic properties of the system for a wide range of parameters. To the best of our knowledge, this is the first systematic and non-perturbative study of the magnetic properties of a two-component inhomogeneous Bose-Hubbard model. It will bring more insight into ongoing experiments on Bose-Bose mixtures in optical lattices. However, at present, it is still challenging to observe these quantum magnetic phases in an optical lattice due to the very low critical temperatures resulting from second-order tunneling processes, and new cooling schemes are needed to reach these temperatures in experiment. Therefore, we subsequently explored the thermodynamics of interacting many-body systems and investigated the validity of spin-gradient demagnetization cooling, which is in principle capable of cooling the system down to the critical temperature of magnetic order. We also calculated the finite-temperature phase diagram and remarkably found that the system can be *heated* from the superfluid into the Mott insulator at low temperature, analogous to the Pomeranchuk effect in ^3He . This provides a promising many-body cooling technique.

We have also investigated the physics of strongly correlated ultracold bosonic gases in optical lattices with long-range interactions. These systems realize extended Bose-Hubbard models, and the physical properties of such gases are dominated by long-range interactions. There are two possible ways to include long-range interactions: coupling a Bose-Einstein condensate to a cavity, or loading dipolar bosonic gases into an optical lattice. Due to the competition between the on-site and long-range interactions, novel quantum phases appear.

For a BEC coupled to an optical cavity, we have investigated self-organized phases (supersolid and checkerboard solid) of both homogeneous and trapped systems by means of RBDMFT. We have found that these self-organized phases are robust against strong onsite interactions at zero temperature, where the self-organized phase transition is solely driven by quantum fluctuations. In the presence of an external harmonic trap, the coexistence of superfluid, Mott-insulating, supersolid and checkerboard solid domains is observed. We find the buildup of these self-organized phases to be strongly influenced by the inhomogeneity induced by an external trap, due to the density dependence of scattering between the pump laser and the cavity mode. Self-organized phases could be detected by combining time-of-flight measurements and the detection of photons leaking from the cavity, while the coexistence of different phases in the presence of an external trap could be directly observed by quantum gas microscopy with single-site resolution. For dipolar systems, we have investigated the strongly correlated dipolar bosonic gases in optical lattices, based on RBDMFT. Specifically, we considered the case of filling $n = 1$ per site at zero temperature for different dipole-dipole interaction strengths. We have mapped out phase diagrams, which contains novel quantum phases, due to the competition between on-site and long-range interactions. We expect that these novel quantum phases would be observed experimentally in the future, through including the strong dipole-dipole interactions as a result of, permanent or induced, magnetic or electric dipole moment, which can be tuned by an applied external magnetic or electronic field.

Finally, we investigated the spectroscopy of strongly correlated bosonic gases in an optical lattice, based on the time-dependent Gutzwiller method, which can efficiently describe the strongly interacting system. We observed two collective modes: the sound mode and the amplitude mode. Both modes have been detected using Bragg spectroscopy in a strongly interacting condensate of ultracold atoms in an optical lattice. This shows that Bragg spectroscopy is a suitable method for probing not only the quasiparticle structure of Bogoliubov mode with full momentum resolution, but also of the more exotic collective amplitude mode excitation by going beyond the linear response regime. For a clear signal of the amplitude mode in a strongly interacting superfluid, a shallow trap on the experimental side and a theoretical treatment beyond the perturbative linear response regime are essential. Whereas a finite Bragg beam intensity is vital for a clear spectroscopic response of the amplitude mode, it leads to a renormalization of the sound- and amplitude-mode resonance energies, which has to be accounted for in a quantitative comparison of experiment and theory. After taking the full spatial trap profile, finite pulse time, and finite intensity of the probing beam into account, Good quantitative agreement between the experimental visibility and the theoretically predicted results from a time-dependent bosonic Gutzwiller calculation is found.

There are still several open questions which should be investigated in further studies. A first important issue is the detection of novel magnetic phases

with long-range spin order, after achieving the necessary ultra-low temperatures for ultracold bosons in optical lattices. This will be the first step towards achieving d-wave superfluidity, and will give us more insight into the underlying physics of high-temperature superconductivity. A second important issue is the stability of the supersolid phase, which is predicted to exist in dipolar bosonic gases, as well as the robustness of the checkerboard phase in the BEC-cavity systems. Further studies, based on BDMFT/RBDMFT, can also be extended to include orbital degrees of freedom and study unconventional Bose-Einstein condensates, such as by including spin-orbit coupling which produces analogs of fractional quantum Hall states or topological insulators [261, 262], and higher-orbital physics [263]. These new quantum systems have drawn a large amount of attention recently and are developing rapidly as a new frontier, due to the high level controllability of optical lattices loaded with ultra-cold bosons, and provide an intriguing opportunity to investigate both the metastable states of bosons pumped into high orbital bands and spin-orbit coupled system with synthetic magnetic fields in systems of neutral atoms. In addition, bosonic dynamical mean field theory can be improved and extended to a cluster formalism for taking into account nonlocal correlations [158–160], or to a nonequilibrium realm for studying dynamics of many-body systems [264].

Kapitel 9

Zusammenfassung und Ausblick

In dieser Arbeit haben wir die stark korrelierten bosonischen Gase in einem optischen Gitter, das meist auf einer bosonischen Version der dynamischen Molekularfeldtheorie und ihrer Ortsraum-Erweiterung basiert, untersucht. Der Schwerpunkt liegt auf möglichen neuartigen Quantenphänomenen dieser Vielteilchensysteme und ihrer entsprechenden zugrunde liegenden Physik, einschließlich Quantenmagnetismus, Paar-Suprafluidität, Thermodynamik, Vielteilchen-Kühlung des Körpers, neuer Art von Physik in der Gegenwart weitreichender Wechselwirkungen und Anregungseigenschaften. Unsere Motivation ist es, Vielkörper-Phänomene relevant für stark korrelierte Materialien mit ultrakalten Gasen im optischen Gitter, die einen hervorragenden Spielplatz für die Untersuchung von Quanten-Systemen mit einem beispiellosen Maß an Präzision und Steuerbarkeit bieten, zu simulieren. Aufgrund ihrer hohen Steuerbarkeit können ultrakalte Gase als ein Quantensimulator von Vielteilchensystemen in der Festkörperphysik, Hochenergie-Astrophysik, und der Quantenoptik betrachtet werden. In dieser Arbeit haben wir speziell mögliche neue Quanten-Phasen, thermodynamische Eigenschaften, Vielkörper-Kühlsysteme und die Spektroskopie von stark korrelierten Vielteilchen-Quantensystemen untersucht. Die Ergebnisse dieser Arbeit sorgen für theoretische Benchmarks bei der Untersuchung von Quantenmagnetismus in kommenden Experimenten und sind ein wichtiger Schritt zum Studieren von Quantenphänomenen von ultrakalten Gasen in Gegenwart von weitreichenden Wechselwirkungen. Unter Berücksichtigung der starken Korrelationen in Gitter-Systemen wurden BDMFT (RBDMFT) entwickelt und umgesetzt, um eine nicht-perturbative Beschreibung der Eigenschaften des homogenen und inhomogenen Bose-Hubbard-Modells einschließlich magnetischer Ordnung am absoluten Nullpunkt und bei endlichen Temperaturen zu erhalten, die mit statischen Molekularfeldmethoden nicht berechnet werden können.

BDMFT behandelt kondensierte und normale Bosonen gleichberechtigt und ist eine nicht-perturbative Methode, die die bosonischen Gase in einem

optischen Gitter beschreibt. Sie kann als eine Erweiterung der Gutzwiller-Methode um $1/z$ angesehen werden, in der z als Gitter-Koordinationszahl bezeichnet wird, und sie erfasst die dynamischen Korrelationen, die vor allem für Multispezies-Systeme in optischen Gittern entscheidend sind. Diese Methode ist gut steuerbar im Grenzfall hoher Gitter-Koordinationszahlen z und wird in unendlichen Dimensionen exakt. Wir leiten die Selbst-Konsistenz-Gleichungen her und präsentieren die BDMFT Gleichungen als eine kontrollierte $1/z$ -Erweiterung bis zu nächstführender Ordnung, basierend auf einer einheitlichen Skalierung $1/z$ des bosonischen Amplituden-Hopping. In führender Ordnung ergibt sich die Gutzwiller Molekularfeldtheorie, während die natürliche Erweiterung für die nächstführenden Terme der Ordnung $O(1/z)$ die BDMFT-Gleichungen ergibt. Wir haben dann Ortsraum-Bosonen-Dynamische-Molekularfeldtheorie für die beschriebenen Systeme in einem inhomogenen Umfeld entwickelt, z. B. in einer externen harmonischen Falle. Der entscheidende Unterschied zur üblichen homogenen BDMFT ist, dass wir über einen Ein-Gitterplatz-Ansatz hinaus gehen und berücksichtigen, dass verschiedene Gitterplätze nicht äquivalent zueinander sind, was zu der Inhomogenität des Systems führt.

Mit diesen neu entwickelten BDMFT/RBDMFT haben wir theoretische Bose-Bose-Mischungen in 2D und 3D optischen Gittern untersucht. Aufgrund der Inter-Spezies-Wechselwirkungen ist das Phasendiagramm sehr vielfältig. Dieses System kann effektiv durch das Bose-Hubbard-Modell beschrieben werden. Wir haben den Fall von Füllungen $n = 1$ und $n = 2$ pro Gitterplatz besonders betrachtet. Wir haben das Phasendiagramm abgebildet und diverse Phasen erhalten: Suprafluid, ungeordneter Mott-Zustand, XY-Ferromagnet und Antiferromagnet für positive Inter-Spezies-Wechselwirkungen und die paarsuprafluide Phase für negative Wechselwirkungen zwischen den Arten. Darüber hinaus haben wir die inhomogenen (eingeschlossenen) bosonischen Gase, die näher an der experimentellen Situation sind, untersucht. Wir haben die Wirkung des externen einengenden Potentials von RBDMFT, die von Gitterplatz-abhängigen Selbst-Energien ausgeht, berücksichtigt. Parallel dazu führten wir auch eine auf einer lokalen Dichtenäherung (LDA) basierte und mit BDMFT kombinierte ergänzende Berechnung durch, die rechnerisch günstiger ist. Beim Vergleich der Ergebnisse der beiden Methoden untersuchten wir die magnetischen Eigenschaften des Systems für eine Vielzahl von Parametern. Nach unserem besten Wissen ist dies die erste systematische und nicht-perturbative Untersuchung der magnetischen Eigenschaften eines inhomogenen Bose-Hubbard-Modells mit zwei Komponenten. Es gibt mehr Einblick in laufende Experimente zu Bose-Bose-Mischungen in optischen Gittern. Aufgrund der sehr niedrigen

kritischen Temperaturen aus Tunnel-Prozessen zweiter Ordnung ist es im Augenblick noch schwierig, diese quantenmagnetischen Phasen in einem optischen Gitter zu erreichen und es sind neuartige Kühl-Systeme erforderlich, um diese Temperaturen im Experiment zu erreichen. Deshalb haben wir anschließend die Thermodynamik der wechselwirkenden Vielteilchensysteme und die Gültigkeit der Spin-Gradienten-Entmagnetisierungs-Kühlung untersucht, die im Prinzip in der Lage ist, das Systems bis auf die kritische Temperatur von magnetischer Ordnung zu kühlen. Wir haben auch das Phasendiagramm für endliche Temperaturen berechnet und bemerkenswert gefunden, dass das System bei niedrigen Temperaturen aus dem Suprafluiden in den Mott-Isolator-Zustand erhitzt werden kann, analog zum Pomeranchuk-Effekt in ^3He . Dies stellt eine vielversprechende Vielteilchen-Kühltechnik dar.

Wir haben auch die Physik von stark korrelierten ultrakalten bosonischen Gasen in optischen Gittern mit langreichweitigen Wechselwirkungen untersucht. Diese Systeme realisieren erweiterte Bose-Hubbard-Modelle und die physikalischen Eigenschaften solcher Gase werden durch langreichweitigen Wechselwirkungen dominiert. Es gibt zwei mögliche Wege zur langreichweitigen Wechselwirkungen: das Koppeln eines Bose-Einstein-Kondensat an einen Hohlraum oder das Laden eines dipolaren bosonischen Gases in ein optisches Gitter. Aufgrund der Konkurrenz zwischen der lokalen- und langreichweitigen Wechselwirkungen erscheinen neue Quanten-Phasen. Für ein BEC, das an einen optischen Resonator, gekoppelt ist haben wir selbstorganisierende Phasen (supersolid und Schachbrettmuster Feststoff) sowohl von homogenen als auch gespeicherten ultrakalten Bose-Gasen, die an einen optischen Hohlraum hoher Güte gekoppelt sind mit Hilfe von RBDMFT untersucht. Wir haben festgestellt, dass diese selbst organisierten Phasen robust sind gegen starke lokale Wechselwirkungen am absoluten Nullpunkt, wo der selbst organisierten Phasenübergang allein durch Quantenfluktuationen getrieben wird. Wir beobachten, dass thermische Fluktuationen den Aufbau von selbstorganisierten Phasen bei endlichen, aber niedrigen Temperaturen verbessern können. In Anwesenheit von einem externen harmonischen Falle beobachten wir die Koexistenz von suprafluiden, Mott-isolierenden, Supersolid und Schachbrettmuster Soliden. Wir beobachten, dass der Aufbau dieser selbstorganisierten Phasen stark von einem inhomogenen Fallenpotential beeinflusst wird, aufgrund der Dichteabhängigkeit der Streuung von Pumplaser und Hohlraum-Mode an Atomen im Hohlraum. Selbstorganisierte Phasen können durch Kombination von Flugzeit-Messungen und des Nachweises von Photonen die aus dem Hohlraum austreten, detektiert werden, während die Koexistenz verschiedener Phasen in

Gegenwart eines externen Falls könnte direkt durch Quantengas Mikroskopie mit Single-Site zu beachtlicher Auflösung. Für dipolare Systeme haben wir die Physik stark korrelierter dipolare bosonischer Gase in optischen Gittern auf der Basis RBDMFT untersucht. Besondere Aufmerksamkeit wird dem Einfluss der langreichweitigen Wechselwirkungen auf die magnetischen Phasen von Zwei-Komponenten bosonischen Gasen in einem optischen Gitter gewidmet, und unser Ziel ist es, das entsprechende Phasendiagramm zu kartieren. Genauer gesagt, haben wir den Fall von Füllung $n = 1$ pro Gitterplatz bei Temperatur Null für verschiedene Dipol-Dipol-Wechselwirkungsstärken betrachtet. Aufgrund der Konkurrenz zwischen der lokalen und langreichweitigen Wechselwirkungen, erscheinen neue Quanten-Phasen in dem Vielteilchen-System wie die Ladungs-Dichte Phasen und vor allem auch geordnete Phasen mit Antiferromagnetismus in der Mott-Domäne. Wir haben beobachtet, dass die supersolide Phase in einem breiten Regime stabil ist aufgrund der weitreichenden Wechselwirkungen. Wir gehen davon aus, dass diese neuen Quanten-Phasen experimentell in der Zukunft beobachtet werden, durch Abstimmen eines angelegten externen elektronischen Feldes, um die Dipol-Dipol-Wechselwirkungen als Folge des permanenten oder induzierten magnetischen oder elektrischen Dipolmoment der Elektronen zu variieren.

Schließlich untersuchten wir die Spektroskopie von stark korrelierten bosonischen Gasen in einem optischen Gitter basierend auf der zeitabhängigen Gutzwiller Methode, die die stark wechselwirkenden Systeme effizient beschreibt. Unser Ziel war es, die Anregungs-Eigenschaften stark korrelierter Vielteilchensysteme zu studieren. Wir beobachteten zwei kollektive Moden: die Sound-Mode und die Amplituden-Mode. Beide Moden wurden mittels Bragg-Spektroskopie erkannt in einem stark wechselwirkenden Kondensat aus ultrakalten Atomen in einem optischen Gitter. Dies zeigt, dass Bragg-Spektroskopie eine geeignete Methode zur Untersuchung nicht nur der Struktur der Quasiteilchen Bogoliubov Mode mit voller Impuls Auflösung ist, sondern auch der eher exotischen kollektiven Amplituden Mode indem man über das linear-response regime hinausgeht. Wir beobachten eine systematische Verschiebung der Schall- und Amplituden-Moden Resonanzfrequenzen aufgrund der endlichen Bragg Strahlintensität. Für ein klares Signal der letzteren in einem stark wechselwirkenden Suprafluid, sind ein flache Falle auf der experimentellen Seite und eine theoretische Behandlung über ein perturbatives lineares Response Regime von wesentlicher Bedeutung. Während eine endliche Bragg Strahlintensität essentiell für eine klare spektroskopische Response der Amplitude-Mode ist, führt dies zu einer Renormierung der Schall- und Amplituden-Resonanz Energien, die

in einen quantitativen Vergleich von Experiment und Theorie berücksichtigt werden muss. Nach der Berücksichtigung des vollen räumlichen Fallem-Profiles, endliche Puls-Zeit und der Endlichkeit der Intensität des Sondierungs-Strahls, erhalten wir eine gute quantitative Übereinstimmung zwischen dem experimentellen Sichtbarkeit und den theoretisch vorhergesagten Ergebnisse aus einer zeitabhängigen bosonischen Gutzwiller Berechnung gefunden.

Es gibt immer noch einige offene Fragen, die in weiteren Studien untersucht werden sollten. Ein erster wichtiger Punkt ist die Detektion von neuen magnetischen Phasen mit einer Spin-Ordnung großer Reichweite, nachdem die erforderlichen extrem niedrigen Temperaturen für ultrakalte Bosonen in optischen Gittern erreicht ist. Dies wird der erste Schritt zur Erreichung der d-Wellen Suprafluidität sein, und gibt uns mehr Einblick in die zugrunde liegende Physik der Hochtemperatur-Supraleitung. Ein zweiter wichtiger Punkt ist die Stabilität der Supersolid-Phase, die Vorhersagen zufolge in dipolaren bosonischen Gasen bestehen soll, sowie die Robustheit des Schachbrett-Phase in den BEC-Resonator-Systemen. Weitere auf BDMFT/RBDMFT basierte Studien, können auch erweitert werden, um orbitalen Freiheitsgrade unkonventionelle Bose-Einstein-Kondensate, wie auch durch die Spin-Bahn-Kopplung, die Analoga der fraktionierten Quanten-Hall-Zustände oder topologischen Isolatoren produziert, und Physik höherer Orbitale. Diese neuen Quanten-Systeme haben vor kurzem eine große Menge Aufmerksamkeit erreicht und entwickeln sich rasch als ein neues Frontgebiet, wegen der hohen Kontrollierbarkeit der optischen mit ultrakalten Bosonen geladenen Gittern, und bieten eine faszinierende Möglichkeit, sowohl die meta-stabilen Zustände von in höhere orbitale gepumpten Bosonen und Spin-Bahn-gekoppelten System mit synthetischen Magnetfelder in Systemen mit neutralen Atomen zu untersuchen. Darüber hinaus kann die bosonische dynamische Mean-Field-Theorie verbessert und zu einem Cluster Formalismus für die Berücksichtigung der nichtlokalen Korrelationen, oder zu einem Nichtgleichgewichts-Bereich für das Studium der Vielteilchendynamik erweitert werden.

Appendix A

The Jaynes-Cummings Model

In this part, we derive the Jaynes-Cummings model, which describes a two-level atom interacting with a single bosonic mode and provides an excellent physical picture for optical cavity in the context of cavity quantum electrodynamics. If we consider only a two-level free atom, the Hamiltonian for the internal degrees of freedom is given by

$$\hat{H}_a = \hbar\omega_0\hat{\sigma}^\dagger\hat{\sigma}^-, \quad (\text{A.1})$$

where $\omega_0 = (E_e - E_g)/\hbar$ is the atomic transition frequency, $\hat{\sigma}^- \equiv |g\rangle\langle e|$, and $\hat{\sigma}^\dagger \equiv |e\rangle\langle g|$. Here we use the Pauli matrix algebra to simplify the notation, with $|g\rangle$ ($|e\rangle$) denoting the ground (excited) state with an energy E_g (E_e).

The single-mode cavity mode is given by

$$\hat{H}_c = \hbar\omega_c\hat{a}^\dagger\hat{a}, \quad (\text{A.2})$$

where \hat{a}^\dagger (\hat{a}) denotes the creation (annihilation) operator of the cavity field.

In this reduced Hilbert space, the electric dipole operator is expressed as

$$\begin{aligned} \hat{\mathbf{d}} &= \mathbf{d}_{eg}|e\rangle\langle g| + \mathbf{d}_{eg}^*|g\rangle\langle e| \\ &= \mathbf{d}_{eg}(\hat{\sigma}^\dagger + \hat{\sigma}^-), \end{aligned} \quad (\text{A.3})$$

where the dipole matrix element $\mathbf{d}_{eg} \equiv \langle e|\hat{\mathbf{d}}|g\rangle$, which is defined to be real. Within the dipole approximation, the interaction between the atom and the cavity mode is described by

$$\hat{H}_{ac} = -\hat{\mathbf{d}} \cdot \hat{\mathbf{E}}_c(\mathbf{r}), \quad (\text{A.4})$$

where the electric field operator of the cavity mode at position \mathbf{r} can be expressed in terms of the creation and annihilation operators as

$$\hat{E}_c = i\sqrt{\frac{\hbar\omega_c}{2\epsilon_0 V}}u(\mathbf{r})\mathbf{e}[\hat{a} - \hat{a}^\dagger], \quad (\text{A.5})$$

where \mathbf{e} is the polarization of the mode, ϵ_0 is the vacuum permittivity, $u(\mathbf{r})$ is the mode function which is determined by the boundary condition of the corresponding system, and V is the cavity volume.

In the rotating-wave approximation, the interaction term (A.4) takes the following form:

$$\hat{H}_{\text{ac}} = i\hbar g(\mathbf{r})(\hat{\sigma}^\dagger \hat{a} - \hat{\sigma}^- \hat{a}^\dagger), \quad (\text{A.6})$$

where $g(\mathbf{r}) = -\sqrt{\frac{\omega_c}{2\hbar\epsilon_0 V}} |\mathbf{d}_{\text{eg}} \cdot \mathbf{e}| u(\mathbf{r})$.

Therefore, the total Hamiltonian of the system is written as:

$$\begin{aligned} \hat{H}_{\text{JC}} &= \hat{H}_a + \hat{H}_c + \hat{H}_{\text{ac}} \\ &= \hbar\omega_0 \hat{\sigma}^\dagger \hat{\sigma}^- + \hbar\omega_c \hat{a}^\dagger \hat{a} + i\hbar g(\mathbf{r})(\hat{\sigma}^\dagger \hat{a} - \hat{\sigma}^- \hat{a}^\dagger). \end{aligned} \quad (\text{A.7})$$

Appendix B

Gutzwiller vs. Mean-Field Approximations

In this part, we will prove the equivalence of the bosonic Gutzwiller and site-decoupling mean-field approximations for a homogeneous system. Here we follow closely the derivation of [144]. In section (4.2) we present the Gutzwiller wave function, which consists of a set of decoupled single-site coherent states and is an efficient method for describing strongly correlated systems in higher dimensional lattices. It provides the possibility to self-consistently determine the Gutzwiller ground state by numerical minimization of the grand canonical potential. Actually, the Gutzwiller ansatz is exactly identical to the mean-field method, which provides a much easier self-consistency condition regarding to only one mean-field parameter.

On the one hand, the modified single-site energy in the Gutzwiller approach can be given by:

$$E - \alpha \left(\sum_{n=0}^{\infty} |f_n|^2 - 1 \right) = \sum_{n=0}^{\infty} |f_n|^2 \left(\frac{U}{2} n(n-1) - \mu n - \alpha \right) + \alpha - JZ \left| \sum_{n=0}^{\infty} f_n^* f_{n+1} \sqrt{n+1} \right|^2, \quad (\text{B.1})$$

where Z denotes the number of nearest neighbors, α is the Lagrange multiplier for the normalization of the ground state, and all complex coefficients $f_n (f_n^*)$ can be varied independently. Taking the derivative with respect to f_n^* yields the conditions:

$$0 = \frac{\partial E}{\partial f_n^*} - \alpha \frac{\partial}{\partial f_n^*} \left(\sum_{n=0}^{\infty} |f_n|^2 - 1 \right) = f_n \left(\frac{U}{2} n(n-1) - \mu n - \alpha \right) - JZ \left[f_{n+1} \sqrt{n+1} \sum_{n=0}^{\infty} f_n f_{n+1}^* \sqrt{n+1} + f_{n-1} \sqrt{n} \sum_{n=0}^{\infty} f_n^* f_{n+1} \sqrt{n+1} \right]. \quad (\text{B.2})$$

On the other hand, the ground-state energy of the single-site mean-field Hamiltonian (4.5) can be written as:

$$E - \alpha \left(\sum_{n=0}^{\infty} |d_n|^2 - 1 \right) = \sum_{n=0}^{\infty} |d_n|^2 \left(\frac{U}{2} n(n-1) - \mu n - \alpha \right) + JZ |\phi|^2 + \alpha - JZ \left[\phi \sum_{n=0}^{\infty} d_n^* d_{n-1} \sqrt{n} + \phi^* \sum_{n=0}^{\infty} d_n^* d_{n+1} \sqrt{n+1} \right], \quad (\text{B.3})$$

where $|\Phi_{MF}\rangle = \sum_{n=0}^{\infty} d_n |n\rangle$ which denotes the mean-field ground state.

As before, this ground-state eigenvalue depends on the coefficients d_n , and a necessary condition for an energy minimum is a vanishing derivative with respect to d_n^*

$$\begin{aligned} \frac{\partial E}{\partial d_n^*} - \alpha \frac{\partial}{\partial d_n^*} \left(\sum_{n=0}^{\infty} |f_n|^2 - 1 \right) &= d_n \left(\frac{U}{2} n(n-1) - \mu n - \alpha \right) - \\ &\quad JZ \left[\phi d_{n-1} \sqrt{n} + \phi^* d_{n+1} \sqrt{n+1} \right] \\ &= 0. \end{aligned} \quad (\text{B.4})$$

In addition, the order parameter ϕ is also determined by minimizing the energy, that is, a necessary condition is

$$\begin{aligned} \frac{\partial E}{\partial \phi^*} &= -JZ \sum_{n=0}^{\infty} d_n^* d_{n+1} \sqrt{n+1} + JZ \phi \\ &= 0, \end{aligned} \quad (\text{B.5})$$

which yields the order parameter

$$\phi = \langle b \rangle = \sum_{n=0}^{\infty} d_n^* d_{n+1} \sqrt{n+1}. \quad (\text{B.6})$$

Finally, one obtains a set of equations, which are the necessary conditions (B.2) for the ground-state energy in the framework of Gutzwiller approximation, after plugging self-consistency Eq. (B.6) into the necessary conditions (B.4). Therefore, both methods lead to the same global minimum, indicating the equivalence of the Gutzwiller and the mean-field ansatz.

Appendix C

Effective Action in BDMFT

In this part, we will derive the effective action for the Hamiltonian (3.12) by following Ref. [11], by using the path integral formalism in the conventional coherent state representation. The partition function Z is written as

$$Z = \int D[\mathbf{b}^*]D[\mathbf{b}] \exp(-S[\mathbf{b}^*, \mathbf{b}]/\hbar). \quad (\text{C.1})$$

Here the notation $\int D[\mathbf{b}^*]D[\mathbf{b}] = \int \prod_{i,\alpha} db_{i\alpha}^* db_{i\alpha}$, where $b_{i\alpha}$ are complex-valued fields. The action $S[\mathbf{b}^*, \mathbf{b}]$ is

$$S[\mathbf{b}^*, \mathbf{b}] = \int_0^{\hbar\beta} d\tau \left\{ \sum_{i,\alpha} b_{i\alpha}^* (\hbar\partial_\tau - \mu_\alpha) b_{i\alpha} - \sum_{\langle ij \rangle, \alpha} \frac{t'_\alpha}{z} (b_{i\alpha}^* b_{j\alpha} + \text{c.c.}) + \frac{1}{2} \sum_{i,\alpha,\beta} U_{\alpha\beta} b_{i\alpha}^* b_{i\alpha} (b_{i\beta}^* b_{i\beta} - \delta_{\alpha\beta}) \right\}, \quad (\text{C.2})$$

where the hopping parameters have been rescaled as $t_\alpha = t'_\alpha/z$, in order to retain a finite kinetic energy in the limit $z \rightarrow \infty$.

Following the same ‘‘cavity’’ method as in deriving the fermionic DMFT equations [129], we now consider a specific site which is denoted by the index 0, and the system with the site 0 excluded is called the cavity system. The corresponding action can be separated into three terms: S_0 , $S^{(0)}$ and ΔS . S_0 , which contains the terms that are exclusively related to the site 0, is given by

$$S_0 = \int_0^{\hbar\beta} d\tau \left\{ \sum_\alpha b_{0\alpha}^* (\hbar\partial_\tau - \mu_\alpha) b_{0\alpha} + \frac{1}{2} \sum_{\alpha,\beta} U_{\alpha\beta} b_{0\alpha}^* b_{0\alpha} (b_{0\beta}^* b_{0\beta} - \delta_{\alpha\beta}) \right\}, \quad (\text{C.3})$$

$S^{(0)}$, which contains the terms without the site 0, is given by

$$S^{(0)} = \int_0^{\hbar\beta} d\tau \left\{ \sum_{i \neq 0, \alpha} b_{i\alpha}^* (\hbar\partial_\tau - \mu_\alpha) b_{i\alpha} - \sum_{\langle ij \rangle^{(0)}, \alpha} \frac{t'_\alpha}{z} (b_{i\alpha}^* b_{j\alpha} + \text{c.c.}) + \frac{1}{2} \sum_{i \neq 0, \alpha, \beta} U_{\alpha\beta} b_{i\alpha}^* b_{i\alpha} (b_{i\beta}^* b_{i\beta} - \delta_{\alpha\beta}) \right\}, \quad (\text{C.4})$$

ΔS , which contains the terms coupling the site 0 to other sites, is given by

$$\Delta S = -\frac{1}{z} \int_0^{\hbar\beta} d\tau \sum_{\langle 0j \rangle, \alpha} t'_\alpha (b_{0\alpha}^* b_{j\alpha} + \text{c.c.}). \quad (\text{C.5})$$

We now derive an effective action for the site 0, defined via

$$Z_{\text{eff}}^0 = \int D[\mathbf{b}_0^*] D[\mathbf{b}_0] \exp(-S_{\text{eff}}^0[\mathbf{b}_0^*, \mathbf{b}_0]/\hbar) \equiv \frac{Z}{Z^{(0)}}. \quad (\text{C.6})$$

Here

$$Z^{(0)} = \int D^{(0)}[\mathbf{b}^*] D^{(0)}[\mathbf{b}] \exp(-S^{(0)}[\mathbf{b}_0^*, \mathbf{b}_0]/\hbar), \quad (\text{C.7})$$

where the functional integral is performed in the cavity system and excludes the fields at site 0, which is denoted by (0).

With this definition, we obtain:

$$Z_{\text{eff}}^0 = \frac{1}{Z^{(0)}} \int D[\mathbf{b}_0^*] D[\mathbf{b}_0] \exp(-S_0[\mathbf{b}_0^*, \mathbf{b}_0]/\hbar) \times \quad (\text{C.8})$$

$$\int D^{(0)}[\mathbf{b}^*] D^{(0)}[\mathbf{b}] \exp(-\{S^{(0)}[\mathbf{b}^*, \mathbf{b}] + \Delta S[\mathbf{b}^*, \mathbf{b}]\}/\hbar). \quad (\text{C.9})$$

Then it can be expanded in powers of ΔS :

$$\int D^{(0)}[\mathbf{b}^*] D^{(0)}[\mathbf{b}] e^{-\frac{S^{(0)} + \Delta S}{\hbar}} = \sum_{k=0}^{\infty} \frac{1}{k! \hbar^k} \int D^{(0)}[\mathbf{b}^*] D^{(0)}[\mathbf{b}] (-\Delta S)^k e^{-\frac{S^{(0)}}{\hbar}}. \quad (\text{C.10})$$

Considering the expectation value in the cavity system

$$\langle A \rangle_{(0)} = \frac{1}{Z^{(0)}} \int D^{(0)}[\mathbf{b}^*] D^{(0)}[\mathbf{b}] A e^{-\frac{S^{(0)}}{\hbar}}, \quad (\text{C.11})$$

this immediately leads to:

$$Z_{\text{eff}}^0 = \int D[\mathbf{b}_0^*] D[\mathbf{b}_0] \exp(-S_0[\mathbf{b}_0^*, \mathbf{b}_0]/\hbar) \sum_k \frac{\langle (-\Delta S)^k \rangle_{(0)}}{\hbar^k k!}. \quad (\text{C.12})$$

Since ΔS contains the small parameter $1/z$, it motivates us to systematically expand the effective action up to a few lowest order in ΔS . Note that $\langle (\Delta S)^k \rangle_{(0)}$ indicates the expectation values of the cavity system, except the site 0. Keeping terms up to the second order in ΔS , we arrive:

$$\langle \Delta S \rangle_{(0)} = -\frac{1}{z} \int_0^{\hbar\beta} d\tau \sum_{\langle 0j \rangle, \alpha} t'_\alpha \left(b_{0\alpha}^*(\tau) \langle b_{j\alpha}(\tau) \rangle_{(0)} + \text{c.c.} \right), \quad (\text{C.13})$$

$$\begin{aligned}
\langle (\Delta S)^2 \rangle_{(0)} &= \frac{1}{z^2} \int_0^{\hbar\beta} d\tau d\tau' \sum_{\langle 0j \rangle, \alpha} \sum_{\langle 0j' \rangle, \beta} t'_\alpha t'_\beta \\
&\quad \left\{ b_{0\alpha}^*(\tau) b_{0\beta}^*(\tau') \langle b_{j\alpha}(\tau) b_{j'\beta}(\tau') \rangle_{(0)} + b_{0\alpha}^*(\tau) b_{0\beta}(\tau') \langle b_{j\alpha}(\tau) b_{j'\beta}^*(\tau') \rangle_{(0)} \right. \\
&\quad \left. + b_{0\alpha}(\tau) b_{0\beta}^*(\tau') \langle b_{j\alpha}^*(\tau) b_{j'\beta}(\tau') \rangle_{(0)} + b_{0\alpha}(\tau) b_{0\beta}(\tau') \langle b_{j\alpha}^*(\tau) b_{j'\beta}^*(\tau') \rangle_{(0)} \right\}.
\end{aligned}$$

By the linked-cluster theorem, it yields for the effective action:

$$S_{\text{eff}}^0 = S_0 + \langle \Delta S \rangle_{(0)} - \frac{1}{2\hbar} (\langle (\Delta S)^2 \rangle_{(0)} - \langle \Delta S \rangle_{(0)}^2), \quad (\text{C.14})$$

here, in deriving the effective action in terms of the expectation values in the cavity system, we re-exponentiate the terms after the expectation value has been taken. In the re-exponentiation, we include terms up to second order in $1/z$. The average can be expressed by the connected Green's function in the cavity system:

$$\begin{aligned}
\mathbf{G}_{i\alpha;j\beta}^{(0)}(\tau, \tau') &= \begin{pmatrix} G_{i\alpha;j\beta}^{(0)d}(\tau, \tau') & G_{i\alpha;j\beta}^{(0)o}(\tau, \tau') \\ G_{i\alpha;j\beta}^{(0)o}(\tau', \tau) & G_{i\alpha;j\beta}^{(0)d}(\tau', \tau) \end{pmatrix} = \\
&- \left\langle \begin{pmatrix} b_{i\alpha}(\tau) - \langle b_{i\alpha}(\tau) \rangle_{(0)} \\ b_{i\alpha}^*(\tau) - \langle b_{i\alpha}^*(\tau) \rangle_{(0)} \end{pmatrix} \cdot [b_{j\beta}^*(\tau') - \langle b_{j\beta}^*(\tau') \rangle_{(0)}, b_{j\beta}(\tau') - \langle b_{j\beta}(\tau') \rangle_{(0)}] \right\rangle_{(0)}.
\end{aligned} \quad (\text{C.15})$$

Due to the possible off-diagonal long-range superfluid order, the Green's functions have a matrix form in the Nambu space.

Appendix D

Superfluid Order Parameter

In this part, we apply two methods to derive the superfluid order parameter in the cavity system by following Ref. [11, 265]. Naively, expectation values in the cavity system need to be identified with those on the impurity site, and in particular equal to the one on site 0 which we have chosen as impurity site: $\langle b_{i\alpha} \rangle = \langle b_{0\alpha} \rangle$, since in the original homogeneous system the expectation value is independent of the lattice position. In the self-consistent process in the section 4.3, however, sites at the edge of the cavity have one neighbor less compared to the impurity site, yielding an error of order $1/z$. For the Green's functions this process has no problem, because they already appear at subleading order in the effective action, but it leads to a relevant correction to the superfluid order parameter and turns out to be essential for quantitatively predictions for the phase boundary.

D.1 The first method: perturbation theory

Qualitatively, the sites j on which $\langle \hat{b}_\alpha \rangle$ is calculated have one neighbor less in the cavity system, because the impurity site has been taken out. Since this is a correction of order $O(1/z)$, this correction for higher dimensions can be implemented by means of first-order perturbation theory in the missing neighbor in $1/z$, which on the Bethe lattice gives rise to results for the superfluid-insulator transition very close to the numerically exact solution [8, 266].

We first rewrite the hopping term in the Anderson Hamiltonian

$$\begin{aligned}\hat{H}_0 &= -zt\phi(\hat{b}^\dagger + \hat{b}) \\ &= -t^*\phi(\hat{b}^\dagger + \hat{b}),\end{aligned}\tag{D.1}$$

where $t^* = zt$.

The corresponding Hamiltonian in the cavity system

$$\begin{aligned}\hat{H} &= -(z-1)t\phi(\hat{b}^\dagger + \hat{b}) \\ &= -t^*\phi(\hat{b}^\dagger + \hat{b}) + \frac{1}{z}t^*\phi(\hat{b}^\dagger + \hat{b}) \\ &= \hat{H}_0 + \hat{H}',\end{aligned}\tag{D.2}$$

where $\hat{H}' = t^* \phi (\hat{b}^\dagger + \hat{b})$. Here, $\lambda \equiv 1/z$ appears as the small parameter in the BDMFT, therefore time-independent perturbation theory can be used to obtain the superfluid order parameter in the cavity system.

$$\begin{aligned}
\phi_{new} &= \langle \tilde{0} | b | \tilde{0} \rangle = \left(\langle 0 | - \lambda \sum_{k \neq 0} c_{0k}^* \langle k | \right) \left(|0\rangle - \lambda \sum_{q \neq 0} c_{0q} |q\rangle \right) \\
&\approx \langle 0 | b | 0 \rangle - \lambda \sum_{k \neq 0} c_{0k}^* \langle k | b | 0 \rangle - \lambda \sum_{q \neq 0} \langle 0 | b | q \rangle c_{0q} \\
&= \langle 0 | b | 0 \rangle - \lambda \sum_{k \neq 0} \frac{\langle 0 | \hat{H}' | k \rangle \langle k | b | 0 \rangle}{E_k - E_0} - \lambda \sum_{q \neq 0} \frac{\langle 0 | b | q \rangle \langle q | \hat{H}' | 0 \rangle}{E_q - E_0} \\
&= \langle 0 | b | 0 \rangle - \lambda t^* \phi_{old} \sum_{k \neq 0} \frac{\langle 0 | b + b^\dagger | k \rangle \langle k | b | 0 \rangle + \langle 0 | b | q \rangle \langle q | b + b^\dagger | 0 \rangle}{E_k - E_0} \\
&= \langle 0 | b | 0 \rangle - \sum_{k \neq 0} \frac{\lambda t^* \phi_{old}}{E_k - E_0} \left(\langle 0 | b | k \rangle + \langle k | b | 0 \rangle \right)^2. \tag{D.3}
\end{aligned}$$

Therefore, the superfluid order parameter in the thermodynamical limit is:

$$\phi_{new} = \frac{1}{z} \sum_n e^{\beta E_n} \left[\langle n | b | n \rangle - \sum_{k \neq 0} \frac{\lambda t^* \phi_{old}}{E_k - E_n} \left(\langle n | b | k \rangle + \langle k | b | n \rangle \right)^2 \right]. \tag{D.4}$$

D.2 The second method

In this part, we will derive a closed formula without invoking the perturbation theory. To derive the order parameter in the cavity system, we assume that the bosonic fields at site j are to a source $J_{j\alpha}$. The partition integral thus depends on this source:

$$Z[J_{j\alpha}, J_{j\alpha}^*] = \int D[\mathbf{b}^*] D[\mathbf{b}] e^{-S[\mathbf{b}^*, \mathbf{b}] / \hbar + \int d\tau \{ b_{j\alpha}^* J_{j\alpha} + J_{j\alpha}^* b_{j\alpha} \}} \tag{D.5}$$

and the order parameter

$$\langle b_{j\alpha}(\tau) \rangle = \frac{\partial}{\partial J_{j\alpha}^*} \ln Z[J_{j\alpha}, J_{j\alpha}^*]. \tag{D.6}$$

In order to derive $Z_{\text{eff}}[J_{j\alpha}, J_{j\alpha}^*]$, we now present the cavity construction with the sources present. Here we only calculate the superfluid order parameter, and thus only keep the first order terms in the sources; if one calculates $1/z$ corrections to the Green's functions, one has to keep second order terms as well.

Defining the short-hand notation $S_J = \int d\tau \{b_{j\alpha}^* J_{j\alpha} + J_{j\alpha}^* b_{j\alpha}\}$, it yields:

$$\begin{aligned} Z_{\text{eff}}[J_{j\alpha}, J_{j\alpha}^*] &= \frac{1}{Z^{(0)}} \int D[\mathbf{b}^*] D[\mathbf{b}] e^{-S[\mathbf{b}^*, \mathbf{b}]/\hbar + S_J} \\ &= \frac{1}{Z^{(0)}} \int D[\mathbf{b}^*] D[\mathbf{b}] e^{-\frac{1}{\hbar}(S_0 + S^{(0)})} \left(1 - \frac{\Delta S}{\hbar} \right. \\ &\quad \left. + \frac{1}{2\hbar^2} (\Delta S)^2 + S_J - \frac{S_J \Delta S}{\hbar} + \dots \right). \end{aligned} \quad (\text{D.7})$$

Integrating out the fields in the cavity and re-exponentiating, we obtain:

$$\begin{aligned} Z_{\text{eff}}[J_{j\alpha}, J_{j\alpha}^*] &= \int D[\mathbf{b}_0^*] D[\mathbf{b}_0] e^{-\frac{S_0}{\hbar}} \left(1 - \frac{\langle \Delta S \rangle_{(0)}}{\hbar} \right. \\ &\quad \left. + \frac{1}{2\hbar^2} \langle (\Delta S)^2 \rangle_{(0)} + \langle S_J \rangle_{(0)} - \frac{\langle S_J \Delta S \rangle_{(0)}}{\hbar} + \dots \right) \end{aligned} \quad (\text{D.8})$$

$$= \int D[\mathbf{b}_0^*] D[\mathbf{b}_0] e^{-\frac{S_0^{\text{eff}}}{\hbar} + \langle S_J \rangle_{(0)} - \frac{1}{\hbar} (\langle S_J \Delta S \rangle_{(0)} - \langle S_J \rangle_{(0)} \langle \Delta S \rangle_{(0)})}. \quad (\text{D.9})$$

Here, the corresponding expectation values are given by:

$$\langle S_J \rangle_{(0)} = \int d\tau \{ \langle b_{j\alpha} \rangle_{(0)}^* J_{j\alpha} + J_{j\alpha}^* \langle b_{j\alpha} \rangle_{(0)} \}, \quad (\text{D.10})$$

$$\begin{aligned} \langle S_J \Delta S \rangle_{(0)} &= - \sum_{\langle 0i \rangle, \beta} \frac{t'_\beta}{z} \int d\tau d\tau' \left\{ \right. \\ &\quad J_{j\alpha}^*(\tau') \left(b_{0\beta}^*(\tau) \langle b_{i\beta}(\tau) b_{j\alpha}(\tau') \rangle_{(0)} + b_{0\beta}(\tau) \langle b_{i\beta}^*(\tau) b_{j\alpha}(\tau') \rangle_{(0)} \right) + \\ &\quad \left. J_{j\alpha}(\tau') \left(b_{0\beta}^*(\tau) \langle b_{i\beta}(\tau) b_{j\alpha}^*(\tau') \rangle_{(0)} + b_{0\beta}(\tau) \langle b_{i\beta}^*(\tau) b_{j\alpha}^*(\tau') \rangle_{(0)} \right) \right\}. \end{aligned} \quad (\text{D.11})$$

Combining this, the superfluid order parameter can be expressed as:

$$\langle b_{j\alpha}(\tau) \rangle = \frac{\partial}{\partial J_{j\alpha}^*} \ln Z_{\text{eff}}[J_{j\alpha}, J_{j\alpha}^*] \quad (\text{D.12})$$

$$\begin{aligned} &= \langle b_{j\alpha}(\tau) \rangle_{(0)} + \frac{1}{\hbar} \sum_{\langle 0i \rangle, \beta} \frac{t'_\beta}{z} \int d\tau' \left\{ \right. \\ &\quad \langle b_{0\beta}^*(\tau') \rangle \left(\langle b_{i\beta}(\tau') b_{j\alpha}(\tau) \rangle_{(0)} - \langle b_{i\beta}(\tau') \rangle_{(0)} \langle b_{j\alpha}(\tau) \rangle_{(0)} \right) + \\ &\quad \left. \langle b_{0\beta}(\tau') \rangle \left(\langle b_{i\beta}^*(\tau') b_{j\alpha}(\tau) \rangle_{(0)} - \langle b_{i\beta}^*(\tau') \rangle_{(0)} \langle b_{j\alpha}(\tau) \rangle_{(0)} \right) \right\}. \end{aligned} \quad (\text{D.13})$$

Using the Green's function, we obtain:

$$\begin{aligned} \langle b_{j\alpha}(\tau) \rangle &= \langle b_{j\alpha}(\tau) \rangle_{(0)} - \frac{1}{\hbar} \sum_{\langle 0i \rangle, \beta} \frac{t'_\beta}{z} \int d\tau' \left\{ \langle b_{0\beta}^*(\tau') \rangle G_{i\beta; j\alpha}^{(0)o}(\tau', \tau) + \right. \\ &\quad \left. \langle b_{0\beta}(\tau') \rangle G_{i\beta; j\alpha}^{(0)d}(\tau', \tau) \right\}. \end{aligned} \quad (\text{D.14})$$

The superfluid order parameter is independent of τ . Based on this, we can perform the integral over τ' and obtain:

$$\langle b_{j\alpha} \rangle = \langle b_{j\alpha} \rangle_{(0)} - \sum_{\langle 0i \rangle, \beta} \frac{t'_\beta}{z} \left(\langle b_{0\beta}^* \rangle G_{i\beta;j\alpha}^{(0)o}(\omega_n = 0) + \langle b_{0\beta} \rangle G_{i\beta;j\alpha}^{(0)d}(\omega_n = 0) \right),$$

which indeed yields a $1/z$ correction to $\langle b_{j\alpha} \rangle_{(0)}$ with respect to $\langle b_{j\alpha} \rangle$. We finally obtain

$$\begin{aligned} t_\alpha \sum_{\langle 0j \rangle} \langle b_{j\alpha} \rangle_{(0)} &= t_\alpha \sum_{\langle 0j \rangle} \left\{ \langle b_{j\alpha} \rangle + \sum_{\langle 0i \rangle, \beta} \frac{t'_\beta}{z} \left(\langle b_{0\beta}^* \rangle G_{i\beta;j\alpha}^{(0)o}(0) + \langle b_{0\beta} \rangle G_{i\beta;j\alpha}^{(0)d}(0) \right) \right\} \\ &= z t_\alpha \phi_\alpha + \sum_{\langle 0i \rangle, \langle 0j \rangle, \beta} \phi_\beta \frac{t'_\alpha t'_\beta}{z^2} \left\{ G_{i\beta;j\alpha}^{(0)o}(0) + G_{i\beta;j\alpha}^{(0)d}(0) \right\} \quad (\text{D.15}) \end{aligned}$$

$$= z t_\alpha \phi_\alpha + \sum_{\beta} \phi_\beta \left\{ \Delta_{\alpha\beta}^d(0) + \Delta_{\alpha\beta}^o(0) \right\} \quad (\text{D.16})$$

$$\equiv z t_\alpha \phi_\alpha^{\text{in}}, \quad (\text{D.17})$$

where $\phi_\alpha = \langle b_{j\alpha} \rangle$ (which we assumed to be real for the ground state) and expressed it in terms of diagonal and off-diagonal elements of the hybridization function at zero frequency. This constitutes the self-consistency equation for the superfluid order parameter.

Appendix E

Self-Energy

In this part, we will derive the formula for the self-energy and hybridization function for two-component lattice bosons, based on the equation of motion of the Green's function:

$$i\omega_n G_{A,B}(i\omega_n) + G_{[H,A],B}(i\omega_n) = \langle [A, B] \rangle. \quad (\text{E.1})$$

The Hamiltonian for the impurity Anderson model can be written as:

$$\begin{aligned} H = & \frac{1}{2} \sum_{\lambda\nu} U_{\lambda\nu} n_\nu (n_\lambda - \delta_{\lambda\nu}) - \sum_{\nu} n_\nu \mu_\nu - \sum_{\nu} z t_\nu (\phi_\nu^* b_\nu + \phi_\nu b_\nu^\dagger) \\ & + \sum_l \epsilon_l a_l^\dagger a_l + \sum_{\nu l} \left(V_{\nu l} (a_l^\dagger b_\nu + b_\nu^\dagger a_l) + W_{\nu l} (a_l b_\nu + b_\nu^\dagger a_l^\dagger) \right). \end{aligned} \quad (\text{E.2})$$

First, let us derive the Green's function $G_{b_\nu b_\lambda^\dagger}$. To obtain it, we first derive some commutation relations:

$$[H, b_\nu] = - \sum_l (V_{\nu l} a_l + W_{\nu l} a_l^\dagger) + \mu_\nu b_\nu - \sum_\lambda U_{\lambda\nu} b_\lambda^\dagger b_\nu b_\lambda + z t \phi_\nu, \quad (\text{E.3})$$

$$[H, a_l] = - \sum_{\nu} (V_{\nu l} b_\nu + W_{\nu l} b_\nu^\dagger) - \epsilon_l a_l, \quad (\text{E.4})$$

$$[H, a_l^\dagger] = \sum_{\nu} (V_{\nu l} b_\nu^\dagger + W_{\nu l} b_\nu) + \epsilon_l a_l^\dagger. \quad (\text{E.5})$$

Using these commutation relations given above, we obtain

$$(i\omega_n - \epsilon_l) G_{a_l b_\lambda^\dagger} = \sum_{\nu} (V_{\nu l} G_{b_\nu, b_\lambda^\dagger} + W_{\nu l} G_{b_\nu^\dagger, b_\lambda^\dagger}), \quad (\text{E.6})$$

$$(i\omega_n + \epsilon_l) G_{a_l^\dagger b_\lambda^\dagger} = - \sum_{\nu} (V_{\nu l} G_{b_\nu^\dagger, b_\lambda^\dagger} + W_{\nu l} G_{b_\nu, b_\lambda^\dagger}), \quad (\text{E.7})$$

$$\begin{aligned} (i\omega_n + \mu) G_{b_\nu, b_\lambda^\dagger} = & \sum_l (V_{\nu l} G_{a_l, b_\lambda^\dagger} + W_{\nu l} G_{a_l^\dagger, b_\lambda^\dagger}) + \sum_{\lambda'} U_{\nu\lambda'} G_{b_\lambda^\dagger, b_\nu b_{\lambda'}, b_\lambda^\dagger} \\ & - z t \phi_\nu G_{1, b_\lambda^\dagger} + \delta_{\nu\lambda}. \end{aligned} \quad (\text{E.8})$$

Inserting Eqs. (6) and (7) into (8), we then obtain

$$\begin{aligned}
(i\omega_n + \mu)G_{b_\nu, b_\lambda^\dagger} = & - \sum_{\nu'l} \left[\left(\frac{V_{\nu l} V_{\nu' l} G_{b_{\nu'}, b_\lambda^\dagger}}{\epsilon_l - i\omega_n} + \frac{V_{\nu l} W_{\nu' l} G_{b_{\nu'}, b_\lambda^\dagger}}{\epsilon_l - i\omega_n} \right) \right. \\
& + \left. \left(\frac{W_{\nu l} V_{\nu' l} G_{b_{\nu'}, b_\lambda^\dagger}}{\epsilon_l + i\omega_n} + \frac{W_{\nu l} W_{\nu' l} G_{b_{\nu'}, b_\lambda^\dagger}}{\epsilon_l + i\omega_n} \right) \right] \\
& + \sum_{\lambda'} U_{\nu\lambda'} G_{b_{\lambda'}, b_\nu b_{\lambda'}, b_\lambda^\dagger} - zt\phi_\nu G_{1, b_\lambda^\dagger} + \delta_{\nu\lambda} \quad (\text{E.9})
\end{aligned}$$

or rewrite it in an alternative form

$$\begin{aligned}
(i\omega_n + \mu)G_{b_\nu, b_\lambda^\dagger} = & - \sum_{\nu'l} \left[\left(\frac{V_{\nu l} V_{\nu' l}}{\epsilon_l - i\omega_n} + \frac{W_{\nu l} W_{\nu' l}}{\epsilon_l + i\omega_n} \right) G_{b_{\nu'}, b_\lambda^\dagger} \right. \\
& + \left. \left(\frac{V_{\nu l} W_{\nu' l}}{\epsilon_l - i\omega_n} + \frac{W_{\nu l} V_{\nu' l}}{\epsilon_l + i\omega_n} \right) G_{b_{\nu'}, b_\lambda^\dagger} \right] \\
& + \sum_{\lambda'} U_{\nu\lambda'} G_{b_{\lambda'}, b_\nu b_{\lambda'}, b_\lambda^\dagger} - zt\phi_\nu G_{1, b_\lambda^\dagger} + \delta_{\nu\lambda}, \quad (\text{E.10})
\end{aligned}$$

where $\Delta_{\nu\nu'}^{(1)} \equiv -\sum_l \left(\frac{V_{\nu l} V_{\nu' l}}{\epsilon_l - i\omega_n} + \frac{W_{\nu l} W_{\nu' l}}{\epsilon_l + i\omega_n} \right)$ and $\Delta_{\nu\nu'}^{(2)} \equiv -\sum_l \left(\frac{V_{\nu l} W_{\nu' l}}{\epsilon_l - i\omega_n} + \frac{W_{\nu l} V_{\nu' l}}{\epsilon_l + i\omega_n} \right)$ are hybridization functions.

Repeating the same process above, we obtain a similar equation for anomalous Green's function:

$$\begin{aligned}
(i\omega_n + \mu)G_{b_\nu, b_\lambda} = & - \sum_{\nu'l} \left[\left(\frac{V_{\nu l} V_{\nu' l} G_{b_{\nu'}, b_\lambda}}{\epsilon_l - i\omega_n} + \frac{V_{\nu l} W_{\nu' l} G_{b_{\nu'}, b_\lambda}}{\epsilon_l - i\omega_n} \right) \right. \\
& + \left. \left(\frac{W_{\nu l} V_{\nu' l} G_{b_{\nu'}, b_\lambda}}{\epsilon_l + i\omega_n} + \frac{W_{\nu l} W_{\nu' l} G_{b_{\nu'}, b_\lambda}}{\epsilon_l + i\omega_n} \right) \right] \\
& + \sum_{\lambda'} U_{\nu\lambda'} G_{b_{\lambda'}, b_\nu b_{\lambda'}, b_\lambda} - zt\phi_\nu G_{1, b_\lambda} \quad (\text{E.11})
\end{aligned}$$

or rewrite it in an alternative form

$$\begin{aligned}
(i\omega_n + \mu)G_{b_\nu, b_\lambda} = & - \sum_{\nu'l} \left[\left(\frac{V_{\nu l} V_{\nu' l}}{\epsilon_l - i\omega_n} + \frac{W_{\nu l} W_{\nu' l}}{\epsilon_l + i\omega_n} \right) G_{b_{\nu'}, b_\lambda} \right. \\
& + \left. \left(\frac{V_{\nu l} W_{\nu' l}}{\epsilon_l - i\omega_n} + \frac{W_{\nu l} V_{\nu' l}}{\epsilon_l + i\omega_n} \right) G_{b_{\nu'}, b_\lambda} \right] \\
& + \sum_{\lambda'} U_{\nu\lambda'} G_{b_{\lambda'}, b_\nu b_{\lambda'}, b_\lambda} - zt\phi_\nu G_{1, b_\lambda}, \quad (\text{E.12})
\end{aligned}$$

where $-\sum_l \left(\frac{V_{\nu l} V_{\nu' l}}{\epsilon_l - i\omega_n} + \frac{W_{\nu l} W_{\nu' l}}{\epsilon_l + i\omega_n} \right)$ and $-\sum_l \left(\frac{V_{\nu l} W_{\nu' l}}{\epsilon_l - i\omega_n} + \frac{W_{\nu l} V_{\nu' l}}{\epsilon_l + i\omega_n} \right)$ are hybridization functions.

We can also obtain the Green's functions of $G_{b_\nu^\dagger b_\lambda}$ and $G_{b_\nu^\dagger b_\lambda^\dagger}$. In total, we will have sixteen Green's functions for the Bose-Bose mixtures. However, only six of them are independent of each other. And we notice that it is very convenient to write the sixteen functions in the form of a matrix:

$$\left(i\omega_n \sigma_z + \mu - \mathbf{\Delta}(i\omega_n) \right) \mathbf{G}(i\omega_n) - \left[\mathbf{UF}(i\omega_n) - zt\phi\mathbf{G}_1(i\omega_n) \right] = \mathbf{I}, \quad (\text{E.13})$$

where $\mathbf{\Delta} \equiv \begin{pmatrix} \Delta_{\lambda\nu}^{(1)} & \Delta_{\lambda\nu}^{(2)} \\ (\Delta_{\lambda\nu}^{(2)})^* & (\Delta_{\lambda\nu}^{(1)})^* \end{pmatrix}$, $\mathbf{UF} \equiv U_{\nu\lambda'}$ $\begin{pmatrix} G_{b_\lambda^\dagger, b_\nu, b_{\lambda'}, b_\lambda^\dagger} & G_{b_\lambda^\dagger, b_\nu, b_{\lambda'}, b_\lambda} \\ G_{b_\lambda^\dagger, b_\nu^\dagger, b_{\lambda'}, b_\lambda^\dagger} & G_{b_\lambda^\dagger, b_\nu^\dagger, b_{\lambda'}, b_\lambda} \end{pmatrix}$, and $\phi\mathbf{G}_1 \equiv \begin{pmatrix} \phi_\nu G_{1, b_\lambda^\dagger} & \phi_\nu G_{1, b_\lambda} \\ \phi_\nu^* G_{1, b_\lambda^\dagger} & \phi_\nu^* G_{1, b_\lambda} \end{pmatrix}$. Then the impurity self-energy can be written as:

$$\mathbf{\Sigma}(i\omega_n) = \left[\mathbf{UG}(i\omega_n) - zt\phi\mathbf{G}_1(i\omega_n) \right] \mathbf{G}^{-1}(i\omega_n). \quad (\text{E.14})$$

This method based on the equations of motion for the Green's function is an accurate way to determine the self-energy. There is also another way to calculate the self energy, which is based on the local Dyson equation. In that case, we can use the Weiss function to derive the self energy: first we can determine the Weiss function from Anderson model; secondly, we can also determine the Weiss function from lattice model using the Dyson equation derived from effective action:

$$\begin{aligned} \mathcal{G}^{-1} &= i\omega_n \sigma_z + \mu - \mathbf{\Delta} \\ &= \mathbf{\Sigma}_{\text{imp}}(i\omega_n) + \mathbf{G}_{\text{imp}}^{-1}(i\omega_n) \\ &= \mathbf{\Sigma}_{\text{lat}}(i\omega_n) + \mathbf{G}_{\text{lat}}^{-1}(i\omega_n). \end{aligned} \quad (\text{E.15})$$

Using the identity of the lattice self-energy and the impurity self-energy, the latter has this form:

$$\mathbf{\Sigma}_{\text{imp}}(i\omega_n) = \mathbf{\Sigma}_{\text{lat}}(i\omega_n) = i\omega_n \sigma_z + \mu - \mathbf{\Delta} - \mathbf{G}_{\text{imp}}^{-1}(i\omega_n). \quad (\text{E.16})$$

In principle, we can use both methods to obtain the local self-energy after diagonalization for the Anderson model. After convergence, these self-energies obtained from the two methods should be the identical.

Appendix F

Lattice Green's Function

In this part, we will derive the non-interacting lattice Green's function in real space. For the non-interacting Bose-Hubbard model, the Hamiltonian is given by:

$$\hat{H} = - \sum_{\langle i,j \rangle, \nu} t_{ij,\nu} \hat{b}_{i\nu}^\dagger \hat{b}_{j\nu} - \sum_{i,\nu} \mu \hat{n}_{i\nu}. \quad (\text{F.1})$$

We can use the equation of motion of the Green's function to derive the formula for the non-interacting case. Here we just derive the Green's functions on the diagonal (the diagonal terms are also a matrix formed by sixteen Green's functions at each site). Using the commutation relation

$$[\hat{H}, \hat{b}_{i\nu}] = \sum_{\langle i,j \rangle} t_{ij,\nu} \hat{b}_{j\nu} + \mu \hat{b}_{i\nu}, \quad (\text{F.2})$$

the non-interacting Green's function can be written as:

$$(\mu + iw_n) G_{b_{i\nu} b_{j\mu}^\dagger} + \sum_{\langle i,j \rangle} t_{ij',\nu} G_{b_{j'\nu} b_{j\mu}^\dagger} = 1. \quad (\text{F.3})$$

By rewriting the Green's functions in a matrix form with site-indexed elements, we obtain

$$\mathbf{G}_{b_\nu b_\mu^\dagger}^{-1} = (\mu + iw_n \sigma_z) + \mathbf{t}, \quad (\text{F.4})$$

where \mathbf{t} is a matrix arising from the hopping term. If we include periodic boundary conditions, the matrix has four (six) more terms for 2D square (3D cubic) optical lattice. Note that $\mathbf{G}_{b_\nu b_\mu}$ and $\mathbf{G}_{b_\nu^\dagger b_\mu^\dagger}$ should be equal to zero, since $[\hat{b}_\nu, \hat{b}_\mu] = 0$ or $[\hat{b}_\nu^\dagger, \hat{b}_\mu^\dagger] = 0$

After obtaining the matrix of Green's functions for each site, we can invert the matrix and the elements on the diagonal yield the local non-interacting Green's functions for each site.

Bibliography

- [1] C. J. Pethick and H. Smith, *Bose-Einstein Condensation in Dilute Gases*, (Cambridge University Press, Cambridge, 2008).
- [2] Inouye, M. R. Andrews, J. Stenger, H. J. Miesner, D. M. Stamper-Kurn and W. Ketterle, *Observation of Feshbach resonances in a Bose-Einstein condensate*, Nature (London) **392**, 151 (1998).
- [3] M. Greiner, O. Mandel, T. Esslinger, T. W. Hänsch and I. Bloch, *Quantum phase transition from a superfluid to a Mott insulator in a gas of ultracold atoms*, Nature (London) **415**, 39 (2002).
- [4] I. Bloch, J. Dalibard and W. Zwerger, *Many-body physics with ultracold gases*, Rev. Mod. Phys. **80**, 885 (2008).
- [5] M. P. A. Fisher, P. B. Weichman, G. Grinstein and D. S. Fisher, *Boson localization and the superfluid-insulator transition*, Phys. Rev. B **40**, 546 (1989).
- [6] H. A. Bethe, *On the theory of metals. I. Eigenvalues and eigenfunctions of the linear atom chain*, Z. Phys. **71**, 205 (1931).
- [7] K. Byczuk and D. Vollhardt, *Correlated bosons on a lattice: Dynamical mean-field theory for Bose-Einstein condensed and normal phases*, Phys. Rev. B **77**, 235106 (2008).
- [8] A. Hubener, M. Snoek and W. Hofstetter, *Magnetic phases of two-component ultracold bosons in an optical lattice*, Phys. Rev. B **80**, 245109 (2009).
- [9] W.-J. Hu and N.-H. Tong, *Dynamical mean-field theory for the Bose-Hubbard model*, Phys. Rev. B **80**, 245110 (2009).
- [10] P. Anders, E. Gull, L. Pollet, M. Troyer and P. Werner, *Dynamical mean field solution of the Bose-Hubbard model*, Phys. Rev. Lett. **105**, 096402 (2010).
- [11] M. Snoek and W. Hofstetter, *Bosonic dynamical mean-field theory*, arXiv:1007.5223.

-
- [12] Y.-Q. Li, M. R. Bakhtiari, L. He and W. Hofstetter, *Tunable anisotropic magnetism in trapped two-component Bose gases*, Phys. Rev. B **84**, 144411 (2011).
- [13] Y.-Q. Li, R. Bakhtiari, L. He and W. Hofstetter, *Pomeranchuk effect and spin-gradient cooling of Bose-Bose mixtures in an optical lattice*, Phys. Rev. A **85**, 023624 (2012).
- [14] G. R. Stewart, *Heavy-fermion systems*, Rev. Mod. Phys. **56**, 755 (1984).
- [15] N. F. Mott, *Metal-Insulator Transitions*, second edition (Taylor & Francis, London, 1990).
- [16] A. Auerbach, *Interacting Electron and Quantum Magnetism*, (Springer-Verlag, New York, 1994).
- [17] E. P. Gross, *Structure of a quantized vortex in boson systems*, Nuovo Cimento **20**, 454 (1961).
- [18] L. P. Pitaevskii, *Vortex lines in an imperfect Bose gas*, Sov. Phys. JETP **13**, 451 (1961).
- [19] W. C. Stwalley, *Stability of spin-aligned hydrogen at low temperatures and high magnetic fields: new field-dependent scattering resonances and predissociations*, Phys. Rev. Lett. **37**, 1628 (1976).
- [20] Ph. Courteille, R. S. Freeland, D. J. Heinzen, F. A. van Abeelen and B. J. Verhaar, *Observation of a Feshbach resonance in cold atom scattering*, Phys. Rev. Lett. **81**, 69 (1998).
- [21] J. T. M. Walraven, *Thermodynamic and collisional properties of trapped atomic gases*, (Bachelior course in University of Amsterdam, 2009).
- [22] U. Schollwöck, *Quantum magnetism*, Lecture Notes in Physics Vol. 645 (Springer, Berlin, 2004).
- [23] C. Trefzger, C. Menotti, B. Capogrosso-Sansone and M. Lewenstein, *Ultracold dipolar gases in optical lattices*, J. Phys. B: At. Mol. Opt. Phys. **44**, 193001 (2011).
- [24] K. De'Bell, A. B. Maclsaac and J. P. Whitehead, *Dipolar effects in magnetic thin films and quasi-two-dimensional systems*, Rev. Mod. Phys. **72**, 225 (2000).
- [25] K. Baumann, C. Guerlin, F. Brennecke and T. Esslinger, *The Dicke quantum phase transition in a superfluid gas coupled to an optical cavity*, Nature (London) **464**, 1301 (2010).

- [26] A. Griesmaier, J. Werner, S. Hensler, J. Stuhler and T. Pfau, *Bose-Einstein condensation of chromium*, Phys. Rev. Lett. **94**, 160401 (2005).
- [27] K. K. Ni, S. Ospelkaus, M. H. G. de Miranda, A. Peér, B. Neyenhuis, J. J. Zirbel, S. Kotochigova, P. S. Julienne, D. S. Jin and J. Ye, *A high phase-space-density gas of polar molecules*, Science **322**, 231 (2008).
- [28] T. H. Maiman, *Stimulated optical radiation in ruby*, Nature (London) **187**, 493 (1960).
- [29] W. D. Phillips, *Nobel Lecture: Laser cooling and trapping of neutral atoms*, Rev. Mod. Phys. **70**, 721 (1998).
- [30] S. Chu, *Nobel Lecture: The manipulation of neutral particles*, Rev. Mod. Phys. **70**, 685 (1998).
- [31] C. N. Cohen-Tannoudji, *Nobel Lecture: Manipulating atoms with photons*, Rev. Mod. Phys. **70**, 707 (1998).
- [32] E. A. Cornell and C. E. Wieman, *Nobel Lecture: Bose-Einstein condensation in a dilute gas, the first 70 years and some recent experiments*, Rev. Mod. Phys. **74**, 875 (2002).
- [33] W. Ketterle, *Nobel lecture: When atoms behave as waves: Bose-Einstein condensation and the atom laser*, Rev. Mod. Phys. **74**, 1131 (2002).
- [34] F. Dalfovo, S. Giorgini, L. P. Pitaevskii and S. Stringari, *Theory of Bose-Einstein condensation in trapped gases*, Rev. Mod. Phys. **71**, 463 (1999).
- [35] A. J. Leggett, *Bose-Einstein condensation in the alkali gases: Some fundamental concepts*, Rev. Mod. Phys. **73**, 307 (2001).
- [36] T. Nikuni, M. Oshikawa, A. Oosawa and H. Tanaka, *Bose-Einstein condensation of dilute magnons in TlCuCl_3* , Phys. Rev. Lett. **84**, 5868 (2000).
- [37] J. Kasprzak, M. Richard, S. Kundermann, A. Baas, P. Jeambrun, J. M. J. Keeling, F. M. Marchetti, M. H. Szymańska, R. André, J. L. Staehli, V. Savona, P. B. Littlewood, B. Deveaud and L. S. Dang, *Bose-Einstein condensation of exciton polaritons*, Nature (London) **443**, 409 (2006).
- [38] J. Klaers, J. Schmitt, F. Vewinger and M. Weitz, *Bose-Einstein condensation of photons in an optical microcavity*, Nature (London) **468**, 545 (2010).
- [39] S. Giorgini, L. P. Pitaevskii and S. Stringari, *Theory of ultracold atomic Fermi gases*, Rev. Mod. Phys. **80**, 1215 (2008).
- [40] B. De Marco and D. C. Jin, *Onset of Fermi degeneracy in a trapped atomic gas*, Science **285**, 1703 (1999).

- [41] S. B. Papp, J. M. Pino, R. J. Wild, S. Ronen, C. E. Wieman, D. S. Jin and E. A. Cornell, *Bragg spectroscopy of a strongly interacting ^{85}Rb Bose-Einstein condensate*, Phys. Rev. Lett. **101**, 135301 (2008).
- [42] S. Giorgini, L. P. Pitaevskii and S. Stringari, *Theory of ultracold atomic Fermi gases*, Rev. Mod. Phys. **80**, 1215 (2008).
- [43] K. M. Jones, E. Iesinga, P. D. Lett and P. S. Julienne, *Ultracold photoassociation spectroscopy: Long-range molecules and atomic scattering*, Rev. Mod. Phys. **78**, 483 (2006).
- [44] T. Köler and K. Góal and P. S. Julienne, *Production of cold molecules via magnetically tunable Feshbach resonances*, Rev. Mod. Phys. **78**, 1311 (2006).
- [45] C. Chin, R. Grimm, P. Julienne and E. Tiesinga, *Feshbach resonances in ultracold gases*, Rev. Mod. Phys. **82**, 1225 (2010).
- [46] I. Bloch, *Ultracold quantum gases in optical lattices*, Nat. Phys. **1**, 23 (2005).
- [47] U. Schneider, L. Hackermüller, S. Will, Th. Best, I. Bloch, T. A. Costi, R. W. Helmes, D. Rasch and A. Rosch, *Metallic and insulating phases of repulsively interacting fermions in a 3D optical lattice*, Science **322**, 1520 (2008).
- [48] R. Jördens, N. Strohmaier, K. Günter, H. Moritz and T. Esslinger, *A Mott insulator of fermionic atoms in an optical lattice*, Nature (London) **455**, 204 (2008).
- [49] T. Esslinger, *Fermi-Hubbard physics with atoms in an optical lattice*, Ann. Rev. Condens. Matter Phys. **1**, 129 (2010).
- [50] D. McKay and B. DeMarco, *Cooling in strongly correlated optical lattices: prospects and challenges*, Rep. Prog. Phys. **74**, 054401 (2011).
- [51] S. Fölling, S. Trotzky, P. Cheinet, M. Feld, R. Saers, A. Widera, T. Müller and I. Bloch, *Direct observation of second order atom tunnelling*, Nature (London) **448**, 1029 (2007).
- [52] S. Trotzky, P. Cheinet, S. Fölling, M. Field, U. Schnorrberger, A. M. Rey, A. Polovnikov, E. A. Demler, M.D. Lukin and I. Bloch, *Time-resolved observation and control of superexchange interactions with ultracold atoms in optical lattices*, Science **319**, 295 (2008).
- [53] P. Medley, D. M. Weld, H. Miyake, D. E. Pritchard and W. Ketterle, *Spin gradient demagnetization cooling of ultracold atoms*, Phys. Rev. Lett. **106**, 195301 (2011).

- [54] T. Gericke, P. Würtz, D. Reitz, T. Langen and H. Ott, *High-resolution scanning electron microscopy of an ultracold quantum gas*, Nat. phys. **4**, 949 (2008).
- [55] W. S. Bakr, J. I. Gillen, A. Peng, S. Fölling and M. Greiner, *A quantum gas microscope for detecting single atoms in a Hubbard-regime optical lattice*, Nature (London) **462**, 74 (2009).
- [56] J. F. Sherson, C. Weitenberg, M. Endres, M. Cheneau, I. Bloch and S. Kuhr, *Single-atom-resolved fluorescence imaging of an atomic Mott insulator*, Nature (London) **467**, 68 (2010).
- [57] T. Lahaye, Tobias Koch, B. Fröhlich, M. Fattori, J. Metz, A. Griesmaier, S. Giovanazzi and T. Pfau, *Strong dipolar effects in a quantum ferrofluid*, Nature (London) **448**, 672 (2007).
- [58] M. Lu, N. Q. Burdick, S. H. Youn and B. L. Lev, *A strongly dipolar Bose-Einstein condensate of dysprosium*, Phys. Rev. Lett. **107**, 190401 (2011).
- [59] R. Heidemann, U. Raitzsch, V. Bendkowsky, B. Butscher, R. Löw and T. Pfau, *Rydberg excitation of Bose-Einstein condensates*, Phys. Rev. Lett. **100**, 033601 (2008).
- [60] H. Mabuchi, Q. A. Turchette, M. S. Chapman and H. J. Kimble, *Real-time detection of individual atoms falling through a high-finesse optical cavity*, Opt. Lett. **21**, 1393 (1996).
- [61] G. Hechenblaikner, M. Gangl, P. Horak and H. Ritsch, *Cooling an atom in a weakly driven high-Q cavity*, Phys. Rev. A **58**, 3030 (1998).
- [62] S. J. van Enk, J. McKeever, H. J. Kimble and J. Ye, *Cooling of a single atom in an optical trap inside a resonator*, Phys. Rev. A **64**, 013407 (2001).
- [63] P. Maunz, T. Puppe, I. Schuster, N. Syassen, P. W. H. Pinkse and G. Rempe, *Cavity cooling of a single atom*, Nature (London) **428**, 50 (2004).
- [64] J. Ye, D. W. Vernooy and H. J. Kimble, *Trapping of single atoms in cavity QED*, Phys. Rev. Lett. **83**, 4987 (1999).
- [65] P. W. H. Pinkse, T. Fischer, P. Maunz and G. Rempe, *Trapping an atom with single photons*, Nature (London) **404**, 365 (2000).
- [66] J. Larson, S. Fernandez-Vidal, G. Morigi and M. Lewenstein, *Quantum stability of Mott-insulator states of ultracold atoms in optical resonators*, New J. Phys. **10**, 045002 (2008).

- [67] P. Domokos and H. Ritsch, *Collective cooling and self-organization of atoms in a cavity*, Phys. Rev. Lett. **89**, 253003 (2002).
- [68] A. T. Black, H. W. Chan and V. Vuletić, *Observation of collective friction forces due to spatial self-organization of atoms: from Rayleigh to Bragg scattering*, Phys. Rev. Lett. **91**, 203001 (2003).
- [69] P. Treutlein, D. Hunger, S. Camerer, T. W. Hänsch and J. Reichel, *Bose-Einstein condensate coupled to a nanomechanical resonator on an atom chip*, Phys. Rev. Lett. **99**, 140403 (2007).
- [70] Y. Colombe, T. Steinmetz, G. Dubois, F. Linke, D. Hunger and J. Reichel, *Strong atom-field coupling for Bose-Einstein condensates in an optical cavity on a chip*, Nature (London) **450**, 272 (2007).
- [71] S. Slama, G. Lremz, S. Bux, G. Zimmermann and P. W. Courteille, *Cavity-enhanced superradiant Rayleigh scattering with ultracold and Bose-Einstein condensed atoms*, Phys. Rev. A **75**, 063620 (2007).
- [72] T. Bourdel, T. Donner, S. Ritter, A. Öttl, M. Köhl and T. Esslinger, *Cavity QED detection of interfering matter waves*, Phys. Rev. A **73**, 043602 (2006).
- [73] I. Bloch, *Ultracold quantum gases in optical lattices*, Nat. Phys. **1**, 23 (2005).
- [74] R. Grimm, M. Weidemüller and Y. B. Ovchinnikov, *Optical dipole traps for neutral atoms*, Adv. At. Mol. Opt. Phys. **42**, 95 (2000).
- [75] I. Bloch and M. Greiner, *Exploring quantum matter with ultracold atoms in optical lattices*, Adv. At. Mol. Phys. **52**, 1 (2005).
- [76] D. McKay and B. DeMarco, *Thermometry with spin-dependent lattices*, New J. Phys. **12**, 055013 (2010).
- [77] D. Jaksch, H.-J. Briegel, J. I. Cirac, C. W. Gardiner and P. Zoller, *Entanglement of atoms via cold controlled collisions*, Phys. Rev. Lett. **82**, 1975 (1999).
- [78] B. Gadway, D. Pertot, R. Reimann and D. Schneble, *Superfluidity of interacting bosonic mixtures in optical lattices*, Phys. Rev. Lett. **105**, 045303 (2010).
- [79] J. E. Jones, *On the determination of molecular fields*, Proc. R. Soc. Lond. A **106**, 463 (1924).
- [80] H. T. C. Stoof, J. M. V. A. Koelman and B. J. Verhaar, *Spin-exchange and dipole relaxation rates in atomic hydrogen: Rigorous and simplified calculations*, Phys. Rev. B **38**, 4688 (1988).

-
- [81] A. Widera, F. Gerbier, S. Fölling, T. Gericke, O. Mandel and I. Bloch, *Coherent collisional spin dynamics in optical lattices*, Phys. Rev. Lett. **95**, 190405 (2005).
- [82] E. A. Burt, R. W. Ghrist, C. J. Myatt, M. J. Holland, E. A. Cornell and C. E. Wieman, *Coherence, correlations, and collisions: what one learns about Bose-Einstein condensates from their decay*, Phys. Rev. Lett. **79**, 337 (1997).
- [83] J. P. Gordon and A. Ashkin, *Motion of atoms in a radiation trap*, Phys. Rev. A **21**, 1606 (1980).
- [84] F. Gerbier and Y. Castin, *Heating rates for an atom in a far-detuned optical lattice*, Phys. Rev. A **82**, 013615 (2010).
- [85] P. Pichler, A. J. Daley and P. Zoller, *Nonequilibrium dynamics of bosonic atoms in optical lattices: decoherence of many-body states due to spontaneous emission*, Phys. Rev. A **82**, 063605 (2010).
- [86] T. A. Savard, K. M. O'Hara and J. E. Thomas, *Laser-noise-induced heating in far-off resonance optical traps*, Phys. Rev. A **56**, R1095 (1997).
- [87] S. Bali, K. M. O'Hara, M. E. Gehm, S. R. Granade and J. E. Thomas, *Quantum-diffractive background gas collisions in atom-trap heating and loss*, Phys. Rev. A **60**, R29 (1999).
- [88] S. Trotzky, L. Pollet, F. Gerbier, U. Schnorrberger, I. Bloch, N.V. Prokof'ev, B. Svistunov and M. Troyer, *Suppression of the critical temperature for superfluidity near the Mott transition: validating a quantum simulator*, Nat. Phys. **6**, 998 (2010).
- [89] J. Hubbard, *Electron correlations in narrow energy bands*, Proc. Roy. Soc. London Ser. A **276**, 238 (1963).
- [90] M. C. Gutzwiller, *Effect of correlation on the ferromagnetism of transition metals*, Phys. Rev. Lett. **10**, 159 (1963).
- [91] J. Kanamori, *Electron correlation and ferromagnetism of transition metals*, Prog. Theor. Phys. **30**, 275 (1963).
- [92] Y. A. Uzyumov, *Hubbard model and strong correlations*, Phys.-Usp. **38**, 385 (1995).
- [93] H. Tasaki, *The Hubbard model - an introduction and selected rigorous results*, J. Phys.: Condens. Matter **10**, 4353 (1998).
- [94] F. H. L. Essler, H. Frahm, F. Göhmann, A. Klümper and V. E. Korepin, *The One Dimensional Hubbard Model*, (Cambridge University Press, Cambridge, 2005).

- [95] D. Jaksch, C. Bruder, J. I. Cirac, C. W. Gardiner and P. Zoller, *Cold bosonic atoms in optical lattices*, Phys. Rev. Lett. **81**, 3108 (1998).
- [96] T. Stöferle, H. Moritz, C. Schori, M. Köhl and T. Esslinger, *Transition from a strongly interacting 1D superfluid to a Mott insulator*, Phys. Rev. Lett. **92**, 130403 (2004).
- [97] I. B. Spielman, W. D. Phillips and J. V. Porto, *Mott-insulator transition in a two-dimensional atomic Bose gas*, Phys. Rev. Lett. **98**, 080404 (2007).
- [98] I. B. Spielman, W. D. Phillips and J. V. Porto, *Condensate fraction in a 2D Bose gas measured across the Mott-insulator transition*, Phys. Rev. Lett. **100**, 120402 (2008).
- [99] H. T. C. Stoof, K. B. Gubbels and D. B. M. Dickerschied, *Ultracold Quantum Field*, (Springer, Dordrecht, 2009).
- [100] C. J. Myatt, E. A. Burt, R. W. Ghrist, E. A. Cornell and C. E. Wieman, *Production of two overlapping Bose-Einstein condensates by sympathetic cooling*, Phys. Rev. Lett. **78**, 586 (1997).
- [101] D. M. Stamper-Kurn, M. R. Andrews, A. P. Chikkatur, S. Inouye, H.-J. Miesner, J. Stenger and W. Ketterle, *Optical confinement of a Bose-Einstein condensate*, Phys. Rev. Lett. **80**, 2027 (1998).
- [102] J. Stenger, S. Inouye, D. M. Stamper-Kurn, H.-J. Miesner, A. P. Chikkatur and W. Ketterle, *Spin domains in ground-state Bose-Einstein condensates*, Nature (London) **396**, 345 (1998).
- [103] K. Bongs and K. Sengstock, *Physics with coherent matter waves*, Rep. Prog. Phys. **67**, 907 (2004).
- [104] M. Lewenstein, A. Sanpera, V. Ahufinger, B. Damski, A. Sen and U. Sen, *Ultracold atomic gases in optical lattices: mimicking condensed matter physics and beyond*, Adv. Phys. **56**, 243 (2007).
- [105] M. Ueda and Y. Kawaguchi, *Spinor Bose-Einstein condensates*, arXiv:1001.2072.
- [106] J. Catani, L. Desarlo, G. Baronitini, F. Minardi and M. Inguscio, *Degenerate Bose-Bose mixture in a three-dimensional optical lattice*, Phys. Rev. A **77**, 011603(R) (2008).
- [107] D. M. Weld, P. Medley, H. Miyake, D. Hucul, D. E. Pritchard and W. Ketterle, *Spin gradient thermometry for ultracold atoms in optical lattices*, Phys. Rev. Lett. **103**, 245301 (2009).
- [108] Tin-Lun Ho, *Spinor Bose Condensates in optical traps*, Phys. Rev. Lett. **81**, 742 (1998).

-
- [109] C. K. Law, H. Pu and N. P. Bigelow, *Quantum spins mixing in spinor Bose-Einstein condensates*, Phys. Rev. Lett. **81**, 5257 (1998).
- [110] J. K. Asbóth, P. Domokos and H. Ritsch, *Correlated motion of two atoms trapped in a single-mode cavity field*, Phys. Rev. A **70**, 013414 (2004).
- [111] J. K. Asbóth, H. Ritsch and P. Domokos, *Collective excitations and instability of an optical lattice due to unbalanced pumping*, Phys. Rev. Lett. **98**, 203008 (2007).
- [112] E. T. Jaynes and F. W. Cummings, *Comparison of quantum and semi-classical radiation theories with application to the beam maser*, Proc. IEEE **51**, 89 (1963).
- [113] C. Maschler, I. B. Mekhov and H. Ritsch, *Ultracold atoms in optical lattices generated by quantized light fields*, Eur. Phys. J. D **46**, 545 (2008).
- [114] C. Maschler and H. Ritsch, *Cold atom dynamics in a quantum optical lattice potential*, Phys. Rev. Lett. **95**, 260401, (2005).
- [115] J. Larson, B. Damski, G. Morigi and M. Lewenstein, *Mott-insulator states of ultracold atoms in optical resonators*, Phys. Rev. Lett **100**, 050401 (2008).
- [116] D. Nagy, G. Szirmai and P. Domokos, *Self-organization of a Bose-Einstein condensate in an optical cavity*, Eur. Phys. J. D **48**, 127 (2008).
- [117] L. He, *Ground state and dynamics of ultracold dipolar fermionic gases*, PhD thesis, Beijing (2009).
- [118] J. Hubbard, *Electron correlations in narrow energy bands. II. the degenerate band case*, Proc. Roy. Soc. London A **277**, 237 (1964).
- [119] J. Hubbard, *Electron correlations in narrow energy bands. III. an improved solution*, Proc. Roy. Soc. London A **281**, 401 (1964).
- [120] E. H. Lieb and F. Y. Wu, *Absence of Mott transition in an exact solution of the short-range, one-band model in one dimension*, Phys. Rev. Lett. **20**, 1445 (1968).
- [121] B. Sutherland, *An introduction to the Bethe ansatz in exactly solvable problems in condensed matter and relativistic field theory*, ed. S. B. Shasstry, S. S. Jha, V. Singh, (Springer-Verlag, 1985).
- [122] T. Koma, *An extension of the thermal Bethe ansatz - one-dimensional Hubbard model*, Prog. Theor. Phys. **83**, 655 (1990).

-
- [123] T. Arai, M. H. Cohen and M. P. Tosi, *Functional-derivative study of the Hubbard model. I. Perturbation method and first-order approximation*, Phys. Rev. B **15**, 1817 (1977).
- [124] V. M. Zharkov, *Perturbation theory and the exchange interaction in the one-dimensional Hubbard model*, Theoret. and Math. Phys. **46**, 88 (1981).
- [125] G. G. Batrouni, R. T. Scalettar and G. T. Zimanyi, *Quantum critical phenomena in one-dimensional Bose systems*, Phys. Rev. Lett. **65**, 1765 (1990).
- [126] K. Freericks and H. Monien, *Phase diagram of the Bose-Hubbard model*, Europhys. Lett. **26**, 545 (1994).
- [127] W. Metzner and D. Vollhardt, *Correlated lattice fermions in $d = \infty$ dimensions*, Phys. Rev. Lett. **62**, 324 (1989).
- [128] A. Georges and G. Kotliar, *Hubbard model in infinite dimensions*, Phys. Rev. B **45**, 6479 (1992).
- [129] A. Georges, G. Kotliar, W. Krauth and M. J. Rozenberg, *Dynamical mean-field theory of strongly correlated fermion systems and the limit of infinite dimensions*, Rev. Mod. Phys. **68**, 13 (1996).
- [130] S. Sachdev, *Quantum magnetism and criticality*, Nat. Phys. **4**, 173 (2008).
- [131] S. Sachdev, *Quantum Phase Transitions*, (Cambridge University Press, Cambridge, 2011).
- [132] B. DeMarco, *An atomic view of quantum phase transitions*, Science **329**, 523 (2010).
- [133] H. Bruus and K. Flensberg, *Many-body Quantum Theory in Condensed Matter Physics: an Introduction*, (Oxford University Press, Oxford, 2004).
- [134] K. Sheshadri, H. R. Krishnamurthy, R. Pandit and T. V. Ramakrishnan, *Superfluid and insulating phases in an interacting-boson model: mean-field theory and the RPA*, Euro. Phys. Lett. **22**, 257 (1993).
- [135] M. C. Gutzwiller, *Correlation of electrons in a narrow s band*, Phys. Rev. **137**, A1726 (1965).
- [136] T. Ogawa, K. Kanda and T. Matsubara, *Gutzwiller approximation for antiferromagnetism in hubbard model*, Prog. Theor. Phys. **53**, 614 (1975).
- [137] B. Edegger, V. N. Muthukumar and C. Gros, *Gutzwiller-RVB theory of high temperature superconductivity: Results from renormalized mean-field theory and variational Monte Carlo calculations*, Adv. in Phys. **56**, 927 (2007).

-
- [138] D. S. Rokhsar and B. G. Kotliar, *Gutzwiller projection for bosons*, Phys. Rev. B, **44**, 10328 (1991).
- [139] W. Zwerger, *Mott-Hubbard transition of cold atoms in optical lattices*, Journal of Optics B **5**, 9 (2003).
- [140] P. Kapitza, *Viscosity of liquid helium below the λ -point*, Nature (London) **141**, 74 (1938).
- [141] J. F. Allen and A. D. Misener, *Flow of liquid helium II*, Nature (London) **141**, 75 (1938).
- [142] L. Landau, *Theory of the superfluidity of helium II*, Phys. Rev. **60**, 356 (1941).
- [143] F. London, *The λ -phenomenon of liquid helium and the Bose-Einstein degeneracy*, Nature (London) **141**, 643 (1938).
- [144] U. Bissbort, *Stochastic mean field theory for the disordered Bose-Hubbard model*, Master Thesis, Frankfurt (2007).
- [145] J. H. de Boer and E. J. W. Verway, *Semi-conductors with partially and with completely filled 3d-lattice bands*, Proc. Phys. Soc. Lond. **49**, 59 (1937).
- [146] N. F. Mott and R. Peierls, *Discussion of the paper by de Boer and Verwey*, Proc. Phys. Soc. Lond. **49**, 72 (1937);
- [147] N. F. Mott, *The basis of the electron theory of metals, with special reference to the transition metals*, Proc. Phys. Soc. Lond. A **62**, 416 (1949).
- [148] N. F. Mott, *On the transition to metallic conduction in semiconductors*, Can. J. Phys. **34**, 1356 (1956); *The transition to the metallic state*, Philos. Mag. **6**, 287 (1961).
- [149] M. Imada, A. Fujimori and Y. Tokura, *Metal-insulator transitions*, Rev. Mod. Phys. **70**, 1039 (1998).
- [150] F. Gebhard, *The Mott Metal-Insulator Transition*, (Springer, Berlin, 1997).
- [151] L.-M. Duan, E. Demler and M. D. Lukin, *Controlling spin exchange interactions of ultracold atoms in optical lattices*, Phys. Rev. Lett. **91**, 090402 (2003).
- [152] E. Altman, W. Hofstetter, E. Demler and M. D. Lukin, *Phase diagram of two-component bosons on an optical lattice*, New. J. Phys. **5**, 113 (2003).

- [153] D. van Oosten, P. van der Straten and H. T. C. Stoof, *Quantum phases in an optical lattice*, Phys. Rev. A **63**, 053601 (2001).
- [154] E. Müller-Hartmann, *Correlated fermions on a lattice in high dimensions*, Z. Phys. B **74**, 507 (1989); *The Hubbard model at high dimensions: some exact results and weak coupling theory*, *ibid.* **76**, 211 (1989).
- [155] U. Brandt and C. Mielsch, *Thermodynamics and correlation functions of the Falicov-Kimball model in large dimensions*, Z. Phys. B **75**, 365 (1989); *Thermodynamics of the Falicov-Kimball model in large dimensions II*, *ibid.* **79**, 295 (1990); *Free energy of the Falicov-Kimball model in large dimensions*, *ibid.* **82**, 37 (1991).
- [156] P. G. J. van Dongen and D. Vollhardt, *Exact mean-field Hamiltonian for fermionic lattice models in high dimensions*, Phys. Rev. Lett. **65**, 1663 (1990).
- [157] M. Caffarel and W. Krauth, *Exact diagonalization approach to correlated fermions in infinite dimensions: Mott transition and superconductivity*, Phys. Rev. Lett. **72**, 1545 (1994).
- [158] M. H. Hettler, A. N. Tahvildar-Zadeh, M. Jarrell, T. Pruschke and H. R. Krishnamurthy, *Nonlocal dynamical correlations of strongly interacting electron systems*, Phys. Rev. B **58**, R7475 (1998).
- [159] G. Kotliar, S. Y. Savrasov, G. Palsson and G. Biroli, *Cellular dynamical mean field approach to strongly correlated systems*, Phys. Rev. Lett. **87**, 186401 (2001).
- [160] S. Fuchs, E. Gull, L. Pollet, E. Burovski, E. Kozik, T. Pruschke and M. Troyer, *Thermodynamics of the 3D Hubbard model on approaching the Néel transition*, Phys. Rev. Lett. **106**, 030401 (2011).
- [161] R. W. Helmes, T. A. Costi and A. Rosch, *Mott transition of fermionic atoms in a three-Dimensional optical trap*, Phys. Rev. Lett. **100**, 056403 (2008).
- [162] M. Snoek, I. Titvinidze, C. Töke, K. Byczuk and W. Hofstetter, *Antiferromagnetic order of strongly interacting fermions in a trap: real-space dynamical mean-field analysis*, New J. Phys. **10**, 093008 (2008).
- [163] C. Weitenberg, M. Endres, J. F. Sherson, M. Cheneau, P. Schauß, T. Fukuhara, I. Bloch and S. Kuhr, *Single-spin addressing in an atomic Mott insulator*, Nature (London) **471**, 319 (2011).
- [164] C. Weitenberg, P. Schauß, T. Fukuhara, M. Cheneau, M. Endres, I. Bloch and S. Kuhr, *Coherent light scattering from a two-dimensional Mott insulator*, Phys. Rev. Lett. **106**, 215301 (2011).

- [165] Private communication with Stefan Kuhr.
- [166] Ş. G. Söyler, B. Capogrosso-Sansone, N. V. Prokof'ev and B. V. Svistunov, *Sign-alternating interaction mediated by strongly correlated lattice bosons*, New J. Phys. **11**, 073036 (2009).
- [167] W. Hofstetter, J. I. Cirac, P. Zoller, E. Demler and M. D. Lukin, *High-temperature superfluidity of fermionic atoms in optical lattices*, Phys. Rev. Lett. **89**, 220407 (2002).
- [168] M. Popp, J.-J. Garcia-Ripoll, K. G. Vollbrecht and J. I. Cirac, *Ground-state cooling of atoms in optical lattices*, Phys. Rev. A **74**, 013622 (2006).
- [169] T. Ho and Q. Zhou, *Squeezing out the entropy of fermions in optical lattice*, Proc. Natl. Acad. Sci. U.S.A **106**, 6919 (2009).
- [170] T. Ho and Q. Zhou, *Universal cooling scheme for quantum simulation*, arXiv:0911.5506.
- [171] J. Catani, G. Barontini, G. Lamporesi, F. Rabatti, G. Thalhammer, F. Minardi, S. Stringari and M. Inguscio, *Entropy exchange in a mixture of ultracold atoms*, Phys. Rev. Lett. **103**, 140401 (2009).
- [172] D. M. Weld, H. Miyake, P. Medley, D. E. Pritchard and W. Ketterle, *Thermometry and refrigeration in a two-component Mott insulator of ultracold atoms*, Phys. Rev. A **82**, 051603 (2010).
- [173] B. Capogrosso-Sansone, Ş. G. Söyler, N. V. Prokof'ev and B. V. Svistunov, *Critical entropies for magnetic ordering in bosonic mixtures on a lattice*, Phys. Rev. A **81**, 053622 (2010).
- [174] R. C. Richardson, *The Pomeranchuk effect*, Rev. Mod. Phys. **69**, 683 (1997).
- [175] L. Luo, B. Clancy, J. Joseph, J. Kinast and J. E. Thomas, *Measurement of the entropy and critical temperature of a strongly interacting Fermi gas*, Phys. Rev. Lett. **98**, 080402 (2007).
- [176] A. Bulgac, J. E. Drut and P. Magierski, *Thermodynamics of a trapped unitary Fermi gas*, Phys. Rev. Lett. **99**, 120401 (2007).
- [177] G. B. Partridge, W. Li, R. I. Kamar, Y. Liao and R. G. Hulet, *Pairing and phase separation in a polarized Fermi gas*, Science **311**, 503 (2006).
- [178] J. T. Stewart, J. P. Gaebler, C. A. Regal and D. S. Jin, *Potential energy of a ^{40}K Fermi gas in the BCS-BEC crossover*, Phys. Rev. Lett **97**, 220406 (2006).

- [179] H. Hu, P. D. Drummond and X.-J. Liu, *Universal thermodynamics of strongly interacting Fermi gases*, Nat. Phys. **3**, 469 (2007).
- [180] S. Nascimbène, N. Navon, K. J. Jiang, F. Chevy and C. Salomon, *Exploring the thermodynamics of a universal Fermi gas*, Nature (London) **463**, 1057 (2010).
- [181] N. Navon, S. Nascimbène, F. Chevy and C. Salomon, *The equation of state of a low-temperature Fermi gas with tunable interactions*, Science **328**, 729 (2010).
- [182] M. Horikoshi, S. Nakajima, Masahito Ueda and T. Mukaiyama, *Measurement of universal thermodynamic functions for a unitary Fermi gas*, Science **327**, 442 (2010).
- [183] F. Werner, O. Parcollet A. Georges and S. R. Hassan, *Interaction-induced adiabatic cooling and antiferromagnetism of cold fermions in optical lattices*, Phys. Rev. Lett. **95**, 056401 (2005).
- [184] T. Paiva, R. Scalettar, M. Randeria and N. Trivedi, *Fermions in 2D optical lattices: temperature and entropy scales for observing antiferromagnetism and superfluidity*, Phys. Rev. Lett. **104**, 066406 (2010).
- [185] R. Jördens, L. Tarruell, D. Greif, T. Uehlinger, N. Strohmaier, H. Moritz, T. Esslinger, L. De Leo, C. Kollath, A. Georges, V. Scarola, L. Pollet, E. Burovski, E. Kozik and M. Troyer, *Quantitative determination of temperature in the approach to magnetic order of ultracold fermions in an optical lattice*, Phys. Rev. Lett. **104**, 180401 (2010).
- [186] A. Widera, O. Mandel, M. Greiner, S. Kreim, T. W. Hänsch and I. Bloch, *Entanglement interferometry for precision measurement of atomic scattering properties*, Phys. Rev. Lett. **92**, 160406 (2004).
- [187] T. Ho and Q. Zhou, *Intrinsic heating and cooling in adiabatic processes for bosons in optical lattices*, Phys. Rev. Lett. **99**, 120404 (2007).
- [188] S. S. Natu and E. J. Mueller, *Domain-wall dynamics in a two-component Bose-Mott insulator*, Phys. Rev. A **82**, 013612 (2010).
- [189] A. Kuklov, N. Prokof'ev and B. Svistunov, *Superfluid-superfluid phase transitions in a two-component Bose-Einstein condensate*, Phys. Rev. Lett. **92**, 030403 (2004).
- [190] A. Kuklov, N. Prokof'ev and B. Svistunov, *Commensurate two-component bosons in an optical lattice: ground state phase diagram*, Phys. Rev. Lett. **92**, 050402 (2004).

- [191] A. Argüelles and L. Santos, *Mott-insulator phases of nonlocally coupled one-dimensional dipolar Bose gases*, Phys. Rev. A **75**, 053613 (2007).
- [192] S. Gürtler, M. Troyer and F.-C. Zhang, *Quantum Monte Carlo study of a two-species bosonic Hubbard model*, Phys. Rev. B **77**, 184505 (2008).
- [193] L. Mathey, I. Danshita and C. W. Clark, *Creating a supersolid in one-dimensional Bose mixtures*, Phys. Rev. A **79**, 011602 (2009).
- [194] A. Hu, L. Mathey, I. Danshita, E. Tiesinga, C. J. Williams and C. W. Clark, *Counterflow and paired superfluidity in one-dimensional Bose mixtures in optical lattices*, Phys. Rev. A **80**, 023619 (2009).
- [195] C. Menotti and S. Stringari, *Detection of pair-superfluidity for bosonic mixtures in optical lattices*, Phys. Rev. A **81**, 045604 (2010).
- [196] M. Iskin, *Strong-coupling expansion for the two-species Bose-Hubbard model*, Phys. Rev. A **82**, 033630 (2010).
- [197] M. Iskin, *Mean-field theory for the Mott insulator-paired superfluid transition in the two-species Bose-Hubbard model*, Phys. Rev. A **82**, 055601 (2010).
- [198] P. Cheng and M.-F. Yang, *Quantum phase transitions in a two-species hard-core boson Hubbard model in two dimensions*, Phys. Rev. B **82**, 180510(R) (2010).
- [199] A. J. Daley, J. M. Taylor, S. Diehl, M. Baranov and P. Zoller, *Atomic three-body loss as a dynamical three-body interaction*, Phys. Rev. Lett. **102**, 040402 (2009).
- [200] Y.-W. Lee and M.-F. Yang, *Superfluid-insulator transitions in attractive Bose-Hubbard model with three-body constraint*, Phys. Rev. A **81**, 061604(R) (2010).
- [201] L. Bonnes and S. Wessel, *Pair superfluidity of three-body constrained bosons in two dimensions*, Phys. Rev. Lett. **106**, 185302 (2011).
- [202] Y.-C. Chen, K.-K. Ng and M.-F. Yang, *Quantum phase transitions in attractive extended Bose-Hubbard model with three-body constraint*, Phys. Rev. B **84**, 092503 (2011).
- [203] G. Thalhammer, G. Barontini, L. De Sarlo, J. Catani, F. Minardi and M. Inguscio, *Double species Bose-Einstein condensate with tunable interspecies interactions*, Phys. Rev. Lett. **100**, 210402 (2008).
- [204] U. Shrestha, *Antiferromagnetism in a bosonic mixture of rubidium (^{87}Rb) and potassium (^{41}K)*, Phys. Rev. A **82**, 041603(R) (2010).

- [205] C. A. Regal and D. S. Jin, *Measurement of positive and negative scattering lengths in a Fermi gas of atoms*, Phys. Rev. Lett. **90**, 230404 (2003).
- [206] A. Hu, L. Mathey, C. J. Williams and C. W. Clark, *Noise correlations of one-dimensional Bose mixtures in optical lattices*, Phys. Rev. A **81**, 063602 (2010).
- [207] M. J. Bhaseen, M. Hohenadler, A. O. Silver and B. D. Simons, *Polaritons and pairing phenomena in Bose-Hubbard mixtures*, Phys. Rev. Lett. **102**, 135301 (2009).
- [208] S. Fernández-Vidal, G. D. Chiara, J. Larson and G. Morigi, *Quantum ground state of self-organized atomic crystals in optical resonators*, Phys. Rev. A **81**, 043407 (2010).
- [209] A. Öttl, S. Ritter, M. Kohl and T. Esslinger, *Hybrid apparatus for Bose-Einstein condensation and cavity quantum electrodynamics: Single atom detection in quantum degenerate gases*, Rev. Sci. Instrum. **77**, 063118 (2006).
- [210] Here we choose the tight confinement $V_y = 30E_R$.
- [211] S. Balibar, *The enigma of supersolidity*, Nature (London) **464**, 176 (2010).
- [212] I. Titvinidze, M. Snoek and W. Hofstetter, *Supersolid Bose-Fermi mixtures in optical lattices*, Phys. Rev. Lett. **100**, 100401 (2008).
- [213] L. Pollet, J. D. Picon, H. P. Büchler and M. Troyer, *Supersolid phase with cold polar molecules on a triangular lattice*, Phys. Rev. Lett. **104**, 125302 (2010).
- [214] B. Capogrosso-Sansone, C. Trefzger, M. Lewenstein, P. Zoller and G. Pupillo, *Quantum phases of cold polar molecules in 2D optical lattices*, Phys. Rev. Lett. **104**, 125301 (2010).
- [215] K. Baumann, R. Mottl, F. Brennecke and T. Esslinger, *Exploring symmetry breaking at the Dicke quantum phase transition*, Phys. Rev. Lett. **107**, 140402 (2011).
- [216] D. Nagy, J. K. Asboth, P. Domokos and H. Ritsch, *Self-organization of a laser-driven cold gas in a ring cavity*, Europhys. Lett. **74**, 254 (2006).
- [217] Z. Hadzibabic, P. Krüger, M. Cheneau, B. Battelier and J. Dalibard, *Berezinskii-Kosterlitz-Thouless crossover in a trapped atomic gas*, Nature **441**, 1118 (2006); Z. Hadzibabic and J. Dalibard, *Two-dimensional Bose fluids: An atomic physics perspective*, Rivista del Nuovo Cimento **34**, 389 (2011).

- [218] U. Bissbort, S. Götze, Y.-Q. Li, J. Heinze, J. S. Krauser, M. Weinberg, C. Becker, K. Sengstock and W. Hofstetter, *Detecting the amplitude mode of strongly interacting lattice bosons by Bragg scattering*, Phys. Rev. Lett. **106**, 205303 (2011).
- [219] J. Larson and M. Lewenstein, *Dilute gas of ultracold two-level atoms inside a cavity: generalized Dicke mode*, New J. Phys. **11**, 063027 (2009).
- [220] D. Nagy, G. Kónya¹, G. Szirmai and P. Domokos, *Dicke-model phase transition in the quantum motion of a Bose-Einstein condensate in an optical cavity*, Phys. Rev. Lett. **104**, 130401 (2010).
- [221] S. Gopalakrishnan, B. L. Lev and P. M. Goldbart, *Emergent crystallinity and frustration with Bose-Einstein condensates in multimode cavities*, Nat. Phys. **5**, 845 (2009).
- [222] S. Yi and L. You, *Trapped atomic condensates with anisotropic interactions*, Phys. Rev. A **61**, 041604 (2000).
- [223] S. Yi and L. You, *Trapped condensates of atoms with dipole interactions*, Phys. Rev. A **63**, 053607 (2001).
- [224] K. Goral, K. Rzazewski and T. Pfau, *Bose-Einstein condensation with magnetic dipole-dipole forces*, Phys. Rev. A **61**, 051601 (2000).
- [225] L. Santos, G. V. Shlyapnikov, P. Zoller and M. Lewenstein, *Bose-Einstein condensation in trapped dipolar gases*, Phys. Rev. Lett. **85**, 1791 (2000).
- [226] S. Ronen, D. C. E. Bortolotti and J. L. Bohn, *Radial and angular rotons in trapped dipolar gases*, Phys. Rev. Lett. **98**, 030406 (2007).
- [227] J. Stuhler, A. Griesmaier, T. Koch, M. Fattori, T. Pfau, S. Giovanazzi, P. Pedri and L. Santos, *Observation of dipole-dipole interaction in a degenerate quantum gas*, Phys. Rev. Lett. **95**, 150406 (2005).
- [228] A. Griesmaier, J. Stuhler, T. Koch, M. Fattori, T. Pfau and S. Giovanazzi, *Comparing contact and dipolar interactions in a Bose-Einstein condensate*, Phys. Rev. Lett. **97**, 250402 (2006).
- [229] T. Lahaye, J. Metz, B. Fröhlich, T. Koch, M. Meister, A. Griesmaier, T. Pfau, H. Saito, Y. Kawaguchi and M. Ueda, *d-wave collapse and explosion of a dipolar Bose-Einstein condensate*, Phys. Rev. Lett. **101**, 080401 (2008).
- [230] K. Goral, L. Santos and M. Lewenstein, *Quantum phases of dipolar bosons in optical lattices*, Phys. Rev. Lett. **88**, 170406 (2002).
- [231] S. Yi, T. Li and C. P. Sun, *Novel quantum phases of dipolar Bose gases in optical lattices*, Phys. Rev. Lett. **98**, 260405 (2007).

- [232] L. Pollet, J. D. Picon, H. P. Büchler and M. Troyer, *Quantum phases of cold polar molecules in 2D optical lattices*, Phys. Rev. Lett. **104**, 125302 (2010).
- [233] M. Debatin, T. Takekoshi, R. Rameshan, L. Reichsöllner, F. Ferlaino, R. Grimm, R. Vexiau, N. Bouloufa, O. Dulieu and HC. Nägerl, *Molecular spectroscopy for ground-state transfer of ultracold RbCs molecules*, Phys. Chem. Chem. Phys. **13**, 18926 (2011).
- [234] E. Müller-Hartmann, *Correlated fermions on a lattice in high dimensions*, Z. Phys. B **74**, 507 (1989).
- [235] L. He and W. Hofstetter, *Supersolid phase of cold fermionic polar molecules in 2D optical lattices*, Phys. Rev. A **83**, 053629 (2011).
- [236] M. Boninsegni, *Supersolid phases of cold atom assemblies*, arXiv:1201.0980.
- [237] S. D. Huber, *Amplitude mode in the quantum phase model*, Phys. Rev. Lett. **100**, 050404 (2008).
- [238] J. T. Stewart, J. P. Gaebler and D. S. Jin, *Using photoemission spectroscopy to probe a strongly interacting Fermi gas*, Nature (London) **454**, 744 (2008).
- [239] C. Schori, T. Stöferle, H. Moritz, M. Köhl and T. Esslinger, *Excitations of a superfluid in a three-dimensional optical lattice*, Phys. Rev. Lett. **93**, 240402 (2004).
- [240] P. T. Ernst, S. Götze, J. S. Krauser, K. Pyka, D. Lühmann, D. Pfannkuche and K. Sengstock, *Probing superfluids in optical lattices by momentum-resolved Bragg spectroscopy*, Nat. Phys. **6**, 56 (2009).
- [241] D. Clément, N. Fabbri, L. Fallani, C. Fort and M. Inguscio, *Exploring correlated 1D Bose gases from the superfluid to the Mott-insulator state by inelastic light scattering*, Phys. Rev. Lett. **102**, 155301 (2009).
- [242] N. Fabbri, D. Clément, L. Fallani, C. Fort, M. Modugno, K. M. R. van der Stam and M. Inguscio, *Excitations of Bose-Einstein condensates in a one-dimensional periodic potential*, Phys. Rev. A **79**, 043623 (2009).
- [243] J. Stenger, S. Inouye, A. P. Chikkatur, D. M. Stamper-Kurn, D. E. Pritchard and W. Ketterle, *Bragg spectroscopy of a Bose-Einstein condensate*, Phys. Rev. Lett. **82**, 4569 (1999).
- [244] D. Stamper-Kurn, A. P. Chikkatur, A. Görlitz, S. Inouye, S. Gupta, D. E. Pritchard and W. Ketterle, *Excitation of phonons in a Bose-Einstein condensate by light scattering*, Phys. Rev. Lett. **83**, 2876 (1999).

- [245] J. J. Kinnunen and M. J. Holland, *Bragg spectroscopy of a strongly interacting Bose-Einstein condensate*, New J. Phys. **11** 013030 (2009).
- [246] S. D. Huber, E. Altman, H. P. Büchler and G. Blatter, *Dynamical properties of ultracold bosons in an optical lattice*, Phys. Rev. B **75**, 085106 (2007).
- [247] R. Roth and K. Burnett, *Dynamic structure factor of ultracold Bose and Fermi gases in optical lattices*, J. Phys. B **37**, 3893 (2004).
- [248] D. van Oosten, D. B. M. Dickerscheid, B. Farid, P. van der Straten and H. T. C. Stoof, *Inelastic light scattering from a Mott insulator*, Phys. Rev. A **71**, 021601(R) (2005).
- [249] G. Pupillo, A. M. Rey and G. G. Batrouni, *Bragg spectroscopy of trapped one-dimensional strongly interacting bosons in optical lattices: Probing the cake structure*, Phys. Rev. A **74**, 013601 (2006).
- [250] A. Rey, P. B. Blakie, G. Pupillo, C. J. Williams and C. W. Clark, *Bragg spectroscopy of ultracold atoms loaded in an optical lattice*, Phys. Rev. A **72**, 023407 (2005).
- [251] K. V. Krutitsky and P. Navez, *Excitation dynamics in a lattice Bose gas within the time-dependent Gutzwiller mean-field approach*, Phys. Rev. A **84**, 033602 (2011).
- [252] J. Ye, J. M. Zhang, W. M. Liu, K. Zhang, Y.-Q. Li and W. Zhang, *Light-scattering detection of quantum phases of ultracold atoms in optical lattices*, Phys. Rev. A **83**, 051604 (2011).
- [253] S. D. Huber, PhD Thesis, ETH Zürich (2008).
- [254] A. F. Ho, M. A. Cazalilla and T. Giamarchi, *Deconfinement in a 2D optical lattice of coupled 1D boson systems*, Phys. Rev. Lett. **92**, 130405 (2004); K. Sengupta, and N. Dupuis, *Mott-insulator-to-superfluid transition in the Bose-Hubbard model: A strong-coupling approach*, Phys. Rev. A **71**, 033629 (2005); M. A. Cazalilla, A. F. Ho and T. Giamarchi, *Interacting Bose gases in quasi-one-dimensional optical lattices*, New J. Phys. **8**, 158 (2006); P. Phipps, H. G. Evertz and M. Hohenadler, *Excitation spectra of strongly correlated lattice bosons and polaritons*, Phys. Rev. A **80**, 033612 (2009); T. D. Grass, F. E. A. dos Santos and A. Pelster, *Real-time Ginzburg-Landau theory for bosons in optical lattices*, Laser Phys. **21**, 1459 (2011).
- [255] C. Menotti and N. Trivedi, *Spectral weight redistribution in strongly correlated bosons in optical lattices*, Phys. Rev. B **77**, 235120 (2008); Y. Ohashi, M. Kitaura and H. Matsumoto, *Itinerant-localized dual character*

- of a strongly correlated superfluid Bose gas in an optical lattice*, Phys. Rev. A **73**, 033617 (2006).
- [256] D. M. Stamper-Kurn and W. Ketterle, *Spinor condensates and light scattering from Bose-Einstein condensates*, Proceedings of Les Houches 1999 Summer School, Session LXXII; arXiv:cond-mat/0005001, (2000).
- [257] D. Jaksch, V. Venturi, J. I. Cirac, C. J. Williams and P. Zoller, *Creation of a molecular condensate by dynamically melting a Mott insulator*, Phys. Rev. Lett. **89**, 040402 (2002).
- [258] M. Snoek and W. Hofstetter, *Two-dimensional dynamics of ultracold atoms in optical lattices*, Phys. Rev. A **76**, 051603(R) (2007).
- [259] D. van Oosten, P. van der Straten and H. T. C. Stoof, *Quantum phases in an optical lattice*, Phys. Rev. A **63**, 053601 (2001).
- [260] F. J. Harris, *On the use of windows for harmonic analysis with the discrete Fourier transform*, Proc. IEEE **66**, 51 (1978).
- [261] Y.-J. Lin, R. L. Compton, K. Jiménez-Garcá, J. V. Porto¹ and I. B. Spielman, *Synthetic magnetic fields for ultracold neutral atoms*, Nature (London) **462**, 628 (2009).
- [262] N. Goldman, I. Satija, P. Nikolic, A. Bermudez, M. A. Martin-Delgado, M. Lewenstein and I. B. Spielman, *Realistic time-reversal invariant topological insulators with neutral atoms*, Phys. Rev. Lett. **105**, 255302 (2010).
- [263] G. Wirth, M. ölschläger and A. Hemmerich, *Evidence for orbital superfluidity in the P-band of a bipartite optical square lattice*, Nat. Phys. **7**, 147 (2011).
- [264] J. K. Freericks and V. M. Turkowski, *Steady-state nonequilibrium dynamical mean-field theory and the quantum Boltzmann equation*, J. Phys.: Conf. Ser. **35**, 39 (2006).
- [265] A. Hubener, *Bosonische dynamische molekularefeld theorie*, Master Thesis, Frankfurt (2009).
- [266] G. Semerjian, M. Tarzia and F. Zamponi, *Exact solution of the Bose-Hubbard model on the bethe lattice*, Phys. Rev. B. **80**, 014524 (2009).

Acknowledgements

First I would like to thank Prof. Dr. Walter Hofstetter for hosting my Ph.D study in his research group at the institute of theoretical physics, Goethe-University Frankfurt. I thank him for introducing me into this challenging research area, for discussions on physics, and for careful proofreading of this thesis. I also want to thank Dr. Liang He, Dr. M. Reza Bakhtiari and Ulf Bissbort, who are my collaborators during my three-year study in Germany, for very helpful discussions and advices. I am really thankful to all people for proofreading my thesis and German corrections, Dr. Liang He, Dr. Daniel Cocks, Dr. Bernd Schmidt, Dr. Andrii Sotnikov, Ulf Bissbort, Michael Buchhold, and Eva Katharina Rafeld.

I thank David Roosen, Dr. Irakli Titvinidze, Denis Semmler, Julia Wernsdorfer, Ulf Bissbort, and Dr. Antonio Privitera for all their invaluable help when I first came to Germany. Special thanks to our group secretary Daniela Wirth-Pagano, not only for the constant and important support, but also for a kindness far beyond her working duties, which helped me a lot during the past three years.

Finally, I would also like to give special thanks to all my Chinese friends in the department of physics and Frankfurt University for their friendly helps, Dr. Qingguo Feng, Dr. Zhe Xu, Dr. Yuzhong Zhang, Dr. Chenguang Zhao, Qiuqin Zhou, Jiangcheng Lin, Ma Yi, Lei Kai, Dr. Jian Wu, Dr. Juan Shen, Qiyan Li, Jun Yang, and Qi Song. I enjoyed all my time with them in Germany.

Curriculum Vitae

Yongqiang Li

- Date of Birth: Dec. 22, 1983
- Place of Birth: Henan, China
- Nationality: Chinese
- Address: Institut für Theoretische Physik,
Goethe-Universität Frankfurt am Main
Max-von-Laue-Str. 1, 60438 Frankfurt am Main, Deutschland
- Phone: +49 (0) 69 798 47849
- E-Mail: liyq@itp.uni-frankfurt.de

Education

- **Feb. 2009 -**, Ph.D, Institute of Theoretical Physics, Goethe-University Frankfurt, Frankfurt/M, Germany,
Thesis: *Strongly Correlated Ultracold Gases in an Optical Lattice*
Advisor: Prof. Dr. Walter Hofstetter
- **Sep. 2005 - Dec. 2007**, M.Sc, Atomic and Molecular Physics, Institute of Physics, National University of Defense Technology, Changsha, P. R. China,
M.Sc thesis: *Influence of Screening Effect of Hot and Dense Plasma on Atomic Properties*
Advisor: Prof. Jianmin Yuan
- **Sep. 2001 - Jun. 2005**, B.Sc, Institute of Applied Physics, National University of Defense Technology, Changsha, P. R. China,
B.Sc thesis: *Calculation of Transitions and Oscillator Strengths for BrXXVI, BrXXVII and BrXXVIII*
Advisor: Prof. Jianmin Yuan

Language skill

Mandarin (native), English (fluent), German (Basic)

Computer skill

OS: Linux, Windows; Programming: C++, FORTRAN, Mathematica

Research interests and techniques

- Novel quantum many-body systems
- Quantum phase transition

- Cross research of ultracold gases, condensed matter physics and quantum optics
- Strongly correlated ultracold gases in optical lattices
- Bose-Bose mixtures in an optical lattice
- Cooling scheme for strongly correlated ultracold gases
- Ultracold bosonic gases in an optical cavity
- Dipolar bosonic gases
- Spectroscopy of strongly correlated bosonic gases
- Bose-Hubbard model
- Bosonic Dynamical Mean Field Theory (BDMFT)
- Time-dependent Gutzwiller method
- Computational physics

Publications

1. Y.-Q. Li, L. He and W. Hofstetter, *Quantum phases of two-component dipolar bosonic gases in an optical lattice*, in preparation.
2. Y.-Q. Li, L. He and W. Hofstetter, *Supersolid phase of strongly correlated bosons in an optical cavity*, arXiv:1205.0813.
3. L. He, Y.-Q. Li, E. Altman and W. Hofstetter, *Magnetic phases of two-component ultracold bosons in a triangular lattice*, arXiv:1205.1806.
4. Y.-Q. Li, L. He and W. Hofstetter, *Anisotropic pair-superfluidity of trapped two-component Bose gases in an optical lattice*, arXiv:1203.4262.
5. Y.-Q. Li, R. Bakhtiari, L. He and W. Hofstetter, *Pomeranchuk effect and spin-gradient cooling of Bose-Bose mixtures in an optical lattice*, Phys. Rev. A **85**, 023624 (2012).
6. Y.-Q. Li, R. Bakhtiari, L. He and W. Hofstetter, *Tunable anisotropic magnetism in trapped two-component Bose gases*, Phys. Rev. B **84**, 144411 (2011).
7. U. Bissbort, S. Götze, Y.-Q. Li, J. Heinze, J. S. Krauser, M. Weinberg, C. Becker, K. Sengstock and W. Hofstetter, *Detecting the amplitude mode of strongly interacting lattice bosons by Bragg scattering*, Phys. Rev. Lett. **106**, 205303 (2011).
8. Y.-Q. Li, J.-H. Wu, Y. Hou and J.-M. Yuan, *Radiative opacities of hot solid-density aluminum plasma using a detailed level accounting model*, J. Phys. B **42**, 235701 (2009).
9. Y.-Q. Li, J.-H. Wu, Y. Hou and J.-M. Yuan, *Changes of transition energies and oscillator strengths of ions in hot and dense plasma: beryllium-like ions for $Z=26-36$* , J. Phys. B **41**, 145002 (2008).
10. Y.-Q. Li, J.-H. Wu, Y. Hou and J.-M. Yuan, *Changes of ionization energies of ions in hot and dense plasma: beryllium-like ions for $Z=26-36$* , Chin. Phys. Lett. **25**, 3627 (2008).
11. Y.-Q. Li, J.-H. Wu and J.-M. Yuan, *Influence of debye-screening on atomic energy levels and oscillator strengths*, Acta Physica Sinica **57**, 4042 (2008).